論文 / 著書情報
Article / Book Information

題目(和文)	イッテルビウム量子気体顕微鏡
Title(English)	Quantum gas microscope for ytterbium atoms
著者(和文)	ﾐﾗﾝﾀﾞ ﾏﾙﾃｨﾝ
Author(English)	Martin Miranda
出典(和文)	学位:博士(理学), 学位授与機関:東京工業大学, 報告番号:甲第10063号, 授与年月日:2016年3月26日, 学位の種別:課程博士, 審査員:上妻 幹旺,金森 英人,古賀 昌久,西田 祐介,相川 清隆
Citation(English)	Degree:Doctor (Science), Conferring organization: Tokyo Institute of Technology, Report number:甲第10063号, Conferred date:2016/3/26, Degree Type:Course doctor, Examiner:,,,,
学位種別(和文)	博士論文
Type(English)	Doctoral Thesis

Quantum gas microscope for ytterbium atoms

Martin Santiago Miranda

A thesis presented for the degree of

Doctor of Philosophy

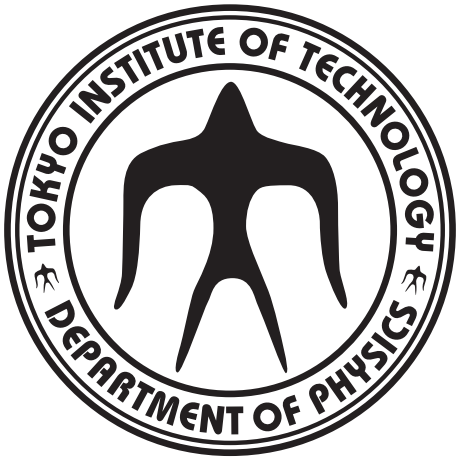

Department of Physics

Tokyo Institute of Technology

Japan

Abstract

In this thesis I report a microscope system for fluorescence imaging of ultra-cold ytterbium atoms trapped in a two-dimensional optical lattice with single-site resolution.

Having a rich variety of isotopes, ytterbium atoms trapped in two-dimensional optical lattices are a promising tool to study many-body quantum phenomena resulting from strongly interacting systems. In particular, quantum simulators using fermionic atoms are useful for studying the Fermi-Hubbard model, which is expected to be the key to elucidate the mechanism of high temperature superconductors.

In order to observe atoms trapped in an optical lattice, a large number of photons is required to obtain a well resolved image. In contrast with to the conventional method of laser-cooling the atoms while observing their fluorescence, in this experiment a deep potential was created using a combination of a shallow ground-state and a deep excited-state potentials, which confines the heated atoms during the imaging process. The resulting quantum gas microscope was able to resolve individual lattice sites in an optical lattice with a 544 nm spacing.

And I'm not happy with all the analyses
that go with just the classical theory,
because nature isn't classical, dammit,
and if you want to make a simulation of nature,
you'd better make it quantum mechanical,
and by golly it's a wonderful problem,
because it doesn't look so easy.

Richard Feynman

Contents

Chapter 1

Introduction

1.1 Historical background of laser cooling

Laser cooling was proposed independently by Hänsch and Schawlow [1] and Wineland and Dehmelt [2] in 1975 and first realized experimentally in 1978 using magnesium ions [3]. The laser cooling techniques were soon extended to neutral atoms in 1981, when an atomic beam of sodium atoms was slowed down to 1.5 K using a resonant laser beam. This was later improved in 1982, when the Zeeman slower technique was successfully used to reduce the temperature of a sodium atomic beam to less than a few tens of mK [4, 5].

One of the most important applications of laser cooling at that time was the possibility of increasing the accuracy of spectroscopy experiments and atomic clocks, which were mainly limited by Doppler effects and time-dilatation shifts [6]. The current definition of a second is the duration of 9192631770 cycles of radiation corresponding to the transition between the two hyperfine levels of the ground state of the cesium-133 atom. Since the realization of laser cooling, the uncertainty of these cesium atomic clocks improved ∼100 times to reach a value of nearly $\sim 3 \times 10^{-16}$. That is, the clock will not gain nor lose a second in more than 100 million years. As big as this number may seem, a new emerging technology called "optical lattice clocks" [7, 8] further improved this number by two orders of magnitude [9, 10] by exploiting optical transitions of ultra-cold neutral atoms, which have frequencies five order of magnitude larger than hyperfine transitions. Today, laser cooling continues to be a fundamental tool for maintaining frequency standards which support our daily lives through global positioning systems (GPS).

In recent years, laser cooling has also become a state-of-the-art tool to investigate many-body physics in the condensed matter field. When atoms are laser cooled to very low temperatures, their spatial extent of the wave packet, which is determined by the thermal de Broglie length $\lambda_{dB} = \sqrt{\frac{2\pi\hbar^2}{m k_B T}}$, increases. When the inter-atomic distance is comparable with the thermal de Broglie length, the wave packets of each atom start to overlap and quantum effects

become important. In the case of bosonic particles, the atomic cloud undergoes a quantum-mechanical phase transition and form a Bose-Einstein condensate (BEC) at $n_0\lambda_{dB}^3 \approx 2.6$, where n_0 is the peak atomic number density.

The history of BEC reaches back to 1924, when Satyendra Nath Bose and Albert Einstein predicted the existence of a new state of matter [11, 12]. In 1937, Kaptisa, Allen and Misener reduced the temperature of ^{4}He and observed that the liquid helium flowed with no viscosity at temperatures below 2.17 K [13, 14]. One year later, theoretical work by Fritz London showed that the zero viscosity phonema observed in liquid helium was evidence of a new superfluid state of matter, which is intimately related to the BEC of the bosonic ^{4}He [15]. The existence and the size of the BEC fraction in superfluid remained controversial for many years, mainly hindered by presence of strong interactions between the atoms in the liquid. In 1968, a ∼10% condensate fraction was observed using neutron scattering techniques [16, 17, 18].

With the aid of laser cooling and evaporative cooling [19] techniques, the first realization of a "pure" BEC in sodium and rubidium was reported by Nobel prize winners Wieman, Cornell and Ketterle [20, 21] in 1995. In contrast with the BEC of helium where the atoms in the liquid are strongly interacting, the condensates formed with ultra-cold gases allowed researchers to study the properties of weakly interacting systems. In the last 20 years the research on BEC has grown explosively, resulting in the observation of many fascinating physics such as condensate interference [22], Anderson localization [23, 24], vortex lattices [25, 26], Berezinskii-Kosterlitz-Thouless transition [27], Feschbach resonances [28, 29], Efimov quantum states [30] and the BCS-BEC crossover [31, 32, 33, 34, 35, 36, 37].

1.2 Quantum simulation and high temperature superconductors

Realization of everyday practical applications is one of the major tasks for laser cooled condensed matter. Ultra-cold atoms trapped in periodical potentials created by light interference (i.e. optical lattices) demonstrated to be a novel tool for studying interacting many-body quantum systems and creating quantum simulators [38, 39], which serve as a tool to understand the physics of solids. Fermionic atoms trapped in optical lattices, in particular, are optimal for simulating the Fermi-Hubbard model, which is believed to be the key to elucidate the mechanism of cuprates high temperature superconductors [40, 41, 42, 43, 44]. Understanding such mechanism could lead to the discovery of room-temperature superconductors, producing a huge impact in our daily lives through the improvement on generation and distribution of electric power, transportation (magnetic levitation), medicine (MRI) and the production of faster and more efficient microprocessors.

Why do we need quantum simulators to study cuprate superconductors? Thirty years have passed since Nobel prize winners Bednorz and Muller first discovered cuprate high tem-

perature superconductors in 1986, but the mechanism responsible of generating these material is still not completely understood. Solid-state physics phenomena resulting in cuprate superconductors is characterized by the movement of electrons inside a crystalline structure. As the electrons are strongly correlated to each other due to the Coulomb interaction between them, a complete understanding of a single electron state requires the knowledge of the state of all the remaining electrons. In order to simulate strongly correlated quantum system like this using a classical computer, the required number of bits would scale exponentially with the size of the system. Quantum Monte Carlo (QMC) methods, which are effective for solving the Bose-Hubbard Model, notoriously suffer from the so-called "minus sign problem" [45] when solving the Fermi-Hubbard Model. Using ultra-cold neutral atoms trapped in optical lattice can circumvent this problem, as the quantum simulation of the Fermi-Hubbard model can be realized in an experimental way.

In recent years, Markus Greiner team in Harvard University successfully implemented a quantum gas microscope with a resolution of 600 nm capable to address single atoms trapped in a two-dimensional optical lattice [46]. By using a system comprised by a solid immersion lens (SIL) and a high numerical aperture objective lens (NA=0.55), they successfully detected single rubidium atoms in a two-dimensional optical lattice. Later in 2010, Immanuel Bloch team also implemented a high resolution microscope capable of addressing individual Rb atoms using a very high resolution objective lens (NA=0.68) [47]. Several demonstrations of a quantum simulators were realized with the assistance of quantum gas microscopes, including the simulation of antiferromagnetic spin chains [48], quantum walks [49], and Ising quantum magnets [50]. Since the creation of these magnificent tools used to observe and manipulate rubidium atoms with single-site resolution, the number of researchers trying to develop quantum gas microscopes for other species, which would allow them to simulate a wider diversity of systems such as strongly correlated Fermi-Hubbard systems, have increased. It was not until 2014 that this technology was successfully extended to ytterbium atoms (this work [51]), and in 2015, to lithium [52, 53, 54], potassium [55, 56, 57] and also ytterbium on a different way [58].

1.3 Purpose of this thesis

The final objective of our research is to realize the quantum simulation of the Fermi-Hubbard model. One of the biggest challenges to overcome is that the temperature required to reach d-wave superfluidity is below the Neel temperature, which is in the order of $T_n/T_F \approx 0.01$, where T_F is the Fermi temperature [59]. Currently, the minimum temperature obtained with fermionic species is in the order of $T/T_F \approx 0.1$, which is one order of magnitude higher than the required temperature. Another difficulty is that temperatures below $T/T_F \approx 0.1$ cannot be

measured using the time-of-flight technique [59]. One idea to reduce the temperature of the atoms is to realize spatial filtering [60], which consists in tailor the lattice potential to create high entropy regions than can be later removed. To measure the temperature, instead of measuring the momentum distribution using the time-of-flight technique it is possible to obtain the temperature from Quantum Monte Carlo fittings of the in-situ distributions. Both of these techniques, however, require that atoms are resolved with single-site resolution. Although a quantum gas microscope is capable of measuring and the optical lattice with single-site resolution, when I started my research the technology was only available for rubidium atoms which have only bosonic isotopes.

The purpose of this thesis is to realize a quantum gas microscope of ytterbium atoms, which have a fermionic isotope (^{173}Yb). One of the advantages of Yb is that the ground state is $^1S_0$, and thus, there is no electronic spin in the ground state resulting in low decoherence times due to magnetic-field fluctuations. Also, the absence of total angular momentum ($J = 0$) results in SU(N) symmetry which prevents spin exchanging collisions. Additionally, Yb have two metastable states with lifetime of several tens of seconds, which are useful for high-resolution spectroscopy [61] and for cooling fermionic atoms in a optical lattice through spacial filtering [60]. The $^3P_2$ state can also be used to to tune inter-atomic interactions through Feshbach resonances [62].

To test the performance of a quantum gas microscope it is convenient to start with the ^{174}Yb bosonic isotope, which have simpler energy structure due to the lack of hyperfine splitting. The quantum gas microscope presented in this work uses the bosonic isotope, but the same method can be applied to the fermionic isotope without major modifications of the system, as explained in the last chapter.

1.4 Thesis overview

This thesis is organized as follows:

Chapter 2: Ytterbium

A briefly description of the properties of Yb atoms and the most important energy levels.

Chapter 3: Quantum gas microscope

This chapter centers in explaining the requirements of a quantum gas microscope and analyzing the possible fluorescence imaging strategies applicable to Ytterbium atoms. The “deep potential” strategy used to obtain a large number of photons during imaging is explained in detail, together with simulations to test the feasibility of the method.

Chapter 4: Experiment: Transport of atoms to the SIL surface

To create a two-dimensional optical lattice with trapped Yb atoms, atoms are first re-

quired to be confined in a pancake-shaped region which is thinner than the depth of field of the objective lens. This chapter focuses in the experimental method used to transport ultra-cold Yb atoms under the surface of the solid immersion lens. The "optical accordion" technique used to create a Bose-Einstein condensate and compress the atoms into a thin layer is also explained in detail.

Chapter 5: Experiment: Fluorescence imaging

In this chapter, the experimental method to load the thin condensate of atoms under the surface of the solid immersion lens into a two-dimensional optical lattice is first explained, followed by an analysis of the fluorescence images that were obtained with the quantum gas microscope using the "deep potential" strategy.

Chapter 6: Extension to fermionic isotopes

This chapter focuses in the requirements to extend the quantum gas microscope of ytterbium atoms to the ^{173}Yb fermionic isotope.

1.5 List of publications

The most relevant parts of this thesis have been summarized in the following journal articles:

- M. Miranda, A. Nakamoto, Y. Okuyama, A. Noguchi, M. Ueda, and M. Kozuma, *All-optical transport and compression of ytterbium atoms into the surface of a solid immersion lens*, Physical Review A **86**, 063615 (2012).

- Martin Miranda, Ryotaro Inoue, Yuki Okuyama, Akimasa Nakamoto, and Mikio Kozuma, *Site-resolved imaging of ytterbium atoms in a two-dimensional optical lattice*, Physical Review A **91**, 063414 (2015).

The following journal article is also related to this thesis:

- Toshiyuki Hosoya, Martin Miranda, Ryotaro Inoue, and Mikio Kozuma, *Injection locking of a high power ultraviolet laser diode for laser cooling of ytterbium atoms*, Review of Scientific Instruments **86**, 073110 (2015).

Chapter 2

Ytterbium

Ytterbium is a rare earth element and member of the lanthanoid group with atomic number 70 and chemical symbol Yb. With only two electrons in the outermost shell resulting in the absence of electronic spin in the ground state, the Yb atom have a similar energy structure compared with other alkaline-earth-metal-like such as Ca, Sr, and Hg.

2.1 General properties

Naturally occurring ytterbium is composed of seven stable isotopes, five of which are fermions and two are bosons. The natural abundance and nuclear spin of each isotope is summarized in Table 2.1. Compared to other elements, the abundance is more homogeneously distributed between the isotopes.

Mass number	Natural abundance	Nuclear Spin	Type
168	0.13	0	Boson
170	3.05	0	Boson
171	14.3	1/2	Fermion
172	21.9	0	Boson
173	16.12	5/2	Fermion
174	31.8	0	Boson
176	12.7	0	Boson

Table 2.1: Stable isotopes of Yb [63]

At room temperature, Yb is a solid metal with silvery color, having an atomic mass of 173.04, a density of 6.97 g/cm^3, and melting point of 1097 K. Ytterbium is mostly non reactive, reacting very slowly to oxygen and water. Due to the high melting point, the saturated vapor pressure at room temperature is very low, thus requiring heating up to 700 K in order to obtain sufficient gas for the experiments.

2.2 Energy structure

Ytterbium have two valence electrons in the outermost shell resulting in a $^1S_0$ ground state with no electronic spin. Similar to other alkaline-earth-metal-like species the excited states are singlet ($S = 0$) or triplet ($S = 1$) states. The energy levels up to 45000 cm^{-1} are summarized in Fig. 2.1. All energy levels were represented by the term symbol $^{2S+1}L_J$, where S is the total electronic spin ($2S+1$ is the multiplicity), L is the total orbital angular momentum of all the electrons in the system (represented by the letters S, P, D for $L = 0,\ldots,2$), and J is the total angular momentum of the system. The important transitions are briefly described bellow.

^{1}S$_0$ $\longleftrightarrow$ ^{1}P$_1$ (399 nm)

An electric dipoled (E1) allowed transition resulting in a strong linewidth of $\Gamma/2\pi =$ 27.9 MHz. The strong radiative pressure of this transition is useful for Zeeman slowing of the atomic beam. In this experiment, this transition was used for fluorescence imaging the atoms in the two-dimensional optical lattice. Additionally, absorption imaging of the atoms is realized using this transition. This transition is essentially cyclic, with a very small branching ratio of roughly 10^{-7} to the $^3D_1$ and $^3D_2$ states [64].

^{1}S$_0$ $\longleftrightarrow$ ^{3}P$_1$ (556 nm)

This singlet to triplet transition is prohibited by the LS coupling selection laws. For heavy atoms as Ytterbium, JJ coupling between the orbital and spin motion in the two valence electrons results in the relaxation of the selection law, resulting in this intercombination transition. With a linewidth of $\Gamma/2\pi = 181$ kHz, this cyclic transition have a low Doppler cooling limit and is ideal for laser cooling in the magneto optical trap.

^{1}S$_0$ $\longleftrightarrow$ ^{3}P$_0$ (578 nm)

In this double forbidden transition, the $^3P_0$ state is very weakly coupled to the ^{1}S$_0$ ground state with decay rates in the order of tens of millihertz. The resulting ultra-narrow transition is called clock-transition. In contrast with the ^{1}S$_0$ $\longleftrightarrow$ $^3P_2$ ultra-narrow transition, the absence of electronic angular momentum in the excited state reduces the effects of magnetic fields, making this transition ideal for the creation of a new frequency standard[65, 66]. Additionally, this transition was implemented for the study of two-orbital SU(N) systems [67], and proposed for the implementation in quantum computation [68] and side-band cooling [69].

^{1}S$_0$ $\longleftrightarrow$ ^{3}P$_2$ (507 nm)

This quadruple magnetic (M2) transition is also an ultra-narrow transition with a linewidth of a few tens of millihertz. In contrast with the ^{1}S$_0$ $\longleftrightarrow$ $^3P_0$ clock transition, the excited state have a large magnetic dipole moment of $3\mu_B$, which is useful to tune dipole-dipole interactions between atoms in an optical lattice [70]. In recent experiments, the narrow

linewidth advantage of this transition was effectively utilized to optical-spectral and magnetic-resonant imaging of atoms trapped in optical lattices [61, 71].

$^1S_0 \longleftrightarrow {}^3D_2$ (404 nm)

This quadrupole dipole (E2) transition with a linewidth of $\Gamma/2\pi = 350$ kHz is useful to excite atoms to the $^3P_2$ and $^3P_0$ states through optical pumping. Atoms excited to the $^3D_2$ state decay into the $^3P_{1,2}$ states with a ratio of 20:3. As the atoms in the $^3P_1$ state decay back to the ground state, after a few cycles all the atoms can be pumped into the $^3P_2$ state [72]. Additionally, by combining the $^1S_0 \longleftrightarrow {}^3D_2$ transition with the dipole allowed $^3P_2 \longleftrightarrow {}^3S_1$ transition, it is possible realize optical pumping to the $^3P_0$ state.

$^1P_1 \longleftrightarrow (6s7s)^1S_0$ (1077 nm)

This dipole allowed transition from the excited $^1P_1$ have a linewidth of $\Gamma/2\pi = 3.0$ MHz was used in this experiment to produce a deep potential in the excited $^1P_1$ state. Atoms excited to the $(6s7s)^1S_0$ state also weakly decay to the $^3P_1$ state with a decay rate of $2\pi \times$ 0.2 MHz [73].

2.3 Scattering lengths

The scattering length of each isotope was estimated in previous experiments using two-color photoassociation spectroscopy [74]. The values for the bosonic ^{174}Yb isotope and the fermionic isotopes (^{171}Yb and ^{173}Yb) were summarized in Table 2.2.

	171	173	174
171	-0.15(19)	-30.6(3.2)	22.7(7)
173		10.55(11)	7.34(8)
174			5.55(8)

Table 2.2: Calculated s-wave scattering lengths in nm for the ^{171}Yb, ^{173}Yb and ^{174}Yb isotopes [74].

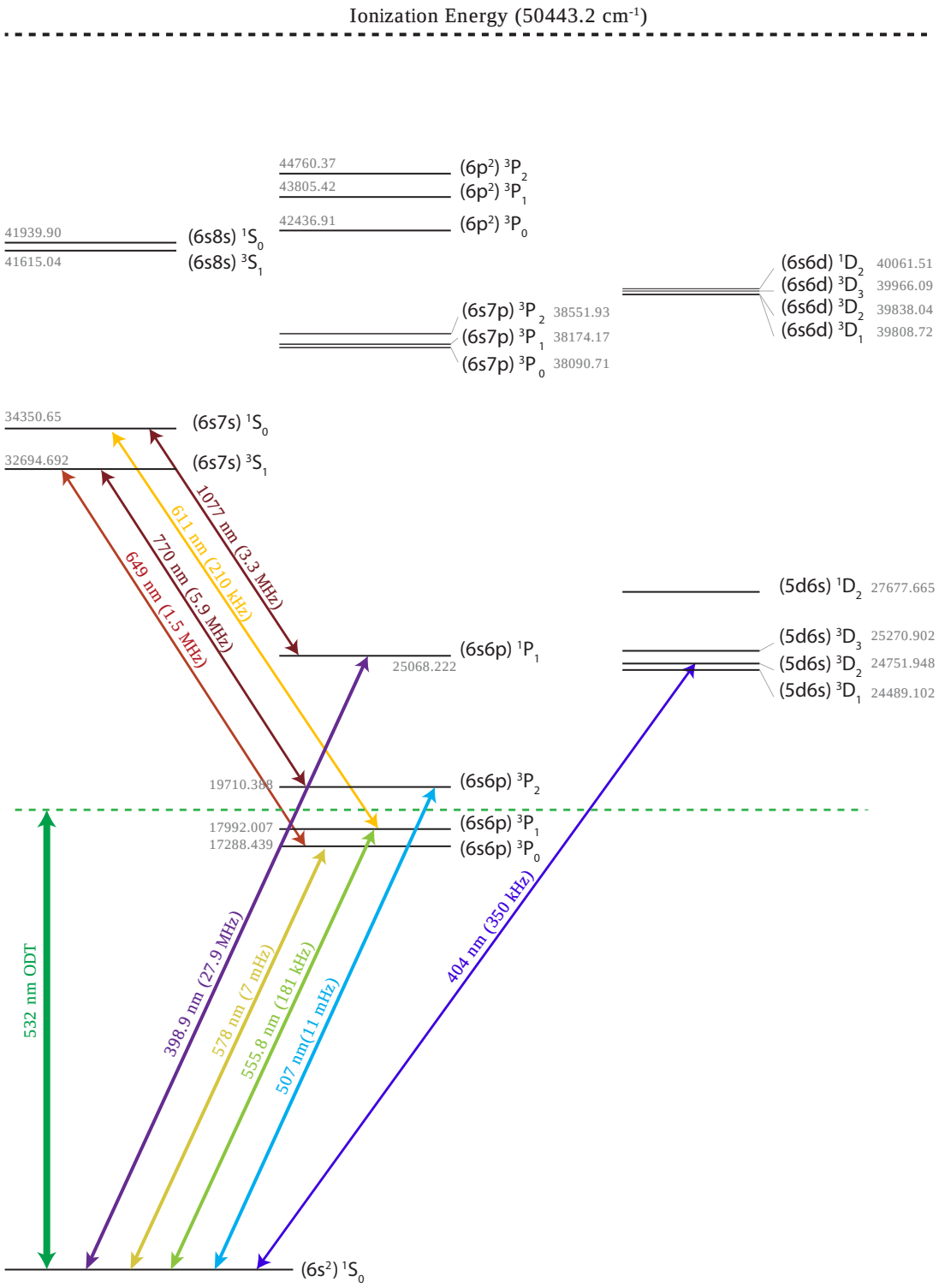

Figure 2.1: Ytterbium energy levels.

Atomic Mass	Isotope Shift (MHz)	Frequency (MHz)
176	-509	751 525 478.5
173(5/2-5/2)	-253	751 525 734.3
174	0	751 525 987.7
173(5/2-3/2)	516	751 526 503.7
172	533	751 526 521.1
173(5/2-7/2)	588	751 526 575.7
171(1/2-3/2)	832	751 526 820.2
171(1/2-1/2)	1154	751 527 141.5
170	1192	751 527 180.2
168	1887	751 527 875.2

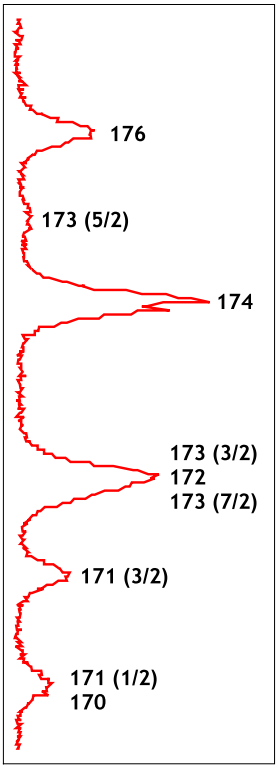

Table 2.3: Isotope shifts and absolute frequencies of the $^1S_0 \rightarrow {}^1P_1$ transition [75].

Atomic Mass	Isotope Shift (MHz)	Frequency (MHz)
173(5/2-7/2)	-2386.7	539 384 174.1
171(1/2-1/2)	-2132.0	539 384 428.8
176	-954.8	539 385 606
174	0	539 386 560.8
172	1000.0	539 387 560.8
170	2286.3	539 388 847.2
173(5/2-5/2)	2311.4	539 382 339.8
168	3655.1	539 380 996.1
171(1/2-3/2)	3804.6	539 380 846.0
173(5/2-3/2)	3805.7	539 380 843.9

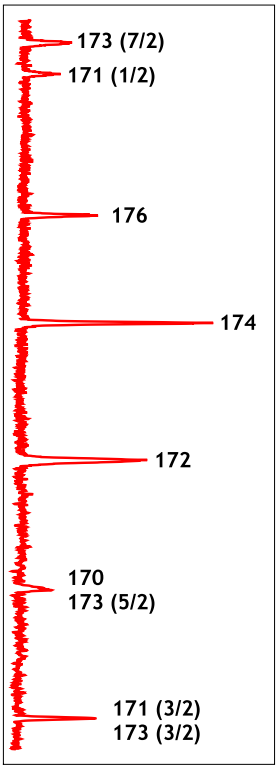

Table 2.4: Isotope shifts and absolute frequencies of the $^1S_0 \rightarrow {}^3P_1$ transition [76, 77].

Chapter 3

Quantum gas microscope

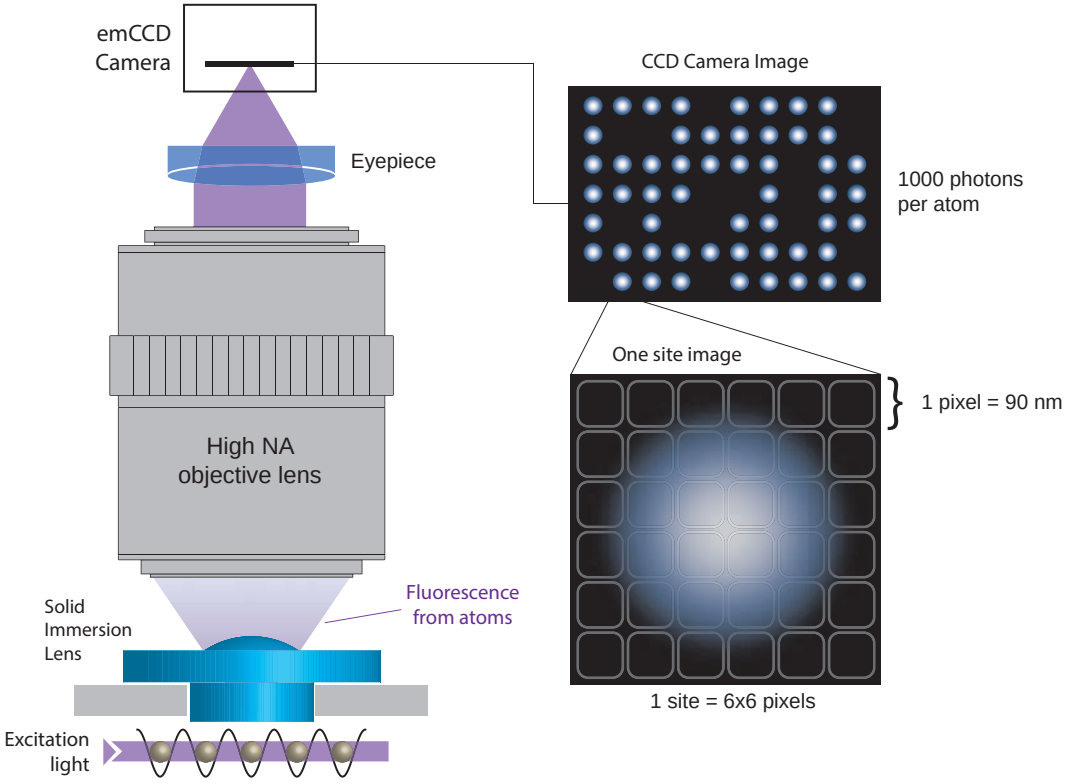

Figure 3.1: Schematic of a quantum gas microscope. The fluorescence from the atoms trapped in a two-dimensional are captured by a high-numerical-aperture microscope and imaged with a CCD camera.

Quantum gas microscopes are high-resolution fluorescence imaging devices capable of resolving individual atoms trapped in a two-dimensional optical lattice [47, 46]. The conventional method to observe atoms trapped in an optical lattice is to excite the atoms and observe the resulting fluorescence using a high-numerical-aperture microscope. Due to the large number of photons required to obtain a well-resolved image, a deep lattice potential is necessary to keep the heated atoms trapped during the imaging process. In the case of rubidium atoms, the polarization- gradient-cooling technique [46, 47, 78] worked effectively

to overcome this difficulty, as it could cool down the atoms to sub-Doppler temperatures while the resultant fluorescence was observed. Unfortunately, this technique is not effective for all the atomic species. In the case of bosonic Yb atoms, for example, the lack of hyperfine splitting makes impossible the application of sub-Doppler cooling mechanisms such as polarization-gradient-cooling, Raman cooling [79, 80, 81, 56, 52], and electromagnetically induced transparency cooling [82, 83, 55].

3.1 Sub-Doppler cooling methods in alkali atoms

In QGM experiments using alkali atoms such as rubidium, lithium and potassium, sub-Doppler techniques are utilized to cool down the atoms while the resultant fluorescence is collected. Temperatures lower than the Doppler cooling limit resulted in trap lifetimes much larger than the exposure(irradiation) time, which is a required condition to obtain a high fidelity in the fluorescence measurement.

3.1.1 Polarization gradient cooling

In the case of rubidium, the polarization gradient cooling technique was utilized. This technique is schematized in Fig. 3.2. First, two counter-propagating beams having linear polarization, which each polarization orthogonal to each other, are used to create a polarization gradient field.

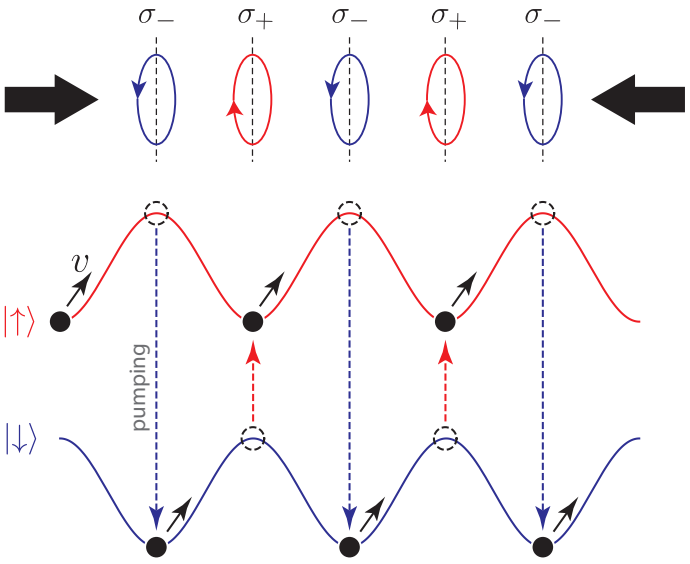

Figure 3.2: Polarization gradient cooling. Two counter-propagating beams with linear and orthogonal polarization create a polarization gradient field. An atom traveling trough this field is repetitively repumped 'downhill' resulting in Sisyphus cooling.

To understand why this field is generated, each of the beams can be written as a superpo-

sition of σ_+ and σ_- polarization beams:

$$E_+ = \frac{1}{\sqrt{2}} \begin{pmatrix} 1 \\ 1 \end{pmatrix} e^{i(kx-\omega t)} \quad , \quad E_- = \frac{1}{\sqrt{2}} \begin{pmatrix} i \\ -i \end{pmatrix} e^{i(-kx-\omega t)}. \tag{3.1}$$

The interference of this two beams produces two independent standing waves for the circular polarizations σ_+ and σ_-, having a relative phase of $\pi/2$:

$$|E_+ + E_-|^2 \propto \begin{pmatrix} \sin^2(kx - \pi/4) \\ \sin^2(kx + \pi/4) \end{pmatrix} \tag{3.2}$$

Next, consider a system having states $|\uparrow\rangle$ and $|\downarrow\rangle$ which only couples to the σ_- and σ_+ polarization, respectively. Suppose, as in Fig. 3.2 that the atom initially has a state $|\uparrow\rangle$ where the potential is minimum. As the atom moves climbing the potential wall, the intensity of the σ_+ standing wave decreases while the intensity of the σ_- one increases. Around the potential maxima, the σ_- light repumps the atom to the $|\downarrow\rangle$ state. In this state, the potential is again a minimum, and the atom will continue moving in the same direction climbing the potential wall, until the σ_- standing wave intensity decreases again and the atom is repumped back to the $|\uparrow\rangle$ state. As the atom repetitiously climb the potential wall, the velocity of the atom can be reduced. This cooling mechanism was named Sisyphus cooling in honor to the king of Ephyra in the Greek mythology, who was punished to roll a heavy ball up to a hill and to throw it back down, repeating this process indefinitely.

The resultant temperature using this cooling method can reach much lower values than the Doppler limit:

$$T \approx \frac{\hbar\Omega^2}{8\Delta} \tag{3.3}$$

as the temperature can be reduced by increasing the detuning Δ of the cooling beams while decreasing their Rabi frequency (laser intensity) Ω^2. Using a large detuning Δ is also an important feature of this cooling method, as it makes it robust against the inhomogeneities of the light shift in the space produced by the AC Stark shift of the optical lattice. Notice, however, that the trade-off for having low atom temperatures is a reduced photon emission rate, and a lower velocity trap range.

3.1.2 Side-band cooling

Side-band cooling is a technique originally used to cool down ions tightly trapped in a harmonic potential. Consider a two level system with ground state $\left|g\right\rangle$ and an excited state $|e\rangle$ with a transition frequency ω_0. When the oscillator quantum vibrational separation ω is suffi-

ciently large, the system can be well described by the eigenstates $|g,n\rangle, |e,m\rangle$, where n and m represent the vibrational energy. A laser light with frequency ω_L couples each of the ground states $|g,n\rangle$ with the excited states $|e,m\rangle$ at the transition frequencies $\omega_L = \omega_0 + (m-n)\omega$. When the natural linewidth of the $|g\rangle \rightarrow |e\rangle$ transition Γ is sufficiently smaller than ω, it is possible to resolve each of the resonances $|g,n\rangle \rightarrow |e,m\rangle$ in the spectrum. The transition corresponding to $\omega_L = \omega_0$ where the vibrational energy remains the same ($|g,n\rangle \rightarrow |e,n\rangle$) is called carrier transition, while the transitions to different vibrational energy $|g,n\rangle \rightarrow |e,n\rangle$ are denominated side-band transitions.

The side-band cooling technique consists in using a cooling beam that reduces the vibrational level by 1 in each excitation $|e,n\rangle \rightarrow |g,n-1\rangle$. After the atom is excited, it spontaneously decay with a high probability to the same vibrational level in the ground state $|e,n-1\rangle \rightarrow |g,n-1\rangle$, completing one cycle and reducing the energy of the atom by $\hbar\omega$. This process is repeated until the atom is in the motional ground state $|g,0\rangle$. The condition that the atom falls with high probability to the same vibrational level in the ground state is satisfied by an atom in the so called Lamb-Dicke regime, where the recoil energy of one photon $\hbar\omega_R$ is smaller than the quantum vibrational separation $\hbar\omega$. This condition is often written as:

$$\eta = \sqrt{\frac{\omega_R}{\omega}} = \sqrt{\frac{\hbar k^2}{2m\omega}} \ll 1 \tag{3.4}$$

where η is the Lamb-Dicke parameter, k is the wavenumber of the cooling light, and m is the mass of the atom.

In the case of $^{40}Ca^{+}$ ions trapped in a Paul trap, the trap frequencies are often in the order of $\omega/2\pi \approx 1\,\text{MHz}$, while the recoil energy of a 729 nm beam is approximately $\omega_R/2\pi \approx 10\,\text{kHz}$, resulting in a Lamb-Dicke parameter of $\eta \approx 0.1$. The ultra narrow transition at 729 nm have a linewidth of less than 1 Hz, which is enough to resolve the side-band transitions.

Summarizing the above, two conditions are necessary to realize side-band cooling: 1) A cooling laser with a line-width much smaller than the vibrational energy ($\Gamma \ll \omega$) in order to resolve the side-bands, and 2) A system satisfying the Lamb-Dicke condition, where the recoil energy is much smaller than the vibrational energy ($\omega_R \ll \omega$).

In the case of neutral atoms trapped in two-dimensional optical lattices, the trap frequencies are often in the order of $\omega/2\pi \approx 100\,\text{kHz}$ and both conditions become more difficult to be satisfied. For example, the narrow intercombination transition of Ytterbium atoms have a linewidth of $\Gamma/2\pi = 180\,\text{kHz}$ and a recoil energy of $\omega_R/2\pi = 3.7\,\text{kHz}$, resulting in $\eta = 0.14$ and $\Gamma/\omega = 1.8$. Although the Lamb-Dicke condition is somehow satisfied, the line-width of the cooling laser is too broad to resolve the side-band transitions.

Two different cooling methods can be used to effectively reduce the linewidth of the cooling laser, namely, Raman cooling and EIT cooling. Both methods were successfully applied to

cool neutral atoms trapped in two-dimensional optical lattice [79], and also in quantum gas microscopes in recent experiments.

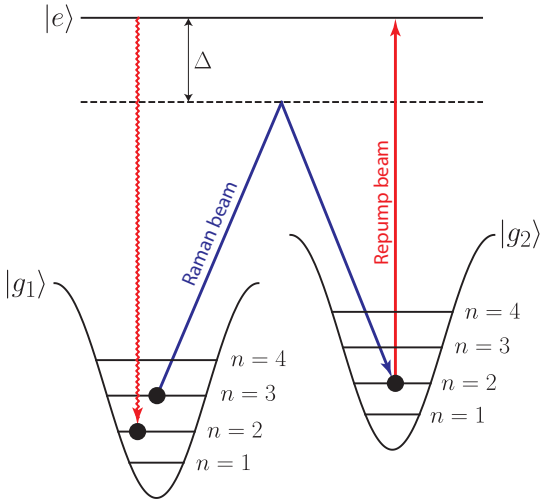

(a) Raman cooling. Two non-resonant beams are used to drive the $|g_1, n\rangle \rightarrow |g_2, n-1\rangle$ Raman transition in a three-level atom. A repump beam is then used to return the atom to the $|g_1, n-1\rangle$ state, completing one cycle of side-band cooling.

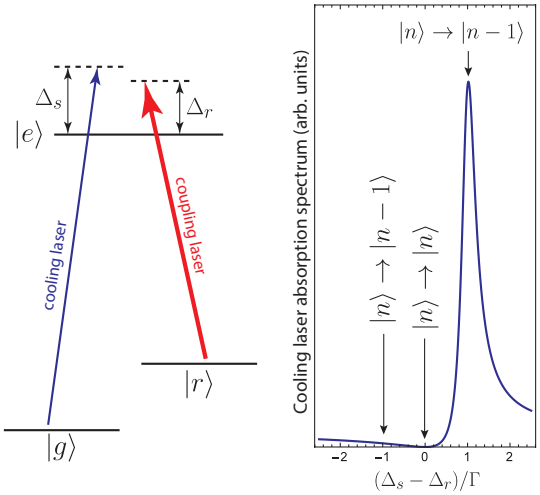

(b) EIT cooling. A strong coupling laser and a weak cooling laser in a Λ-configuration produce a Fano-like profile in the absorption spectrum (right graph). The detuning and Rabi frequency of each beam can be choosen in such a way that the blue side-band excitation is suppressed, resulting in side-band cooling.

Figure 3.3: Two different sub-Doppler cooling methods used to cool down alkali atoms in an optical lattice.

The Raman cooling method consists in using a three-level system to drive a Raman transition, as shown in Fig. 3.3a. A three-level lambda system is usually used for Raman cooling, where two of the energy levels ($|g_1\rangle$ and $|g_2\rangle$) are stable or metastable states, but a ladder system can be also utilized. First, two non-resonant laser beams detuned by Δ are used to drive a Raman transition the $|g_1\rangle \rightarrow |g_2\rangle$ transition through an intermediate transition $|e\rangle$. The linewidth of the Raman transition is given by the formula

$$\Gamma_{\text{raman}} = \frac{\Omega_{ge1}\Omega_{ge2}}{\Delta} \tag{3.5}$$

where Ω_{ge1} and Ω_{ge2} are the Rabi frequencies driving the $|g_1\rangle \rightarrow |e\rangle$ and $|g_2\rangle \rightarrow |e\rangle$ transitions, respectively. It is clear in this equation that the linewidth of the Raman transition can be reduced by increasing the detuning Δ, which is useful to resolve the side-band transition $|g_1, n\rangle \rightarrow |g_2, n-1\rangle$ necessary for side-band cooling. After the atom is transferred to the $|g_2, n-1\rangle$ state, a new beam resonant to the $|g_2\rangle \rightarrow |e\rangle$ transition is used to optically pump the atom back to the $|g_1\rangle$ transition. If the Lamb-Dicke condition is satisfied, the atom will be returned $|g_1, n-1\rangle$ to the state, completing one cycle of side-band cooling.

The electromagnetically induced transparency (EIT) cooling utilizes a strong coupling laser detuned by Δ_r to the $|r\rangle \rightarrow |e\rangle$ transition to tailor the absorption spectrum of a coupling

laser detuned to the $|g\rangle \rightarrow |e\rangle$ transition (see Fig. 3.3b). The resultant absorption spectrum when $\Delta_r > 0$ is a Fano-like profile having a zero at $\Delta_s = \Delta_r$ corresponding to the $|g,n\rangle \rightarrow |e,n\rangle$ carrier transition. The idea to produce effective side-band cooling is to choose the coupling laser detuning Δ_r and a Rabi frequency Ω_r such that it satisfies the equation:

$$\Gamma = \frac{\sqrt{{\Delta_r}^2 + {\Gamma_r}^2} - \Delta_r}{2}. \tag{3.6}$$

In this case, the narrow peak of the Fano-like profile coincides with the red-sideband transition $|g,n\rangle \rightarrow |e,n-1\rangle$. This method thus enhances the red side-band transition while it cancels the carrier excitation, which is an ideal condition for side-band cooling.

3.1.3 Sub-doppler cooling in Yb atoms

In the case of the bosonic isotopes of Yb, the lack of hyperfine and magnetic sub-levels in the ground state impedes the use of sub-doppler techniques such as Polarization gradient cooling, Raman cooling and EIT cooling. One idea for realizing sub-doppler cooling is by using two-photon transitions such as the ${}^1\mathrm{S}_0 \rightarrow {}^3\mathrm{P}_1 \rightarrow (6s7s)^1\mathrm{S}_0$ transition having linewidths of $\Gamma/2\pi = 181\,\mathrm{kHz}$ and $\Gamma/2\pi = 210\,\mathrm{kHz}$. Fermionic isotopes have a nuclear spin and consequently hyperfine structure in the excited levels. Raman cooling could be possible in principle by using different magnetic sub-levels of the ground state. Also, by using the metastable state ${}^3P_2$ as a cooling basis (which have hyperfine splitting in the fermionic case) it is possible to realize polarization gradient cooling, Raman cooling or EIT cooling.

3.2 Simulation

For the following sections, a computer simulation will be used to test the Doppler cooling and deep potential methods. The simulation realized is semi-classical with the following properties:

Optical lattice The optical potential utilized for the simulations is given by:

$$V(x,y,z) = V_0 \sin^2(k_z z)\left[\sin^2(k_x x) + \sin^2(k_y y)\right]. \tag{3.7}$$

where $k_x = k_y = \frac{2\pi}{\lambda_{\mathrm{lat}} \cos\theta_{\mathrm{acc}}}$ and $k_z = \frac{2\pi}{\lambda_{\mathrm{lat}} \sin\theta_{\mathrm{acc}}}$. All simulations were realized for the case $\theta_{\mathrm{acc}} = 6°$. Note that V_0 is the lattice depth in the xy plane, while the depth in the z direction is $2V_0$. Due to the geometry of this potential, the hoppings in the z direction will be negligible compared with the ones in the xy plane.

Movement The mechanics of the particle is considered to be classical. For a particle with mass m and position $\mathbf{r}(t)$, the differential equation that governs the movement is given

by:

$$m\ddot{\mathbf{r}}(t) = F(\mathbf{r}, t) \tag{3.8}$$

where F is the force at the position $\mathbf{r}$ and time t. Using the Euler method, the position of a particle is calculated by the following equations.

$$\begin{cases} \dot{\mathbf{r}}(t+\delta t) = \dot{\mathbf{r}}(t) + \dfrac{F(\mathbf{r}, t)}{m}\delta t \\ \mathbf{r}(t+\delta t) = \mathbf{r}(t) + \dot{\mathbf{r}}(t)\delta t \end{cases} \tag{3.9}$$

Wannier functions are not considered for the simulation. The initial position and velocity of the atom is always $\mathbf{r}(t) = 0$ and $\dot{\mathbf{r}}(t) = 0$, respectively.

Photons absorption and emission The probability of absorbing a photon between t and $t + \delta t$ is given by the formula:

$$p(t) = \frac{\Gamma}{2} \frac{s_0}{1 + s_0 + 4\left(\frac{\Delta(\mathbf{r}) + \mathbf{k}\cdot\dot{\mathbf{r}}(t)}{\Gamma}\right)^2}\delta t \tag{3.10}$$

where $\mathbf{k}\cdot\dot{\mathbf{r}}$ represents the Doppler effect and $\Delta(\mathbf{r})$ is the detuning of the laser including Stark shift effects at the position $\mathbf{r}$. In the case of a magic-wavelength, the detuning is homogeneous and $\Delta(\mathbf{r})$ is constant. When an atom absorbs a photon, the velocity of the particle is immediately increased by $\frac{\hbar\mathbf{k}}{m}$. Absorption is immediately followed by a photon emission in a random direction.

Population and Rabi oscillations For a multi-level atom, the population in each state $|i\rangle$ is given by $\rho_{ii}(t, \mathbf{r})$. The force experienced by the atom is given by:

$$F(\mathbf{r}, t) = -\sum_i \rho_{ii}(t, \mathbf{r}) \nabla V_i(\mathbf{r}) \tag{3.11}$$

where $V_i(\mathbf{r})$ is the optical lattice potential on the the state $|i\rangle$. Note that ρ_{ii} depends on the time, as Rabi oscillations are considered instead of using time averages. For states that are not coupled by a light beam, spontaneus emission rates resulting in transition from a excited state $|i\rangle$ to a state with a lower energy $|j\rangle$ are calculated using the formula $\rho_{ii}\Gamma_{ij}$.

Each simulation is stopped when the atom hops to a neighboring site ($|k_i r_i(t)| > \frac{\pi}{2}$). The lifetime is calculated averaging the obtained photons after 500 repetitions.

3.3 Doppler cooling in ytterbium

This section is dedicated to study the possibility of using Doppler cooling to cool down the atoms in the QGM scheme. As the Doppler cooling strongly depends on the detuning of the cooling laser beam Δ, it is important to consider the light shift inhomogeneities that arise from having different AC Stark shift in the ground and excited states. The first part of this section is dedicated to study the simplest Doppler cooling setup, where the lattice wavelength λ_{lat} is set to the magic-wavelength λ_{magic} one. In this setup, the wavelength of the lattice ODT is chosen such that the result AC Stark shift in the ground and excited states are exactly the same for every position in space, which produces an homogenous light shift in the space and determines a constant detuning for every point in space $\Delta(x,y,z) = \Delta(0,0,0)$.

3.3.1 Magic-wavelength potential and $^1S_0$-$^3P_1$ molasses

The $^1S_0$-$^3P_1$ cooling transition in Yb, having a low Doppler cooling limit of $4.4\,\mu$K, could in principle allow one to obtain long lifetimes even with low potential depths. Simulation results shown in Fig. 3.4a shows the lifetime (in photons) dependency on the potential depth $2V_0$. For this simulation a six beam molasses setup is used, with each beam having a saturation intensity of $s_0 = 1$ and a detuning of $\Delta/\Gamma = -0.8$.

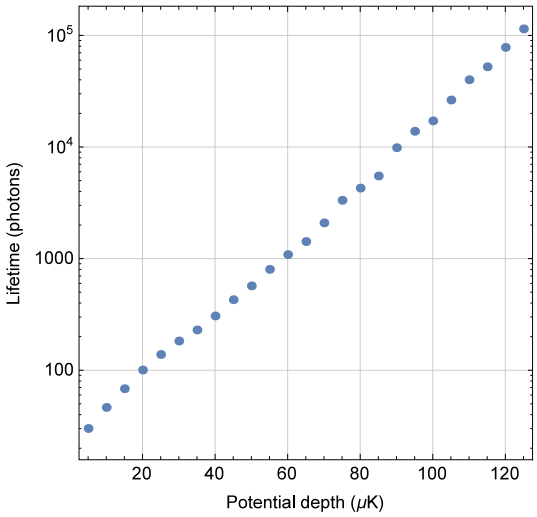

(a) Lifetime dependency on the potential depth $2V_0$ for $s_0 = 1$ and $\Delta/\Gamma = -0.8$.

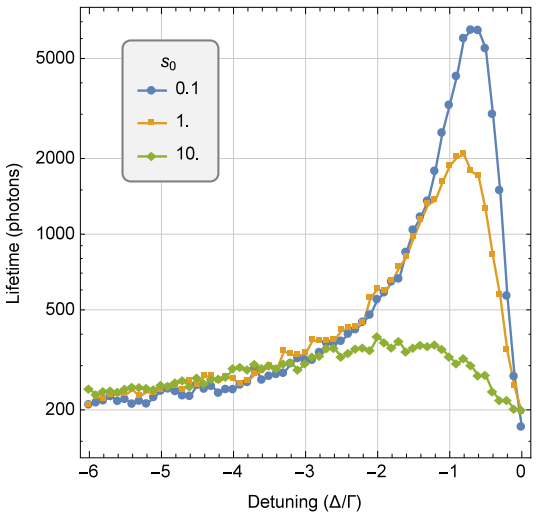

(b) Lifetime dependency on the detuning Δ for different saturation intensities s_0. The potential depth is fixed at $90\,\mu$K

Figure 3.4: Lifetimes obtained from the simulation for a magic-wavelength potential using the $^1S_0 - {}^3P_1$ transition.

Note that the vertical axis in the figure is in the logarithmic scale. By increasing the potential depth by $30\,\mu$K the lifetime can be increased one order of magnitude. This is compatible with the Doppler theory, in which atoms have a Gaussian velocity distribution.

To clarify this point, consider the velocity distribution of an atom during Doppler cooling

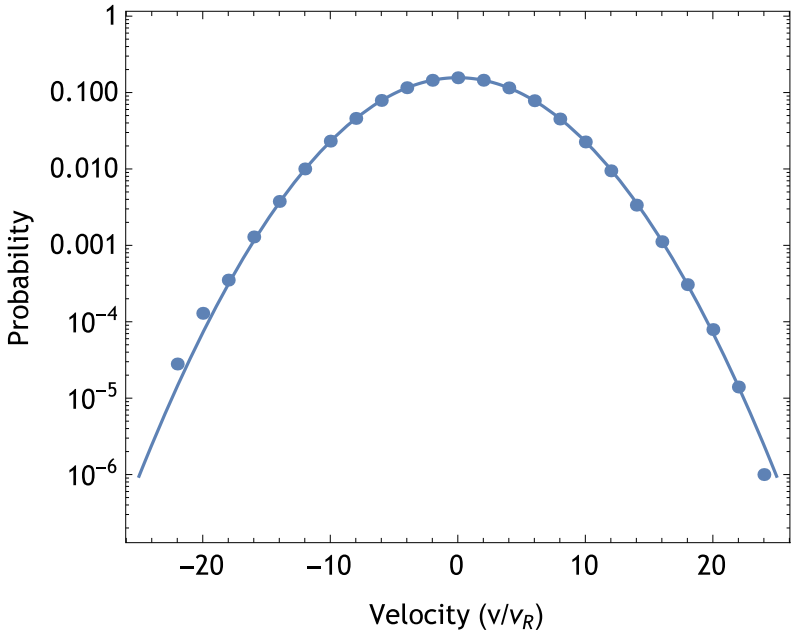

Figure 3.5: Velocity distribution of an atom during Doppler cooling. The velocity unit is in recoil units $v_R = \hbar k/m$. The solid line corresponds to a Gaussian fitting.

shown in Fig. 3.5. The profile was obtained from a simple one-dimensional simulation in the free space, for a detuning of $\Delta = -\Gamma/2$ and a saturation intensity of $s_0 = 10^{-3}$. The temperature obtained from the width of the Gaussian profile

$$f_{1D}(v) \propto e^{-\frac{mv^2}{2k_B T}} \tag{3.12}$$

resulted in $T = 4.5\,\mu$K, which is the Doppler cooling limit. In the three-dimensional case, the lattice depth in the z direction is $2V_0$ while the lattice depth in the x and y directions is V_0. Consequently, the atom will mostly escape in the x and y directions and the problem can be considered as two-dimensional. The velocity distribution corresponding to the 2D case is:

$$f_{2D}(v) \propto v\, e^{-\frac{mv^2}{2k_B T}} \tag{3.13}$$

An atom escapes the lattice site when its kinetic energy is larger than the lattice depth V_0. The probability of having an atom with the escape velocity or larger is:

$$p\left(v \geq \sqrt{\frac{2V_0}{m}}\right) = \int_{v=\sqrt{2V_0/m}}^{\infty} f_{2D}(v)dv \propto e^{-\frac{V_0}{k_B T}} \tag{3.14}$$

which decreases exponentially with the potential depth. The lifetime dependency on the laser-cooling detuning Δ and saturation s_0 is shown in Fig. 3.4b, where the potential depth was fixed to $2V_0 = 90\,\mu$K. For $s_0 = 0.1$ the optimal saturation was obtained at $\Delta/\Gamma = -0.6$. Note that this result also follows the standard Doppler cooling theory where the Doppler cooling

temperature is

$$k_B T = \frac{\hbar\Gamma}{4} \frac{1 + s_0 + \left(\frac{2\Delta}{\Gamma}\right)^2}{\frac{2\Delta}{\Gamma}} \tag{3.15}$$

and the Doppler cooling limit is determined by

$$k_B T = \frac{\hbar\Gamma}{2}\sqrt{1+s_0} \quad \text{when} \quad \Delta = -\frac{\Gamma}{2}\sqrt{1+s_0}. \tag{3.16}$$

For higher laser cooling saturation, the temperature increases and the optimal detuning Δ increases by a ratio of $\sqrt{1+s_0}$, which produces a significant reduction in the lifetime. The photon emission rate is also an important factor in the QGC, as the lifetime of the atomic cloud is limited by other factors such as background collisions and lattice light absorptions. Consequently, a saturation of at least $s_0 = 1$ is desired for the experiment. For the following subsections, the analysis will be limited to a saturation of $s_0 = 1$.

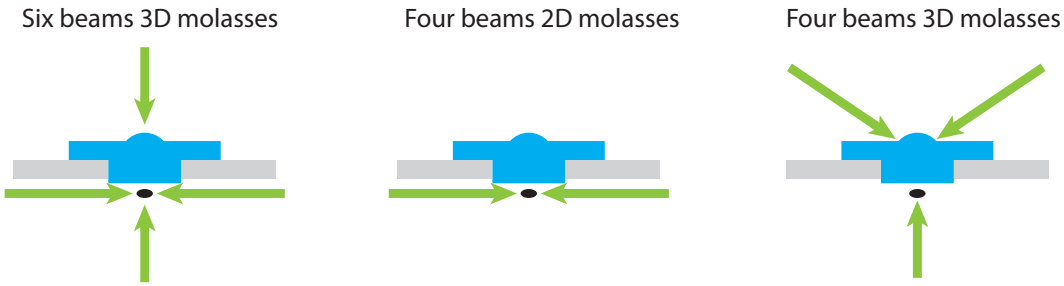

Figure 3.6: Three different cooling schemes. (left) 3D molasses cooling using 6 beams in the $\pm x$,$\pm y$ and $\pm z$ directions. (center) 2D molasses using 4 beams in the $\pm x$ and $\pm y$ directions. (right) 4 beams in the Brewster angle directions allows cooling in the three dimensions.

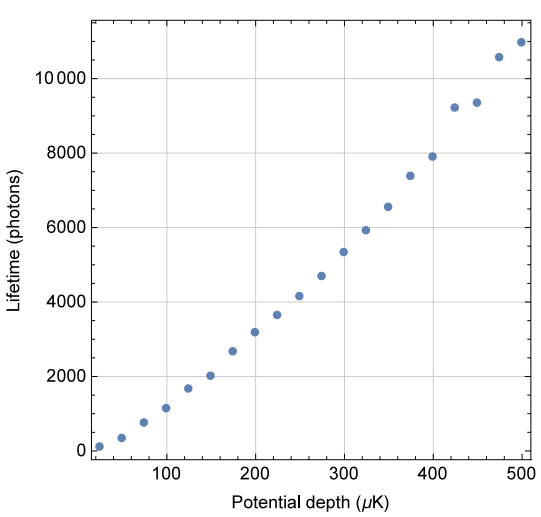

(a) 2D molasses using 4 beams in the $\pm x$ and $\pm y$ directions.

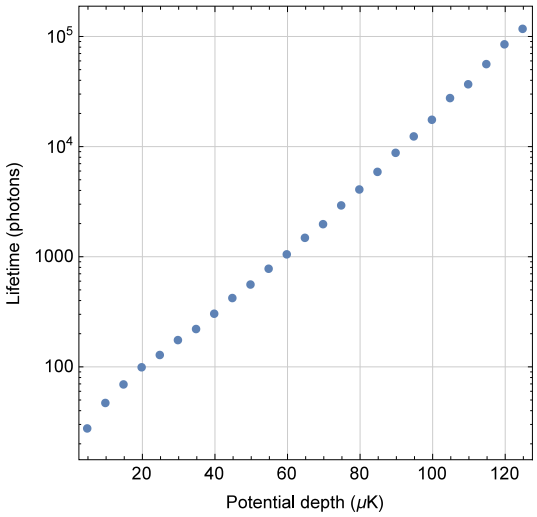

(b) 4 beams setup as shown in the Fig. 3.6(right) setup.

Figure 3.7: Lifetime as a function of the potential depth $2V_0$ for $s_0 = 1$ and $\Delta/\Gamma = -0.8$ for two different molasses setup.

Another important point to consider is that in the QGM setup the objective lens is placed

over the solid immersion lens along the z direction (Fig. 3.1). This means that the molasses beams in the $+z$ direction would enter directly into the camera CCD sensor. One idea to avoid this problem is to use cooling only in the $\pm x$ and $\pm y$ directions (Fig. 3.6). Simulation results in Fig. 3.6 shows that, in the case of a 2D cooling, the heating along the z direction causes a significant reduction in the lifetime. In contrast to the potential depth of $2V_0 = 90\,\mu$K required to obtain a lifetime of 10000 photons in the 3D molasses case, a potential $2V_0 = 450\,\mu$K would be required to obtain the same lifetime for the 2D molasses approach. Moreover, in this case the lifetime only increases linearly with the potential depth, so a further increment in the lifetime would require a very large potential. Another possible idea is to use four cooling beams in the

$$\hat{k}_1 = (\cos\theta_B, 0, -\sin\theta_B)$$
$$\hat{k}_2 = (-\cos\theta_B, 0, -\sin\theta_B)$$
$$\hat{k}_3 = (0, \cos\theta_B, +\sin\theta_B)$$
$$\hat{k}_4 = (0, \cos\theta_B, \sin\theta_B)$$

directions, where θ_B is the Brewster angle. It can be easily seen that with this setup cooling is possible in all directions. Simulation results in Fig. 3.7b show that this setup produces equal performance as the obtained in the six beams molasses.

3.3.2 Estimation of the magic-wavelength for the $^1S_0$-$^3P_1$ transition

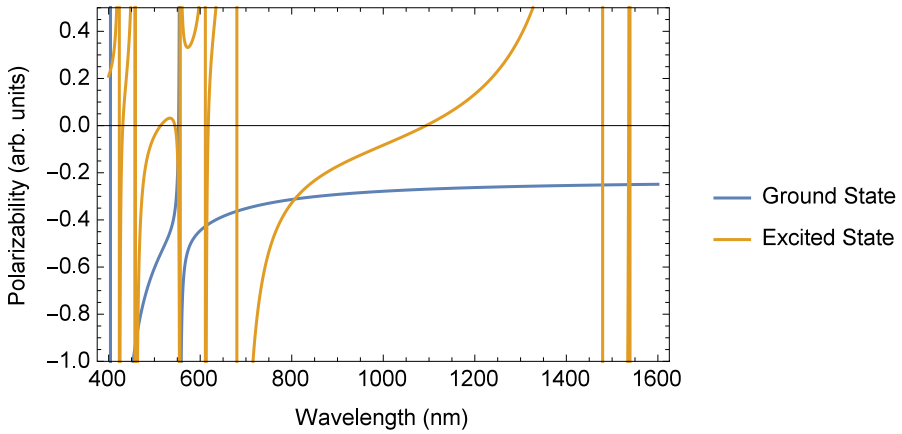

Figure 3.8: Polarizability in the ground $^1S_0$ state and excited $^3P_1$ state as a function of the optical dipole trap wavelength. Magic-wavelengths were found 424 nm, 463 nm, 551 nm, 612 nm, 800 nm and 1.53 μm.

The magic-wavelength for the $^1S_0$-$^3P_1$ transition is estimated using all the energy levels up to 42000 cm^{-1}. For the calculations, a linear polarized light was used and only the $m = 0$ sublevel in both the ground and excited states were considered. In the case of the ground

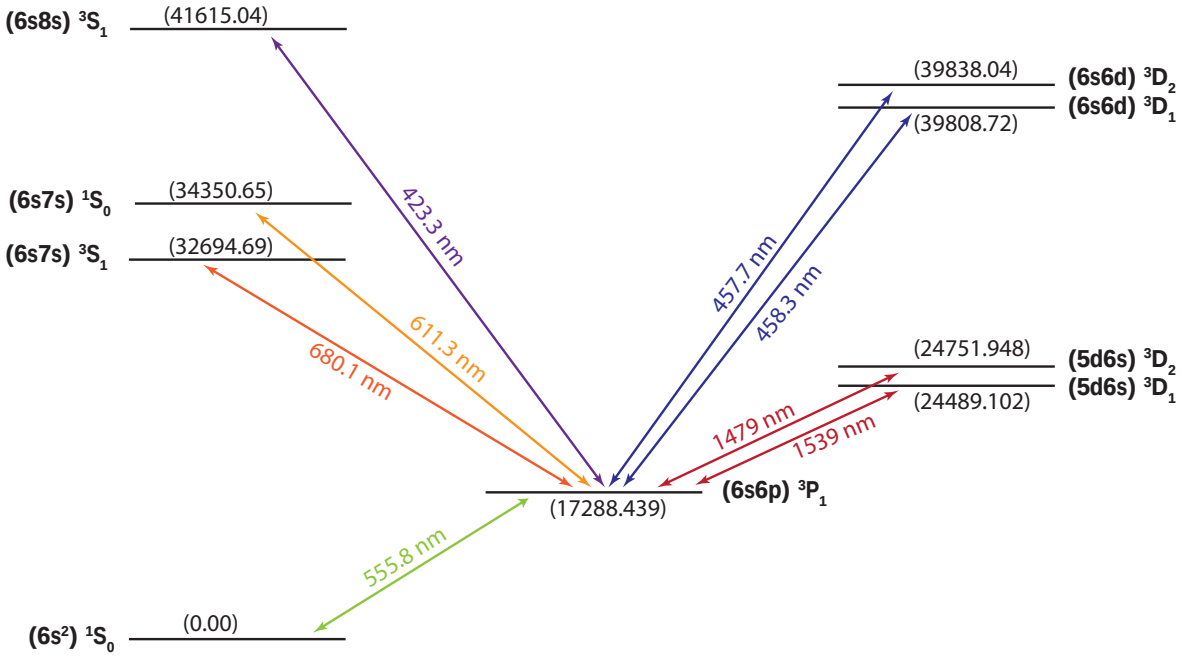

From	To	Wavelength	Linewidth	Refs.
$(6s6p)^3P_1$	$(5d6s)^3D_1$	1539 nm	16 kHz	[84]
$(6s6p)^3P_1$	$(5d6s)^3D_2$	1479 nm	320 kHz	[84]
$(6s6p)^3P_1$	$(6s7s)^3S_1$	680.1 nm	4.3 MHz	[84]
$(6s6p)^3P_1$	$(6s7s)^1S_0$	611.3 nm	210 kHz	[85]
$(6s6p)^3P_1$	$(6s6d)^3D_1$	457.7 nm	2.6 MHz	[86, 87]
$(6s6p)^3P_1$	$(6s6d)^3D_2$	458.3 nm	2.4 MHz	[86, 87]
$(6s6p)^3P_1$	$(6s8s)^3S_1$	423.3 nm	2.7 MHz	[86, 87]
$(6s^2)^1S_0$	$(6s6p)^3P_1$	555.8 nm	182 kHz	

Figure 3.9: Transitions considered for the excited $^3P_1$ state, and their respective wavelength and line-widths.

state, the $^1S_0$-$^1P_1$, $^1S_0$-$^3P_1$ and $^1S_0$-$^3D_1$ transitions were used. The transitions from the excited state were summarized in the Fig. 3.9. Although only the transition information for the lower levels is known [84, 85], the lifetime and relative intensities of the upper transitions could be used to roughly estimate the transition linewidths [86, 87] of the remaining transitions.

The calculation results are shown in Fig. 3.8. Six different magic wavelengths with negative polarizability where found, whose wavelengths are 424 nm, 463 nm, 551 nm, 612 nm, 800 nm and 1.53 μm. Only the magic-wavelength at 800 nm is far detuned, which makes it a good candidate for creating the two-dimensional optical lattice. Laser sources at 800 nm are also readily available, for example using a Ti:sapphire laser or a tapered amplifier.

3.3.3 Deviation from magic-wavelength for the $^1S_0$-$^3P_1$ transition

What would happen if the lattice wavelength is different from the magic-wavelength one?. When the atom energy increases due to heating, the atom moves inside the trap, which changes the detuning of the laser cooling and consequently the cooling condition is altered. If the light-shift deviation δ defined by the change of detuning $\Delta(x,y,z)$ when the atom moves half the lattice spacing

$$\delta = \Delta(\pi/2k_x,0,0) - \Delta(0,0,0) \tag{3.17}$$

is positive, then the detuning absolute value increases when the atom moves [see Fig. 3.10(right)], reducing the efficiency of the Doppler cooling. Similarly, when $\delta < 0$ the detuning absolute value decreases when the atom moves. Eventually, if the deviation is large, the sign of the detuning changes producing heating [see Fig. 3.10(left)].

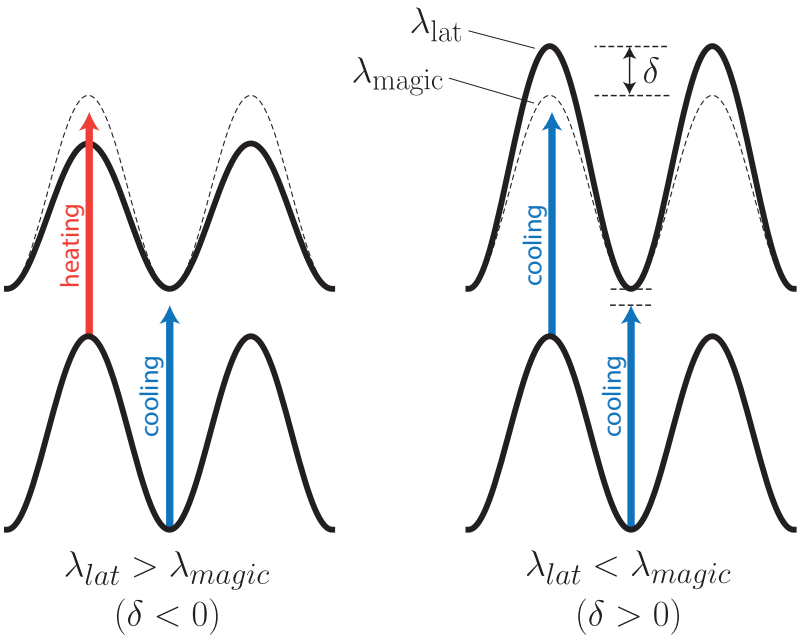

Figure 3.10: (left) If the polarizability in the excited state is lower than the one in the ground state, the detuning of the cooling beams is reduced until eventually heating occurs. (right) A higher polarizability in the excited state do not produce heating, but the efficiency of the Doppler cooling is reduced.

Figure 3.11a shows the simulation results when the lattice wavelength is shifted from the magic wavelength. For the simulation the potential depth was fixed to $2V_0/k_B = 90\,\mu$K. The asymmetry of the lifetime dependency on the light-shift deviation δ is in agreement to the surmise that a negative δ results in heating and consequently a fast reduction in the lifetime, while a positive δ only reduces the efficiency of cooling and the lifetime is not greatly affected.

The light-shift deviation δ as a function of lattice wavelength $\lambda_{\rm lat}$ at a fixel potential depth $2V_0/k_B = 90\,\mu$K is shown in Fig. 3.11b. The $^3P_1$-$^3S_1$ transition at 680 nm causes a rapid increment in δ for wavelengths shorter than the magic wavelength. For $\lambda_{\rm lat} = 700$ nm the light-shift

deviation is $\delta \approx 20\Gamma$ which reduces the lifetime to ~ 8000 photons. On the other hand, the change in deviation is smaller ($\delta \approx -3\Gamma$ for $\lambda_{\text{lat}} = 900\,\text{nm}$) but it results in a similar reduction in lifetime.

In conclusion, simulation results shows that it is possible to obtain $\sim 10^4$ photons by using a potential depth of $2V_0/k_B = 90\,\mu\text{K}$ in a magic-wavelength potential at $\lambda_{\text{lat}} = 800\,\text{nm}$. This potential can be realized using 100 mW of power per beam in the retro-reflected accordion setup, or using 450 mW of power per beam if the standing wave is created by interference of six individual beams. Also, even if the lattice wavelength is deviated by 100 nm from the magic-wavelength, lifetimes of $\sim$8000 photons can be still obtained.

The disadvantages of using this setup is that long exposure times ($\sim$100 ms) would require making the system robust against mechanical vibrations. Also, the maximum power obtainable at this wavelength is currently limited to 5W using a Ti:sapphire laser pumped by 20 W of light. Additionally, short wavelengths for the lattice result in increased heating due to spontaneous emission, which is a critical factor to consider when realizing quantum simulations on the Fermi-Hubbard model.

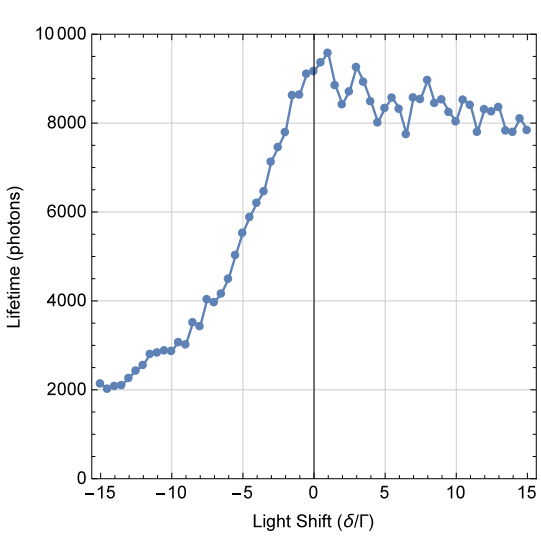

(a) Simulation results of the lifetime dependency on light-shift deviation δ.

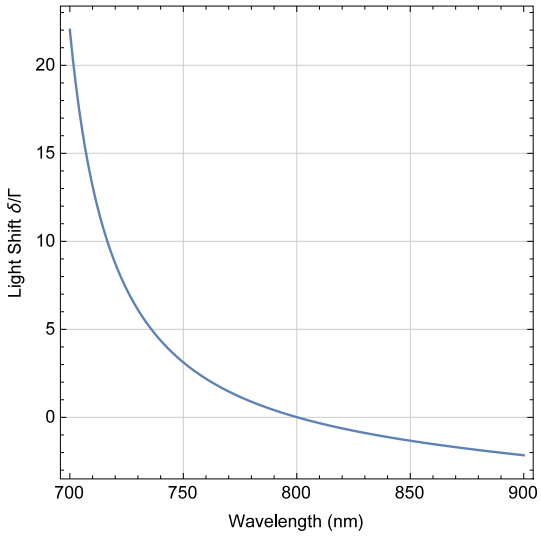

(b) Light-shift deviation δ as a function of lattice wavelength λ_{lat}.

Figure 3.11: Simulation and wavelength calculations for deviations from the magic-wavelength. In both cases the potential depth was fixed to $2V_0/k_B = 90\,\mu\text{K}$.

3.3.4 Magic-wavelength potential and $^1\text{S}_0$-$^1\text{P}_1$ molasses

Despite the fact that the $^1\text{S}_0$-$^1\text{P}_1$ transition have a high Doppler cooling limit and, in consequence, it is not suitable for cooling, it is interesting to study the lifetime of atoms when this cooling transition is used. Simulation results in Fig. 3.12a shows the lifetime dependency on the potential depth $2V_0$. For this simulation a six beam molasses setup is used, with each

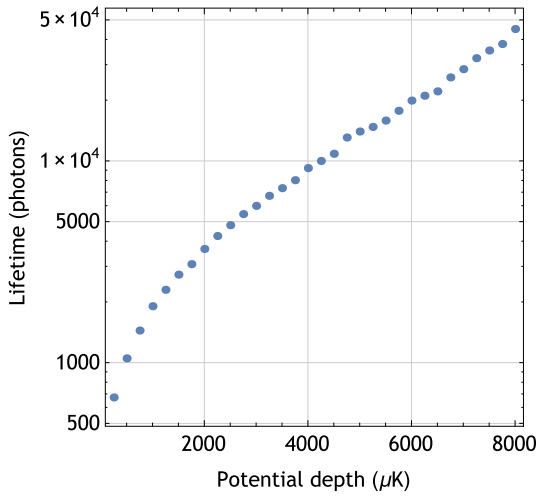

(a) Lifetime dependency on the potential depth $2V_0$ for $s_0 = 1$ and $\Delta/\Gamma = -0.8$.

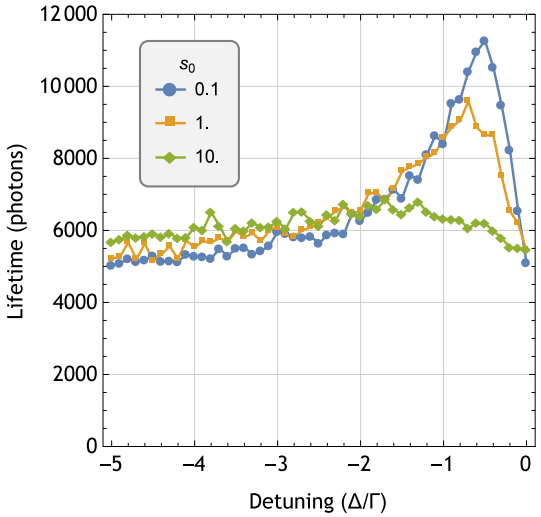

(b) Lifetime dependency on the detuning Δ for different saturation intensities s_0. The potential depth is 4 mK.

Figure 3.12: Lifetime in photons as a function of the potential depth $2V_0$ for a magic-wavelength potential using the $^1S_0 - {}^1P_1$ transition.

beam having a saturation intensity of $s_0 = 1$ and a detuning of $\Delta/\Gamma = -0.8$. For large potential depths, the lifetime still increase exponentially respect to potential depth $2V_0$.

The lifetime dependency on the laser-cooling detuning Δ and saturation s_0 is shown in Fig. 3.12b, where the potential depth was fixed to $2V_0 = 4$ mK. For $s_0 = 0.1$ the optimal saturation was obtained at $\Delta/\Gamma = -0.6$. One important difference compared with the cooling with the $^1S_0$-$^3P_1$ transition is the lifetime baseline at ~5500 photons, which appears even for zero detuning and high saturation intensities.

The presence of a baseline in the lifetime is related to the fact that atoms in the simulation start with zero velocity and require a finite time to thermalize. Consider the one-dimensional case of an atom that scatters photons in random directions. The resultant heating after N scatterings is $N E_{r399}$, where E_{r399} is the one photon recoil energy $\hbar k/2m$. When the amount of heating equals the lattice depth V_0 the atom escapes the trap and is lost. The lifetime of the atom is then

$$N \approx \frac{V_0}{E_{r399}} = \frac{2mV_0}{\hbar^2 k^2} \approx 5800 \,\text{photons} \tag{3.18}$$

for a potential of $V_0/k_B = 2$ mK. This value is noticeably close to the photons baseline in Fig. 3.12b.

3.3.5 Estimation of the magic-wavelength for the $^1S_0$-$^1P_1$ transition

The magic-wavelength for the $^1S_0$-$^1P_1$ transition was estimated using the transitions summarized in Fig. 3.14. In the case of the ground state, the $^1S_0$-$^1P_1$, $^1S_0$-$^3P_1$ and $^1S_0$-$^3D_1$ transitions were used. The transition linewidth information was obtained from [88, 86, 89, 90]. The

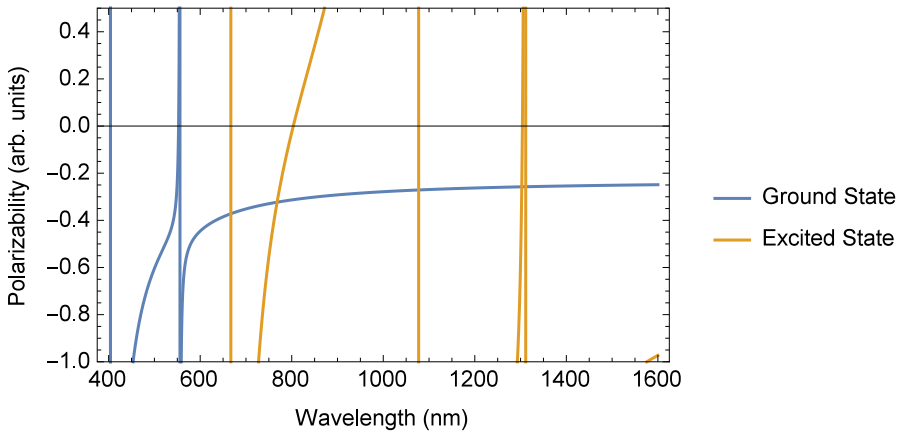

Figure 3.13: Polarizability in the ground $^1S_0$ state and excited $^1P_1$ state as a function of the optical dipole trap wavelength. Two magic-wavelengths were found at $\lambda_{\text{lat}} = 775\,\text{nm}$ and $\lambda_{\text{lat}} = 1.30\,\mu\text{m}$.

$(6s6d)^3D$ states also decay slowly into the $^1P_1$ state but were omitted from the calculations as their transition strength is negligible compared with the nearby $^1P_1$-$(6s6d)^1D_2$ transition.

Two magic-wavelengths were found at $\lambda_{\text{lat}} = 775\,\text{nm}$ and $\lambda_{\text{lat}} = 1.30\,\mu\text{m}$. Creation of a potential depth of $2V_0/k_B = 4\,\text{mK}$ at $\lambda_{\text{lat}} = 775\,\text{nm}$ would require 10 W of power per beam, and 13 W of power per beam in the case of $\lambda_{\text{lat}} = 1.30\,\mu\text{m}$.

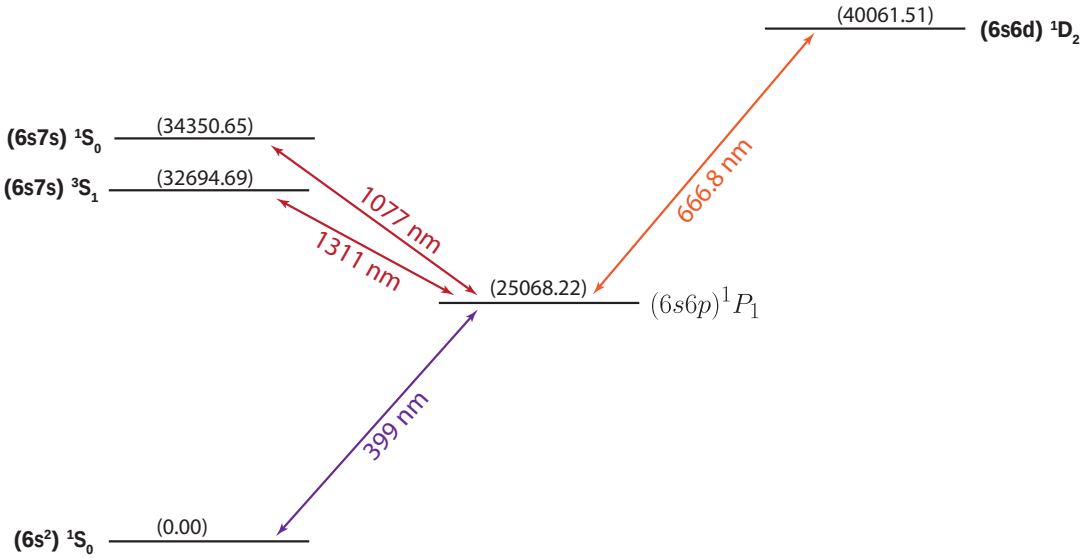

From	To	Wavelength	Linewidth	Refs.
$(6s6p)^1P_1$	$(6s7s)^3S_1$	1311 nm	25 kHz	[89]
$(6s6p)^1P_1$	$(6s7s)^1S_0$	1077 nm	3.0 MHz	[90, 88]
$(6s6p)^1P_1$	$(6s6d)^1D_2$	667.0 nm	4.5 MHz	[86]
$(6s^2)^1S_0$	$(6s6p)^1P_1$	398.9 nm	27.9 MHz	

Figure 3.14: Transitions considered for the $^1P_1$ state with their respective wavelength and linewidth.

3.4 The deep potential approach

In Sec. 3.3.4 the lifetime of atoms using a magic-wavelength potential and the $^1S_0$-$^1P_1$ molasses was studied. It was found that even for zero detunings and large saturation intensities of the laser cooling beam, a condition in which laser cooling has no effect, nearly ∼5500 photons could be obtained. Atoms starting at zero velocity require finite time to heat resulting in a finite number of photons obtained before the atom escapes from the trap. If a deep enough potential is prepared, would it be possible to attain a large number of photons without the use of any laser cooling technique? The answer is yes, and it is the strategy selected in this work for creating a quantum gas microscope of ytterbium atoms.

Without the Doppler cooling requirement, utilization of magic-wavelength potentials is no longer needed. For the excitation beam the preferable choice is to use the $^1S_0 - {}^1P_1$ as it is less prone to be affected by Doppler effects and additionally because it produces a higher microscope resolution.

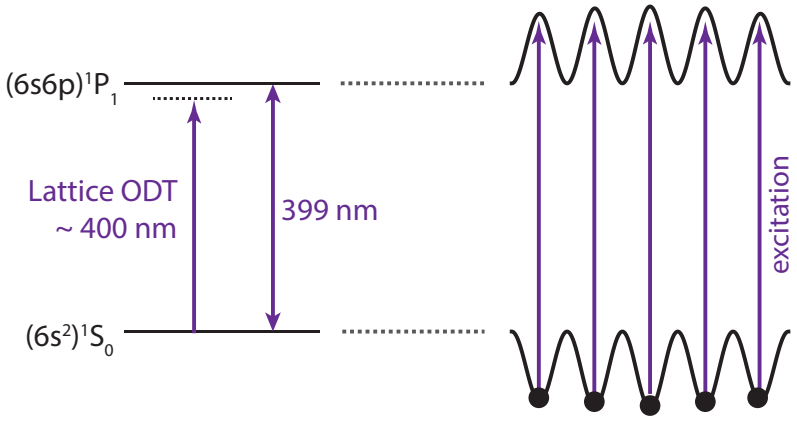

Figure 3.15: Creation of a deep potential using a lattice near-resonant to the $^1S_0 - {}^1P_1$ transition.

The conventional method for creating deep potentials is choosing a lattice wavelength that is near-resonant to a transition from the ground state (see Fig. 3.15). In the case of ytterbium, the natural choice is to use a lattice wavelength near-resonant to the strong $^1S_0 - {}^1P_1$ transition. One problem of using this transition is that high-power laser sources are not readily available in the NUV region. If the available power per beam is 100 mW, a lattice wavelength detuned by only 1 nm ($\lambda_{\text{lat}} = 400$ nm) is necessary to create a potential of $2V_0/k_B = 4$ mK. In this case, even for very small lattice powers the scattering rates in the ground state are on the order of $10s^{-1}$ for potential depths of a few μK, which is not a good condition for creating a Bose-Einstein condensate (BEC) and a Mott insulator. Another problem of using this transition is that the wavelengths of the lattice light and the excitation light are similar and it results difficult to reduce the effects of stray lights.

In this work, instead of creating a deep potential in the ground state, the optical lattice

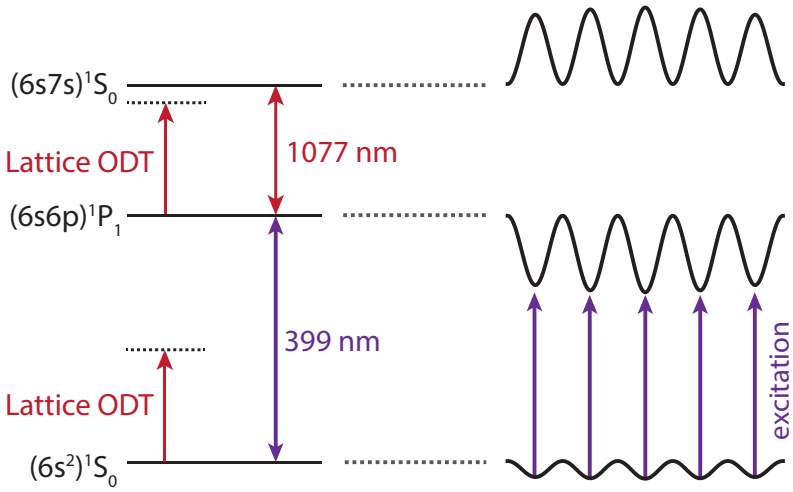

Figure 3.16: Creation of a deep potential using a lattice near-resonant to the $^1\mathrm{P}_1 - (6s7s)^1\mathrm{S}_0$ transition.

wavelength was selected such that the potential in the excited state is deep and the one in the ground state is shallow. The selected wavelength was of $\lambda_{\mathrm{lat}} = 1082\,\mathrm{nm}$, which is red detuned by only $\Delta_{\mathrm{lat}}/2\pi = 1.2\,\mathrm{THz}$ to the upper $^1\mathrm{P}_1 - {}^1\mathrm{S}_0$ transition (wavelength 1077.2 nm, natural linewidth 3MHz) which creates a deep potential in the excited state that is 200 times larger than that in the ground state. Other possible choices would be using a wavelength near-resonant to the $^1\mathrm{P}_1 - (6s6d)^1D_2$ transition (wavelength 667.0 nm) or the $^1\mathrm{P}_1 - (6s8s)^1\mathrm{S}_0$ transition (wavelength 592.7 nm).

To see the advantages of this system, consider first the case in which the excitation light is not present in the system. As the lattice light is far off resonant from any of the transitions from the ground state, the shallow potential results in small scattering rates ($10^{-3}\,\mathrm{s}^{-1}$ for $V_0/k_B = 2\,\mu\mathrm{K}$) ideal for preparing Hubbard systems in their ground state. During the imaging process, the resonant excitation light illuminates the atoms and couples the lower $^1\mathrm{S}_0$ and excited $^1\mathrm{P}_1$ states. Atoms then experience an average potential between the deep excited-state potential and the shallow ground-state one. This deep potential is useful to trap the atoms during the imaging process. Note that for the average approximation to be true, the Rabi frequency should be much larger than the trap frequency in the optical lattice, which is normally satisfied by the strong $^1\mathrm{S}_0 - {}^1\mathrm{P}_1$ transition with large saturated intensities.

A computer simulation is used to test the deep potential approach and to determine the initial experimental parameters such as lattice detuning Δ_{lat}, lattice power P_{lat} and the saturation intensity of the excitation beam s_0. As optical molasses is no longer needed for Doppler cooling only one excitation beam in the $+x$ direction was used in the simulation. Simulation results are shown in Fig. 3.17, where the lifetime dependency on lattice power P_{lat} for 3 different saturation intensities ($s_0 = 100$, 1000 and 10000) and 10 different lattice detunings ($\Delta_{\mathrm{lat}}/2\pi = 0.1, 0.2, \ldots, 1.0\,\mathrm{THz}$) were tested. In general, large saturation intensities pro-

duce longer lifetimes because the resultant power broadening is useful to reduce the effects of Doppler shifts and light-shift inhomogeneities; i.e. large saturation intensities maintain the population in the $^1P_1$ state as high as possible.

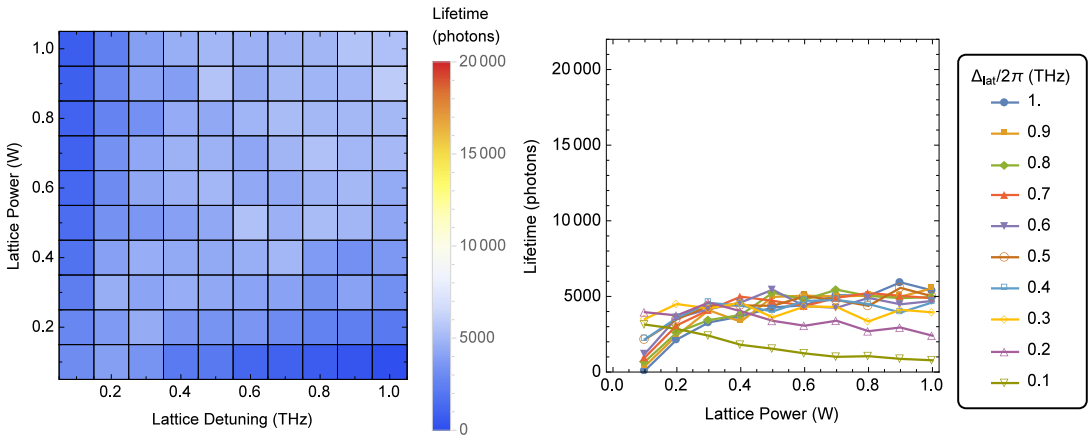

(a) Excitation beam saturation intensity $s_0 = 100$

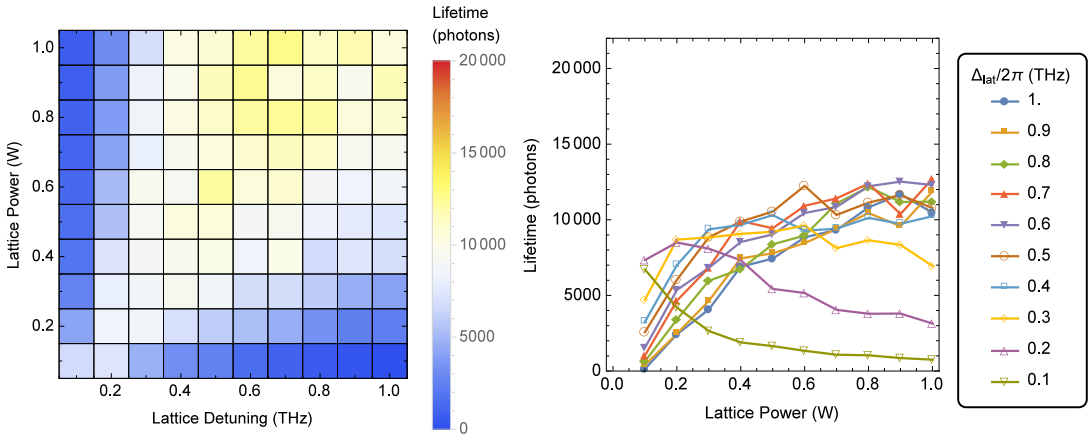

(b) Excitation beam saturation intensity $s_0 = 1000$

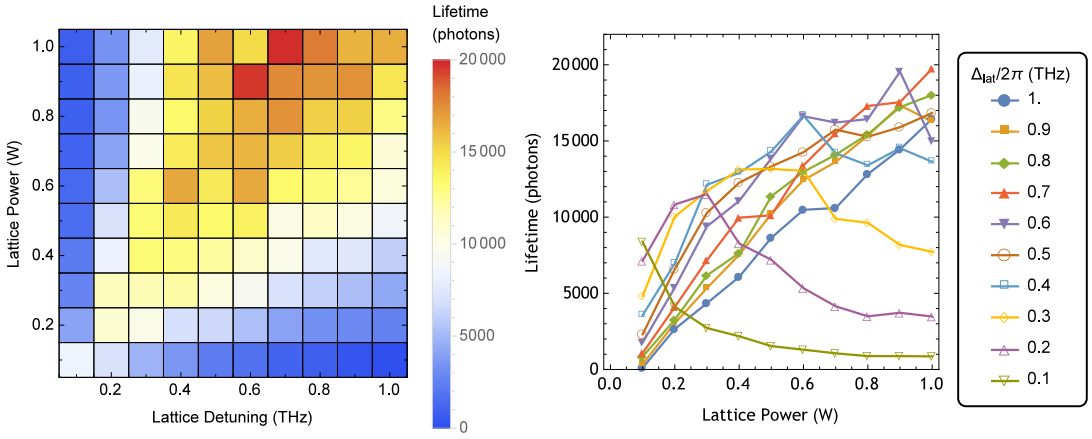

(c) Excitation beam saturation intensity $s_0 = 10000$

Figure 3.17: Simulation results. Lifetime dependency on the lattice power P_{lat} and lattice detuning Δ_{lat} for 3 different excitation beam saturation intensities (s_0). Left: Density plot of the lifetime for 10 different lattice detunings and powers. Right: Dependency of lifetime for different lattice powers, with each curve representing a different lattice detuning.

3.5 Lifetime and limitations of the deep-potential approach

In the deep potential approach, the mean lifetime of an atom is limited by three factors:

Heating

When the atoms are excited to ^{1}P$_1$ state by the excitation beam, the consequent scattering produces a random momentum kick which heats the atom. As there is no cooling scheme present in the system, the atom total energy will eventually exceed the potential barrier of the lattice site, resulting in atom hopping.

Dipole trap beam absorption

As a result of the lattice beam being near resonant to the upper ^{1}P$_1$-(6s7s)^{1}S$_0$ transition, the absorption of the dipole trap beam occurs in the order of a few tens of microseconds. As the potential in the $(6s7s)^1$S$_0$ state is strongly repulsive and the decay rate is comparable to the trap frequency, the atom is lost after a number of excitations.

Branching to the ^{3}P$_1$ state

The absorption of the dipole trap beam also leads to a branching to the ^{3}P$_1$ state. The branching ratio of the $(6s7s)^1$S$_0$ state is known to be approximately 1:10 [90, 88]. As the state ^{3}P$_1$ is long lived and the potential in this state is shallow, the atom will be lost if it falls into this state.

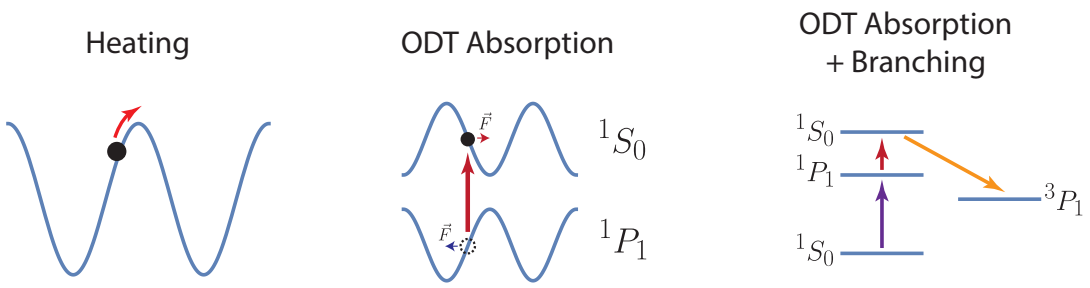

Figure 3.18: The three factors limiting the lifetime on the deep potential approach.

The heating due to N random photons scattering is

$$\Delta E = \frac{p^2}{2m} = \frac{(\sqrt{N}\hbar k_{\text{exc}})^2}{2m} = N\frac{\hbar^2 k_{\text{exc}}^2}{2m}, \tag{3.19}$$

which is proportional to the number of scattered photons. When the kinetic energy is comparable with the site potential $V_0 \approx \Delta E$ the atom will escape from the site. The lifetime (in photons) n_{heat} due to heating can be written as

$$n_{\text{heat}} = N = a\,V_0 \tag{3.20}$$

where a is a constant in the order of $a \approx 2m/\hbar^2 k_{\text{exc}}^2$.

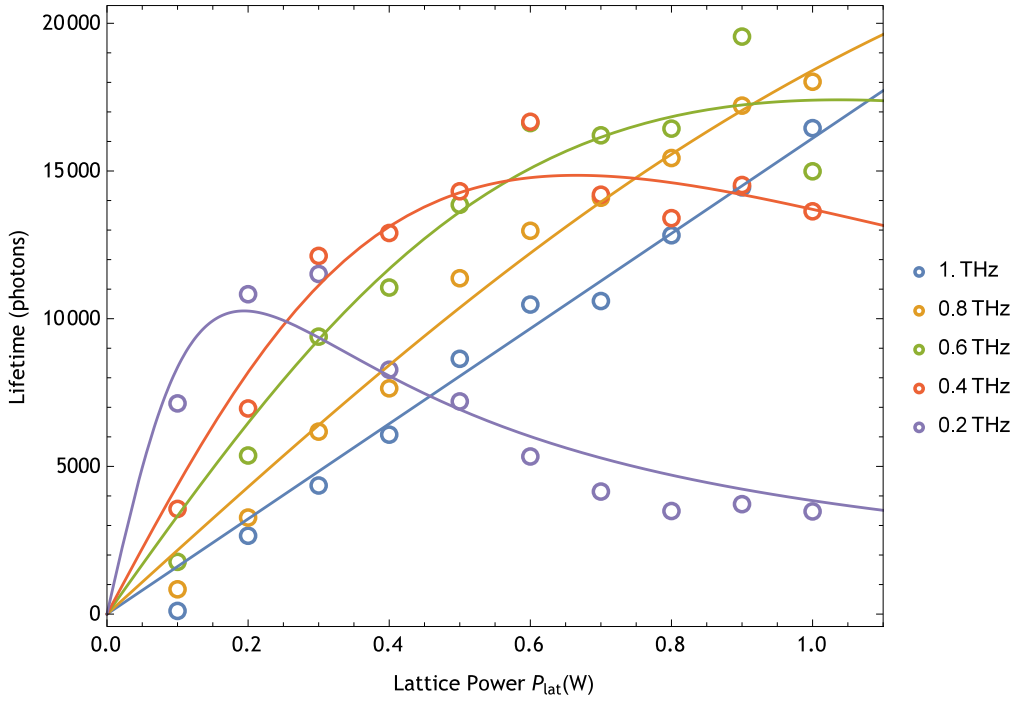

Figure 3.19: Simulation lifetime results for different Δ_{lat}. Each curve was fitted with the lifetime in Eq. 3.23.

The other two factors related to the dipole trap beam absorption can be considered as one, as both of these rates are proportional to the population in the $(6s7s)^1S_0$ state. Consequently, the lifetime (in photons) due to the dipole trap beam absorption n_{exc} can be expressed as

$$n_{exc} \propto \frac{1}{\rho_{55}} = b\frac{\Delta_{lat}}{V_0} \tag{3.21}$$

where b is a constant and ρ_{55} is the population in the $(6s7s)^1S_0$ state. Finally, if these two process are independent, the total lifetime (in photons) results in

$$n = \left(\frac{1}{n_{heat}} + \frac{1}{n_{exc}}\right)^{-1} = \left(\frac{1}{a\,V_0} + \frac{V_0}{b\,\Delta_{lat}}\right)^{-1}. \tag{3.22}$$

This model is tested using the simulation results obtained in Fig. 3.17. To check the dependency of lifetime on lattice power P_{lat}, Eq. can be rewritten as

$$n = \left(\frac{1}{A P_{lat}} + \frac{P_{lat}}{B}\right)^{-1}. \tag{3.23}$$

where A and B are two parameters depending only in the lattice detuning Δ_{lat}

$$A(\Delta_{lat}) = a\frac{V_0}{P_{lat}} \propto \frac{1}{\Delta_{lat}} \quad , \quad B(\Delta_{lat}) = b\frac{P_{lat}}{V_0}\Delta_{lat} \propto \Delta_{lat}^2 \tag{3.24}$$

as $V_0 \propto P_{lat}/\Delta_{lat}$. Figure 3.19 shows the fitting result of each simulation results for different

lattice detunings Δ_{lat}.

The obtained parameters A and B for each of the detuning Δ_{lat} is shown in Fig. 3.20. Each of the parameters was fitted using a power function.

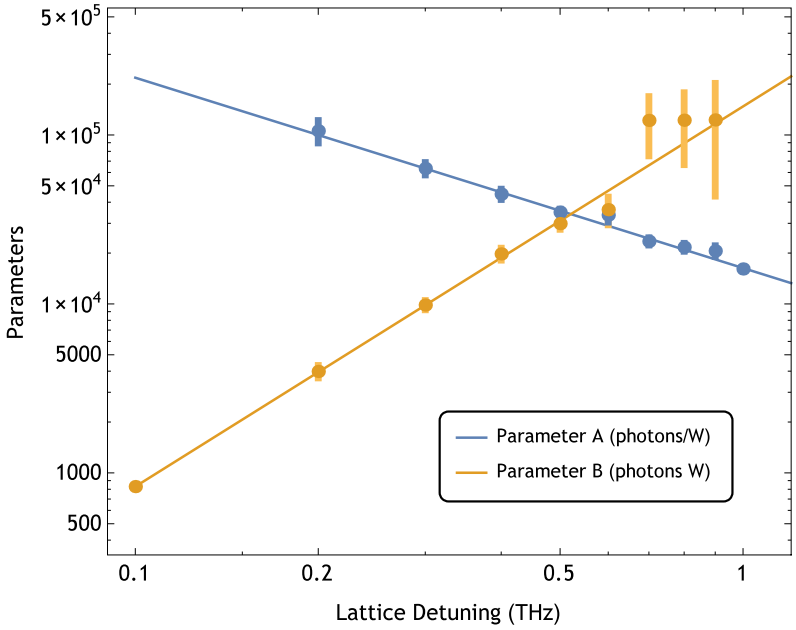

Figure 3.20: Dependency of parameters A and B on the lattice detuning Δ_{lat} for the simulation results. Each curve was fitted using a power function.

Knowing the parameters A and B, the maximum lifetime obtainable for a given P_{lat} is:

$$n_{max}(P_{lat}) = n(P_{lat}, \Delta_{best}) : \frac{\partial n}{\partial \Delta_{lat}}(P_{lat}, \Delta_{best}) = 0. \tag{3.25}$$

Table 3.1 summarizes the results for three different saturation intensities. For high saturation intensities of the excitation beam, the lifetime model $A \propto {\Delta_{lat}}^{-1} \wedge B \propto {\Delta_{lat}}^{2}$ is in well agreement with the fitting results.

s_0	A (10^4 photons/W)	B (10^4 photons W)	n_{max} (10^4 photons)	Δ_{best} (THz)
10^4	$1.63(3){\Delta_{lat}}^{-1.13(4)}$	$14.8(9){\Delta_{lat}}^{2.25(3)}$	$1.8{P_{lat}}^{0.33}$	$0.64{P_{lat}}^{0.59}$
10^3	$1.42(1){\Delta_{lat}}^{-1.15(8)}$	$6.6(6){\Delta_{lat}}^{1.88(6)}$	$1.3{P_{lat}}^{0.24}$	$0.71{P_{lat}}^{0.65}$
10^2	$1.11(4){\Delta_{lat}}^{-0.71(6)}$	$0.98(6){\Delta_{lat}}^{0.87(6)}$	$0.53{P_{lat}}^{0.10}$	$1.22{P_{lat}}^{1.26}$

Table 3.1: Parameters A and B, max lifetime and best detuning for different saturation intensities. The units of Δ_{lat} and P_{lat} are THz and W, respectively.

3.5.1 Excitation beam radiative force effects

From the simulation results in Fig. 3.17, it can be seen that for large detunings Δ_{lat} and small lattice powers P_{lat} the fitting does not coincide well with the experimental data. This is due to the effect of the excitation beam, whose radiative force tilts the lattice potential reducing the

effective trap force. The reason for not using an excitation beam in the retro-reflected setup is only technical, as it would require to introduce expensive 3" optics with broadband coatings capable of transmitting the accordion beam and the excitation beam.

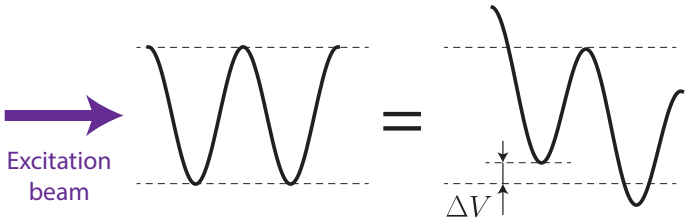

Figure 3.21: As the excitation beam is not in the retro-reflection setup, the beam exerts a net radiative force on the atoms, tilting the optical lattice potential while reducing the effective lattice depth.

The total potential including the potential due to the radiative force of the excitation beam is:

$$V(x,y,z) = -V_0 \sin(k_z z)^2 \left(\cos(k_x x)^2 + \cos(k_y y)^2\right) - \frac{\hbar k_{\text{exc}} \Gamma}{2} \frac{s_0}{1+\left(\frac{2\Delta}{\Gamma}\right)^2 + s_0} x \tag{3.26}$$

Here, we consider the worst scenario, in which the saturation is large ($s_0 \gg 1$) and the detuning including Doppler shift is negligible ($2\Delta/\Gamma \ll s0$). Then:

$$V \approx -V_0 \cos(k_z z)^2 \left(\cos(k_x x)^2 + \cos(k_y y)^2\right) - \frac{\hbar k_{\text{exc}} \Gamma}{2} x \tag{3.27}$$

The potential maxima and minima for $z = 0$ corresponds to:

$$\frac{\partial V}{\partial x} = V_0 k_x \sin(2k_x x) - \frac{\hbar k_{\text{exc}} \Gamma}{2} = 0 \tag{3.28}$$

resulting in

$$x_0 = \frac{1}{2k_x} \arcsin \zeta \quad , \quad x_1 = \frac{\pi}{2k_x} - \frac{1}{2k_x} \arcsin \zeta \tag{3.29}$$

where $\zeta = \frac{\hbar k_{\text{exc}} \Gamma}{V_0 k_x}$. Note that for $\zeta = 1$, both points coincide ($x_0 = x_1$) and the lattice tilts completely. ζ is then an important scaling factor to determine whether the excitation beam radiation effects are negligible or not. For the experiments parameters, the minimum required potential V_{limit} is:

$$V_{\text{limit}} = \frac{\hbar k_{\text{exc}} \Gamma}{2k_x} = 1.9 \text{ mK} \tag{3.30}$$

The resultant effective potential can be calculated replacing Eq. 3.29 in Eq. 3.27.

$$\Delta V = V(x_1, y, 0) - V(x_0, y, 0) = V_0 \left[\sqrt{1-\zeta^2} - \zeta\left(\frac{\pi}{2} - \arcsin \zeta\right)\right] \tag{3.31}$$

Using this equation the reduction of effective potential for different values of ζ can be calculated. These values are summarized in the following table.

ζ	0	0.1	0.2	0.3	0.4	0.5	0.6	0.7	0.8	0.9	1
$\frac{\Delta V}{V_0}$	100%	85%	71%	57%	45%	33%	24%	16%	9%	3%	0%

Table 3.2: Effective potential ΔV compared with V_0 for different values of ζ. For a potential depth that is 10 times larger than V_{limit}, the effective potential is reduced by 15%.

Knowing the reduction of the potential due to the radiative force, the lifetime τ_1 can be rewritten as:

$$\tau_1 = AP_{\text{lat}}\left[\sqrt{1-\zeta^2}-\zeta\left(\frac{\pi}{2}-\arcsin\zeta\right)\right] \tag{3.32}$$

$$= AP_{\text{lat}}\left[\sqrt{1-\frac{s}{P_{\text{lat}}}^2}-\frac{s}{P_{\text{lat}}}\left(\frac{\pi}{2}-\arcsin\frac{s}{P_{\text{lat}}}\right)\right] \tag{3.33}$$

As the ζ parameter depends on the lattice potential, a new parameter $s(\Delta_{\text{lat}}) = \zeta P_{\text{lat}} = \frac{\hbar k_{\text{exc}}\Gamma}{2V_0 k_x} P_{\text{lat}}$ is defined, which is independent to the lattice power, as $V_0 \propto P_{\text{lat}}$. Using this equation for the lifetime, fitting for large Δ_{lat} can be greatly improved, as shown in Fig. 3.22.

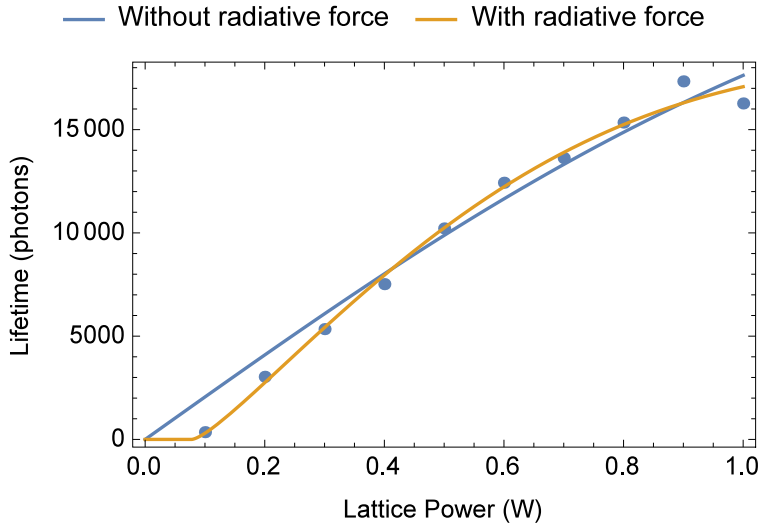

Figure 3.22: Lifetime of atoms in simulation, correspoding to $\Delta_{\text{lat}}/2\pi = 0.9\,\text{THz}$ and $s_0 = 10000$. The solid lines are fittings corresponding to $s = 0$ (no radiative force effects) and $s > 0$.

	s(W)	A (10^4 photons W)	B (10^4 photons/W)
Without radiative force	0	2.06(15)	12.3(79)
With radiative force	0.078(16)	2.98(27)	4.89(85)

Table 3.3: Parameters A and B obtained from fitting the simulation results for $\Delta_{\text{lat}}/2\pi = 0.9\,\text{THz}$ and $s_0 = 10000$. Two different fitting models (with and without radiative forces) are compared.

The obtained parameters for each fitting is summarized in the following table. The added parameter tends to increase the resultant value of A and decrease the value of B. Also, from

the obtained s it is possible to estimate the minimum required lattice power as $P_{\text{lat}} = s$ when $\zeta = 1$. For these parameters, the potential depth is

$$V_0 = 1.2(4)\,\text{mK} \quad \text{for } P_{\text{lat}} = 0.078(16)\,\text{W and } \Delta_{\text{lat}}/2\pi = 0.9\,\text{THz} \tag{3.34}$$

which is in very well accordance to the potential obtained in Eq. 3.30.

3.6 Solid immersion lens

Observation with a microscope system is limited by the diffraction limit:

$$d = \frac{0.61\lambda}{n \sin\alpha} \tag{3.35}$$

where λ is the wavelength of the incident light, n is the index of refraction of the medium being imaged in, and α is the half-angle subtended by the optical objective lens. In order to improve the diffraction limit of a lens system, it is necessary get closer to the object (to increment the half-angle) or use a medium with better refraction index than the air. The oil immersion lens works with that principle: By filling the space between the object and the lens with oil, the diffraction limit can be improved by a factor of ~ 1.5.

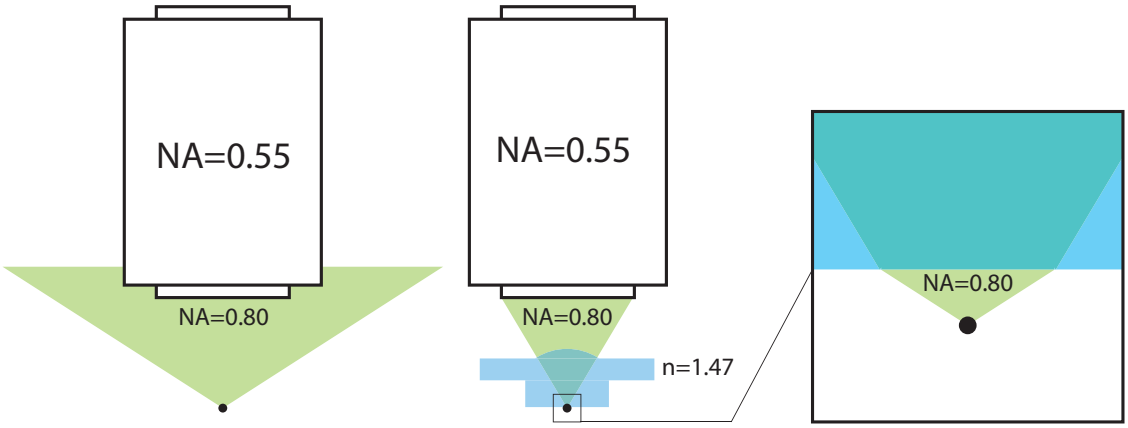

Figure 3.23: A solid immersion lens placed between the sample and the objective lens increases the numerical aperture of the system.

When observing an optical lattice, it is difficult to get closer to the lattice as the optical lattice resides inside a vacuum chamber, and techniques as the oil immersion lens cannot be used for obvious reasons. A solid immersion lens (SIL) works in the same principle as liquid immersion lens, with the liquid replaced by a solid lens of high refractive material. By simply introducing a solid immersion lens between the sample and the objective lens, the resolution of the system can be improved by a factor of the index of refraction of the hemispherical lens [91]. This technique was utilized to observe Rb atoms with resultant high numerical apertures of ~ 0.8[46]. Another importance of the SIL here is that it makes possible to create a stable

optical trap by fixing the position of the lattice with respect to the SIL flat surface by using the optical accordion technique. This technique will be explained in detail in Sec. 4.6.

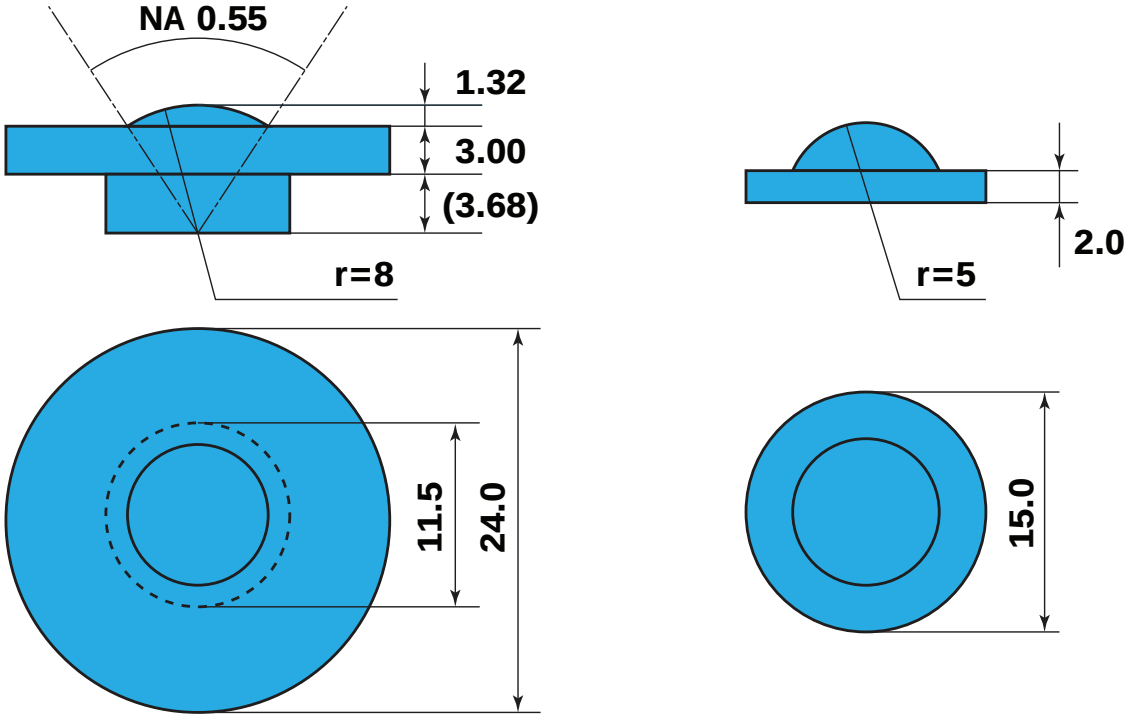

Figure 3.24: Drawing of the old and new versions of the SIL.

The SIL used for this work and also for the previous experiments are schematically shown in Fig. 3.24. Both versions of the SIL are made of fused silica glass. The new version of the SIL it is divided into three parts. The upper part is a spherical cap with a radius of 8 mm and a height of 1.32 mm, corresponding to a numerical aperture of 0.55. The middle part consists of a 3-mm-thick disk with a diameter of 24 mm, and the lower part is a 3.68 mm thick disk with a diameter of 11.5 mm. All three parts were optically contacted, and the lower flat and upper spherical surfaces were super-polished to reduce stray light. The old version of the SIL was formed by only two optically-contacted parts, consisting in 3 mm thick disk with a diameter of 15 mm and a spherical cap with a radius of 5 mm and a height of 3 mm, corresponding to a numerical aperture of 0.9.

The new version of the SIL is attached to the glass cell by placing the SIL on the cell upper surface, were a through hole of 12 mm of diameter was opened. The SIL was finally glued to the glass cell using a vacuum leak sealant (SPI Vacseal) compatible with ultrahigh vacuum. The old version of the SIL, on the other hand, is located inside the cell. The lens was attached into a jig and glued into the upper wall of the glass cell (see Fig. 3.25).

The new version of the SIL have two important advantages respect to the old one. The first advantage is that the 3 mm thick glass present over the old version produces spherical aberrations that needs to be compensated with specially designed objectives lenses. These

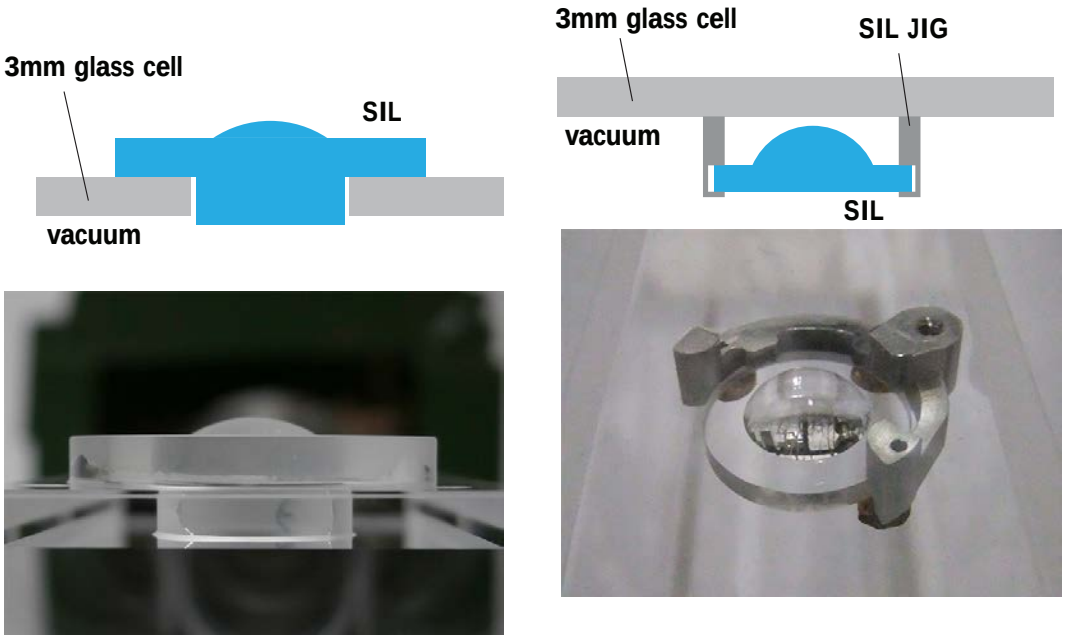

(a) New version (b) Old version

Figure 3.25: SIL attached to the glass cell.

objective lenses are not commercially available and are often high-priced. The glass also produces transmission losses that reduces the collection efficiency of the microscope system. The second advantage is that the aperture of the spherical cap was reduced to 0.55 (which is the same aperture of the objective lens). As shown in 3.26, a beam incident onto the flat surface of the SIL by an angle of incidence of 55.8° (the Brewster angle) is refracted into an angle slightly larger than the aperture of the spherical cap. This angle of refraction ensures that the beam will enter and exit from flat surfaces, resulting in no stray reflections that can produce undesired interference patterns.

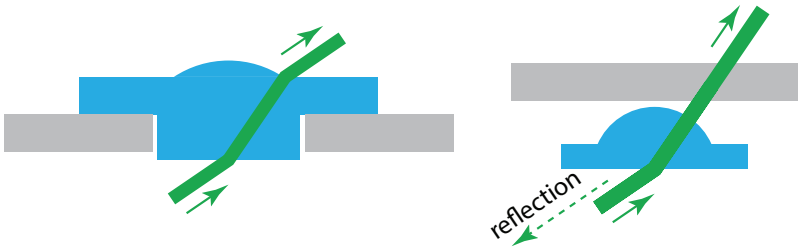

Figure 3.26: The new version of the SIL avoids reflections by reducing the aperture of the spherical cap.

Chapter 4

Experiment: Transport of atoms to the solid immersion lens surface

4.1 Introduction

As seen in the previous chapter, the solid immersion lens is a very useful tool that can be used to increase the numerical aperture and collection efficiency of the microscope system. Another important feature of this lens is the possibility of creating a standing wave by reflecting a laser beam onto the flat surface of the lens, and using the resulting standing wave as an optical trap. As the position of this standing wave is fixed with respect of the lens surface, it is possible to trap atoms with high stability at a fixed position respect to the lens. This technique, which is denominated "optical accordion", will be explained in detail in the following sections.

For experiments using trapped atoms in a two-dimensional optical lattice, ultra-high vacuum and good optical access to the sample is desired. For this reason, the solid immersion lens is allocated in a square glass cell separated from the main metallic chamber, where the ultra-cold atoms are first prepared. Observation by a high resolution microscope system requires that atoms remain confined in a pancake-shaped region which is thinner than the depth of field of the objective lens and is located sufficiently close to the surface of the lens. In rubidium experiments, a system of multiple coils was used to create a moving magnetic trap, which was used to transport the atoms to the surface of the lens. In the case of ytterbium, the lack of electronic spin impedes the use of magnetic fields.

This chapter focuses on the experimental procedure to transport the atoms to the surface of the solid immersion lens using an all-optical method. The procedure is schematized in Fig. 4.1, with the numbers representing the temperature of the atoms, and distance from the SIL surface to them.

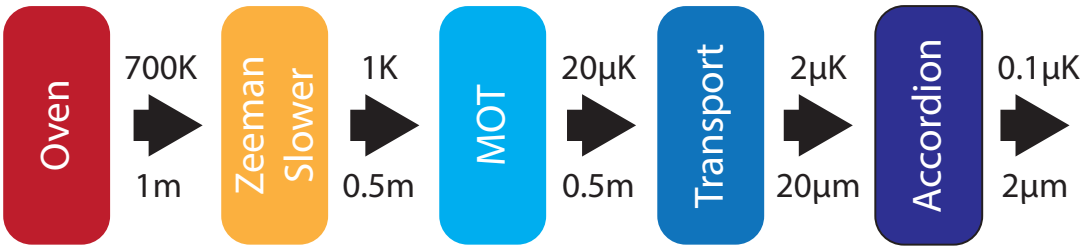

Figure 4.1: Experimental steps to prepare a BEC under the surface of the SIL. The numbers corresponds to the atomic cloud temperature and the distance to the surface of the SIL.

4.2 Oven

At room temperature, the saturated vapour pressure of ytterbium is roughly 3×10^{-21} torr and practically no atoms cannot be obtained from a solid sample. The conventional method to increase the number of atoms is increase the vapour pressure to $\sim 10^{-3}$ torr by heating the sample with an oven. The saturated vapour pressure of ytterbium as a function of temperature is shown in Fig. 4.2. The solid line is a theoretical estimation using the experimentally obtained heat of sublimation and applying it to the Clausius-Clapeyron equation [92]

$$\log_{10} p \approx 6.943 - \frac{8656}{T} - 0.0004647\,T + 0.6390\log_{10} T, \tag{4.1}$$

where p is the pressure in torr, and T is the temperature in K. The four points in the graph corresponds to data in [93].

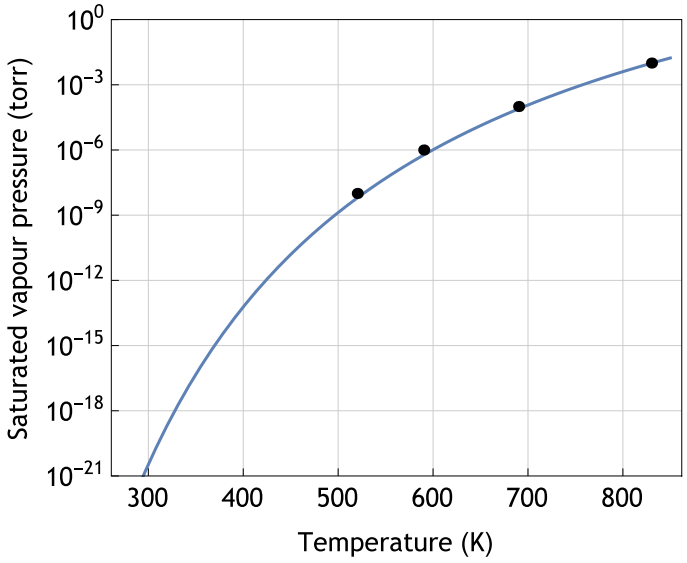

Figure 4.2: Saturated vapour pressure of ytterbium as a function of temperature.

In the experiment, the oven (EpiQuest STHKC-1300SH-lC) is heated to 700 K, which results in a vapour pressure of 1×10^{-4} torr. This pressure is enough to obtain a sufficient number of atoms in the magneto-optical trap. The heated atoms exit from a 2.6 mm diameter orifice and are collimated using a 30 mm long, 4 mm inner diameter nozzle that also serves as differential

pumping tube.

4.3 The vacuum chamber

As the oven is heated to 700 K, the vacuum in the chamber surrounding the oven degrades to 10^{-8} torr. To reduce losses due to background collisions, main experiments realized in the glass cell requires a vacuum level of 10^{-11} torr. To reach this vacuum level, the vacuum system is divided in three chambers separated with a nozzle that acts as differential pumping tube and isolates the vacuum up to 1 or 2 orders of magnitude, as shown in figure 4.3.

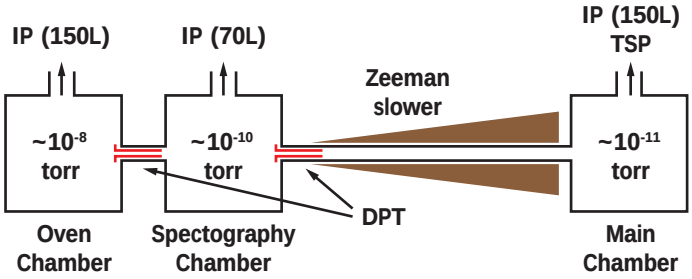

Figure 4.3: Schema of the vacuum chamber, showing the three main chambers. IP: Ion pump, TSP: titanium sublimation pump, DPT: interconnected by differential pumping tubes

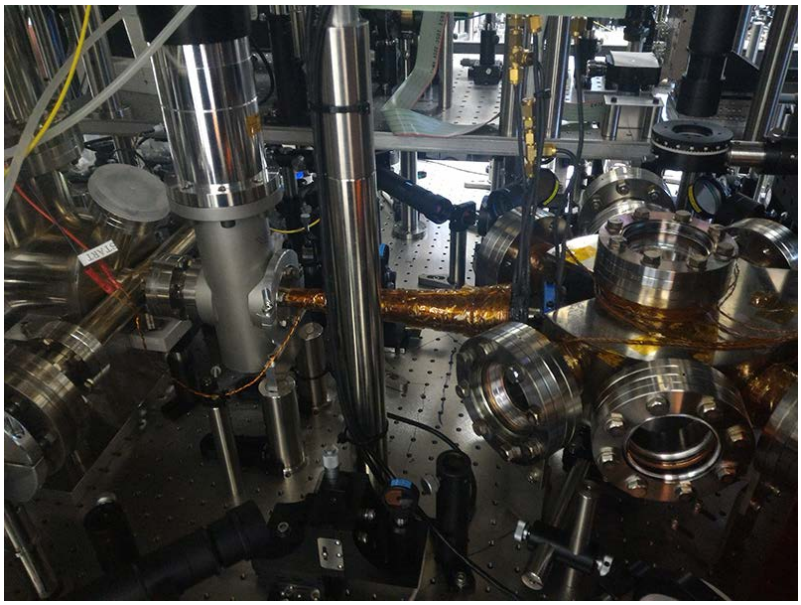

Figure 4.4: Photo of the vacuum chamber.

The glass cell is attached to the main chamber, where the main experiments are realized, having an ultra high vacuum (UHV) level of $\sim 10^{-11}$ torr. The main chamber is pumped with a 150 litters ion pump (Varian VacIon Plus 150) and a titanium sublimation pump (TSP). The spectrography chamber is between the main chamber and the oven chamber, and have a vacuum level of $\sim 10^{-10}$ torr, and is connected to the main chamber through the Zeeman slower.

Spectrography experiments using the atomic beam are realized in this area. It is pumped with a 70 litters ion pump (Varian VacIon Plus 75). The oven chamber is pumped with a 150 litters ion pump and have a vacuum level of 10^{-9} torr. Initially, the whole chamber was baked out to 250 °C for 2 weeks.

4.4 Laser cooling of Yb atoms

Ytterbium have two suitable transitions for laser cooling, the $^1S_0 \rightarrow {}^1P_1$ strong transition and the $^1S_0 \rightarrow {}^3P_1$ narrow inter-combination transition. Cooling properties of both transitions are summarized in table 4.1.

	$^1S_0 \longleftrightarrow {}^1P_1$	$^1S_0 \longleftrightarrow {}^3P_1$
Wavelength	398.8 nm	555.8 nm
Natural linewidth	$2\pi\times$ 27.9 MHz	$2\pi\times$ 181 KHz
Saturation Intensity	57 mW/cm^2	0.14 mW/cm^2
Doppler cooling limit	650 μK	4.4 μK

Table 4.1: Characteristic values for lowermost transitions of ^{174}Yb

Initial experiments with Ytterbium were realized in 1999 using the $^1S_0 \rightarrow {}^1P_1$ transition, obtaining 10^6 atoms [64]. However, a branching from the $^1P_1$ excited state to the sub-stable triplet states $^3P_0$ and $^3P_2$ limited the final number of trapped atoms. Afterwards, the same team succeeded in magneto-optical trapping of Ytterbium atoms with the intercombination transition, obtaining a much larger number of atoms at a temperature of 20 μK [94].

In this experiment the $^1S_0 \rightarrow {}^3P_1$ transition is used for magneto-optical trapping, while the Zeeman slower utilizes the strong $^1S_0 \rightarrow {}^1P_1$ transition for slowing down the atomic beam exiting from the oven.

4.4.1 Zeeman slower

Atoms heated by the oven have a temperature of ~ 700 K and a RMS speed of ~ 300 m/s. In contrast with this velocity, the capture velocity of a magneto optical trap (MOT) using the narrow transition $^1S_0 \rightarrow {}^3P_1$ is less than 10 m/s, meaning that only a small portion of the atomic beam can be captured by the MOT. In order to increase the number of trapped atoms, the temperature of the atomic beam needs to be further reduced. The conventional method to do this is by using a Zeeman slower device which combines the laser cooling technique with the Zeeman shift produced by a strong magnetic field.

The Zeeman slower device used in the experiment is shown in Fig. 4.5. Atoms that exit from the oven are collimated into an atomic beam and travel through a long tube towards

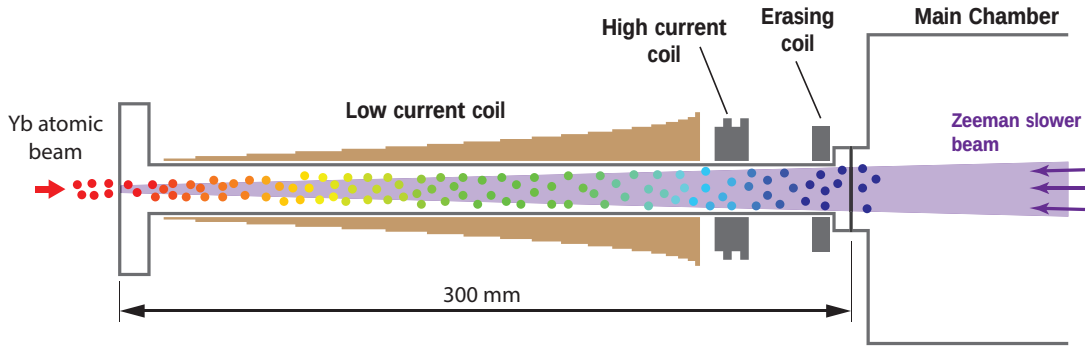

Figure 4.5: The Zeeman slower device. The atomic beam is slowed down by a laser cooling beam detuned to the ${}^1S_0 \rightarrow {}^1P_1$ transition. A magnetic field is used to create a Zeeman shift that cancels the change in the Doppler shift.

the main chamber. A laser beam detuned from the ${}^1S_0 \rightarrow {}^1P_1$ transition is shinned into the atomic beam in the opposite direction, slowing the atoms by laser cooling. To understand why a magnetic field is used, the equation of radiative force exerted by a laser beam is:

$$F = \frac{\hbar k}{\tau_{\text{scat}}} = \hbar k \times \frac{\Gamma}{2} \frac{s_0}{1 + 4\left(\frac{\Delta - kv}{\Gamma}\right)^2 + s_0} \tag{4.2}$$

where Γ is the natural linewidth of the ${}^1S_0 \rightarrow {}^1P_1$ transition, v is the velocity of the atom, and s_0, k and Δ are the saturation intensity, wave-number and detuning of the cooling beam. Note that the force is maximum when the detuning of the laser beam equals the shift due to Doppler effect ($\Delta = kv$). Suppose that the laser beam detuning is set such that the radiative force is maximum for the atom initial velocity. When the atoms slow down, the change in velocity leads to a change in Doppler shift, reducing the effectiveness of the cooling process. A magnetic field is used to create a Zeeman shift that cancels the change in Doppler shift, such that:

$$\Delta - kv(x) - \alpha B(x) = 0 \tag{4.3}$$

for every position x, where B is the magnetic field at the position x, and α is a constant determined by the Zeeman effect. The acceleration exerted by the laser cooling beam at every position x is then:

$$a = \frac{F}{m} = \hbar k \times \frac{\Gamma}{2} \frac{s_0}{1 + s_0}. \tag{4.4}$$

For large saturations ($s_0 \gg 1$) this acceleration is roughly 5×10^5 m/s^2, which can be used to cool down atoms travelling at a speed of 300 m/s in a few milliseconds. The distance d_s required to slow down the atoms is:

$$d_s = \frac{{v_0}^2}{2a} \approx 100 \text{ mm} \tag{4.5}$$

where $v_0 = 300\,\mathrm{m/s}$ is the initial velocity. The required shape for the magnetic field $B(x)$ is then

$$B(x) = \frac{\Delta - k v(x)}{\alpha} = \frac{k v_0 - \sqrt{v_0^2 - 2a x}}{\alpha} = \frac{k v_0}{\alpha}\left(1 - \sqrt{1 - \frac{x}{d_s}}\right) \tag{4.6}$$

where g is the Lande g-factor and μ_B is the Bohr magneton. For $x = x_s$, the resultant peak magnetic field is

$$B(x_s) = \frac{k v_0}{\alpha} = \frac{k\hbar v_0}{g\mu_B} \approx 560\,\mathrm{G}. \tag{4.7}$$

The required magnetic field is created using a set of 3 coils, as shown in Fig. 4.5. The first coil is made using a 1 mm diameter coil (low current coil), while the second (high current coil) and third (erasing coil) coils are created using a 3 mm hollow pipe which is cooled down with water passing inside the pipe. The position of the atoms trapped in the center of the main chamber by the MOT is highly dependent on both the offset and gradient of the magnetic field. The third coil is used to eliminate the magnetic field at the center of the main chamber by creating a negative magnetic field. The resultant magnetic field is shown in Fig. 4.6.

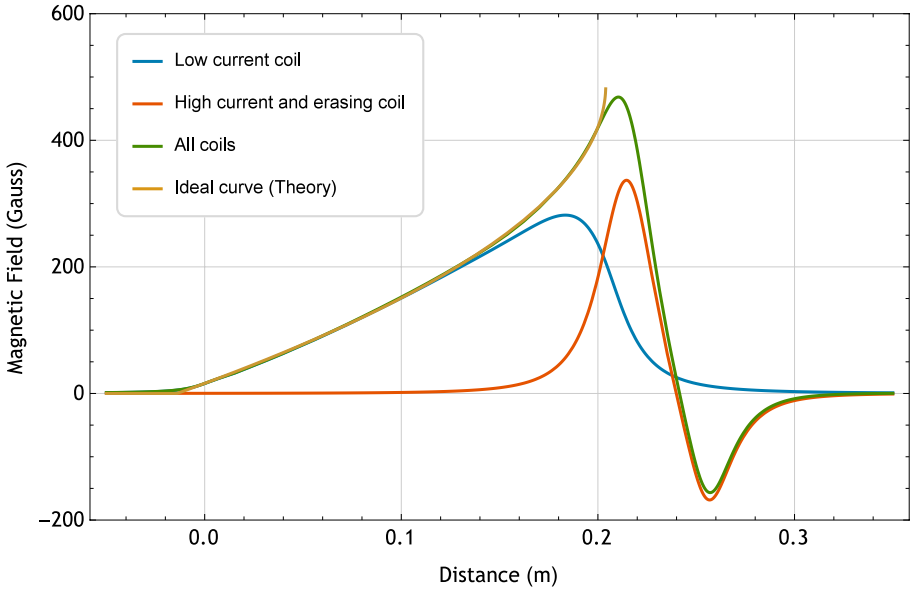

Figure 4.6: Magnetic field generated by the Zeeman slower coils compared to the theoretical required magnetic field.

The currents used for the low current coil, high current coil and erasing coil are 2.1 A, 67 A and 67 A respectively. At the center of the main chamber ($x = 0.345\,\mathrm{m}$), the resultant bias magnetic field is less than 0.1 G, while the gradient magnetic field is less than 0.2 G/cm. The ideal curve in the plot was drawn using the parameters $B(x_s) = 487\,\mathrm{G}$ and $x_s = 218\,\mathrm{mm}$.

To test the performance of the Zeeman slower, the fluorescence spectrum of the atomic beam is measured at the main chamber. The probe beam intersects the atomic beam at an angle of 80 degrees. Due to the Doppler shift effects, the resultant fluorescence spectrum reflects the velocity distribution of the atomic beam. The results of this experiment is shown in

Fig. 4.7. When the Zeeman beam is activated, the fast part of the spectrum (left side of the graph) moves to the show part (right side of the graph), indicating that the atoms are being effectively slowed down.

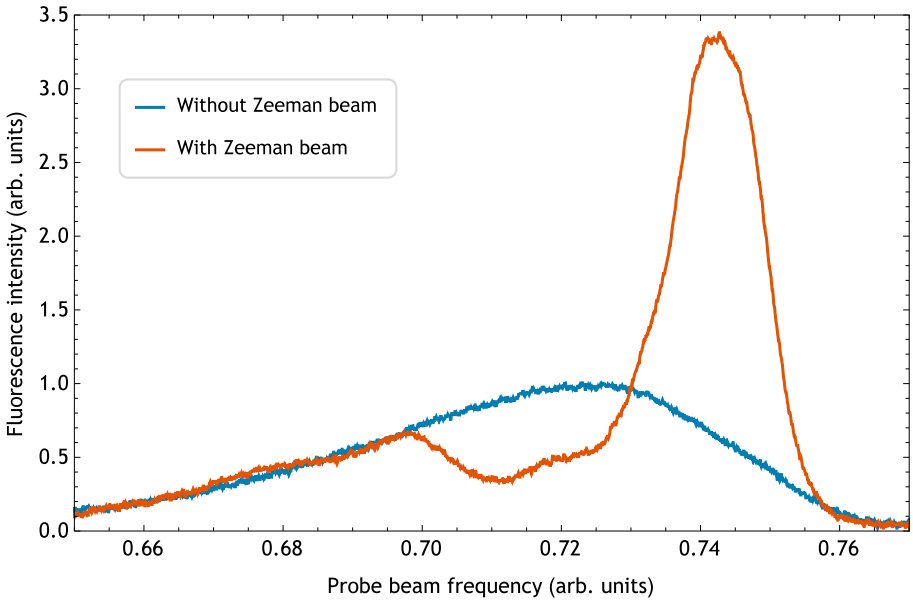

Figure 4.7: Spectrography of the atomic beam showing the performance of the Zeeman Slower.

The laser source for the Zeeman beam at 398.9 nm is generated by a frequency doubling bow-tie ring cavity with a BiBO crystal. In the initial experiments, a PPKTP crystal in a bow-tie cavity was used to second harmonic generation, but the conversion efficiency was low (13% for a 1 W input) and optical damage was observed in short-time operation. The fundamental light is generated by a Ti:Sapphire laser ($\sim$ 1.6 W at 798 nm, Coherent MBR-110) which is pumped by a green solid-state laser (10W at 532 nm, Coherent Verdi V-10). The output power of the ring cavity is typically $\sim$ 300 mW with very good short-time and long-time stability.

An ultra-low expansion cavity (Finesse 500, FSR 1.5 GHz) is utilized to frequency lock the external cavity of the Ti:Sapphire laser. The frequency of the Zeeman Slower beam is detuned $-2\pi \times 700$ Mhz. Two double pass acousto-optic modulator are used to create the light for the absorption imaging system.

4.4.2 Magneto optical trap

After slowing down the atoms with the Zeeman Slower, atoms are trapped into the magneto optical trap (MOT). This trap is composed by three retro-reflected, orthogonal beams that are red-detuned to the ${}^1S_0 \rightarrow {}^3P_1$ transition and provide Doppler cooling in all directions. As the cooling beams themselves only reduce the velocity of the atoms and do not provide a restoring force, two coils in the anti-helmholtz configuration are used to add a magnetic field gradient, which provides the required restoring force to the cooling beams. As a result, all the atoms

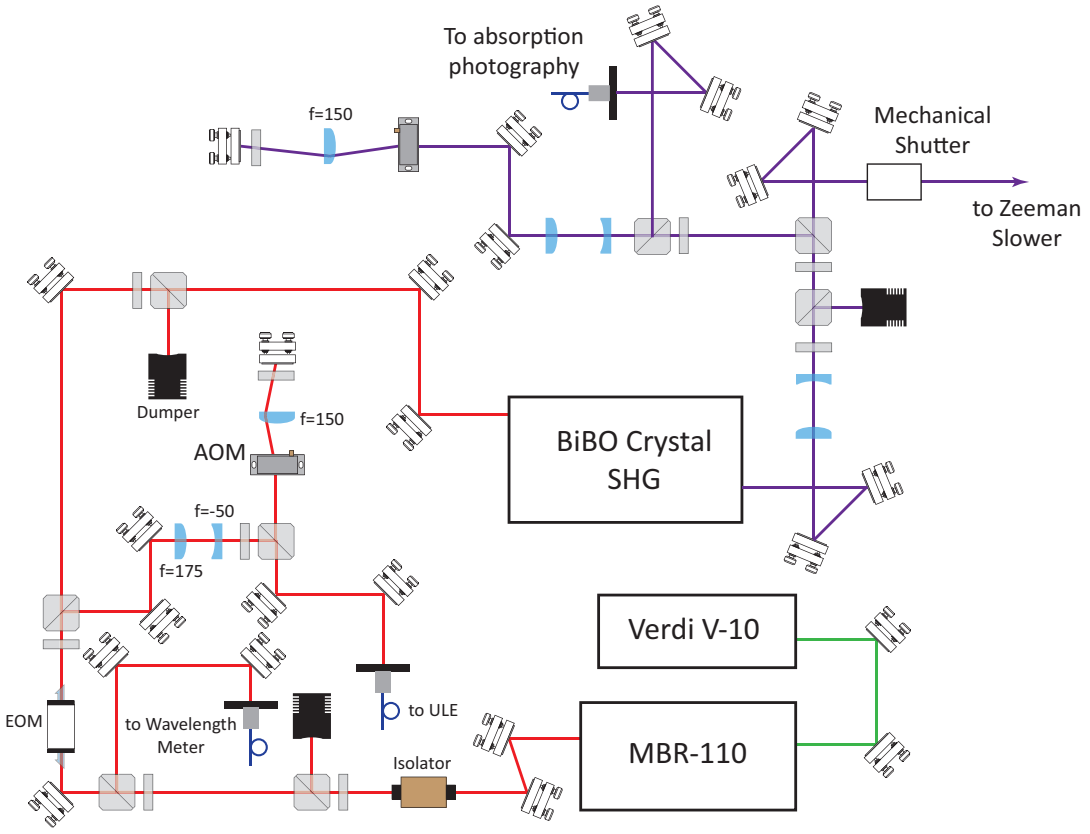

Figure 4.8: Laser system for 399 nm ($^1S_0 \longleftrightarrow {}^1P_1$ transition)

gathers around the zero of the magnetic field.

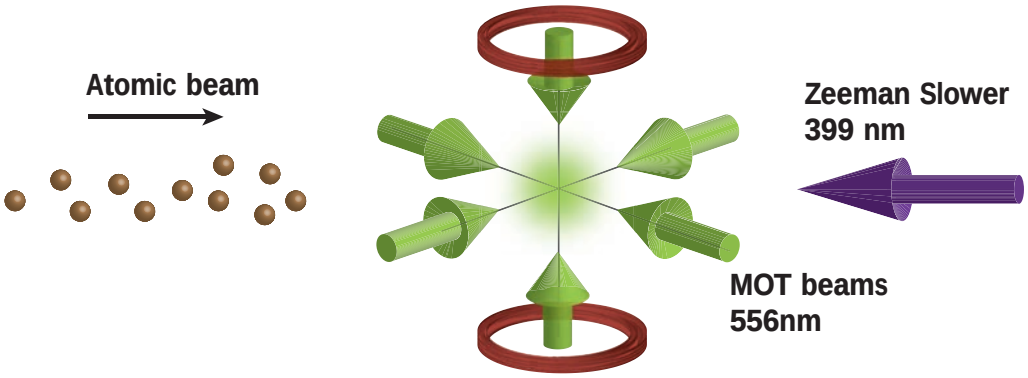

Figure 4.9: Atoms slowed down by the Zeeman slower are trapped into the magneto optical trap, which combines Doppler cooling and a quadrupole magnetic field formed by two coils.

The two coils that form the quadrupole magnetic field are separated by an average distance of 100 mm, with each coil having 150 turns and an average coil diameter of 65mm;. When a current of 0.3 A flows through the coils, a gradient magnetic field of 0.5 G/cm in the XY axis and -1.0 G/cm in Z axis is created.

Each cooling beam has a beam diameter of 1 cm and a power of 13 mW and 26 mW in the XY and Z directions, respectively. This results in a laser intensity of $I = 17$ mW/cm$^2 = 118 I_s$ and 33 mW/cm$^2 = 236 I_s$ in the XY and Z directions, respectively. The detuning is set to $-2\pi\times$

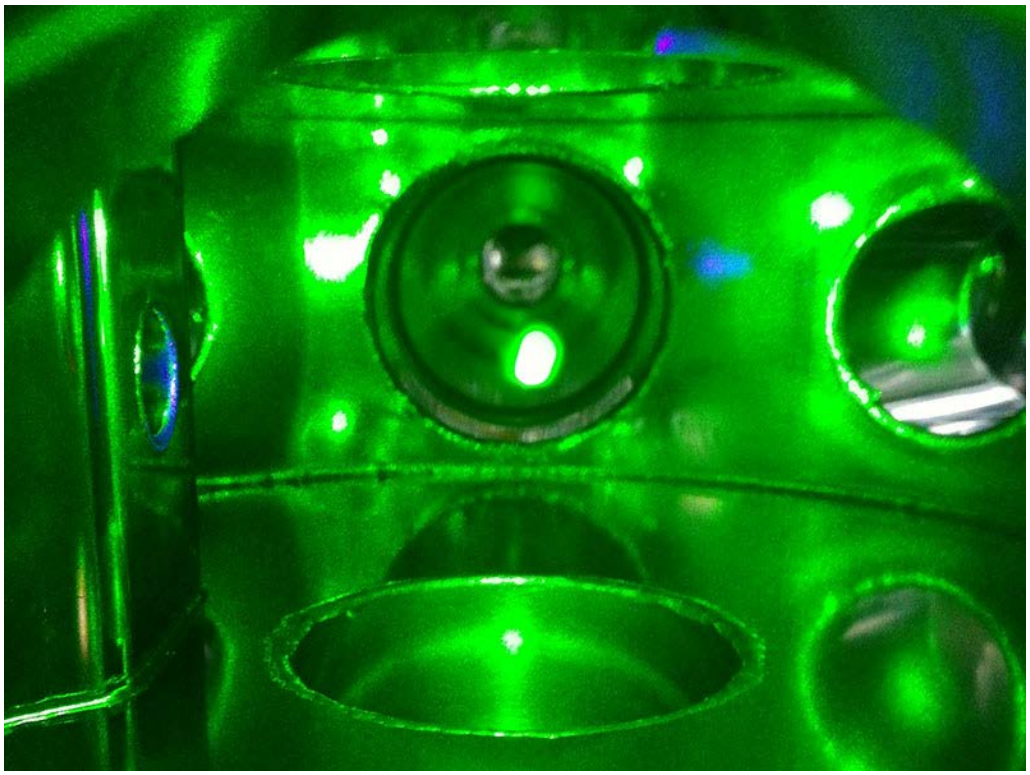

Figure 4.10: Atoms trapped in the MOT after 10 seconds of loading time.

2 MHz = 11Γ. Note that the intensity and detuning used here are larger than the required for optimal laser cooling, where $I \ll I_s$ and $\Delta = \Gamma/2$. These large intensities and detunings increase the capture velocity range, which results in an increased number of atoms in the trap. Figure 4.10 shows the trapped atoms inside the main chamber after 10 seconds of loading.

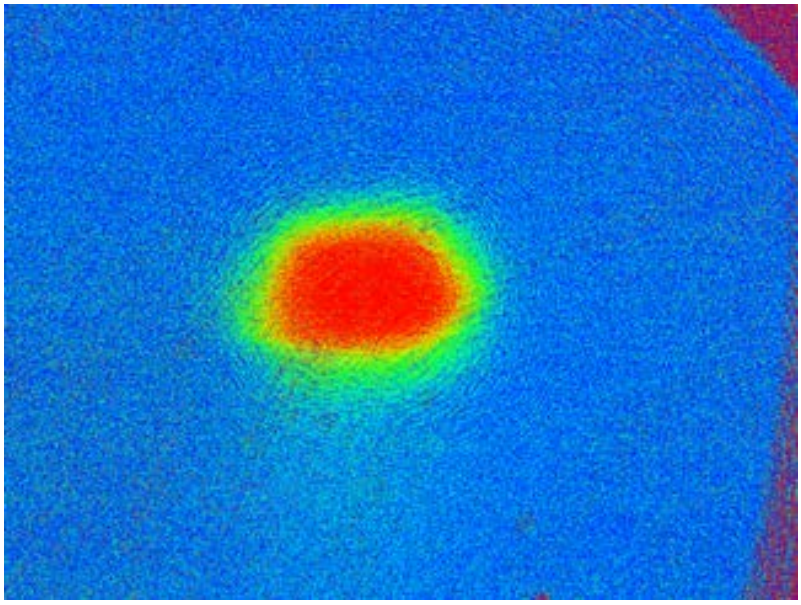

Figure 4.11: Absorption image of the atoms trapped in the MOT after a time-of-flight of 11 ms.

To load as much as atoms as possible in the optical dipole trap, the density of the trapped

atoms is increased (compression) while reducing their temperature. This is done by incrementing the current of the coils to 3A during 50 ms, while decreasing the intensity and detuning of the cooling beams. The trapped atoms after compression is shown in Fig. 4.11. The final number of atoms after compression and cooling is 3×10^8. The temperature of the atoms was 13 μK.

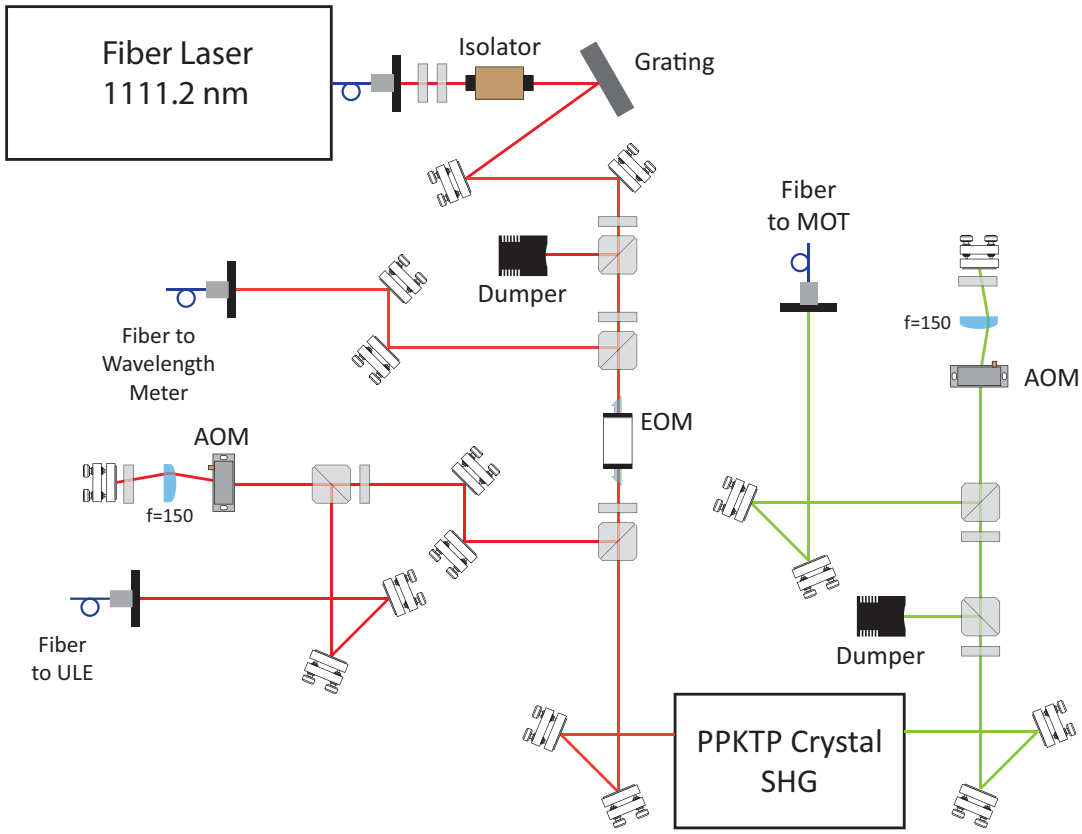

Figure 4.12: Laser system for the $^1S_0 \longleftrightarrow {}^3P_1$ transition at 556 nm.

The 555.8 nm laser beam is generated by a frequency doubling bow-tie ring cavity with a PPKTP crystal. The fundamental light is generated by a fiber Laser (Menlo system). An isolator and a reflective grating are used to protect the fiber laser against back-reflections. The output power of the ring cavity is typically $\sim$ 200 mW at 555.8 nm. An ultra-low expansion cavity (Finesse 5000, FSR 1.5 GHz) is utilized to frequency lock the fiber laser.

4.5 Transport using optical dipole traps

Evaporative cooling using a crossed optical dipole trap (ODT) is the conventional method to further cool down Yb atoms after the MOT. In this method, atoms in the MOT are first loaded into a single ODT. The second ODT is then introduced, which crosses the first ODT at the center of the trap. The intensity of the first ODT is gradually reduced resulting in evaporative cooling, where the hot atoms are removed while the overall temperature of the remaining atoms is reduced. In this experiment, a cross ODT is also utilized to reduce the temperature of the atoms, but each of the ODT beams have the additional purpose of transporting the atoms near the surface of the SIL. After loading the atoms into the first, horizontal ODT, the trap is translated 450 mm from the center of the MOT chamber to a distance of few millimeters away under the surface of the SIL. The second, vertical ODT is then introduced to realize evaporative cooling. After cooling the atoms, the vertical ODT is converted into a conveyor belt, which is useful to further transport the atoms to a distance of a few tens of micrometers to the SIL surface.

4.5.1 The optical system

The high power optical beam required for optical trapping is derived from a continuous-wave, frequency doubled, diode-pumped solid-state laser (Coherent Verdi V18) with an output of 18 W at a wavelength of 532 nm. The optical system is shown in Fig. 4.13. The same optical source is used to generate the horizontal and vertical ODT beams. Details of the system will be explained in the following sections.

4.5.2 Horizontal ODT: Loading

Atoms trapped in the MOT are first loaded into the horizontal ODT by focusing the ODT beam into the center of the compressed atomic cloud. The focused beam is created by a pair of lenses situated on top a moving air-bearing stage (Aerotech ABL15050). The air-bearing stage can move up to 500 mm and it ensures a smooth movement during the transport process reducing the heating effects produced by mechanical vibrations. The beam profile at the waist of the horizontal ODT is a circular beam with a radius of 29 μm resulting in a potential depth of 560 μK. The absorption images before and after loading the atoms in the ODT are shown in Fig. 4.14. Initially 3.5×10^7 atoms at a temperature of 50 μK are loaded into the horizontal ODT.

4.5.3 Horizontal ODT: Lifetime and temperature

The number and temperature of atoms as a function of trap holding time is shown in Fig. 4.15. The number of atoms is shown in a semi-logarithmic graph and it was fitted using a double

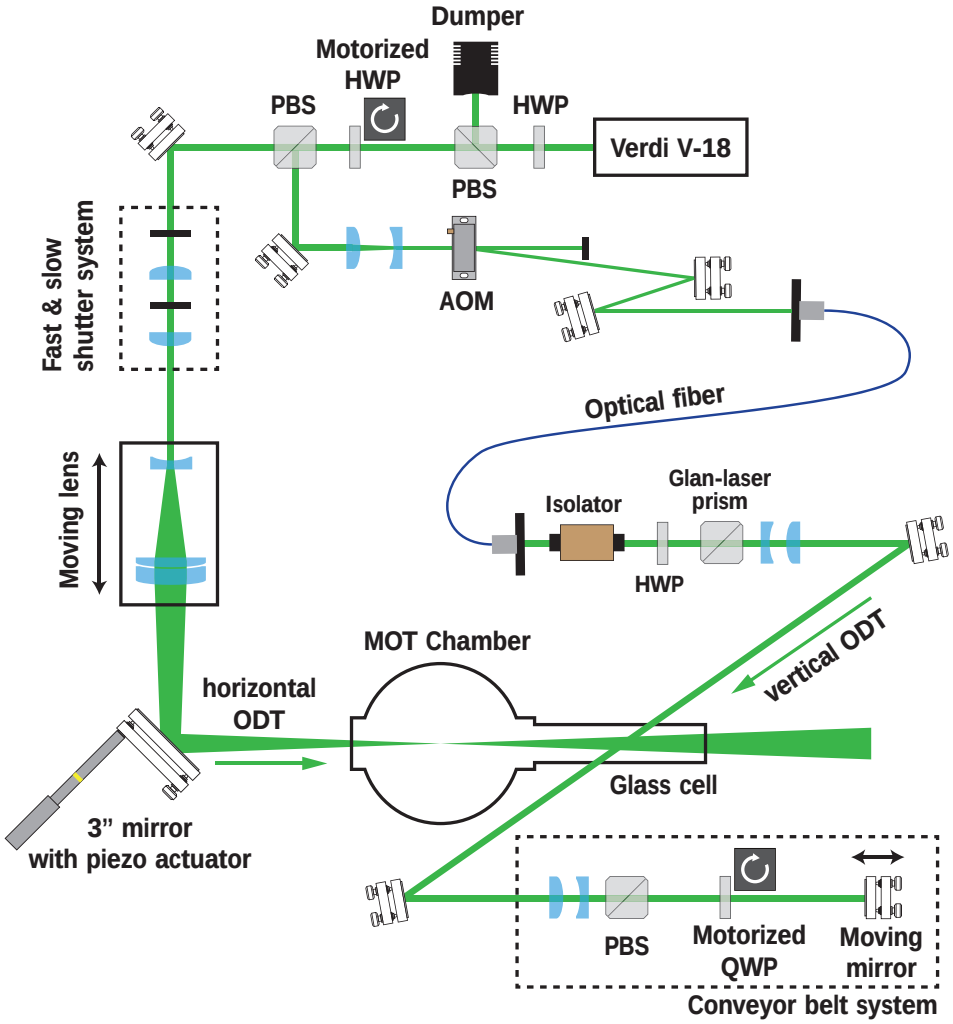

Figure 4.13: Optical system for the horizontal and vertical ODT derived from a 18 W, frequency-doubled DPSS laser.

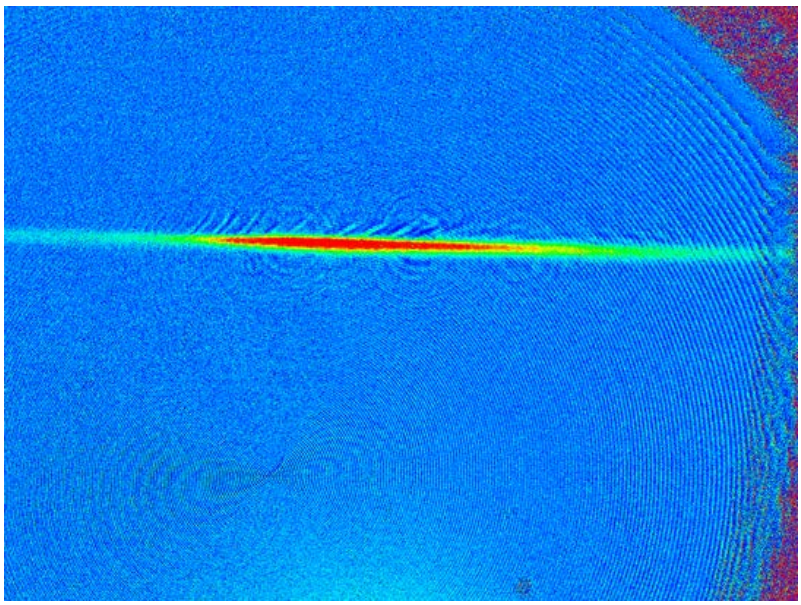

Figure 4.14: Absorption images of atoms after loading into the horizontal ODT.

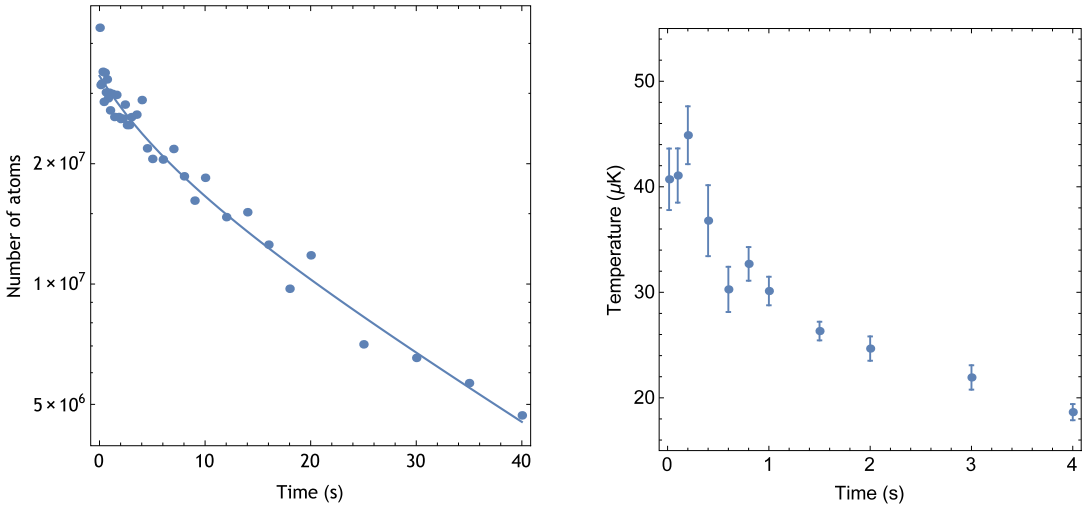

Figure 4.15: Number and temperature of atoms after loading as a function of holding time.

exponential curve

$$N(t) = N_1 e^{-t/\tau_1} + N_2 e^{-t/\tau_2} \tag{4.8}$$

resulting in decay times of $\tau_1 = 5\,\mathrm{s}$ and $\tau_2 = 24\,\mathrm{s}$. The first decay time is due to two-body collisions that results in evaporative cooling of atoms in the trap. The evaporative cooling results in a decrease of temperature, as seen in the temperature plot in Fig. 4.15. The second decay time is due to one-body losses such as collisions with background gas and scatterings due to the optical-dipole trap.

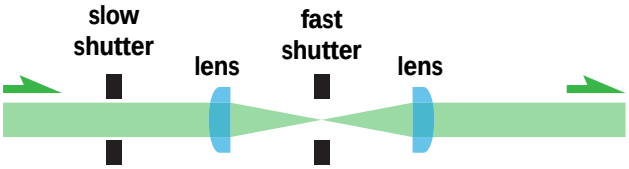

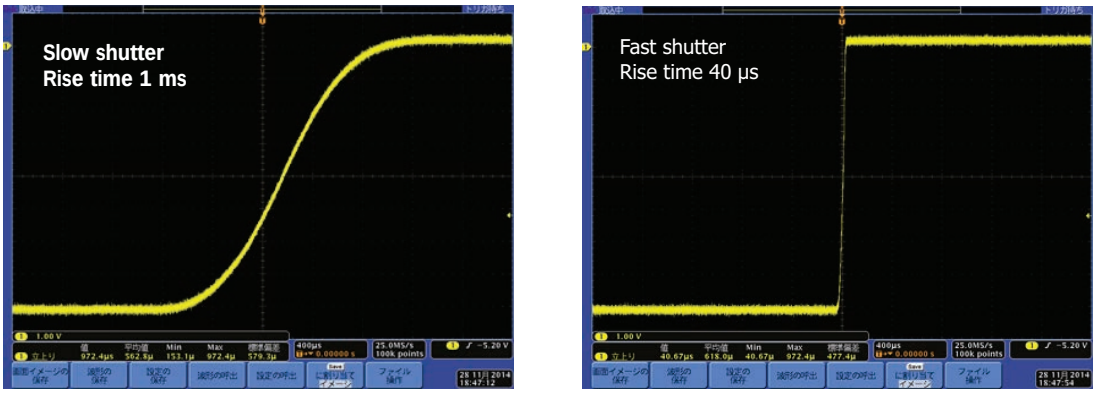

Figure 4.16: Fast and slow shutter system used for temperature measurement.

Note that there are two mechanical shutters for the horizontal ODT in the optical system (Fig. 4.13). To measure the temperature of trapped atoms the conventional method is to suddenly release the trap and measure the thermal expansion of the atoms. This rapid release

condition is satisfied when the release time is faster comparable to the inverse of the trap frequency of the dipole trap. Such fast release speeds are realized using a “fast mechanical shutter” that shuts the beam at the point where its focused, as shown in Fig. 4.16. As the high power density at the beam waist may damage the mechanical shutter, a second ”slow mechanical shutter“ is activated at almost the the same time, which shuts down the beam a few milliseconds after the fast shutter. This ensures that the high power density only impacts the fast shutter for very short times.

4.5.4 Horizontal ODT: Transport

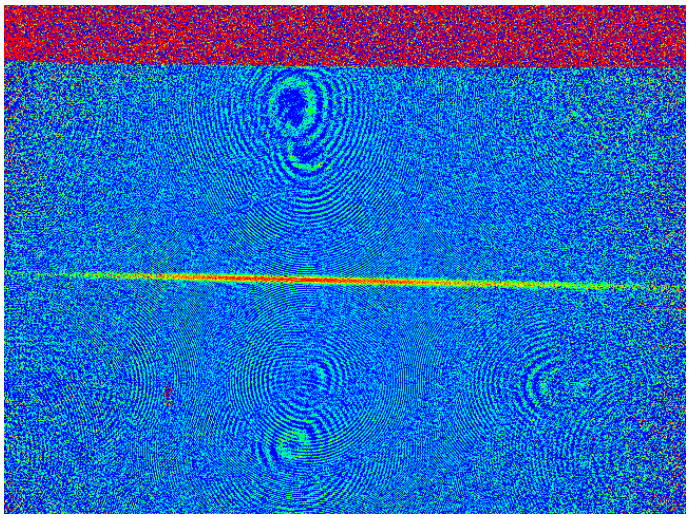

Figure 4.17: Absorption imaging of the atoms in the horizontal ODT after transport.

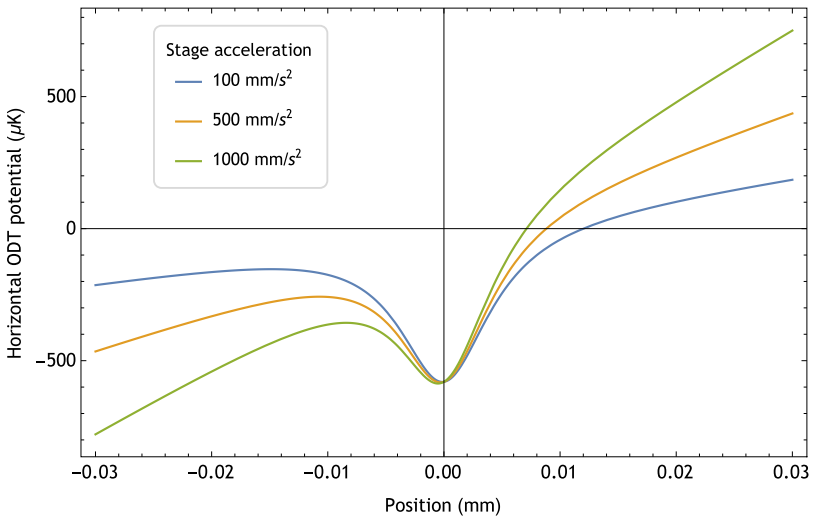

Figure 4.18: Potential depth along the propagating axis of the horizontal ODT for different stage accelerations.

Atoms trapped in the horizontal ODT are mechanically transported by translating the position of the optical trap. The pair of lenses that focuses the horizontal ODT are located on

top of a translating air-bearing stage. During transport, the position of the stage moves by 450 mm to transport the atoms a few millimeters below the surface of the SIL. The absorption imaging images of the atoms after transport are shown in Fig. 4.17.

The stage movement consists in an uniformly accelerated and decelerated motion with an acceleration of 0.3 m s^2, taking 2.5 s to move a distance of 450 mm. Although the air-bearing stage used in this experiment is capable of accelerations up to 1 m/s^2, such fast accelerations result in spilling due the inertial force experimented by the atoms. Figure 4.18 shows the potential depth including the inertial force of the stage along the propagation axis of the horizontal ODT for different stage accelerations. The curves where calculated for a beam with a power of 16 W and a beam waist of 29 μm. For the maximum acceleration of 1 m/s^2 the potential depth is greatly reduced, resulting in spilling of atoms.

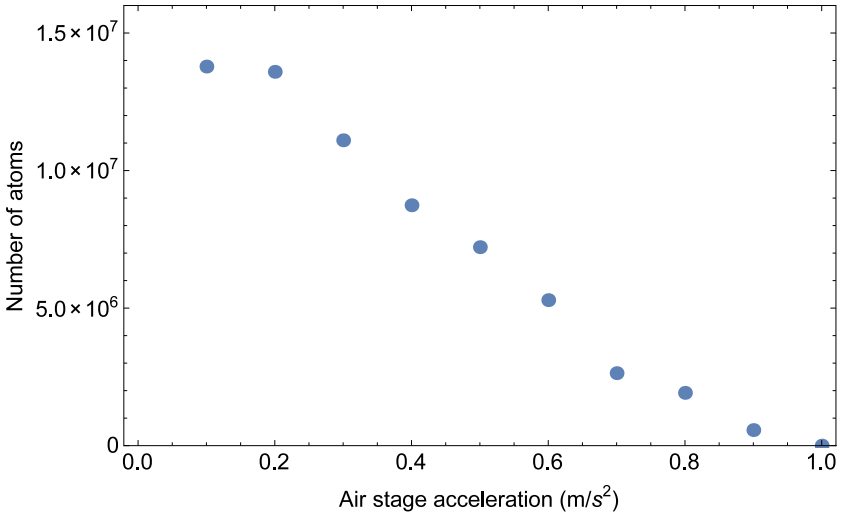

Figure 4.19: Number of atoms after transport as a relation to the stage acceleration.

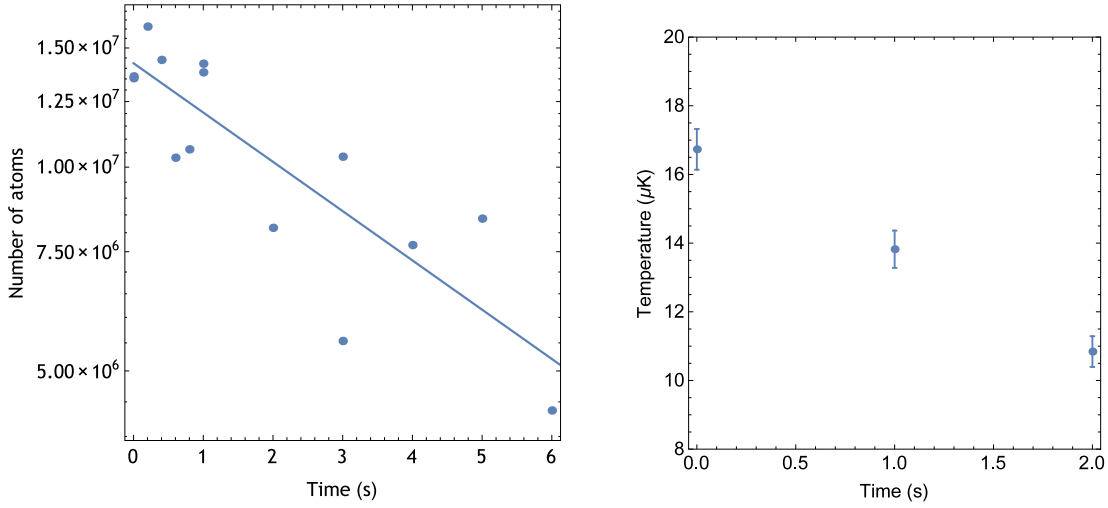

Figure 4.20: Number and temperature of atoms after transport as a function of holding time.

The relation between number of atoms after transport and the acceleration of the stage

was experimentally checked. The results are shown in Fig. 4.19. For an acceleration of $1\,\mathrm{m\,s^2}$ all the atoms were lost. Low accelerations resulted in a larger number of atoms after transport.

The number and temperature of the transported atoms as a function of trap holding time is shown in Fig. 4.20. The number of atoms is shown in a semi-logarithmic graph and it was fitted using an exponential curve. The resultant lifetime was of 6 s. The temperature of the atoms also is reduced during the first seconds of holding time, which is an indication that evaporative cooling continues after transport.

The initial number of atoms and temperature was 1.4×10^7 and $17\,\mu$K, respectively. Note that the number of atoms and temperature are lower compared to that in the MOT chamber after a holding time of 2.5 s (equivalent to the transport time), which means that the inertial force experimented during transport accelerate the evaporative cooling process.

4.5.5 Vertical ODT: Evaporative cooling using a cross ODT

After the first stage of transport using the horizontal ODT, atoms are positioned 2.7 mm under the surface of the solid immersion lens. At this point, a second beam (vertical ODT) is introduced, intersecting the horizontal ODT at the beam waist to form a crossed ODT trap. The evaporative cooling procedure is schematized in Fig. 4.21. In order to eliminate reflections from the surface of the SIL, the beam incidence angle is at Brewster angle respect to the plane surface of the lens. The polarization was carefully selected using a Gran-laser prism (see Fig. 4.13). Note that the Brewster angle for fused silica at 532 nm is of 34.4°, which is 1° larger than the aperture of the spherical cap of the SIL (a numerical aperture of 0.55 is equivalent to 33.4°). This ensures that both the incident beam and the retro-reflected beam (see the vertical transport section) will both enter and exit from flat surfaces, thus avoiding any stray light interference that may complicate the transport process.

To align the horizontal ODT with the vertical one, a 12 mm motorized actuator (Thorlabs Z812) was attached to the mirror mount that reflects the horizontal ODT right before the viewport. The motorized actuator is attached to the horizontal knob of the mirror, and can be moved with 0.2 μm precision. As the distance between the two knobs is approximately 60 mm, and the distance from the mirror to the center of the solid immersion lens is 600 mm, by moving the actuator by $0.2\,\mu$m the beam position at the bottom of the solid immersion lens moves approximately $4\,\mu$m. For a vertical beam with a beam waist of $50\,\mu$m, it suffices to move the horizontal beam at intervals of $40\,\mu$m. A distance of ± 1 mm can be covered within 50 measurements, which takes less than 20 minutes for this experiment speed. To verify that the two beams are crossed, the horizontal beam power is reduced to 1 W. When the two beams are correctly crossed, evaporative cooling occurs and the atoms shrink to the intersection of the two crossed ODT.

To control the intensity of the horizontal ODT, the common approach is to use an acousto-

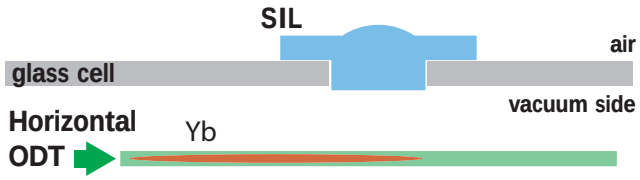

(a) Atoms are originally trapped inside the horizontal ODT positioned 2.7 mm under the solid immersion lens.

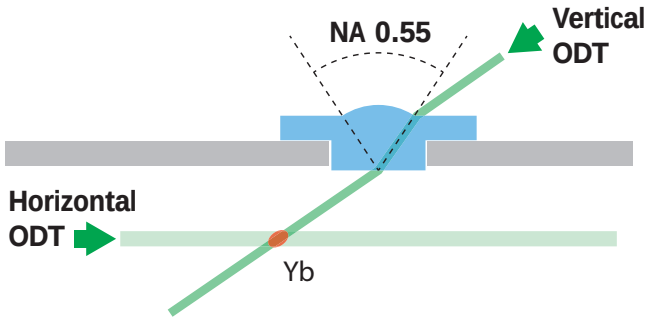

(b) The vertical ODT beam is introduced, intersecting the horizontal ODT beam at the beam waist. Evaporative cooling is realized by decreasing the intensity of the horizontal ODT.

Figure 4.21: Cooling of atoms by evaporated cooling.

optical modulator (AOM). The intensity of the diffracted beam can be controlled by changing the amplitude of the input signal. One of the disadvantages of this method is that the intensity of the first order diffraction is usually around 80%, and consequently, not all of the power can be used for the optical trap. Also, when the amplitude of the input signal changes, the pointing stability of the diffracted beam deteriorates. In this experiment, instead of using an AOM, a motorized half-wave-plate in conjunction with a polarized-beam splitter (PBS) is used to control the power of the horizontal ODT, as shown in Fig. 4.22. By using this method nearly all the power can be used in the optical trap. Additionally, when the power of the horizontal ODT is reduced by moving the half-wave plate, instead of dumping the remaining power it can be recycled and used back for the vertical ODT.

The utilized motor is a stepping motor (Plexmotion PMSB-B56D1DHW) with a hollow axis with inner diameter of 16 mm. The micro-stepping driver (PDSA-BA) is able to move the motor in 16 micro-steps, with one micro-step representing a rotation of $\pi/1600$. The timing for the movement is controlled by a micro-controller Arduino Nano. The driver have 5 TTL inputs: CW and CCW move the motor in clockwise or counterclockwise direction, respectively, when the corresponding TTL input changes its value (step-down or step-up). ENABLE input enables or disables the current to the motor, STEP activates or deactivates micro-stepping, and AUTO_CURRENT manages whatever the motor current stops automatically after 100 ms of input inactivity. For our experiments we change only CW and CCW inputs, which are

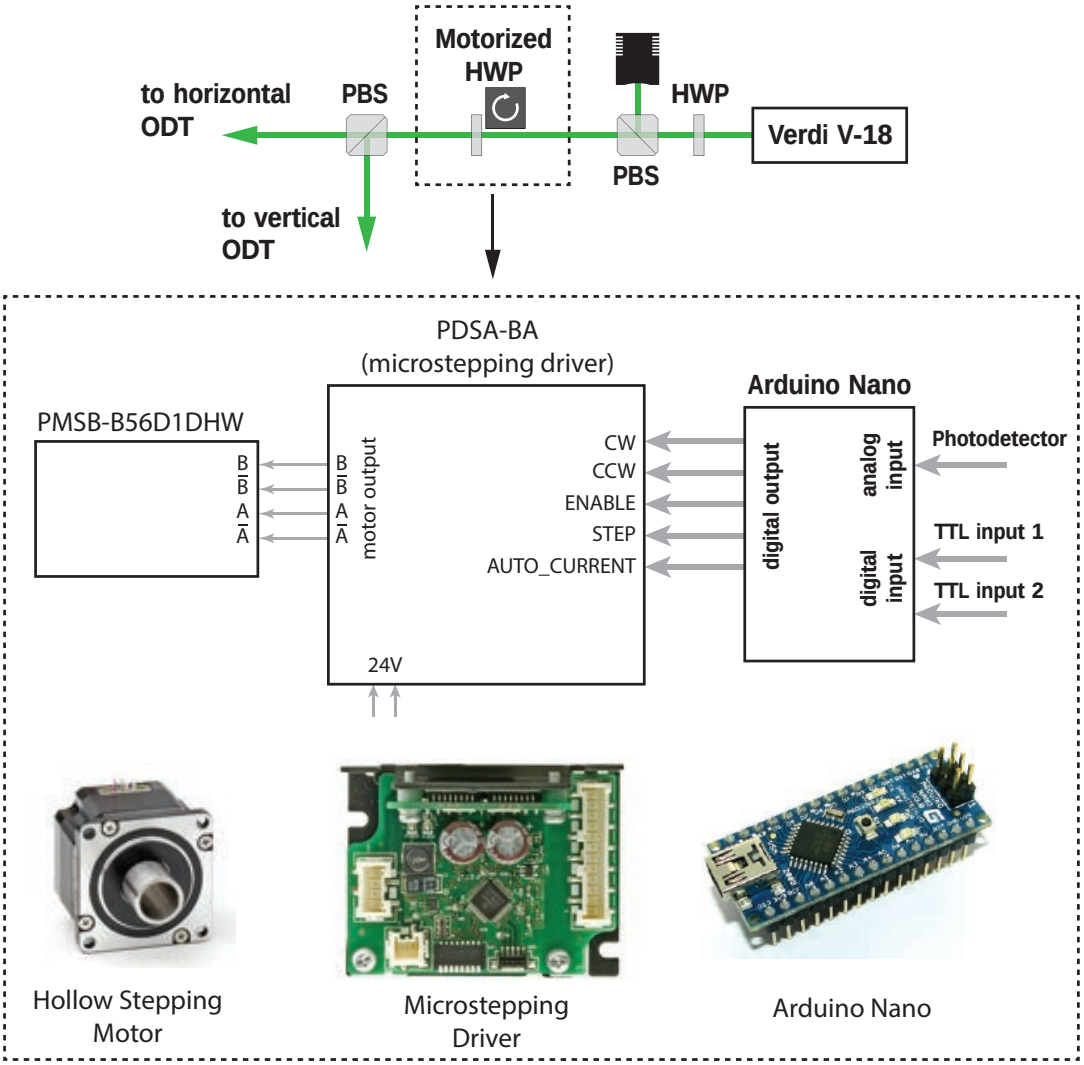

Figure 4.22: System used to control the intensity of the horizontal ODT beam consisting in a motorized wave-plate and polarized beam splitter.

controlled by the digital output of the micro-controller Arduino Nano. Initially, the motor is initialized such as the transmittance of the PBS after the motor-controlled wave-plate is maximum. To do this, the transmitted power is measured with a photo-detector and feed-backed to the micro-controller. When the TTL input 1 is activated, the motor rotates 360 degrees (3200 microsteps) and finds the optimal initial position. The TTL input 2 controlsãČżthe evaporated cooling: When the input is activated, the motor rotates and the intensity of the horizontal ODT is gradually reduced, and when the input is off, the motor goes back to the initial position.

The vertical ODT beam have a beam waist of 40 μm and a final power after evaporation of 1 W. After 4 s of evaporative cooling, 1.0×10^6 atoms at a temperature of 2 μK were obtained. Further cooling of the atoms is possible, but excessively cooled atoms are more susceptible to heating and loss during the vertical transportation stage. Absorption images of atoms before and after evaporation are shown in Fig. 4.23.

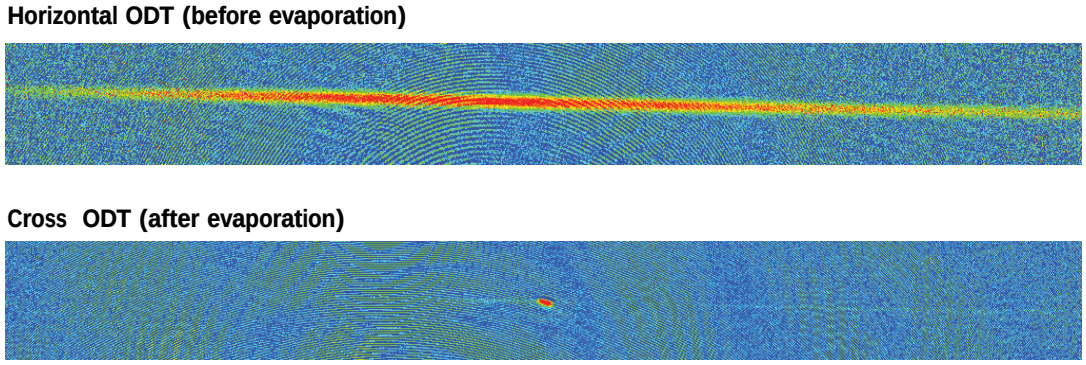

Figure 4.23: Absorption images of atoms before and after evaporative cooling. The final number of atoms is 1.0×10^6 atoms at a temperature of $2\,\mu$K.

4.5.6 Vertical ODT: Transport

The second stage of transport consists in using the vertical ODT as conveyor belt to transport the atoms vertically. Details of the transport process are schematized in Fig. 4.24. To adiabatically transform the vertical ODT into a conveyor belt, a motorized quarter-wave plate in conjunction with a PBS is used to gradually increase the intensity of the retro-reflected beam (see the conveyor belt system in Fig. 4.13) in 100 ms. After the vertical ODT is converted into a conveyor belt, atoms are tightly confined into the standing wave of the vertical ODT, and the horizontal ODT can be removed completely. Finally, the retro-reflected mirror that is situated in top of a air-bearing stage is moved, and the atoms are transported to the surface of the SIL.

When the atoms are too close to the surface, absorption images such as in Fig. 4.17 cannot be used to observe the atoms due to the scatterings by the edge of the surface of the SIL. To observe atoms near the surface, a different absorption imaging approach was used. This system was schematized in Fig. 4.25. The procedure consists in using a probe beam that is incident to the center of the SIL by a shallow angle. As the probe beam reflects into the surface of the SIL, the surface acts as a mirror, resulting in two symmetrical absorption images of the atoms.

The distance between the atoms and the surface of the SIL d is related to the distance D between the center of the two symmetrical images by

$$d = M \frac{D}{2\cos\theta} \tag{4.9}$$

where M is the magnification ratio and θ is the incidence angle of the probe beam. The absorption images during transport using this imaging method are shown in Fig. 4.26. After the vertical transport, 1.0×10^6 atoms at a temperature of $2\,\mu$K were obtained. The final distance between the atoms and the surface was of $20\,\mu$m.

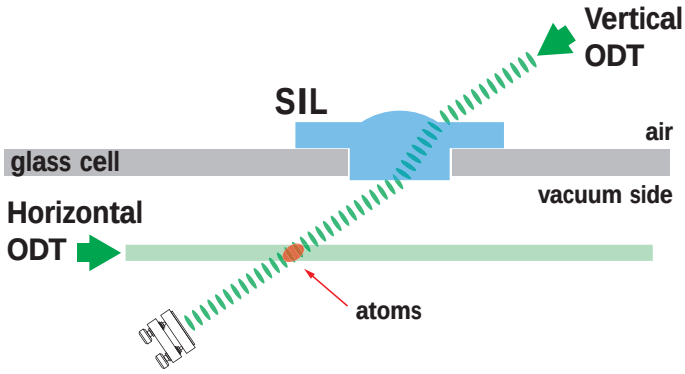

(a) The vertical ODT is retro-reflected to form an optical conveyor belt.

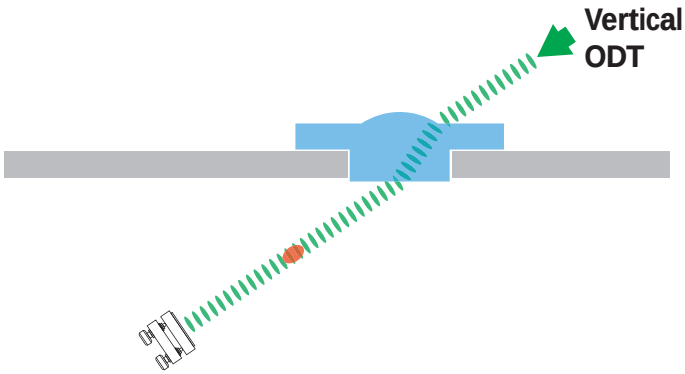

(b) The horizontal ODT is completely removed.

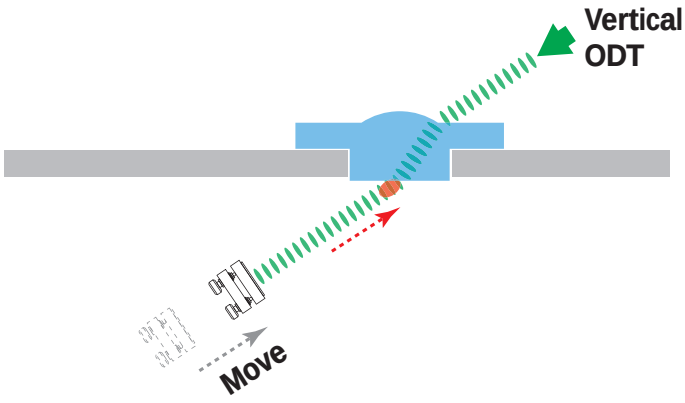

(c) By moving the retro-reflecting mirror, the atoms are transported to the surface of the SIL.

Figure 4.24: Vertical transport of atoms using an optical conveyor belt.

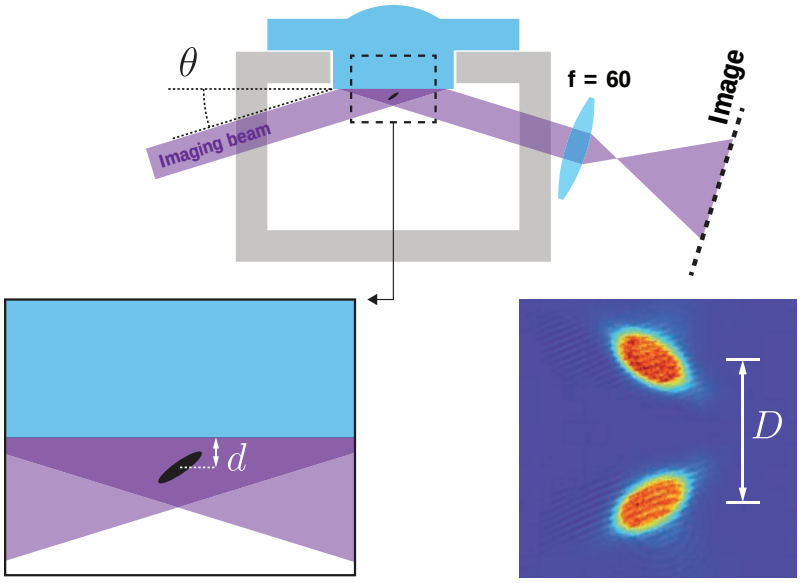

Figure 4.25: Absorption imaging system using the surface of the SIL as a mirror. The probe beam is reflected by the surface of the SIL, generating two symmetrical images of the atomic cloud. The incindence angle θ and the distance D between the two images can be used to precisely calculate the distance d from the atoms to the surface of the SIL.

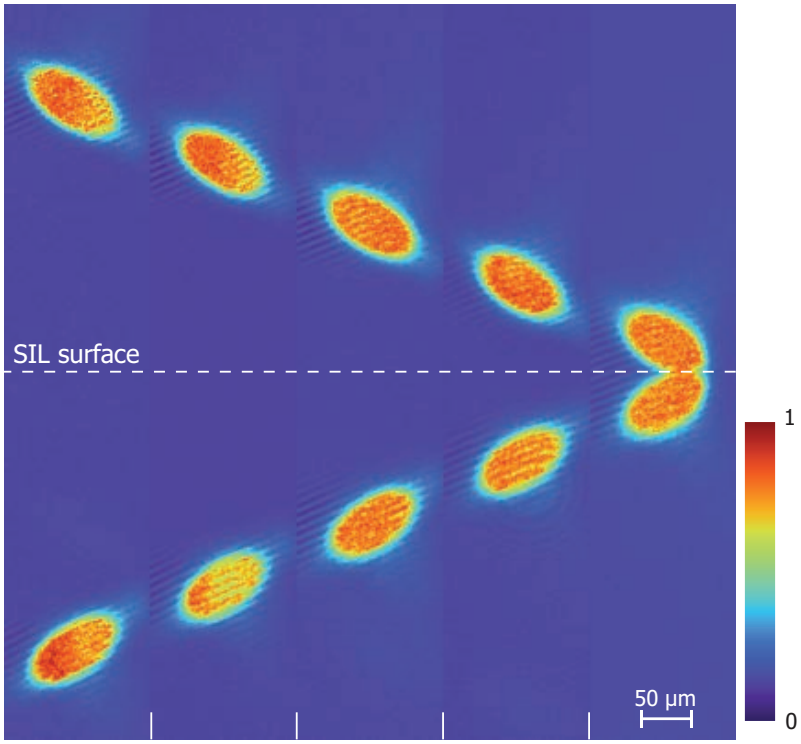

Figure 4.26: Absorption images of atoms during transport. In each image the air-bearing stage moves by 10 μm along the vertical ODT propagating axis.

4.6 Optical accordion

Observation of atoms by a high resolution microscope system requires that atoms remain confined in a pancake-shaped region which is thinner than the depth of field of the objective lens. In previous experiments with rubidium atoms using a solid immersion lens, a thin layer of atoms was prepared by compressing an atomic cloud between the gradient potential of a magnetic field and a repulsive potential created by a blue-shifted evanescent wave [95]. In the case of ytterbium atoms having a very small magnetic moment, magnetic fields cannot be used to trap the atoms.

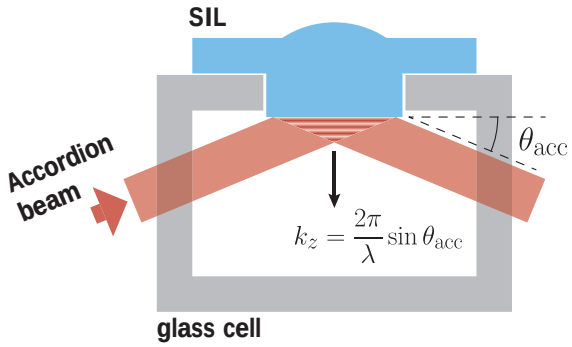

Figure 4.27: The optical accordion method. An accordion beam reflected into the surface of the SIL creates a standing wave which spacing can be manipulated by changing the angle of incidence.

To compress ytterbium atoms into a thin layer, an all-optical approach is mandatory. One idea is to compress the atoms using an "optical accordion". An optical accordion is an optical lattice with manipulable spacing. The first realization of an optical accordion used a lens to focus two parallel beams [96]. When the two beams cross at the focal point, an optical lattice with spacing that depends on the separation of the two beams and the focal length of the lens is created. The spacing of this optical lattice was manipulated by changing the separation of the two beams. This method, however, cannot be applied directly to this experiment as the thin layer of atoms should be positioned directly under the surface of the SIL where the optical access is limited. Another disadvantage of using this method here is that the position of the standing wave is determined by the relative phase of the two beams which is normally unstable due to fluctuations in the surrounding air temperature and density.

Here, a novel method to create an optical accordion near the surface of the solid immersion lens is presented. As shown in Fig. 4.27, an optical accordion can be created when an incident beam (accordion beam) is reflected into the surface of the SIL. As the incident beam and reflected beam interfere, an standing wave is produced with a spacing that only depends on the incidence angle of the accordion beam. The lattice spacing a_z can be manipulated by

changing the incidence angle, related by the equation

$$a_z = \frac{\lambda}{2\sin\theta_{\text{acc}}}. \tag{4.10}$$

Th optical accordion created by surface reflection have two important advantages over the two-beams approach. First, as the relative phase between the incident and reflected beam is determined by the boundary condition of the surface, the position of the lattice is always "locked" respect to the surface. This ensures a stable trap that is useful when using a high resolution microscope system that have very limited depth of field. Second, as the standing wave is created by a single beam and its reflection, only half of the power is required compared to that of the two-beam approach.

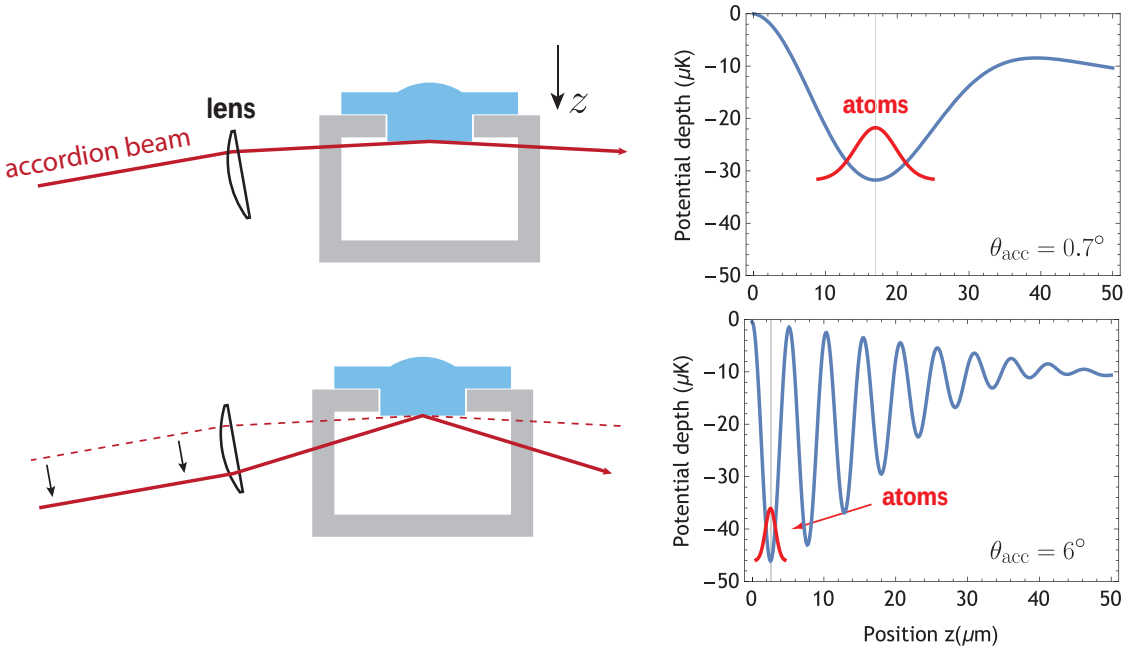

Figure 4.28: Potential of the accordion beam during loading and compression. The potential plot was calculated for a single accordion beam with a power of 1 W.

After the vertical transport, atoms are located 20 μm away from the surface. By introducing the accordion beam at a initial angle of $\theta_{\text{acc}} = 0.7$, all the atoms can be loaded into the first layer of the standing wave, as shown in Fig. 4.28. The intensity of the accordion potential is then decreased to realize evaporative cooling and create a Bose-Einstein condensate. Finally, the accordion beam incidence angle is increased to compress the condensate into a thin layer.

4.6.1 System for changing the accordion angle

The apparatus used to change the incident angle of the accordion beam consists of a lens (accordion lens) and a moving mirror, as shown in Fig. 4.29. The focal point of the lens is

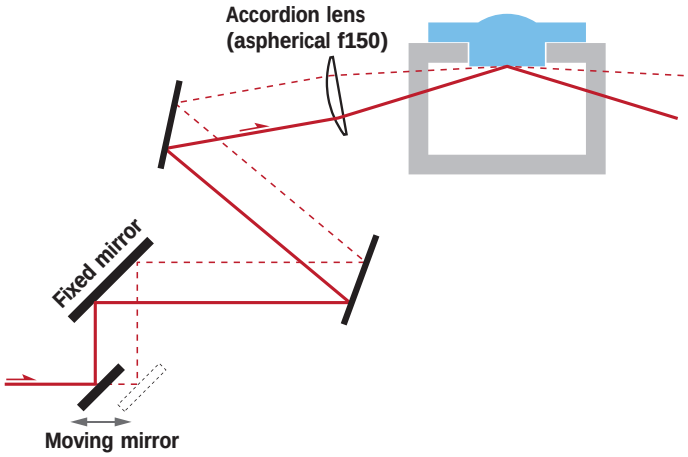

Figure 4.29: System used to change the angle of incidence of the accordion beam. When the mirror moves, the accordion beam displaces laterally. The accordion lens focal point is set to the center of the SIL, resulting in a change in the angle of incidence.

aligned to the center of the SIL. When the mirror moves the beam displaces laterally, resulting in a change of incidence angle. The accordion lens is tilted by $-6°$ respect to the z axis. The mirror is placed on top of a air-bearing mechanical stage to avoid mechanical vibrations (Aerotech ABL10050, see Fig. 4.30). As the mechanical stage moves a maximum distance of 50 mm, the accordion angle can be changed from $\theta_{\text{acc}} = 0°$ to $15°$.

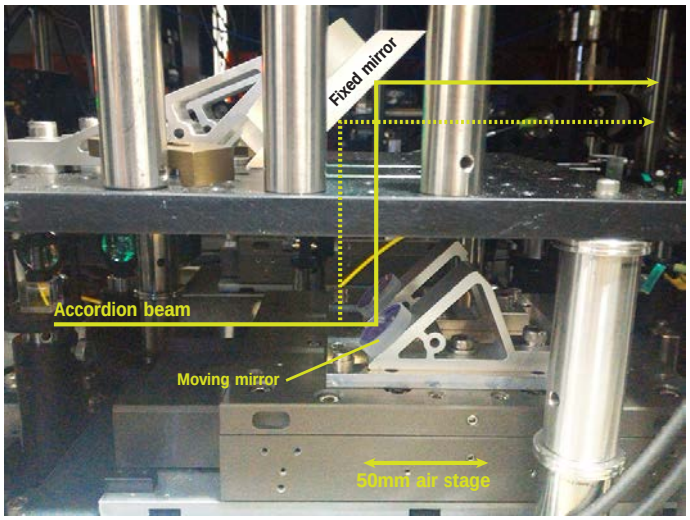

Figure 4.30: Photo of the accordion optical setup schematized in Fig. 4.29

The photo of the optical setup used in the experiment is shown in Fig. 4.30. The moving mirror placed in top of the air-bearing stage is a $1''$ mirror, while the fixed one is a $2''$ by $3''$ elliptical mirror. Both mirrors are tilted by $45°$ respect to the z axis, resulting in a z displacement of the accordion beam when the stage moves. Note that only one air-bearing stage is used to move the mirrors of two different accordion beams.

4.6.2 Optical system

The accordion beam is derived from a fiber amplifier (ALS-IR-1SP-SF) with 15 W of output power. It is seeded by a 50 mW laser generated by a external-cavity laser diode (ECLD) using a Toptica fabry-perot laser-diode chip (LD-1080-0300-1). The optical system after the output of the fiber amplifier is schematized in Fig. 4.31. Although the fiber amplifier includes an output isolator in the laser head, an extra isolator was used to protect the fiber amplifier against strong reflections such as the retro-reflected accordion beam. A transmission grating is used to remove the amplified stimulated emissions of the laser amplifier, as it will be explained in detail in the next chapter. The 1st index refracted beam is then divided into two beams that form each of the accordion beams. The amplitude and frequency of each accordion beam is controlled by acousto-optical modulators (AOM).

After compression, all the atoms are located into a thin layer close to the surface of the SIL. To maximize the surface of the optical trap and at the same time maintain its potential deep enough, the cross section of the accordion beam at the waist was selected to be an ellipse with a waist of 27 μm and 41 μm along the vertical (z) and horizontal (x, y) directions, respectively.

The beam profile of the accordion beam before inciding the accordion lens have a beam diameter of 25 mm and 40 mm (see Fig. 4.32) in the vertical and horizontal directions, respectively. To create such a beam shape, two pairs of beam shaping lenses and one anamorphic prism were utilized.

4.6.3 Accordion lens design

As the accordion angle is changed from shallow angles ($\theta_{\text{acc}} \approx 1°$) during loading to steep angles during compression ($\theta_{\text{acc}} \approx 12°$), the beam is vertically displaced by tens of millimeters by the moving mirror. The optical accordion technique requires that every displaced beam always focus into the center of the SIL. For this condition to be satisfied it is important to ensure that spherical aberrations of the accordion lens are kept to a minimum. The optical aberrations where simulated using a lens design software (Zemax) for two different types of commercially available lenses, as shown in Fig. 4.33.

The simulation includes the aberration generated by the glass cell, that have a thickness of 3 mm and index of refraction of 1.45. As the accordion lens is tilted by $-6°$ respect to the glass cell, the glass cell in the simulation was tilted by 6° respect to the lens. Figure 4.33 shows the simulation result for two different lenses, a spherical (Thorlabs LA1002-C) and an aspherical lens (Thorlabs AL75150-C). The ray fan plot shown in the figure displays how much the beam moves on the screen when the incident beam displaces vertically (transverse ray aberration). Note the striking difference between the aberration of the two lenses, even when the vertical scale in the aspherical lens plot is one order of magnitude smaller. The aspherical lens per-

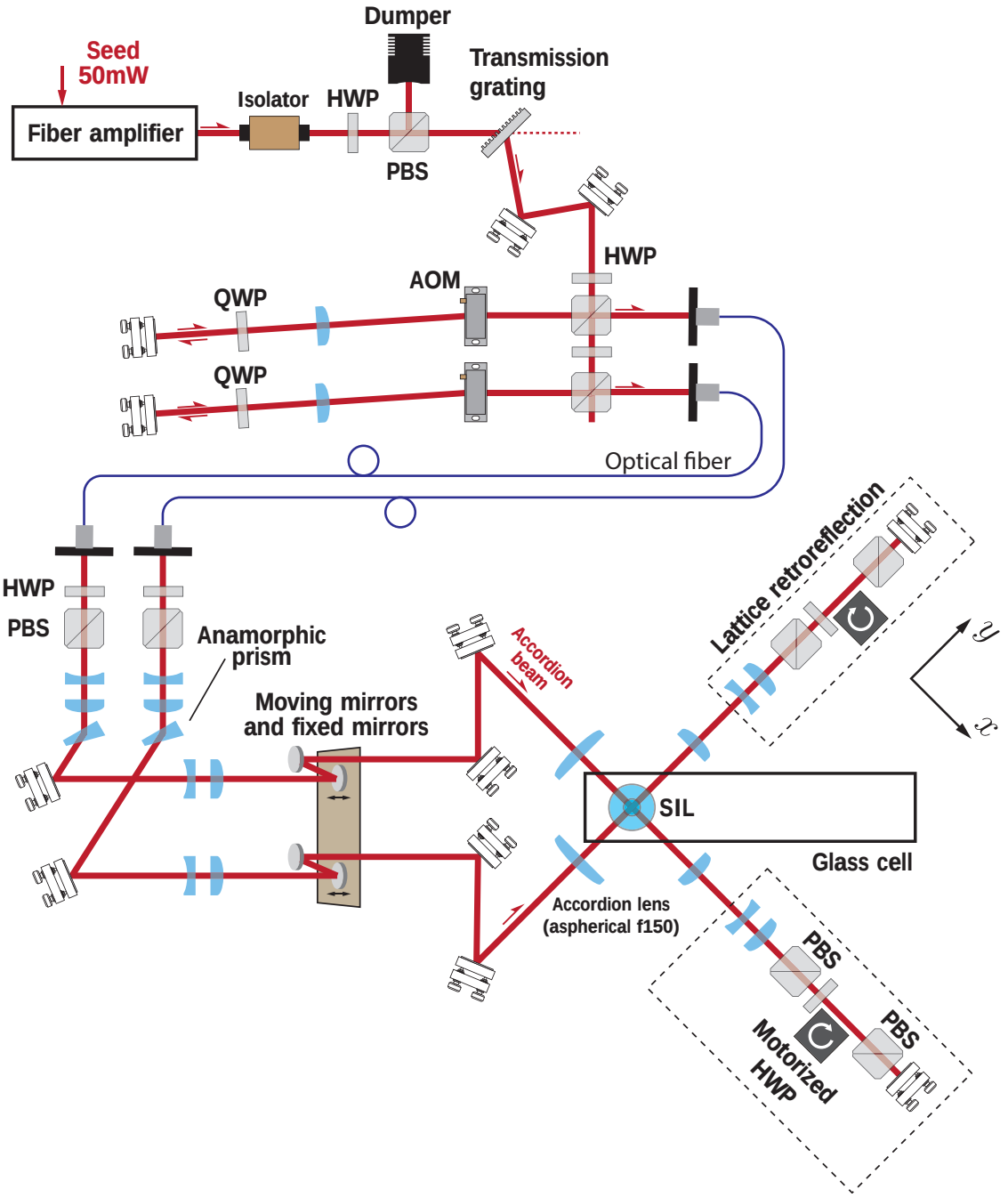

Figure 4.31: Laser system for the accordion beams.

forms even better when the glass cell is not present, meaning that the spherical aberration here is limited mainly by the glass cell. For the experiments, the Thorlabs AL75150-C aspherical lens was selected. Although it is possible to correct the glass cell aberration by using a custom ordered aspheric lens, the commercially available lens selected here was sufficient to successfully compress the atoms up to $\theta_{\mathrm{acc}} = 12°$. For the final fluorescence imaging experiments, an angle of incidence of only $\theta_{\mathrm{acc}} = 6°$ was used. Consequently, the system designed here have a large design margin sufficient for the experiments.

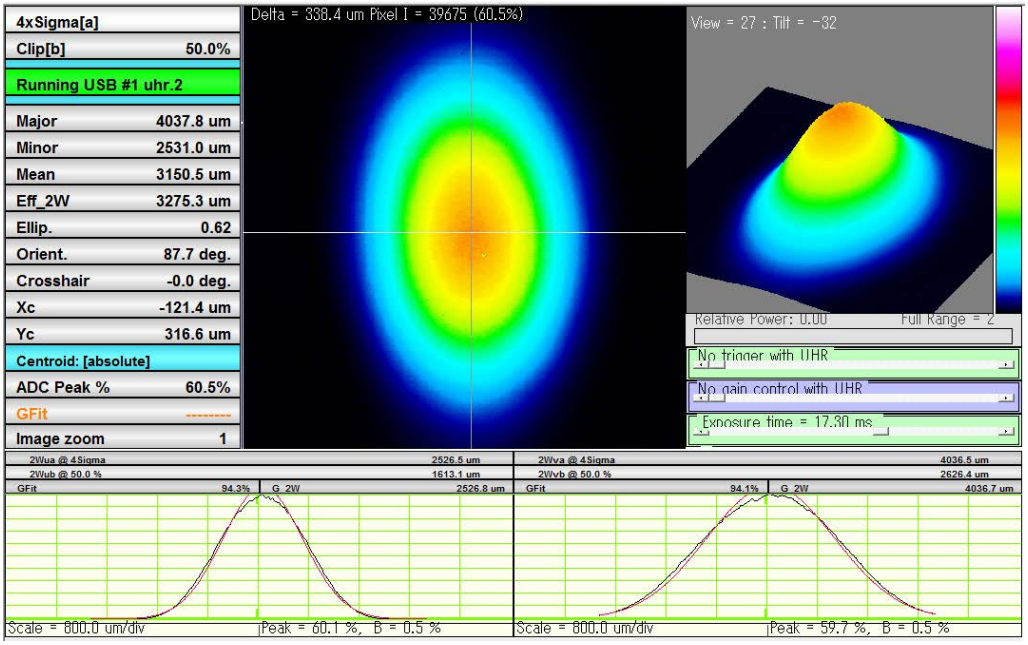

Figure 4.32: Cross section of the accordion beam before inciding the accordion lens. The vertical and horizontal axes represent the z and x, y directions, respectively.

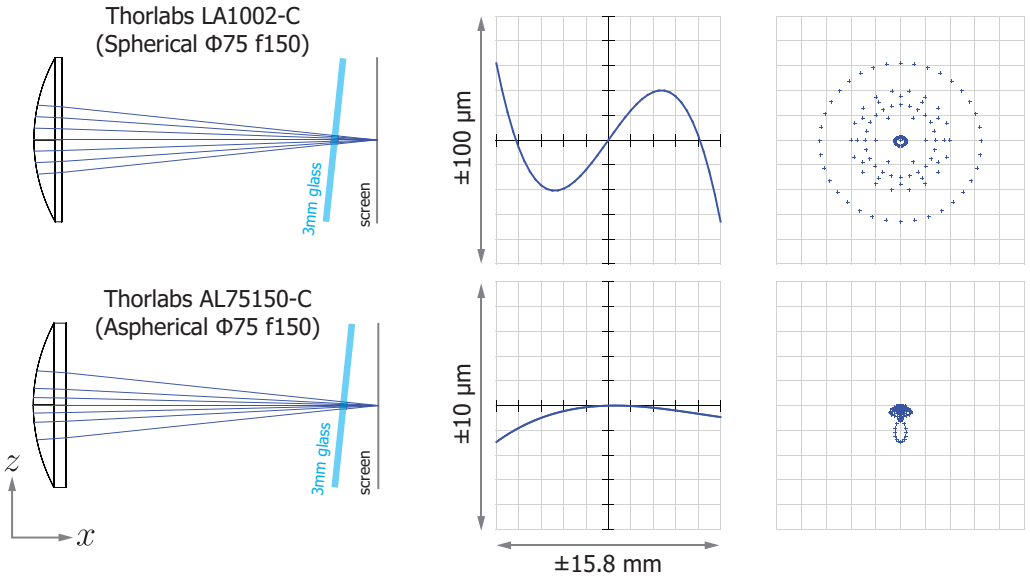

Figure 4.33: Spherical aberration simulation using the software Zemax. Two different lenses are compared.

4.6.4 Removal of amplified spontaneous emission

The ytterbium-doped fiber amplifier used as light source for the accordion beam have the disadvantage inherent to all the fiber amplifiers, which is the production of amplified spontaneous emission (ASE). One of the problems of using this source here is that the accordion beam wavelength was selected to be near resonant to the $^1P_1 \longleftrightarrow {}^1S_0$ at 1077 nm in order to create the deep potential in the $^1P_1$ state required by the fluorescence imaging experiment. If the ASE at the transition wavelength is strong enough to excite the atom into the $(6s7s)^1S_0$,

the lifetime of the atom during the imaging process can be considerably reduced. First, an optical spectrum analyzer was used to measure the ASE of the laser system for a pump light at 1081 nm, as shown in Fig. 4.34. In the figure is also shown the spectrum after adding a long-pass filter (Semrock BLP01-1064) and a transmission grating (Ibsen photonics FSTG-PCG-1250-10XX-986) directly before the fiber coupling device.

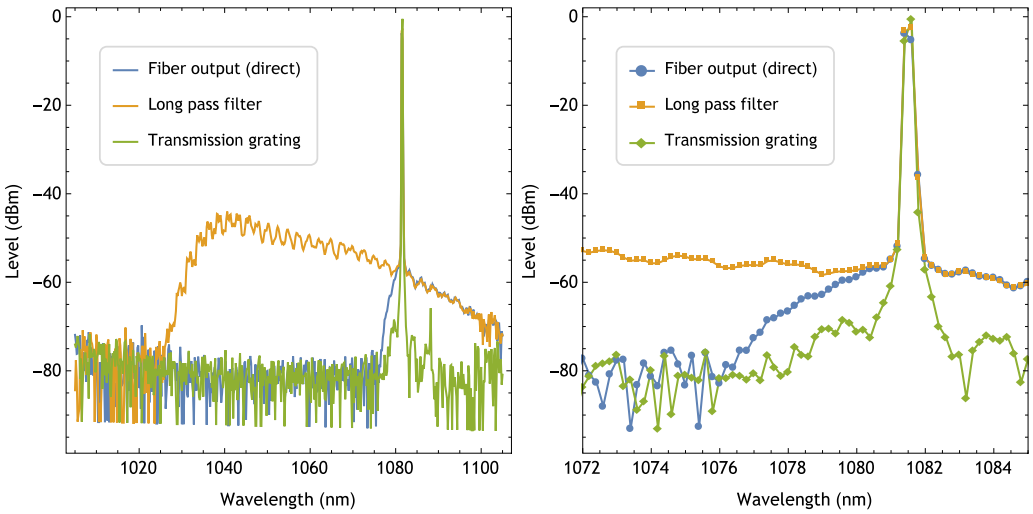

Figure 4.34: Spectrum of the fiber amplifier output. The input power is 60 mW and the resolution was set to 0.1 nm. The plot at right shows a detailed measurement nearby the resonance wavelength (1077 nm). Note that the baseline at −80 dBm is the detection limit of the instrument.

The maximum allowed ASE (laser power at the resonance wavelength) for the experiment can be calculated with the formula

$$P_{\mathrm{ASE}} = \frac{1}{2} I_s s_0 \bar{w}_0^2 \pi = 0.5\,\mathrm{pW} \tag{4.11}$$

where $I_s = 0.3\,\mathrm{mW/cm^2}$ is the saturation intensity of the $^1\mathrm{P}_1 \longleftrightarrow {}^1\mathrm{S}_0$ transition, $s_0 = I/I_s = 10^{-4}$ is the ratio of the light intensity I to the saturation intensity, and $\bar{w}_0$ is the average radius of the beam waist. Note that $s_0 = 10^{-4}$ here is the inverse of the number of photons required for the fluorescence imaging. In terms of power spectral density (PSD), this value can be rewritten as :

$$\delta P_{\mathrm{ASE}}(\omega) = P_{\mathrm{ASE}} \frac{R_\omega}{\Gamma} = -53\,\mathrm{dBm/nm} \tag{4.12}$$

where R_ω is the resolution in terms of angular frequency (0.1 nm represents roughly $2\pi \times$ 25 GHz), and $\Gamma/2\pi = 3.0$ MHz is the linewidth of the transition. Looking back to the plot at Fig. 4.34, the PSD of the ASE at the resonance wavelength was −45 dBm/nm for an input power of 60 mW. For the lattice power used in the experiment during the fluorescence imaging, the PSD increases by a factor of 25 dB to −20 dBm/nm, which is 33 dB stronger than the estimated maximum δP_{ASE}.

To reduce the effects of the ASE a transmission grating (Ibsen photonics FSTG-PCG-1250-10XX-986) was introduced directly after the output of the laser amplifier (see Fig. 4.31). The measurement using the optical spectrum analyzer shows that the ASE is reduced by at least −25 dB at the resonance wavelength (see in Fig. 4.34).

The filtering capability of a transmission grating can be numerically estimated. The diffraction angle θ_m of the ray with index m in the case of a transmission grating can be calculated using the formula

$$d(\sin\theta_m - \sin\theta_i) = m\lambda \tag{4.13}$$

where $d = 800\,\text{nm}$ is the grating period, θ_i is the angle of incidence, and λ is the wavelength of the input beam. For the experiment $m = -1$ was used, resulting in

$$\sin\theta_{-1} = \sin\theta_i - \frac{\lambda}{d}. \tag{4.14}$$

The dispersion of the grating results from the derivative of the previous equation,

$$\frac{\partial\theta_{-1}}{\partial\lambda} = -\frac{1}{d\cos\theta_{-1}} = -0.098^\circ/\text{nm} \tag{4.15}$$

for $\lambda = 1081\,\text{nm}$ and $\theta_i = 41.7^\circ$ (the angle of incidence according to the specification sheet).

To calculate how much of a dispersed beam couples into a fiber, the idea is to calculate the power coupling coefficient of two Gaussian beams ψ_a and ψ_b at a plane S [97], as

$$K_{ab} = \left|\iint \psi_a \psi_b \, dS\right|^2. \tag{4.16}$$

In the case of two Gaussian beams with the same beam waist w_0 tilted by an angle θ respect to each other, Eq. 4.16 reduces to

$$K_{ab} = \exp\left[-\left(\frac{\pi\theta\, w_0}{\lambda}\right)^2\right]. \tag{4.17}$$

Finally, replacing Eq. 4.15 into the transmission grating Eq. 4.17, the fiber coupling efficiency

$$T(\lambda_d) = \exp\left[-\left(\frac{\pi(\lambda-\lambda_d)w_0}{d\cos\theta_{-1}\lambda}\right)^2\right]. \tag{4.18}$$

of a dispersed beam with wavelength λ_d is obtained. Figure 4.35 shows the transmission for $\lambda = 1081\,\text{nm}$ and $w_0 = 500\,\mu\text{m}$. For a change of wavelength of 1 nm, the transmission of the fiber coupling is reduced by −30 dB. Figure 4.34 shows that for a change of wavelength of 1 nm the PSD is reduced by roughly −15 dB by using a transmission grating, which is much less than the expected theoretical reduction. It is possible to think that detection limit of the spectrum analyzer limits the peak width of the carrier signal. Two facts reinforced this hypothesis: 1) a

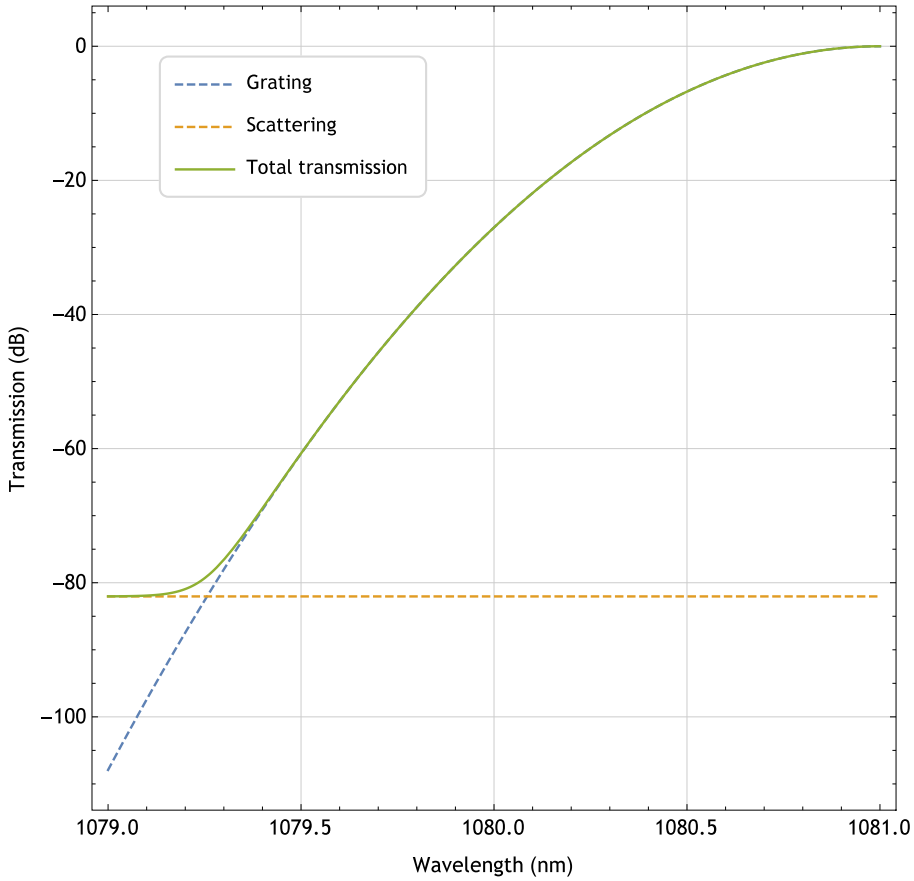

Figure 4.35: Transmission of the grating including fiber coupling, for a central wavelength of $\lambda = 1081\,\text{nm}$.

measure of the spectrum of a single-mode Ti:S output spectrum, which should be extremelly sharp, resulted in a similar profile. 2) When a long pass filter was used in combination to the transmission grating, the transmission profile remained unchanged. If the long pass filter reduces the ASE at 1077 nm by 20dB and the grating reduces it by 25dB, using a combination of both should result in a reduction of 45dB. Experimental results, however, showed no changes in the spectrum when the long pass filter was added after the transmission grating.

The scattering in the optics before and including the grating also limit the extinction ratio of the ASE. Supposing that the optical elements are $D = 1\,\text{m}$ away from the fiber coupling, and only the cross section equivalent to the beam surface (πw_0^2) couples into the fiber. then only $\frac{\pi w_0^2}{4\pi D^2} = -72\,\text{dB}$ of the scattered light will be transmitted. If only 10% of the total power scatters in the optical elements, then at least $-82\,\text{dB}$ of the ASE will always couple into the fiber for all the wavelengths.

In conclusion, the ASE should be reduced by at least 33dB for the experiments when the number of photons required is ~ 10000. The optical spectrum analyzer used to test the grating showed a reduction of at least 25dB, which is possibly limited by the detection performance of the apparatus. In theory, the transmission grating would reduce the ASE intensity by at least 80dB which is five order of magnitude higher than the required for the experiment. It should

be noted that our team previously tested the performance of reflective gratings for linewidth filtering in [98], showing good agreement between the theory and the experimental results. One way to ensure that the ASE is completely removed would be to use ultra-steep band-pass or long-pass filters, which are very costly but guarantee a reduction of at least 60dB.

4.6.5 Alignment of the accordion lens

As explained in a previous section, in order to compress the atoms using the optical accordion system, the focus of the accordion lens should be precisely positioned on the center of the SIL. The alignment of the accordion lens was realized using three axis stage where the 3" aspherical lens holder was mounted, as shown in Fig. 4.36.

Figure 4.36: The accordion lens mounted in a three axis stage.

For a precise alignment it is convenient to observe the atoms from two different angles. In the case of this experiment, the reflected absorption imaging technique was used to observe the atoms from one side, while the fluorescence resultant from absorption imaging was captured by the microscope system using an objective lens with small magnification (Mitsutoyo M Plan Apo SL 20X). Initially, atoms after vertical transport were observed as shown in Fig. 4.37. To test whether the accordion beam intersects the atoms, the accordion beam is activated while the vertical ODT is suddenly cut, and the atoms are observed after 3 ms of time-of-flight. If the accordion beam is not correctly aligned to the center of the SIL, the atoms fall due to gravity on the z direction. On the other hand, in the case of a correct alignment the atoms are trapped by the accordion potential and expand along the y (accordion beam propagation) axis (bottom images of Fig. 4.37). If the accordion beam is not correctly aligned,

the position of accordion lens in the x and z direction should be modified until the atoms are trap.

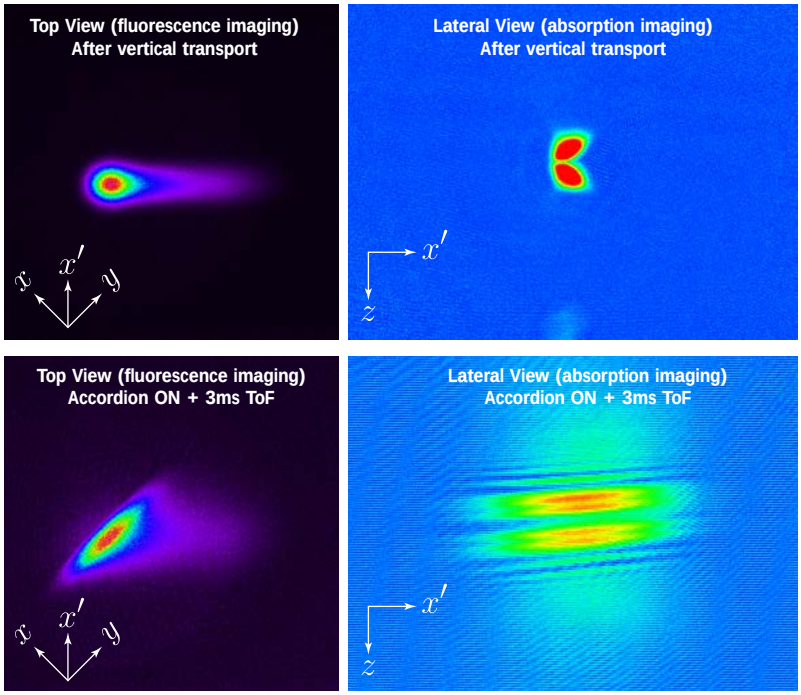

Figure 4.37: Absorption and fluorescence imaging of atoms used for the alignment of the accordion lens.

Note that there are three degrees of freedom on the position of the accordion lens, from which only two can be determined using the alignment mentioned before; it is possible to cross the atoms with the accordion beam even when the focal plane of the lens is not positioned at the center of the SIL. The third degree of freedom is determined when the accordion beam crosses the atoms for two different angle of incidence. The alignment procedure is as follows: suppose that for an accordion angle $\theta_{\text{acc}} = \theta_1$ the correct position of the lens is (x_1, y, z_1) and for a different angle $\theta_{\text{acc}} = \theta_2$ the correct position is (x_2, y, z_2). The goal is to change the position y such that both $\Delta x = x1 - x2$ and $\Delta z = z1 - z2$ converges to zero. In other words, the accordion lens focal plane crosses the center of the SIL if and only if for two different angles θ_{acc} the accordion beam traps the atoms. This procedure can be realized in a systematic way ensuring a precise alignment of the accordion lens.

4.6.6 Loading of atoms into the optical accordion

The experiment procedure to load the atoms into the accordion potential consists in gradually reducing the vertical ODT retro-reflected intensity and at the same time increasing the intensity of the accordion beam (Fig. 4.38b). After loading the atoms, a BEC is created using evaporative cooling by reducing the intensity of the accordion beams (Fig. 4.38c). As seen in Fig. 4.31 there are two different orthogonal accordion beams in the x and y directions. The

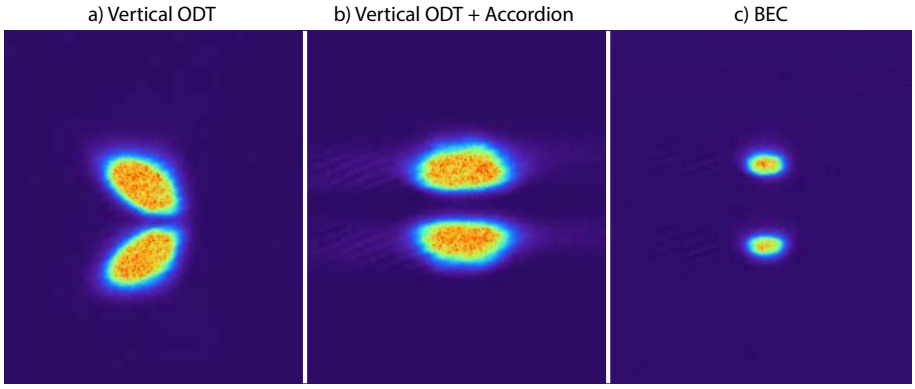

Figure 4.38: Absorption imaging of atoms. a) After vertical transport. b) After loading the atoms into the first layer of the optical accordion. c) After creating a BEC.

reason for using two accordion beams is that each of the beams can be later retro-reflected to form a two-dimensional optical lattice.

4.6.7 Bose-Einstein condensate: Single accordion

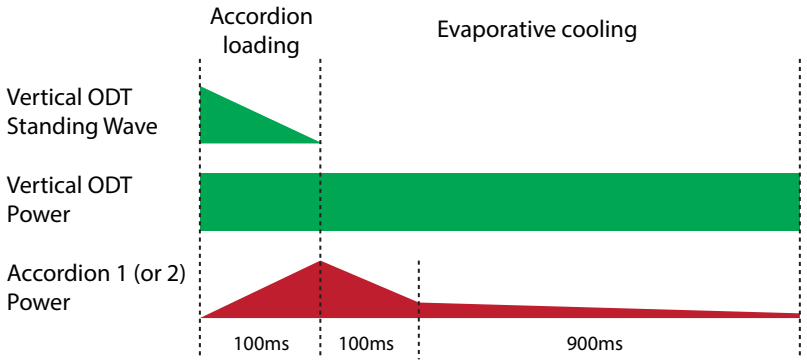

Figure 4.39: Time sequence for creating a BEC with a crossed-dipole trap using a single accordion beam.

Although there are two orthogonal accordion beams, it is possible to create a BEC using a single accordion. For alignment and optimization purposes, it is convenient to first create the BEC using a crossed trap between the vertical ODT and each of the accordion beams separately. Figure 4.40 shows the time sequence used to load the transported atoms into the first layer of the optical accordion and create a BEC. First, the intensity of the retro-reflected vertical ODT is reduced in order to transform the optical conveyor belt back into a traveling wave. At the same time, the power of the accordion beam is increased to 2.1 W, and atoms are loaded into the first layer of the accordion potential. To create a BEC, the intensity of the vertical ODT is maintained constant while the intensity of the accordion beam is reduced to 500 mW in an quasi-exponential way. Figure 4.40 shows the time-of-flight of the BEC for each of the accordion beams. Due to the strong potential produced by the vertical ODT beam, the BEC expands anisotropically in a direction almost perpendicular to the vertical ODT propa-

gation axis.

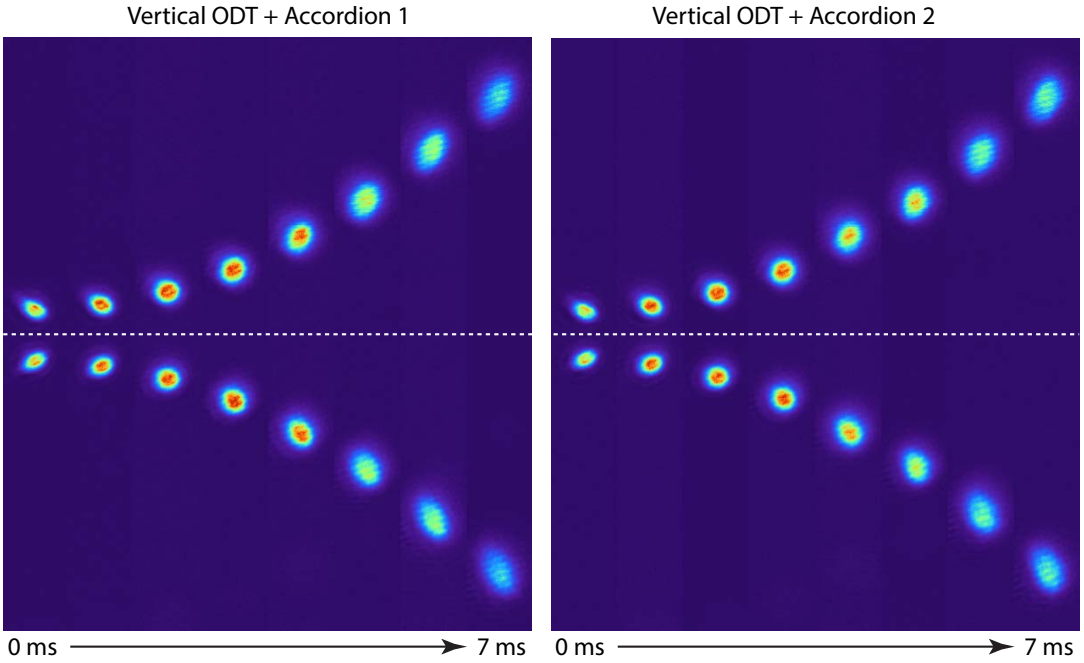

Figure 4.40: Time-of-flight of the BEC up to 7 ms for each of the two different accordion beams.

The number of atoms as a function of the holding time after creating the BEC is shown in Fig. 4.41. The results were fitted using a three-body and one-body loss model for a three-dimensional BEC [99]:

$$\frac{dN}{dt} = -\gamma N^{9/5} - \alpha N \tag{4.19}$$

whose solution is given by:

$$N(t) = \left[\left(N_0{}^{-4/5} + \frac{\gamma}{\alpha}\right) e^{\frac{4}{5}\alpha t} - \frac{\gamma}{\alpha}\right]^{-5/4} \tag{4.20}$$

resulting in an initial three-body loss ratio $\left(\gamma N^{4/5}\right)^{-1} = 1.4\,\text{s}$ and $\tau = 23\,\text{s}$.

4.6.8 Bose-Einstein condensate: Double accordion

After optimizing each of the accordion beams to create a BEC, it is possible to create a 3-beam-crossed ODT formed by the two combined accordion beams (double accordion) and the vertical ODT. In this case, the time sequence to create the BEC consists in first reducing the power of the optical accordions and later removing the vertical ODT completely, as shown in Fig. 4.42. This procedure resembles an evaporative cooling technique using a dimple trap [29]. Figure 4.43 shows the time-of-flight of the BEC in the double accordion case. The final power of the accordion beams is 300 mW.

Figure 4.43 shows the time-of-flight of the BEC. In contrast with the time-of-flight images

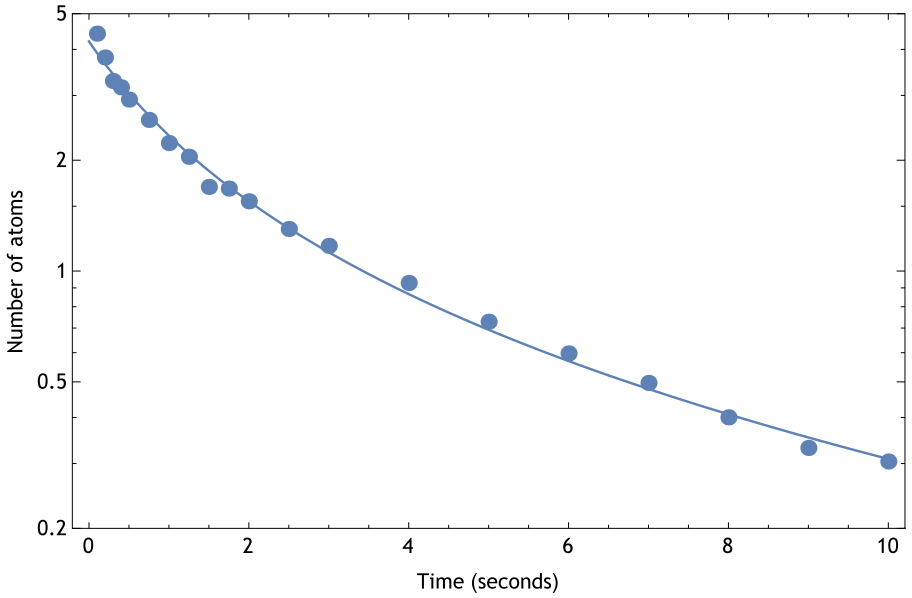

Figure 4.41: Lifetime of atoms after creating the BEC.

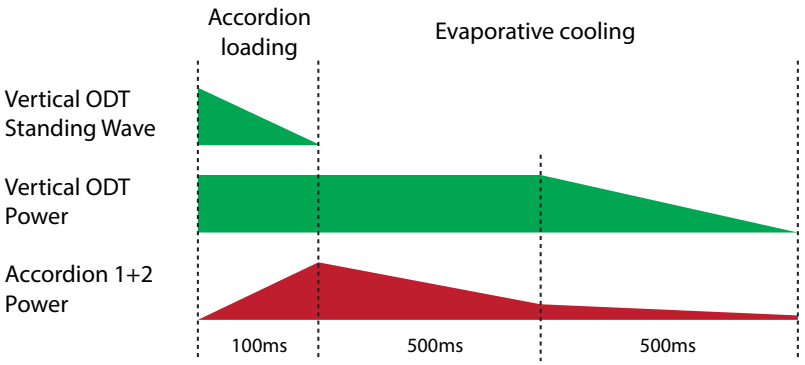

Figure 4.42: Time sequence for creating a BEC with a crossed-dipole trap using a double accordion beam.

of the BEC when only one accordion beam was used, the absence of the vertical ODT here results in a symmetrical trap in the x and y directions. As the trap frequency in the z direction is higher, the cloud expands anisotropically where the z direction is slightly elongated.

The number of atoms as a function of the holding time after creating the BEC is shown in Fig. 4.44. The results were fitted using a three-body and one-body loss model, resulting in $\left(\gamma N^{4/5}\right)^{-1} = 69\,\mathrm{s}$ and $\tau = 71\,\mathrm{s}$.

4.6.9 Compression of atoms

After creating the BEC, atoms are compressed by moving the air-stage where the moving mirrors are situated (see Fig. 4.29). The absorption images after compression are shown in Fig. 4.45.

Note that for steep angle of incidences the atoms move very close to the surface and the mirrored absorption images become superposed. In the case of Fig. 4.45, the air-stage moves

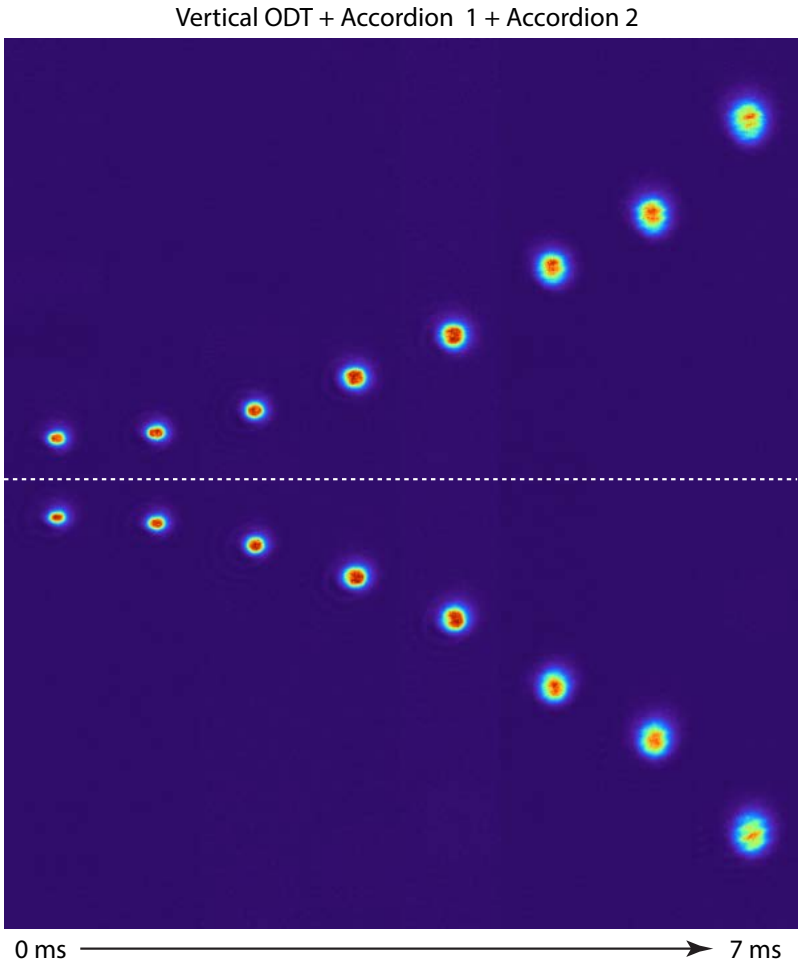

Figure 4.43: Absorption images of the atoms for the double accordion setup. Time-of-flights are between 0 ms and 7 ms.

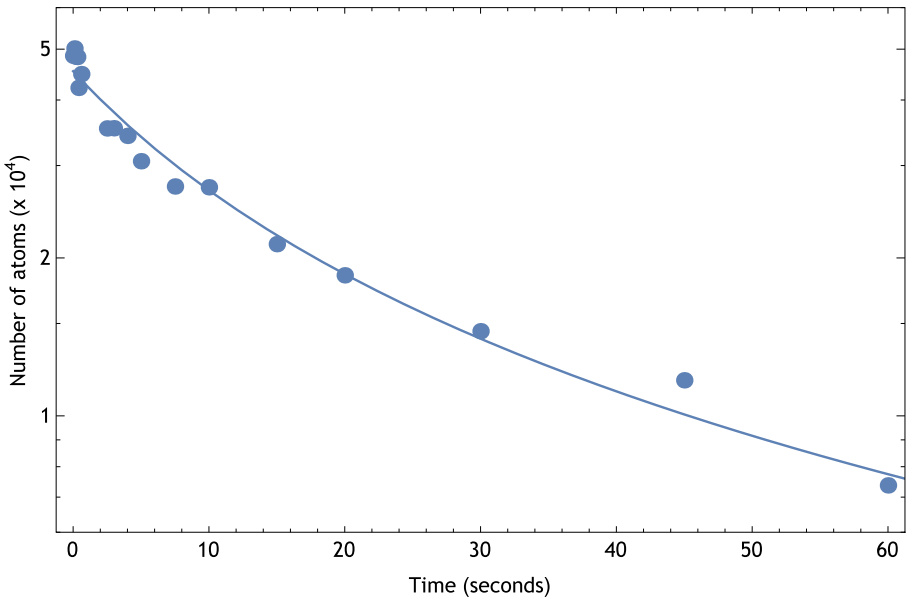

Figure 4.44: Lifetime of atoms after creating the BEC in the double accordion setup.

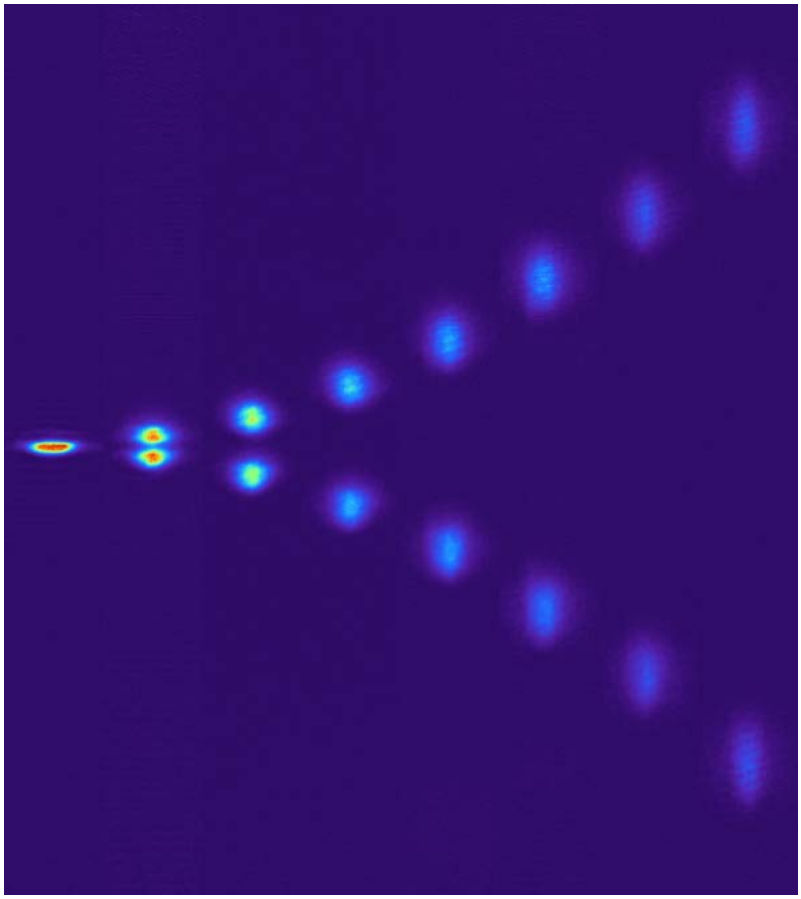

Figure 4.45: Absorption images of the atoms after compression. Time-of-flights are between 0 ms and 7 ms.

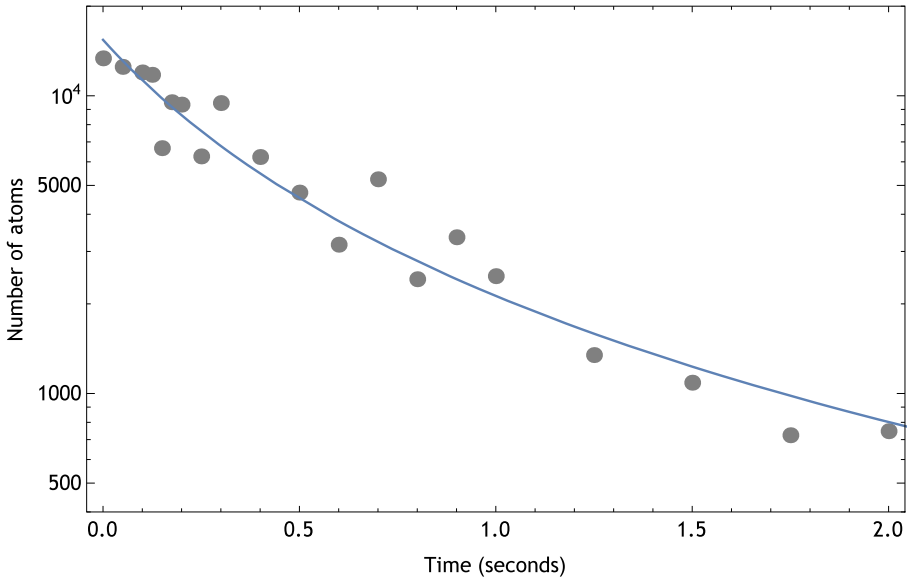

Figure 4.46: Lifetime of atoms after compression. The solid line is a fitting using a two-body loss model.

27.3 mm with a constant acceleration and deceleration of 1m/s^2, requiring 330 ms. The final angle after compression was $\theta_{\text{acc}} = 11°$, resulting in a strong confinement in the z axis which

produces a highly anisotropic density profile after free expansion. The number of atoms as a function of the holding time after compressing the atoms is shown in Fig. 4.46. The results was fitted using a two-body losses curve resulting in an initial loss rate of $\left(\beta \langle n \rangle_r\right)^{-1} \approx 300\,\text{ms}$. A three-body model did not fit properly with the results. The three-body losses rate was estimated theoretically as $\left(\frac{K_3}{6}\langle n^2 \rangle_r\right)^{-1} = 260\,\text{ms}$, which is comparable with the initial loss rate obtained in the fitting. This means that the lifetime profile is probably determined by a combination of two-body and three-body losses, which cannot be solved analytically.

Note that the final experiments were realized at $\theta_{\text{acc}} = 6°$. This angle is sufficient to produce a condensate gas in the 2D regime and it provides deeper potentials as the reflectivity of the SIL decreases as θ_{acc} increases. The lifetime at this angle resulted in $\approx 2\,\text{sec}$.

4.6.10 Density profile of the BEC

The integrated density profile in the horizontal direction of the BEC before compression is shown in Fig. 4.47 for three different stages of evaporative cooling and 7 ms of time-of-flight. When the accordion beams power is 170 mW the atomic cloud is a mixture of a thermal gas and a condensate fraction resulting in a bimodal density profile (see Fig. 4.47(a)). The thermal cloud have a Gaussian profile from which a temperature of 180 nK was estimated. The condensate part of the cloud represent 20% of the total atoms and have a Thomas-Fermi (parabolic) distribution. After further reducing the accordion beams power to 120 mW the evaporative cooling process finishes resulting in a pure BEC with not discernible thermal component (see Fig. 4.47(c)). The estimated critical temperature is $T_c \approx 200\,\text{nK}$.

After compressing the atoms to $\theta_{\text{acc}} = 6°$ the trap frequency in the vertical(z) direction is increased by a factor of ~10 (cf. Appendix A.2), while the trap frequencies in the horizontal(x, y) directions only increase by a factor of ~2. The potential depth is also increased by a factor of ~8. Consequently, the resultant integrated density profile in the horizontal direction (see Fig. 4.48) have a very similar shape to the density profile before compression. The thermal component on the atom reappears (see Fig. 4.48(top)) if the power of the accordion beams is maintained constant during compression, possible due to an increment of three-body collisions leading to heating. The thermal component disappear completely after the power of the accordion beam is further reduced.

The vertical integrated density profile of the compressed BEC is shown in Fig. 4.49. Notice that the density profile does not match a Thomas-Fermi distribution but instead a Gaussian one. This condition arises when the Thomas-Fermi approximation is no longer valid and the mean field energy E_{mfe} becomes smaller or comparable to the vibrational energy separation $\hbar\omega_z$, as:

$$E_{\text{mfe}} = \frac{4\pi\hbar^2 a n}{m} < \hbar\omega_z \tag{4.21}$$

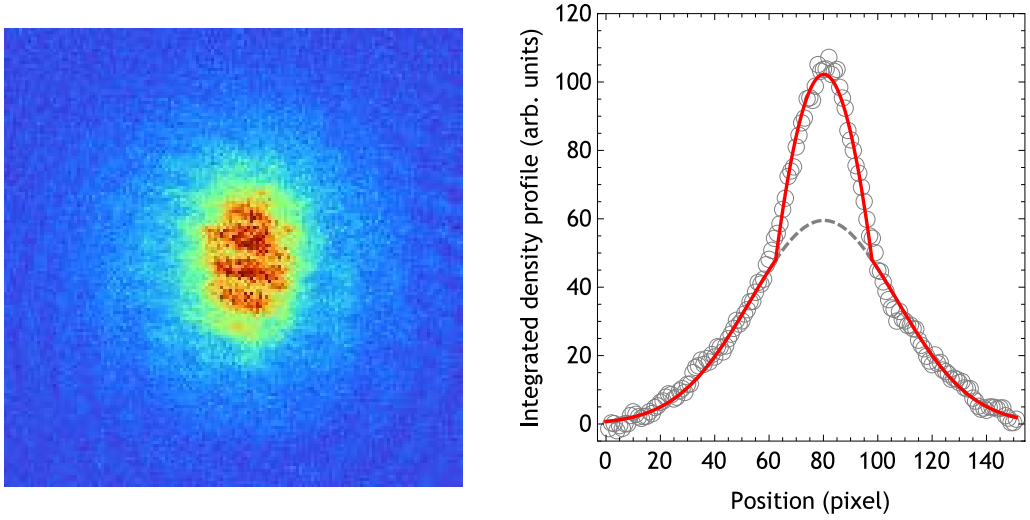

(a) Condensate fraction ~20%. $T = 180\,\mathrm{nK}$. $P_{\mathrm{acc}} = 170\,\mathrm{mW}$.

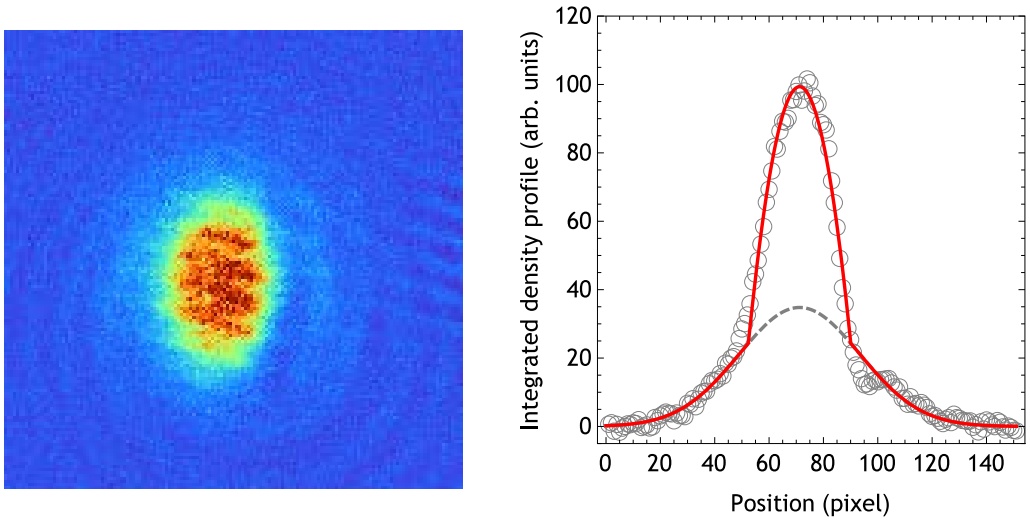

(b) Condensate fraction ~40%. $T = 140\,\mathrm{nK}$. $P_{\mathrm{acc}} = 140\,\mathrm{mW}$.

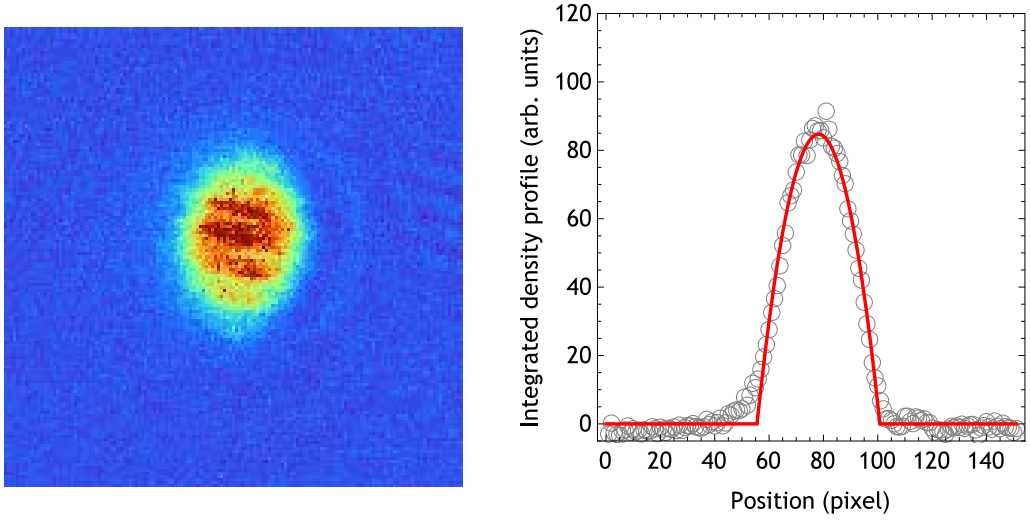

(c) Condensate fraction ~100%. $P_{\mathrm{acc}} = 120\,\mathrm{mW}$.

Figure 4.47: Horizontal integrated density profile of the BEC before compression, for three different potential depths. The time-of-flight is 7 ms.

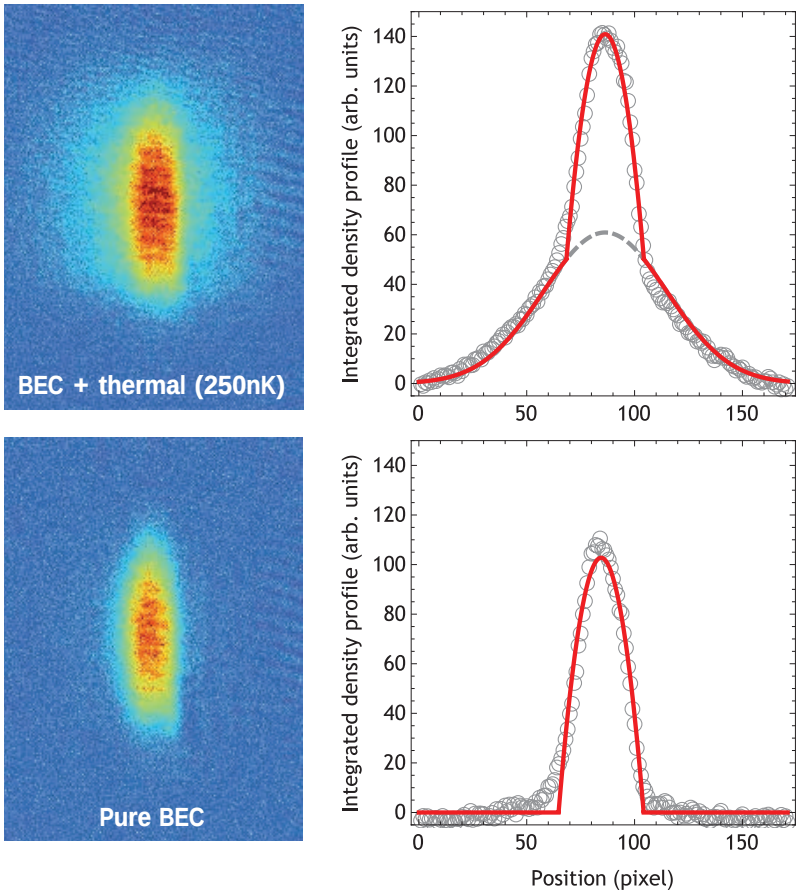

Figure 4.48: Horizontal integrated density profile of the BEC after compression to $\theta_{\text{acc}} = 6°$ for two different potential depths. The time-of-flight is 7 ms.

where a is the scattering length of ytterbium (see Table 2.2) and n is the peak number density of atoms. Eq. 4.21 can be rewritten as:

$$N < \sqrt{\frac{32\hbar}{225ma^2}} \sqrt{\frac{\omega_z^3}{\omega_{xy}^4}} \approx 10000 \tag{4.22}$$

where $\omega_z/2\pi = 1.7\,\text{kHz}$ and $\omega_{xy}/2\pi = 0.06\,\text{kHz}$ was used for the calculations.

For the number of atoms after compression, the mean field energy is comparable with the vibrational energy separation $\hbar\omega_z$ resulting in a Gaussian profile in the z direction. For the quantum gas microscope experiments, the number of atoms is usually reduced to ~ 1000 or less by further reducing the potential depth. In that case, the condition of Eq. 4.22 is satisfied and the condensate behaves as a 2D quantum gas.

4.6.11 Stability of the system

The short-term stability of the system is shown in Fig. 4.50. Considering the complexity of the transport and compression process, the number of atoms in the compressed condensate is very stable. Even for compression up to $\theta_{\text{acc}} = 10°$ the fluctuation in the number of atoms

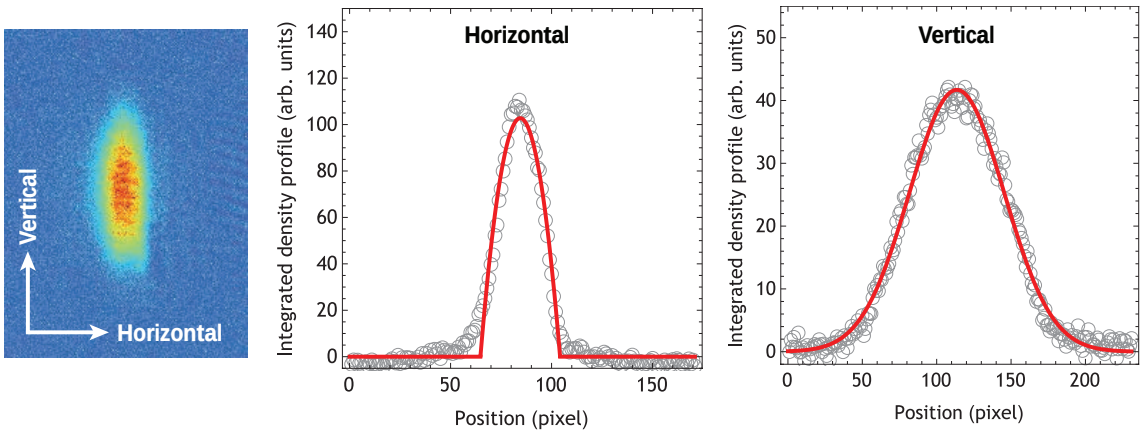

Figure 4.49: Integrated density profile along the horizontal and vertical axis. The horizontal profile match a Thomas-Fermi distribution while the vertical distribution is Gaussian.

is less than 10%. It is not clear what determines the stability of the system at this point.

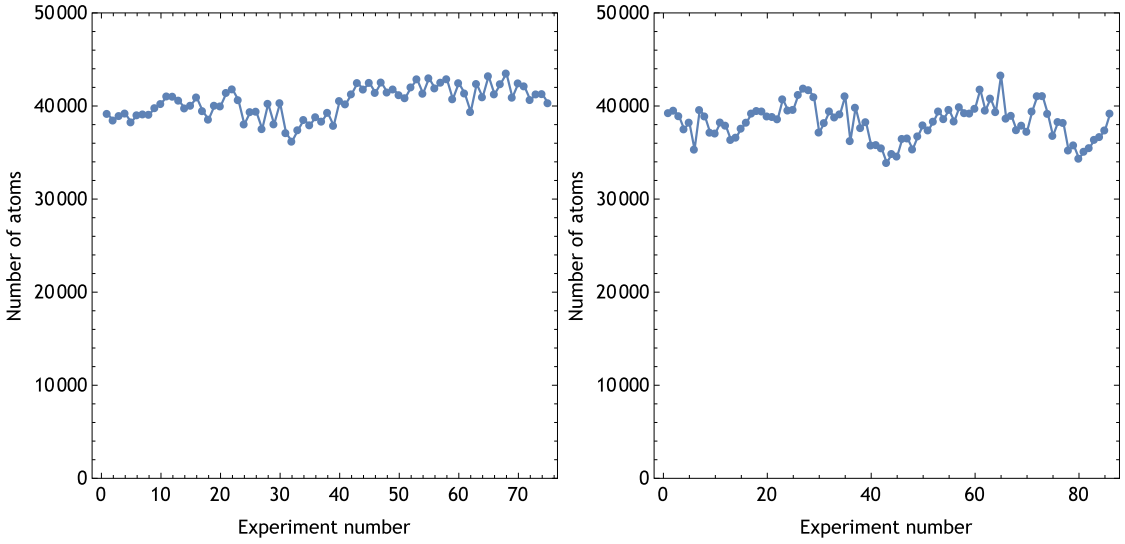

(a) Single accordion beam (x axis)

(b) Single accordion beam (y axis)

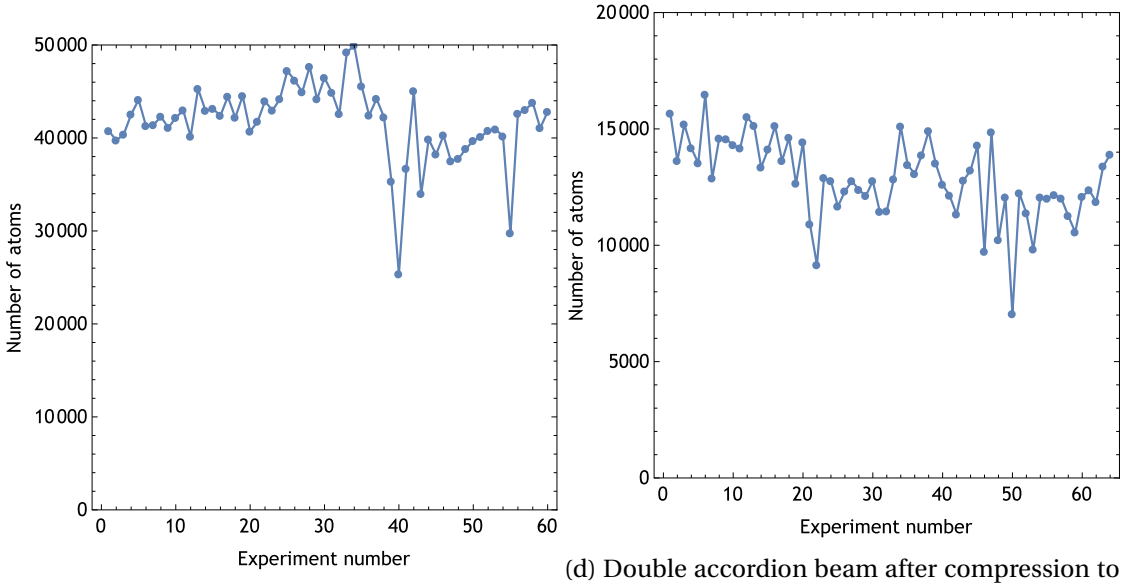

(c) Double accordion beam ($x + y$ axis)

(d) Double accordion beam after compression to $\theta_{\mathrm{acc}} = 10°$

Figure 4.50: Stability of the system during $60 \sim 80$ shots.

Chapter 5

Experiment: Fluorescence imaging

In the previous chapter a BEC of atoms was compressed into a thin pancaked-shape condensate near the surface of the SIL using the optical accordion technique. Such an atomic cloud was a required condition for observing atoms using a high numerical aperture microscope system as the atoms need to be confined in a region thinner than the depth of field of the objective lens. This chapter centers in the experimental setup used to load the compressed atoms into a two-dimensional optical lattice and the imaging process to realize fluorescence imaging of the atoms with single-site resolution.

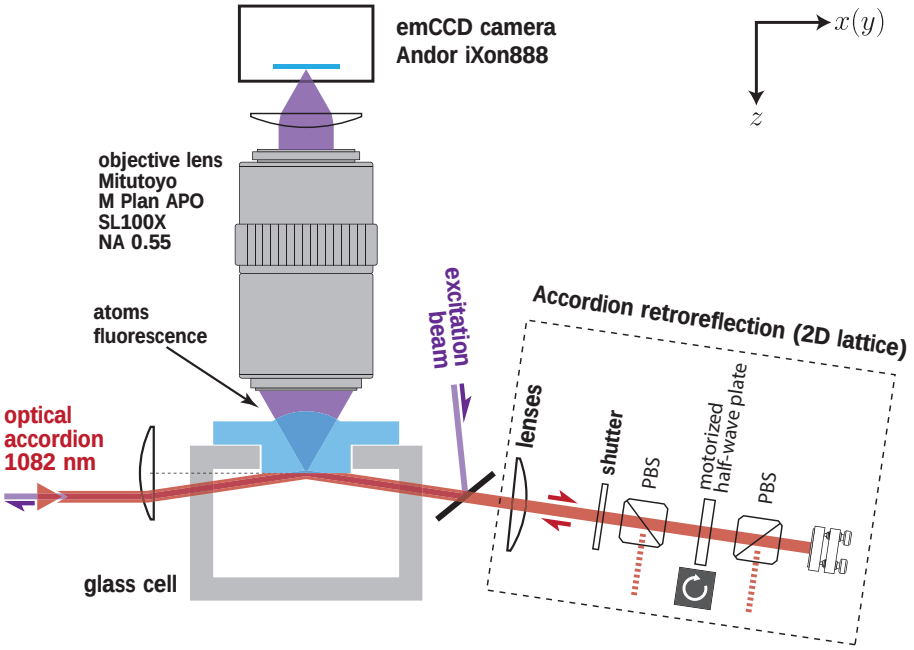

Figure 5.1: High numerical aperture system used for observing atoms fluorescence.

The experimental apparatus used to trap and image atoms in a two-dimensional optical lattice is shown in Fig. 5.1. The two-dimensional optical lattice is created by retro-reflection of the optical accordion beams, as it will be explained in detail in Sec. 5.1. Section 5.3 focuses on the imaging process using a deep potential in the excited state. This is followed by an analysis

of the resolution of the system in Sec. 5.4.1. Finally, the lattice reconstruction algorithm and the lifetime of the system are discussed in sections 5.4.2 and 5.4.3.

5.1 Loading of atoms into the 2D optical lattice

Atoms trapped in the first layer of the accordion lattice are loaded into the two-dimensional optical lattice by retro-reflecting the optical accordions. The retro-reflection system shown in Fig. 5.1 is comprised by a mechanical shutter, two polarized beam splitters and a half-wave plate mounted on a stepping motor with the same properties as the one explained in Sec. 4.5.5. After opening the mechanical shutter, the stepping motor rotates 400 micro-steps (equivalent to 45°) with a constant acceleration and deceleration of 2×10^5steps/s^2. As two polarized beam splitters are used, the retro-reflected intensity is proportional to $\sin^4(\frac{\text{step}}{400}\frac{\pi}{2})$. The potential depth during loading can be roughly estimated with the equation:

$$V(x,y,z)=V_{\text{acc}}(x,y,z)\left[\left(1+R-2\sqrt{R}\right)+4\sqrt{R}\cos^2(k_x x)+4\sqrt{R}\cos^2(k_y y)\right] \tag{5.1}$$

where $R(t)$ is the intensity of the retro-reflected beam divided by the accordion beam intensity, $V_{\text{acc}}(x,y,z)$ is the accordion potential, and $k_x = k_y = 2\pi\cos\theta_{\text{acc}}/\lambda_{\text{lat}}$ are the wavenumbers in the x and y direction, respectively. For an optical accordion with an incident angle of $\theta_{\text{acc}} = 6°$, the resultant lattice spacing is of 544 nm. Figure 5.2 shows the transmittance of the different optical elements used for retro-reflection and the reflectance of the surface of the SIL for an incident angle of $\theta_{\text{acc}} = 6°$.

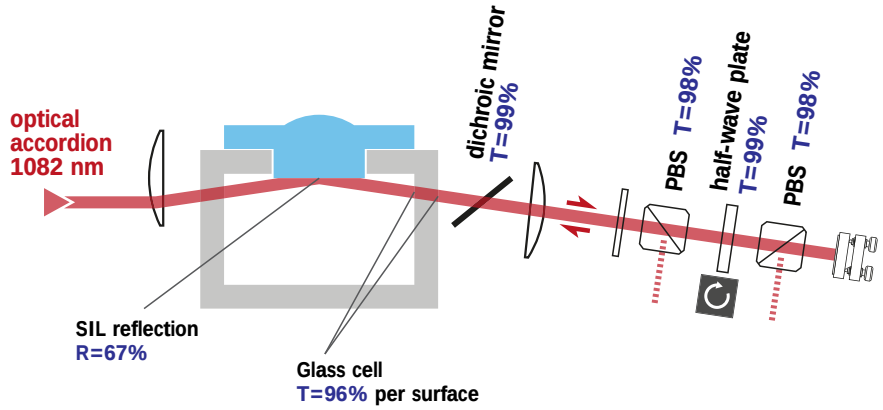

Figure 5.2: Optical losses of the optical accordion and retro-reflection system.

Considering the losses of all these optical elements, only 50% of the total power can be retro-reflected. The reflected intensity can be written as:

$$R = 0.50\times\cos^4\left(\frac{\text{step}(t)}{400}\frac{\pi}{2}\right). \tag{5.2}$$

Figure 5.3 shows the variation in the potential relative to the accordion potential $V(0,0,z)/V_{\text{acc}}(0,0,z)$

during loading time. The curves represent the relative offset $1+R-2\sqrt{R}$ and the relative lattice depth $4\sqrt{R}$.

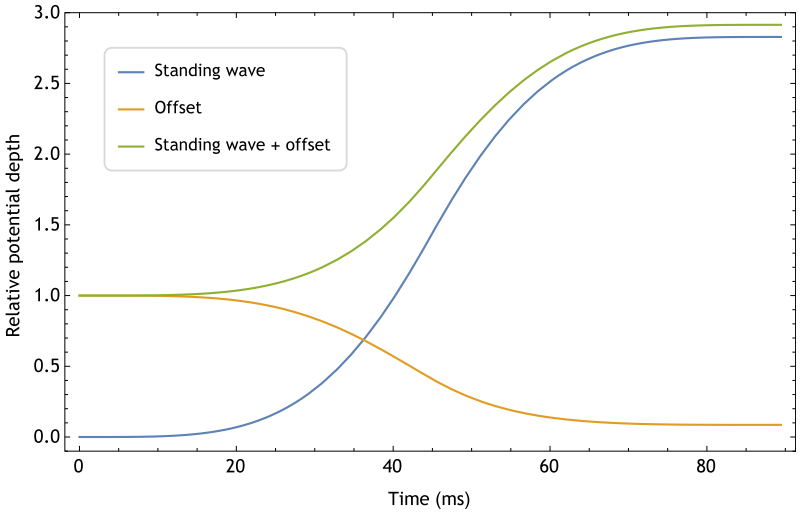

Figure 5.3: Change in the offset potential and lattice depth during loading. The potential units are relative to the initial accordion potential.

Initially, all the atoms are located in the first layer of the optical accordion at $z_0 = 2.6\,\mu$m. Using Eq. 5.1, the lattice depth is

$$V_0 = 4\sqrt{R}\,V_{\text{acc}}(0,0,z_0) = 2.8\,V_{\text{acc}}(0,0,z_0) \tag{5.3}$$

nearby the central region of the trap. After loading, the estimated depth was $V_0/k_B = 1.9\,\mu$K or $V_0/E_r = 40$, and the trap frequencies were $(\omega_x,\omega_y,\omega_z)/2\pi = (12,12,1.8)$kHz.

5.2 Laser system

The laser system used to derive the excitation beam is shown in Fig. 5.4. A Ti:sapphire laser was frequency-doubled using a bow-tie cavity and a BiBO non-linear crystal. The output of the cavity was fed into an acousto-optical modulator (AOM) in the double-pass configuration, that serves as optical shutter and frequency shifter. The output of the AOM was coupled into an optical fiber, obtaining 30 mW of power at the fiber output. Due to the high output power of the excitation light and the limited extinction ratio of the AOM (−60 dB in the best case), it is important to use a mechanical shutter to avoid heating during transport and compression. The exposure pulse used for imaging is generated immediately after the mechanical shutter opens, which is detected by a photo-detector placed after the shutter. The frequency of the Ti:S laser was locked using a frequency-offset locking system, which consists in using the beat-note produced by the interference of the excitation and Zeeman slowing laser system as a feed-back signal.

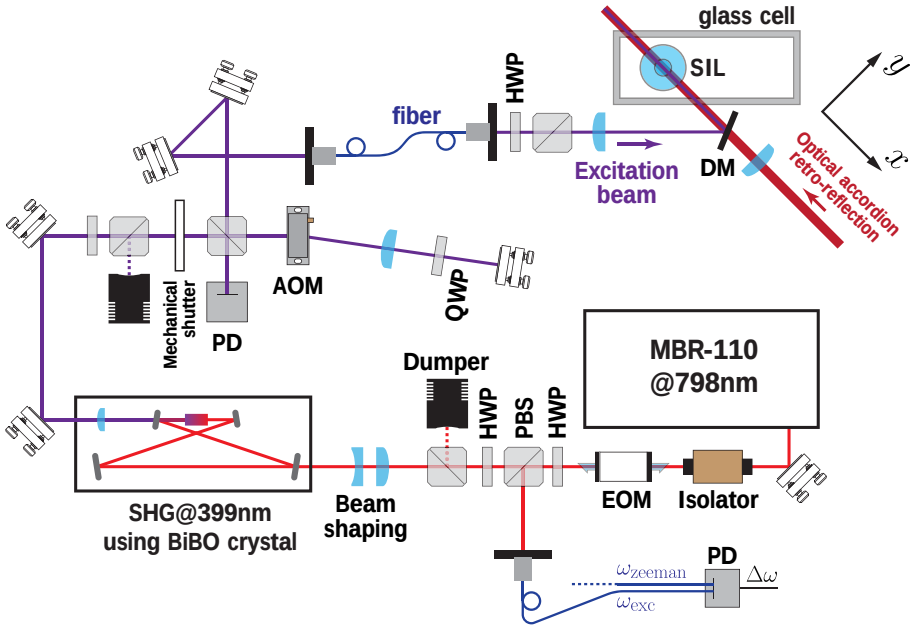

Figure 5.4: Laser system for the excitation beam

5.3 Imaging of atoms

The strategy to obtain a sufficient number of atoms, previously discussed in Sec. 3.4, consists in creating a deep potential in the excited state and using a resonant excitation beam to couple the ground state with the excited one. The resultant deep effective potential is capable of containing the atoms that are heated during fluorescence imaging.

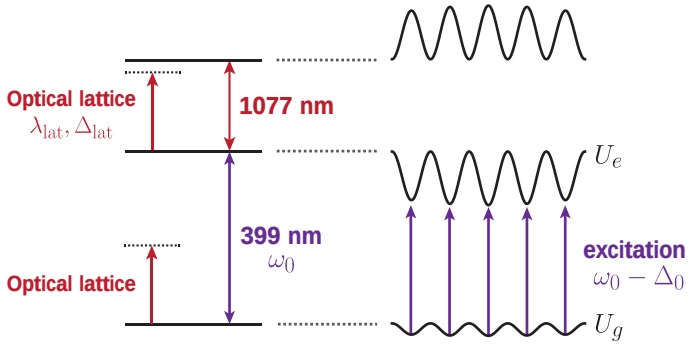

Figure 5.5: Deep potential method utilized during fluorescence imaging.

The imaging process starts by increasing the power of the accordion (lattice) beams to $P_{\text{lat}} = 2\,\text{W}$ in 10 ms. For this lattice power and a lattice detuning of $\Delta_{\text{lat}}/2\pi = 1.0\,\text{THz}$, the resultant lattice depth in the ground and excited state are $U_g/k_B = 280\,\mu\text{K}$ and $U_e/k_B = 62\,\text{mK}$, respectively. In the case of an atom experiencing an average lattice depth $U_0 = (Ue + Ug)/2$, the corresponding trap frequencies are $(\omega_{xy}, \omega_z)/2\pi = (1.6, 0.23)\,\text{MHz}$.

The excitation light, which is aligned on the same optical axis as the optical accordion, is inserted from the retro-reflection side using a longpass dichroic mirror (Thorlabs DML650L). The beam waist was set to $100\,\mu\text{m}$, corresponding to a peak intensity of $95\,\text{W/cm}^2$ or $1600\,I_s$,

where I_s is the saturation intensity of the $^1S_0$-$^1P_1$ transition. The excitation beam is resonant with the shifted transition, which determines $\Delta_0 = (U_e - U_g)/k_B$.

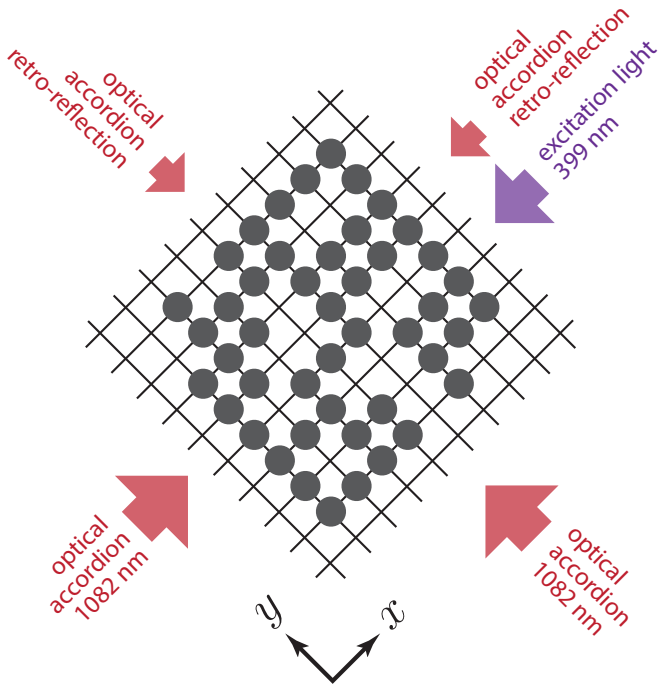

Figure 5.6: Direction and polarization of each of the accordion beams and excitation beamãĂĂduring fluorescence imaging, as seen from the CCD camera.

Figure 5.6 shows the direction and polarization of each of the accordion beams and the excitation beam as seen from the microscope system. Note that the excitation light is shinned from only one direction and it is not retro-reflected, resulting in a net radiative force. Details and a quantitative estimation of this force were explained in detail in Sec. 3.5.1. Note also that as the optical lattice beams are symmetrical in each direction the excitation beam could be in principle either inserted from either the x direction or the y direction (or both at the same time). Experimentally, however, there was a noticeable degradation in the fluorescence intensity when the excitation beam was inserted from the y direction. It was later discovered that the small frequency shift used to avoid interference of the two accordion beams broke the apparent symmetry of the system uniquely determining a "good direction" for excitation. Details of this asymmetry are studied in Appendix 5.5.

A single-shot image of the Yb atoms trapped in a two-dimensional optical lattice after 100 μs of exposure time is shown in Fig. 5.7. The solid angle of the imaging system implies that only 21% of the total photons can be collected by the objective lens, which results in a total photon collection efficiency of ~5% for the microscope system. This value includes the transmittance of the SIL (87%), the objective lens (56%) and the low-pass filters (92%), and also the quantum efficiency of the CCD camera (~0.5 e^-/photon at 399 nm).

An average of 100 photons per atom was collected (~2000 photons emitted) by the CCD

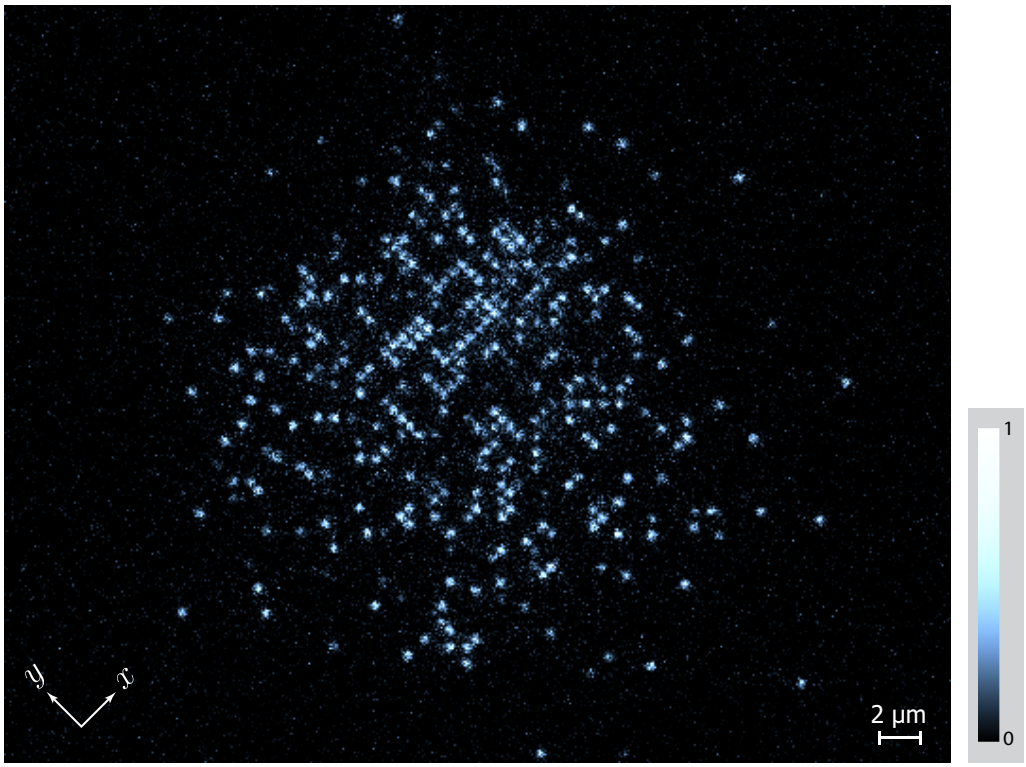

Figure 5.7: Single-shot image of the Yb atoms trapped in a two-dimensional optical lattice after 100 μs of exposure time

camera in the 100 μs of exposure time. This number of photons is one order of magnitude smaller than the expected from the simulations. The definition of the image is, however, notoriously sharper than the expected. Two factors contributed to the increase in definition: 1) The resolution of this microscope system is less than half compared with that of previous experiments with rubidium (cf. Sec. 5.4.1). This increases the fluorescence density by a factor of ~4. 2) The extremely short exposure times used in this experiment (5 order of magnitude smaller than the rubidium experiments) result in a dramatic reduction in the background dark noise (cf. Fig. 5.17). Both effects lead to an increment in the S/N ratio of the obtained image.

5.4 Analysis of the microscope performance

This section is focused in studying the performance of the microscope, which includes an analysis of resolution, lifetime and fidelity of the system. For this purpose of study it is convenient to use very sparsely populated lattices (filling < 0.05) in order to reduce the effects of photo-association (PA) and hopping. Photo-association effects in multiply occupied sites result in the formation of molecules that lead to the loss of atoms in times of the order of a few to tens of microseconds. As the short imaging times in the system are comparable with these times, PA losses modify the shape of the histogram and affect the lifetime estimation.

5.4.1 Microscope resolution

The point spread function (PSF) is obtained by averaging the fluorescence images of different isolated sites, as shown in Fig. 5.8. In total, 277 individual sites over 32 different images were used for the average, resulting in the PSF in Fig.5.9.

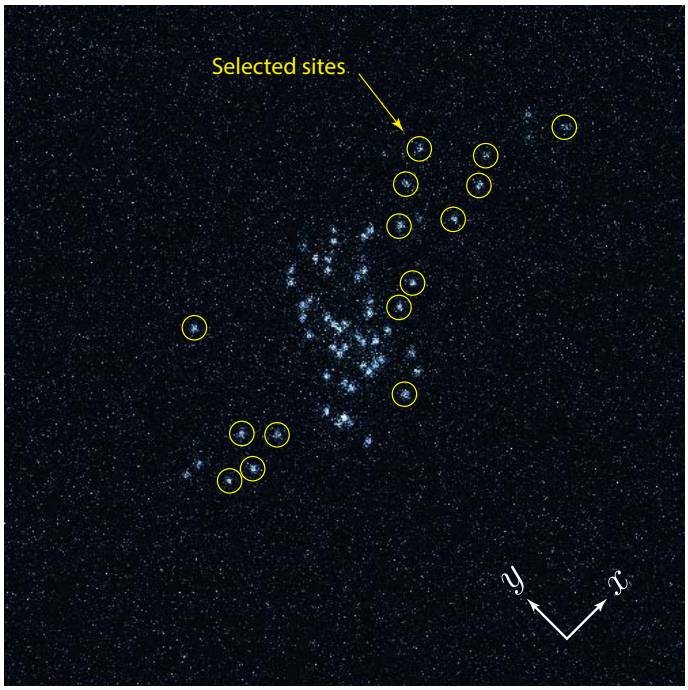

Figure 5.8: Example of selected isolated sites in a single fluorescence image.

The resolution of the microscope system is obtained by fitting the intensity profile along each axis using a Gaussian function. The resultant FWHM average resolution was 319(2) and 317(1) nm in the x and y directions, respectively.

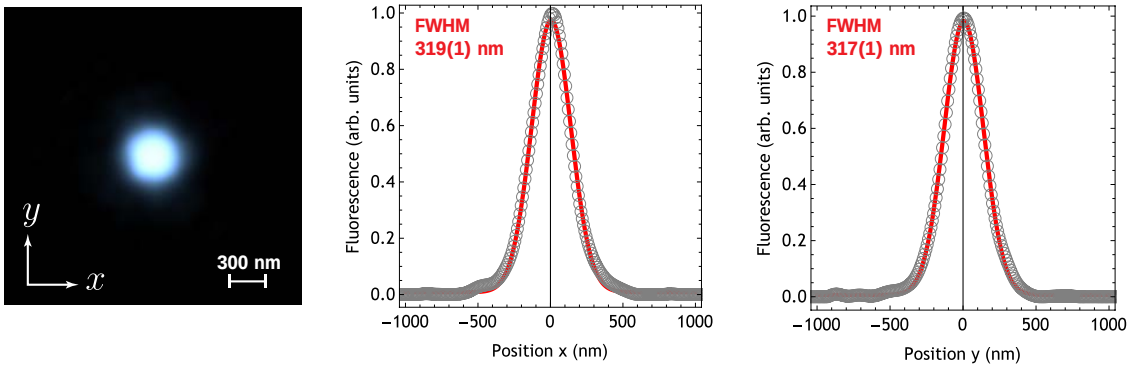

Figure 5.9: Averaged fluorescence intensity in isolated sites. The PSF along the x and y axis were fitted using Gaussian functions.

For a microscope system with a NA of 0.81 and an imaging wavelength of $\lambda = 399\,\text{nm}$, the minimum possible resolution based on the Rayleigh criterion is $0.51\lambda/\text{NA} = 250\,\text{nm}$, which is only 20% smaller than the obtained average resolution.

5.4.2 Lattice reconstruction

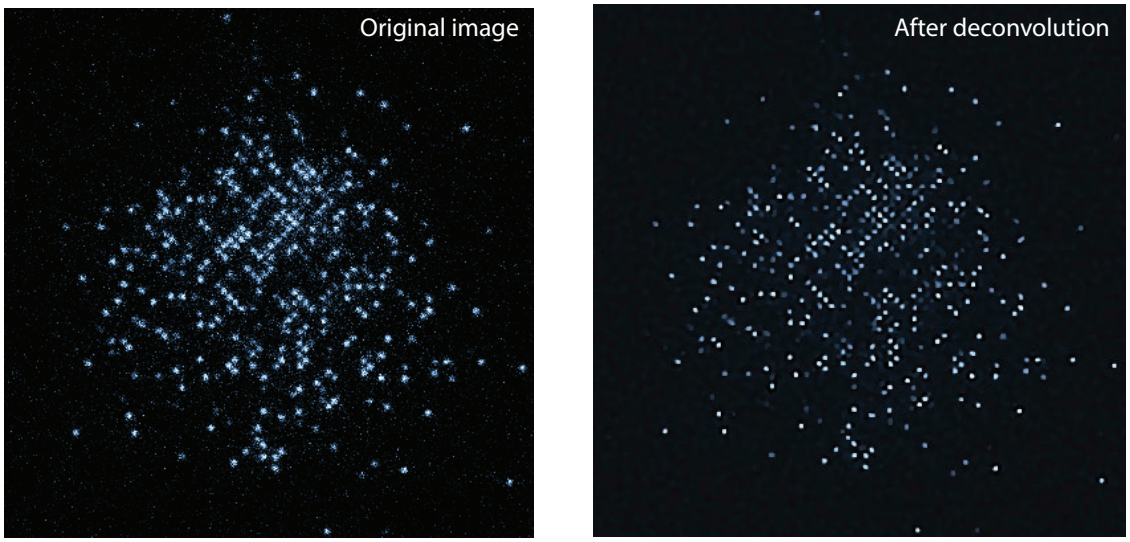

Figure 5.10: Deconvolution of a sparse image using the PSF obtained in Fig. 5.9

The reconstruction of the original distribution of atoms from the fluorescence images is discussed here. The algorithm used for reconstruction was created with the Mathematica software, and consists of three steps: 1) Deconvolution, 2) Lattice fitting, and 3) Binning.

1) Deconvolution

Using a Gaussian matrix with the same size that the obtained from the averaged PSF in Fig. 5.9, the image is deconvoluted using the "TotalVariation" algorithm. The resultant deconvoluted image for a typical sparse image is shown in Fig. 5.10.

2) Lattice fitting

The direction, spacing and phase of the two-dimensional optical lattice is determined by maximizing the total fluorescence of each site when only the central 3×3 pixels of each site is considered. As this process takes a considerable amount of processing time, the direction and spacing is obtained from a single image and later fixed for the rest of the images. Figure 5.11 (c) shows a typical result. The determined lattice directions where 43.55(2° and 135.51(2)° for the x and y directions, respectively. The lattice resultant spacing was 6.205(5) pixels, from where the magnification M of the microscope system can be obtained:

$$M = 6.205P \times \frac{2\cos\theta_{\text{lat}}}{\lambda_{\text{acc}}} = 148.3 \tag{5.4}$$

where $P = 13\,\mu$m is the pixel size of the CCD camera. As the refractive index for fused silica at 399 nm is $n = 1.47$ and the magnification of the objective lens is 100X, the expected magnification ratio was $1.47 \times 100 = 147$, which is very close to the obtained

value. The effective pixel size in the object plane is $P/M \approx 88\,\text{nm}$.

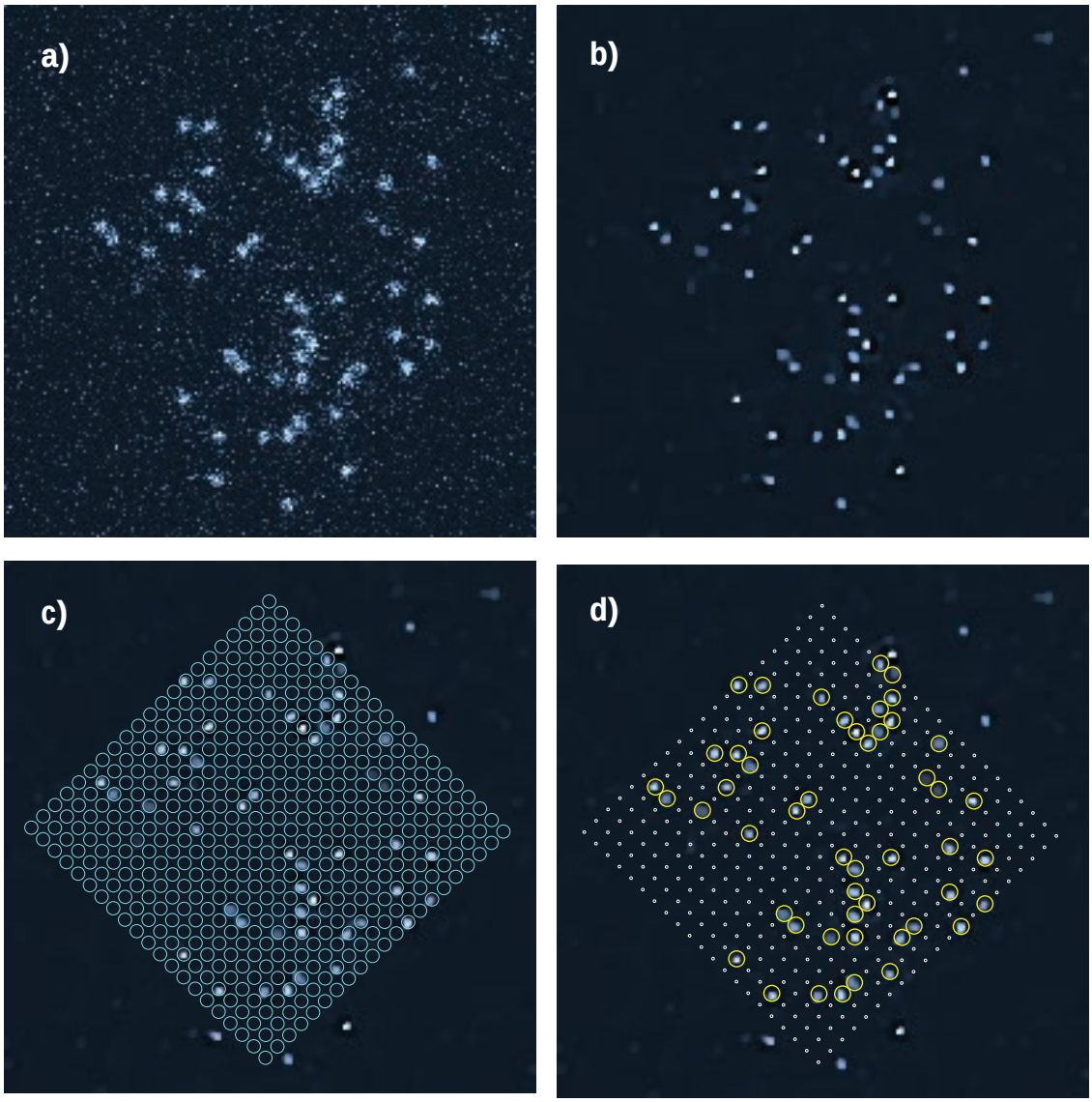

Figure 5.11: Reconstructed process for a sparse image and a exposure time of 40 μs. a) Original image. b) Deconvoluted image. c) Lattice fitting. d) Binning and atom distribution detection.

3) Binning

The binning process consists in adding the fluorescence of the central 3×3 pixels of each site to determine the total atom fluorescence. A site is determined to be occupied if the total number of photons (in the central 3×3 binned part) is greater than a threshold L. Figure 5.11 (d) shows the final distribution of atoms for each site, when a threshold of $L = 130$ photons is used.

The photons per site distribution is shown in Fig. 5.12 in the case of the single image in Fig. 5.11 and in the case of 171 images.

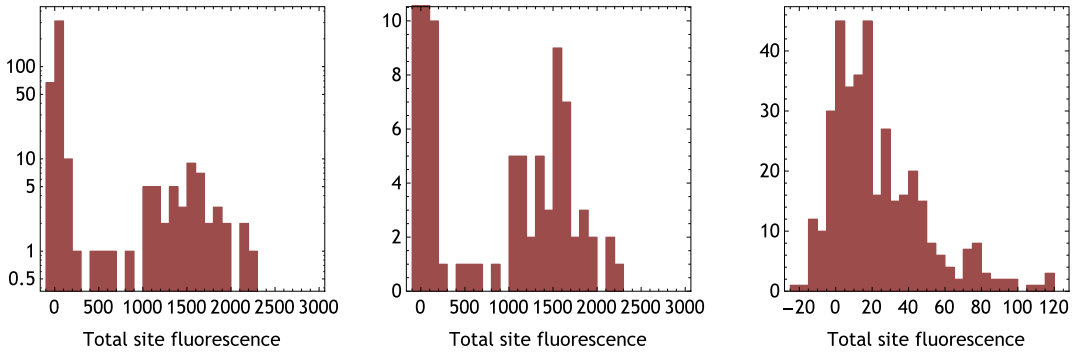

(a) Histogram for the single image shown in Fig. 5.11

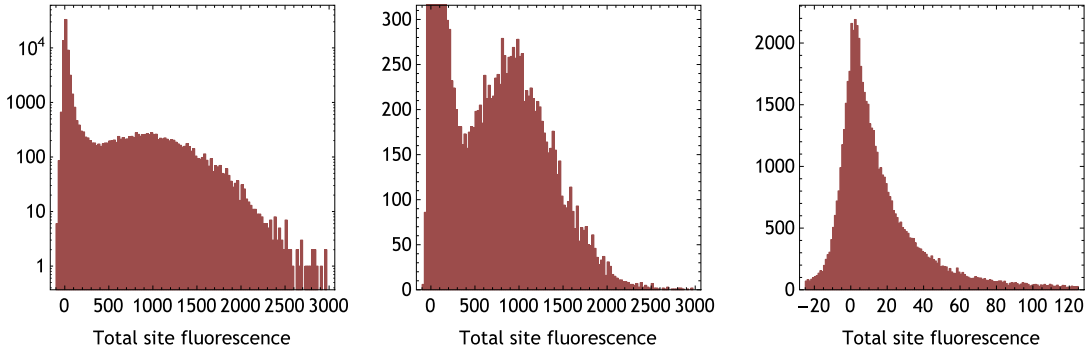

(b) Total histogram over 171 images.

Figure 5.12: Histogram of total fluorescence per site. left) Log scale, center) Magnificated fluorescence peak in linear scale. right) Magnificated background peak in linear scale.

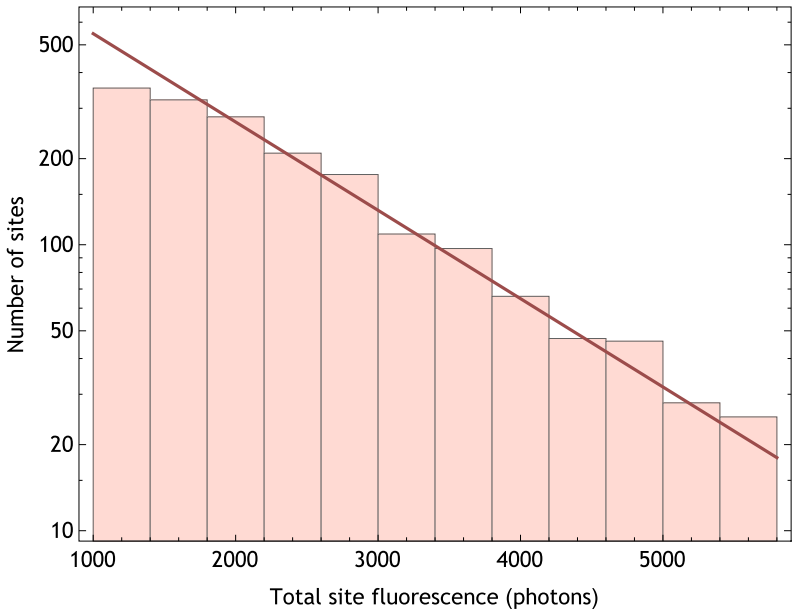

Figure 5.13: Lifetime obtained from histogram by exponential fitting for $P_{\text{lat}} = 1.1\,\text{W}$ and $\Delta_{\text{lat}}/2\pi = 1.0\,\text{THz}$. The exposure time was $300\,\mu\text{s}$

5.4.3 Lifetime analysis

During the imaging process, atoms absorb the excitation light and are heated up due to random light scattering. After a number of scatterings, the atom escapes from the site and is lost.

The lifetime of the atoms was determined using the histogram of the total intensity in each site. Assuming that the number of photons emitted by each atom is proportional to the lifetime, and the number of atoms decreases exponentially, the shape of the histogram is also expected to decay exponentially for exposure times much longer than the lifetime. Figure 5.13 shows a typical histogram result for $P_{\text{lat}} = 1.1\,\text{W}$ and $\Delta_{\text{lat}}/2\pi = 1.0\,\text{THz}$, where an exposure time of $300\,\mu\text{s}$ was used.

For the analysis in this section, the lifetime of atoms will be expressed always in photons. Although using units of time for the lifetime is the natural physical choice, the lifetime in seconds is not a good quantity for the analysis here. As the emission rate depends on the potential depth and saturation intensity, a longer lifetime in seconds does not necessary mean that the atom is emitting more photons. Consider for example the case where the the saturation intensity is very low ($s_0 \ll 1$). As the emission rate is very low, the lifetime in seconds is expected to be large. However, the number of mean photons emitted will be reduced due to the low population of atoms in the $^1\text{P}_1$ state, which is not beneficial to the "deep potential" method. Also, the lifetime in seconds cannot be directly measured, as the number of total emitted photons is measurable but the number of atoms is undetermined. The method to measure lifetime using the histogram exponential decay, on the other hand, does not depend on the number of atoms. For a given potential depth and saturation it is possible to estimate the emission rate knowing the lifetime in photons and the histogram of fluorescence per site. The expected emission rate obtained in the simulations is in the range between 60 to 84 photons/μs. The maximum emission rate $2/\Gamma \approx 88$ photons/μs.

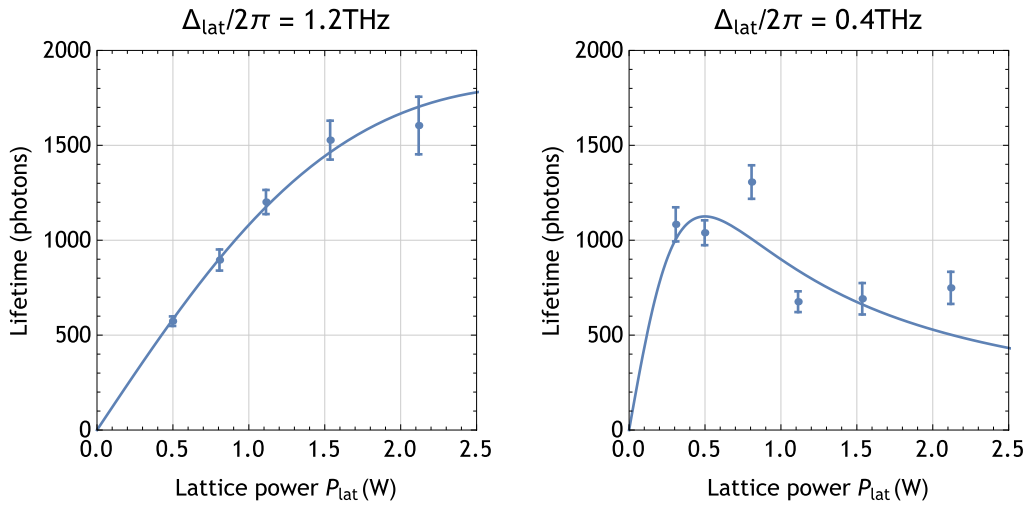

Figure 5.14: Lifetime dependency on lattice power P_{lat}. The solid curves are fitting using Eq. 3.23.

The lifetime analysis here is essentially the same as the one realized for the simulation data in Sec. 3.5. The dependence of the lifetime (in photons) n on the lattice power P_{lat} for

five different lattice detunings $\Delta_{lat}/2\pi = 0.4$, 0.6, 0.8, 1.0 and 1.2 THz is fitted with the Eq. 3.23. Figure 5.14 shows the measured lifetimes as a function of the lattice power P_{lat} for two different lattice detunings $\Delta_{lat}/2\pi = 0.4$ THz and $\Delta_{lat}/2\pi = 1.2$ THz.

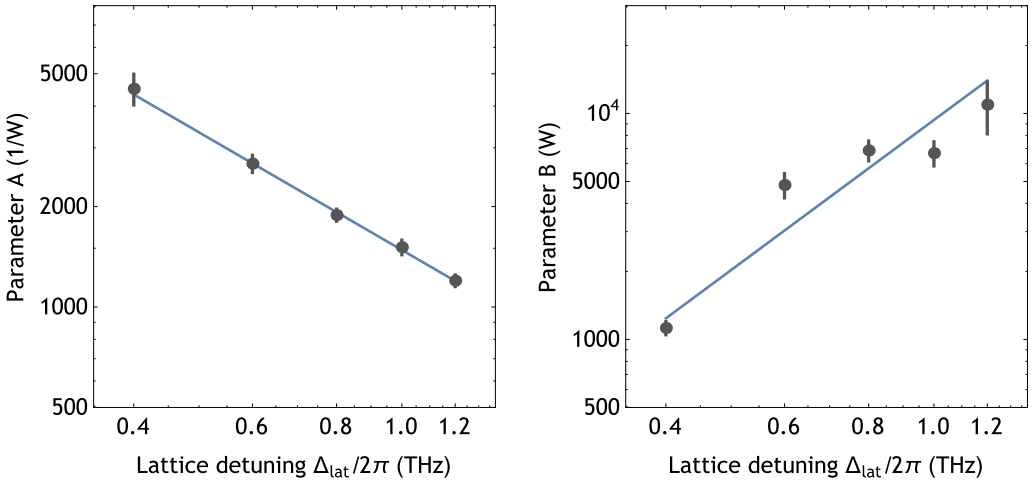

Figure 5.15: Lattice detuning $\Delta_{lat}/2\pi$ dependency of the parameters A and B. The solid curves are fittings using a power equation.

From the fitting results different parameters A and B are obtained for each lattice detuning Δ_{lat}. These parameters were plot in Fig. 5.15 and fitted using power equations, resulting in:

$$A = \frac{1480 \pm 40}{(\Delta_{lat}/2\pi)^{1.17\pm0.08}}\,\mathrm{W}^{-1} \quad , \quad B = (9400 \pm 1100)(\Delta_{lat}/2\pi)^{2.21\pm0.12}\,\mathrm{W} \tag{5.5}$$

where $\Delta_{lat}/2\pi$ is in the units of THz. Replacing the equations for the parameters A and B into the Eq. 3.23 and calculating the derivative by Δ_{lat}, the maximum lifetime and optimal detuning for a given P_{lat} results in:

$$n(P_{lat}) \approx 1470 {P_{lat}}^{0.31} \quad \text{at} \quad \Delta_{lat}/2\pi \approx 0.70 {P_{lat}}^{0.59} \tag{5.6}$$

where the units of P_{lat} and $\Delta_{lat}/2\pi$ are in W and THz, respectively. For the maximum lattice power $P_{lat} = 2.1$ W currently available in this system, the optimal lifetime is of $\sim$1850 photons at $\Delta_{lat}/2\pi \approx 1.1$ THz. The estimated photon emission rate is 25 photons/μm corresponding to a maximum lifetime of 74 μS.

Equation 5.6 plot is shown in Fig. 5.16. Upgrading the fiber amplifier system to achieve an output of $P_{lat} = 10$ W would increase the lifetime to $\sim$3000 photons at $\Delta_{lat}/2\pi \approx 2.7$ THz ($\lambda_{lat} \approx$ 1088 nm). Fortunately, high-power laser sources are readily available for this wavelength.

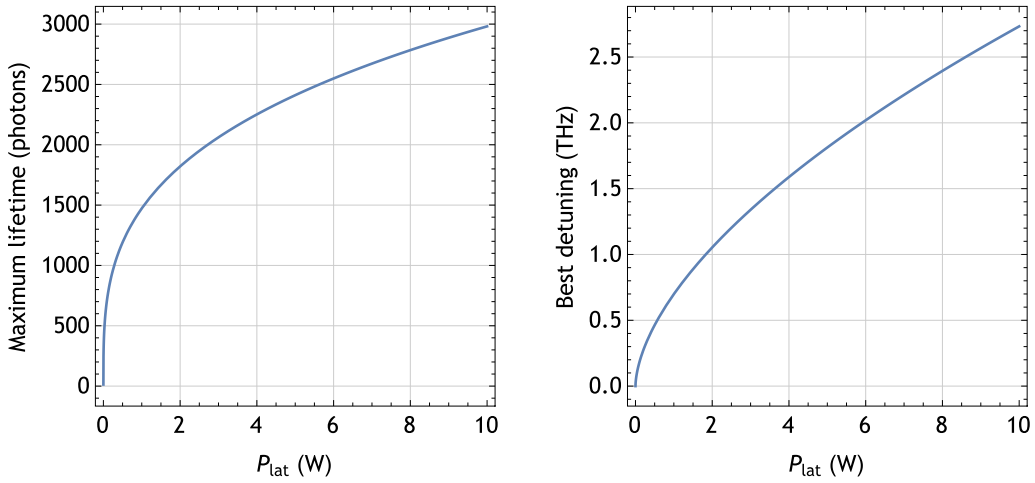

Figure 5.16: Maximum obtainable lifetime for a given power P_{lat} and the optimal lattice detuning $\Delta_{lat}/2\pi$.

5.4.4 Fidelity

The fidelity of the quantum gas microscope is determined by three main factors: 1) background noise, 2) losses and 3) hopping.

In the case of the background signal, the fidelity is reduced when the reconstruction algorithm wrongly evaluates an empty site as a filled one. The probability of making such an error can be estimated by processing 34 empty images with the reconstruction algorithm and analyzing the shape of the resultant histogram. Fig. 5.17 shows the total histogram for the processed images. For a threshold set in 150 photons, only 18 sites of the 9702 total sites resulted in a signal of more than the threshold. This means that there is a $< 0.2\%$ probability of wrongly evaluating a empty site as an occupied one.

The width of the background signal is determined by dark noise, readout noise and light scattering background. One of the advantages of this microscope system is that the dark noise is negligibly small due to the very short exposure times. In the case of this system, light scattering of the excitation beam limits the width of the background signal.

The losses can be estimated knowing that the atoms have a lifetime of 1850 photons for a lattice power of $P_{lat} = 2.1\,\mathrm{W}$. If the atom density decay exponentially, then $1-\exp(-150/1850) \approx 8\%$ of the atoms are lost before emitting 150 photons. The reconstruction algorithm wrongly determines these filled sites as empty sites.

The usual method to evaluate hopping effects is to take multiple images from the same lattice and verify whether each atom position have changed or not. In this experimental setup the lifetime and exposure time are very short and it is technically difficult to utilize this method. However, hopping effects are greatly reduced because the atoms that escape from the site and hop to neighboring sites have a high kinetic energy and cannot be cooled by

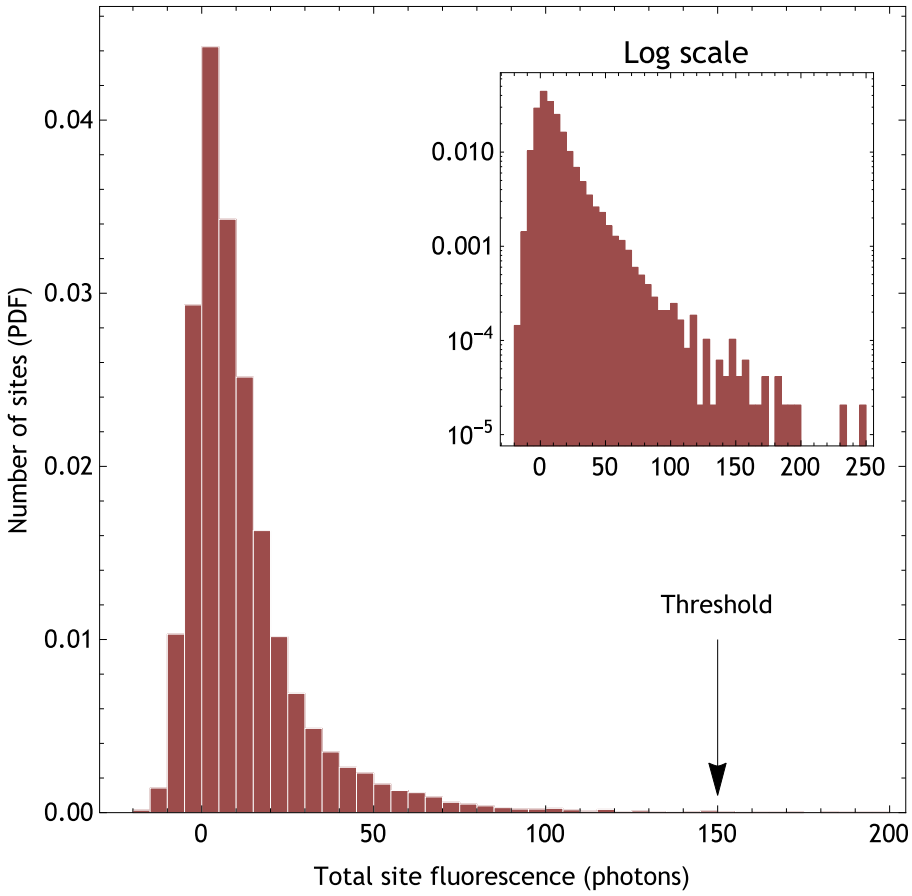

Figure 5.17: Histogram as a probability density function of the background signal. A total of 34 empty images were processed.

the excitation beam. Such atoms are expected to hop indefinitely until they are lost, emitting a reduced number of photons in the neighboring sites. As an alternative way to estimate hopping effects we measured the intensity correlation function $g^{(2)}(R) = \langle I(r)I(r+R)\rangle/\langle I(r)^2\rangle$ of occupied sites in 200 sparse lattice images. This resulted in correlations of $(1.03(18), 1.03(24), 1.03(19))$ for inter-atomic distances $R = (1, \sqrt{2}, 2) \times 544\,\text{nm}$. These correlation values indicates that hopping events do not produce enough photons to be counted as an occupied site.

5.5 Light shift in a 5-level diamond system

The AC Stark shift generated by two orthogonal optical accordion (lattice) beams with orthogonal polarizations is studied here (see Fig. 5.6). For the calculations the quantization axis is set in the y axis. The accordion beam propagating in the x direction have π polarization, while the accordion beam propagating in the y direction is in the $\frac{1}{\sqrt{2}}(\sigma_+ + \sigma_-)$ polarization.

The ground state $^1S_0$ and the excited state $(6s6p)^1S_0$ are labeled as $|1\rangle$ and $|5\rangle$, respectively. The excited state $^1P_1$ have three sublevels labeled as $|2\rangle = |m'_J = -1\rangle$, $|3\rangle = |m'_J = 0\rangle$ and $|4\rangle =$

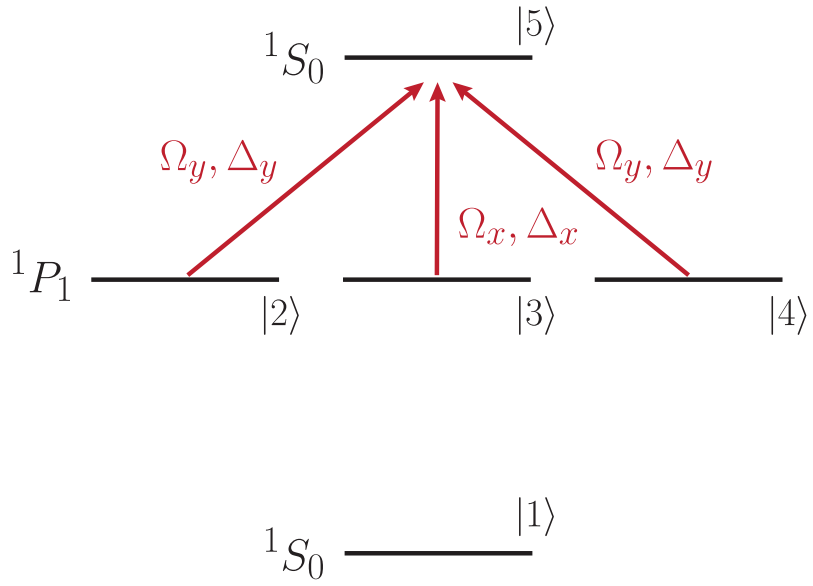

Figure 5.18: "Deep potential" as a five energy-level system in diamond shape.

$|m'_J = +1\rangle$. The accordion beam propagating in the x direction couples the energy levels $|3\rangle$ and $|5\rangle$. Correspondingly, the optical accordion propagating in the y direction couples $|2\rangle$ and $|4\rangle$ with $|5\rangle$ (see Fig. 5.18).

Consider the case in Fig. 5.6 where there is only one excitation beam propagating in the x direction and with π polarization. As the atom is excited into the $|3\rangle$ state, the atom experiences a deep potential due to the coupling of the states $|3\rangle$ and $|5\rangle$. As the optical accordion beam in the y direction only couples the states $|2\rangle$ and $|4\rangle$ with $|5\rangle$, the atom will not experience this potential, and consequently, it will be only trapped along the "deep potential" generated by the optical accordion in the x direction. If this is the case, the deep potential method would only apply in one direction when one excitation beam is used.

Two things were noticed and later theoretically understood during the realization of this experiment: 1) Only one excitation beam is necessary to produce a two-dimensional "deep potential" and 2) The "deep potential" is not symmetrical with respect to the x and y directions. There is always a unique "good direction" for excitation that produces brighter and sharper fluorescence images.

Both of this phenomena can be explained by the theory that follows. Consider the Hamiltonian for the unperturbed system H_0 and the interaction terms:

$$\begin{aligned}
H_0 &= \hbar\omega_2 |2\rangle\langle 2| + \hbar\omega_3 |3\rangle\langle 3| + \hbar\omega_4 |4\rangle\langle 4| + \hbar\omega_5 |5\rangle\langle 5| \\
H_{25} &= -\frac{\hbar\Omega_y}{2}\left(e^{-i\omega_y t} + e^{i\omega_y t}\right)(|2\rangle\langle 5| + |5\rangle\langle 2|) \\
H_{35} &= -\frac{\hbar\Omega_x}{2}\left(e^{-i\omega_x t} + e^{i\omega_x t}\right)(|3\rangle\langle 5| + |5\rangle\langle 3|) \\
H_{45} &= -\frac{\hbar\Omega_y}{2}\left(e^{-i\omega_y t} + e^{i\omega_y t}\right)(|4\rangle\langle 5| + |5\rangle\langle 4|)
\end{aligned} \tag{5.7}$$

which results in a total Hamiltonian given by:

$$H = H_0 + H_{25} + H_{35} + H_{45} = \hbar \begin{pmatrix} \omega_2 & 0 & 0 & -\frac{\Omega_y}{2} e^{i\omega_y t} \\ 0 & \omega_3 & 0 & -\frac{\Omega_x}{2} e^{i\omega_x t} \\ 0 & 0 & \omega_4 & -\frac{\Omega_y}{2} e^{i\omega_y t} \\ -\frac{\Omega_y}{2} e^{-i\omega_y t} & -\frac{\Omega_x}{2} e^{-i\omega_x t} & -\frac{\Omega_y}{2} e^{-i\omega_y t} & \omega_5 \end{pmatrix}. \tag{5.8}$$

Here the rotating wave approximation, where the terms representing a photon emission with excitation (e.g. $e^{-i\omega_x t} |5\rangle \langle 3|$) or a photon absorption with de-excitation (e.g. $e^{i\omega_x t} |3\rangle \langle 5|$) are neglected, was used. It is convenient also to introduce the effective Hamiltonian $\tilde{H}$ associated with the rotating-frame effective field:

$$\tilde{H} = U^\dagger H U - i\hbar U^\dagger \frac{\partial U}{\partial t} \tag{5.9}$$

where the unitary matrix U is defined as:

$$U = \begin{pmatrix} e^{i\omega_y t} & 0 & 0 & 0 \\ 0 & e^{i\omega_x t} & 0 & 0 \\ 0 & 0 & e^{i\omega_y t} & 0 \\ 0 & 0 & 0 & 1 \end{pmatrix}. \tag{5.10}$$

Equation 5.9 results in:

$$\tilde{H} = \hbar \begin{pmatrix} \omega_2 + \omega_y & 0 & 0 & -\Omega_y/2 \\ 0 & \omega_3 + \omega_x & 0 & -\Omega_x/2 \\ 0 & 0 & \omega_4 + \omega_y & -\Omega_y/2 \\ -\Omega_y/2 & -\Omega_x/2 & -\Omega_y/2 & \omega_5 \end{pmatrix} \tag{5.11}$$

and knowing that $\omega_e = \omega_2 = \omega_3 = \omega_4$, $\omega_y = \omega_5 - \omega_e + \Delta_y$ and $\omega_x = \omega_5 - \omega_e + \Delta_x$, it can be rewritten to:

$$\tilde{H} = \hbar \begin{pmatrix} \Delta_y & 0 & 0 & -\Omega_y/2 \\ 0 & \Delta_x & 0 & -\Omega_x/2 \\ 0 & 0 & \Delta_y & -\Omega_y/2 \\ -\Omega_y/2 & -\Omega_x/2 & -\Omega_y/2 & 0 \end{pmatrix} + \hbar I \omega_5. \tag{5.12}$$

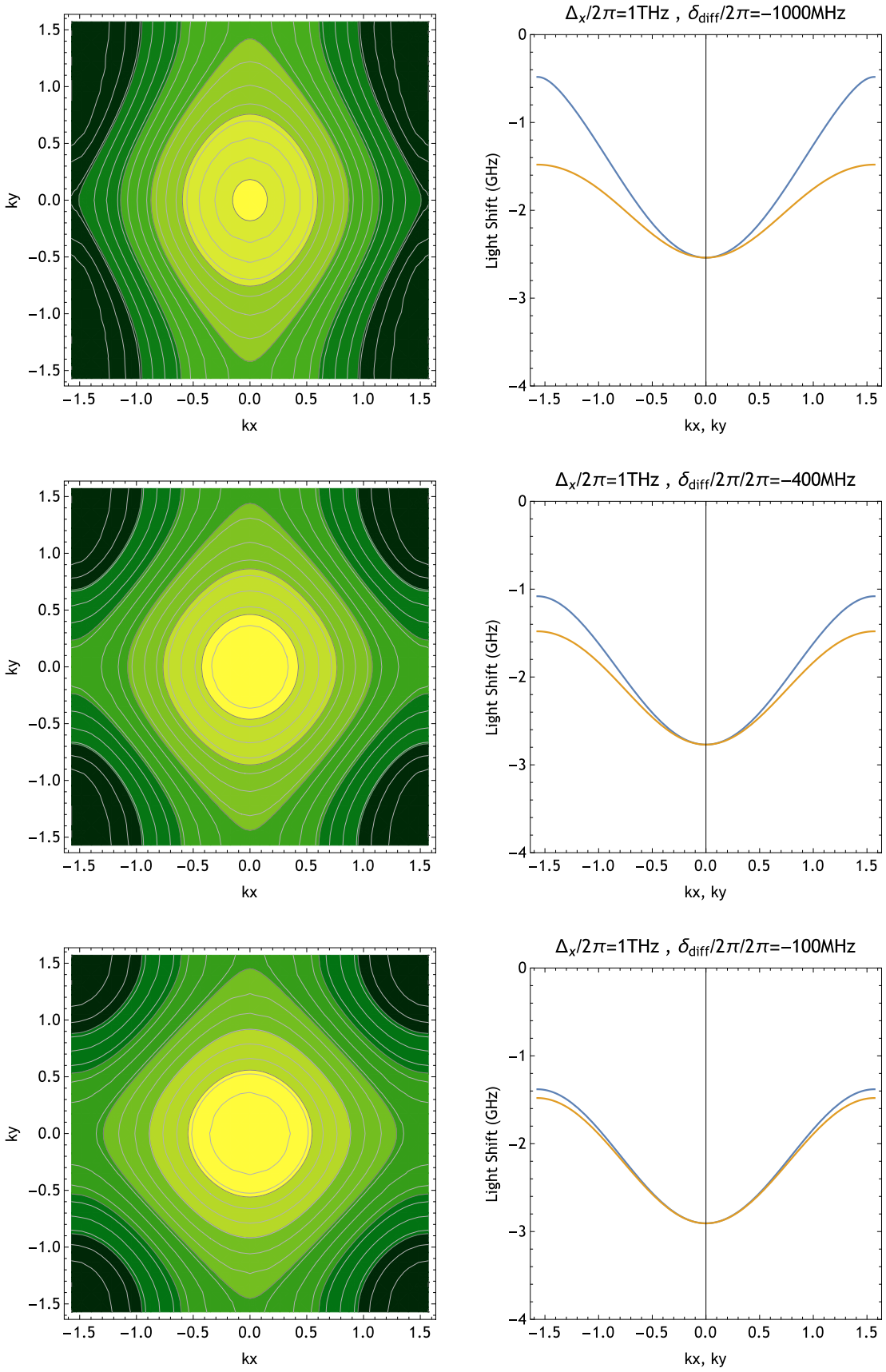

Figure 5.19: Light shift variation in a lattice site for different Δ.

The eigenvalues of the effective Hamiltonian are found by solving

$$|\tilde{H} - \lambda I| = 0 \tag{5.13}$$

for different detunings Δ_x, Δ_y and different Rabi frequencies Ω_x, Ω_y. In the case of a two-dimensional optical lattice where each of the lattice beams have the same power P_{lat} and different detuning $\Delta_x \neq \Delta_y$, the parameters are rewritten as:

$$\begin{aligned} \Omega_x &= \Omega \cos(k\,x) \\ \Omega_y &= \frac{1}{\sqrt{2}} \Omega \cos(k\,y) \\ \Delta_y &= \Delta_x + \delta_{\text{diff}} \end{aligned} \tag{5.14}$$

where the Rabi frequency is $\Omega/2\pi = 77\,\text{GHz}$ for $P_{\text{lat}} = 2.1\,\text{W}$. The resultant eigenstates are composed by one "deep" eigenstate which couples the state $|5\rangle$ with a linear combination of $|2\rangle$, $|3\rangle$, $|4\rangle$, and two eigenstates that are not coupled with $|5\rangle$ and produce flat potentials. The presence of such an eigenstate explains why is possible to realize the "deep potential" method with only one excitation beam. This is produced by the Raman coupling between the two accordion beams, that couples the state $|3\rangle$ with $|2\rangle$ and $|4\rangle$. Fig. 5.19 shows the dependency on the "deep" eigenvalue when moving along the x and y directions of the optical lattice. An asymmetry in the light shift profile results from large frequency differences $\delta_{\text{diff}}/2\pi \sim 1\,\text{GHz}$ between the two lattice beams. The asymmetry disappears for frequency differences smaller than 100 MHz.

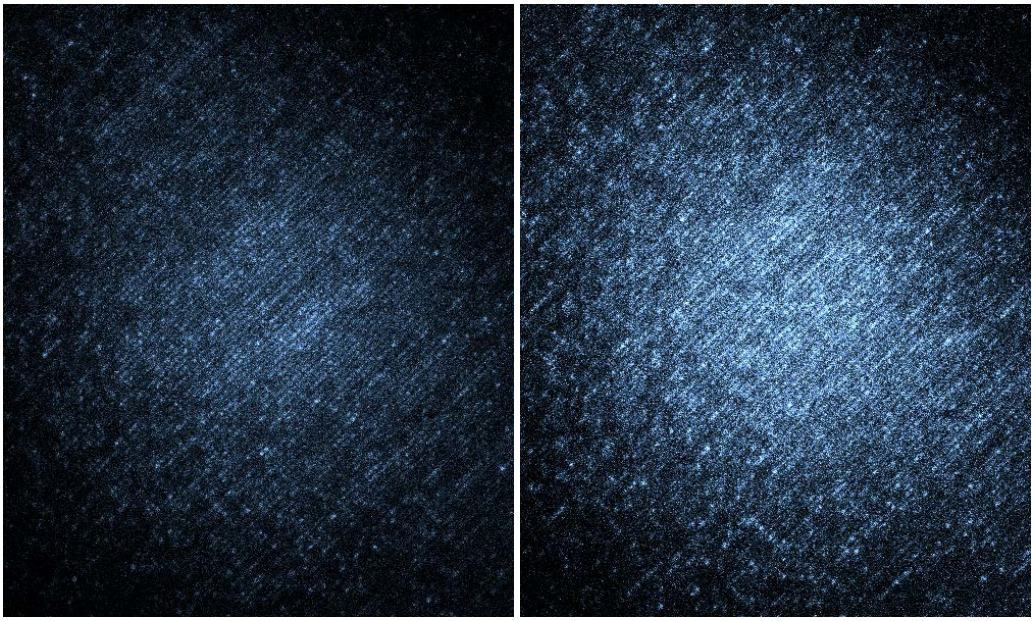

(a) "Bad direction" illumination (b) "Good direction" illumination

Figure 5.20: Fluorescence images of a tightly filled two-dimensional optical lattice for $\delta_{\text{diff}}/2\pi = 440\,\text{MHz}$ for two different directions of excitation.

The sign of δ_{diff} breaks the symmetry of the system. and a "good direction" for excitation exists. Fig. 5.20 shows the fluorescence images of a two-dimensional lattice for two different directions of excitation. The total fluorescence increases by a factor of two in the "good direction" case. The "good direction" and "bad direction" become reversed when the frequency offset sign changed ($\delta_{\text{diff}} \rightarrow -\delta_{\text{diff}}$).

Note that a non-zero frequency difference δ_{diff} is necessary in the experiment to avoid light interferences between the two lattice beams. For the final experiments a frequency difference $\delta_{\text{diff}}/2\pi = 80\,\text{MHz}$ was used.

Chapter 6

Extension to fermionic isotopes

This section focuses in the requirements to extend the quantum gas microscope of ytterbium atoms to the ^{173}Yb fermionic isotope. The s-wave scattering length of this fermionic isotope is $a = 10.55(11)$, which is positive and roughly two times bigger compared to that of the bosonic ^{174}Yb. Fermi degeneracy was experimentally demonstrated in 2007 for a six-spin-component atomic gas [100] where temperatures of $T/T_F = 0.37$ were obtained via evaporative cooling. A two-spin-component Fermi degenerate can be generated by pumping the atoms to the $|m_F| = 5/2$ states using a π polarized light [101, 102]. The lowest temperatures reported to the date are $T/T_F = 0.14$[101].

The process to create a two-dimensional condensate under the surface of the solid immersion lens is all-optical and it does not depend on the hyperfine structure of the excited state. Consequently, it can be directly be applied to the ^{173}Yb fermionic isotope with only minor changes in the optical system:

Zeeman Slower The $^1S_0 \rightarrow {}^1P_1$ transition from $F = 5/2$ to $F' = 7/2$ is used to slow the atoms. The isotope shift from ^{174}Yb is 588 MHz (cf. Table 2.3). To shift the frequency it suffices to modify the AOMs such that the fundamental wave shifts by 147 MHz (the AOMs are in the double-pass configuration).

Horizontal and Vertical transport No changes required.

Magneto Optical Trap The $^1S_0 \rightarrow {}^3P_1$ transition from $F = 5/2$ to $F' = 7/2$ is used to slow the atoms. The isotope shift from ^{174}Yb is 3805.7 MHz (cf. Table 2.4). The wavelength is shifted by using an adjacent transmission peak in the reference cavity (ULE, FSR 3.0 GHz), and changing the frequency of the AOMs by 805 MHz.

Optical Accordion After loading the atoms into the optical accordion, a π polarized light tuned to the $^1S_0 \rightarrow {}^3P_1(F = 5/2 \rightarrow F' = 3/2)$ is used to pump the atoms to the $|m_F| = 5/2$ states. The evaporation and compression procedure that follows requires no changes.

6.1 Deep potential

The deep potential method used to trap the bosonic ^{174}Yb during the fluorescence imaging process involves a 5-energy level system that was studied in detail in Appendix 5.5 and experimentally in Chapter 5. In the case of the fermionic isotope ^{173}Yb, the presence of nuclear spin $I = 5/2$ results in hyperfine splitting of the $^1P_1$ state, as shown in Fig. 6.1.

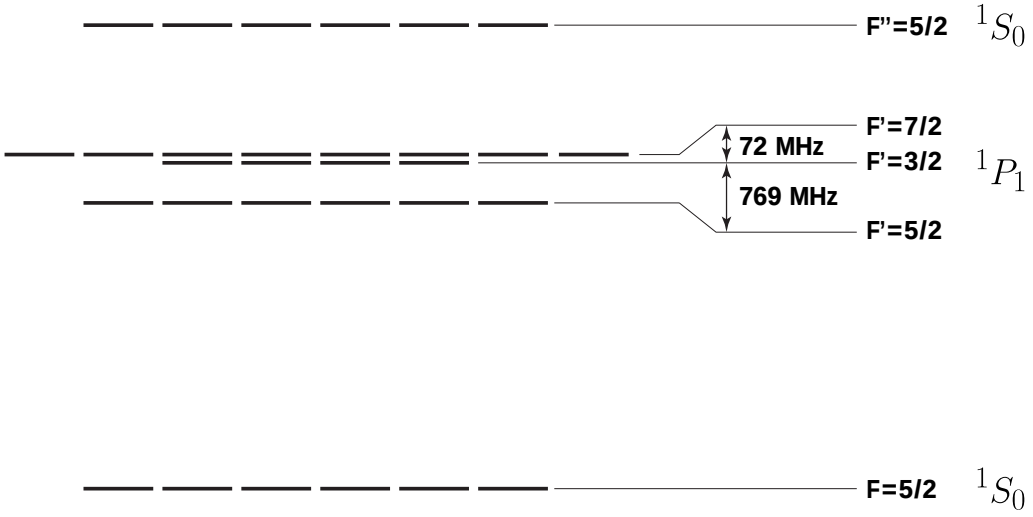

Figure 6.1: Hyperfine splitting of ^{173}Yb.

In the presence of a nuclear spin, the Hamiltonian can be written as $H = H_{\text{hfs}} + H_{\text{stark}}$. Here, H_{hfs} is the hyperfine splitting interaction given by:

$$H_{\text{hfs}} = A_{173}\mathbf{I}\cdot\mathbf{J} + B_{173}\frac{6(\mathbf{I}\cdot\mathbf{J})^2 + 3\mathbf{I}\cdot\mathbf{J} - 2\mathbf{I}^2\mathbf{J}^2}{2I(2I-1)2J(2J-1)}. \tag{6.1}$$

where $A_{173} = 57.682(29)\,\text{MHz}$ and $B_{173} = 609.065(98)\,\text{MHz}$ are the hyperfine splitting constants of the $^1P_1$ state in ^{173}Yb [75]. For this section $\hbar$ will be abbreviated for the sake of convenience. When there are no external fields present, the Hamiltonian of the system is simply $H = H_{\text{hfs}}$ which is diagonal in the basis of $|F, m_F\rangle$ where F is the total angular momentum related to the operator $\mathbf{F} = \mathbf{J} + \mathbf{I}$. The diagonal matrix elements are:

$$\langle F, m_F | H_{\text{hfs}} | F, m_F \rangle = \frac{1}{2}\hbar A_{173} G + \hbar B_{173}\frac{\frac{3}{2}G(G+1) - 2I(I+1)2J(J+1)}{2I(2I-1)2J(2J-1)} \tag{6.2}$$

where $G = F(F+1) - I(I+1) - J(J+1)$. F takes the values $F = |J-I| \ldots |J+I| = 3/2, 5/2, 7/2$ for $J = 1$ and $I = 5/2$ resulting in:

$$\begin{aligned}
\langle 3/2, m_F | H_{\text{hfs}} | 3/2, m_F \rangle / 2\pi &= 224\,\text{MHz} \\
\langle 5/2, m_F | H_{\text{hfs}} | 5/2, m_F \rangle / 2\pi &= -545\,\text{MHz} \\
\langle 7/2, m_F | H_{\text{hfs}} | 7/2, m_F \rangle / 2\pi &= 296\,\text{MHz}
\end{aligned} \tag{6.3}$$

which corresponds to the hyperfine splitting shown in Fig. 6.1. H_{stark} is the stark shift interaction described in Appendix A.1. When the hyperfine splitting interaction is not present, the Hamiltonian $H = H_{\text{hfs}}$ can be approximated as being diagonal in the basis of $|m_J, m_I\rangle$ with resulting energy shifts that are only dependent on m_J. In this case, the resultant diagonal matrix elements are exactly the same as the obtained for the bosonic ^{174}Yb (cf. Appendix 5.5).

When both interactions are present, the Hamiltonian $H = H_{\text{hfs}} + H_{\text{stark}}$ is in general not diagonal in neither the $|F, m_F\rangle$ basis nor the $|m_J, m_I\rangle$ basis. The eigenvalues and eigenstates can be only calculated by numerical diagonalization of the total Hamiltonian. Theoretical calculations and experimental verifications of the Stark shift for strong fields were realized for sodium and lithium in the case of DC fields [103, 104], and for rubidium in the case of far-detuned ODTs [105, 106]. The calculations in this thesis follows a similar procedure, with the difference that there are two strong fields corresponding to each of the accordion (lattice) beams. The two accordion beams have orthogonal direction and polarization, resulting in a strong Raman coupling between different m_J sublevels.

6.1.1 AC Stark shift

The AC stark shift between a ^{1}P$_1$ sublevel $|m_J, m_I\rangle$ and a (6s7s)^{1}S$_0$ sublevel $|m'_J, m'_I\rangle$ is related to the term (cf. Sec. A.1):

$$\begin{aligned}
&\langle m_J, m_I | \, e\hat{r} \, | m'_J, m'_I \rangle = \\
&\langle m_J, m_I | \left[\sum_{F, m_F} |F, m_F\rangle \langle F, m_F| \right] e\hat{r} \left[\sum_{F', m'_F} |F', m'_F\rangle \langle F', m'_F| \right] |m'_J, m'_I\rangle = \\
&\sum_{F, m_F} \sum_{F', m'_F} \langle m_J, m_I | F, m_F\rangle \langle F, m_F | \, e\hat{r} \, | F', m'_F\rangle \langle F', m'_F | m'_J, m'_I\rangle
\end{aligned} \tag{6.4}$$

where $\langle m_J, m_I | F, m_F\rangle$ is the Clebsch-Gordan coefficient defined by:

$$\langle m_J, m_I | F, m_F\rangle = (-1)^{J-I+m_F} \sqrt{2F+1} \begin{pmatrix} J & I & F \\ m_J & m_I & -m_F \end{pmatrix} \tag{6.5}$$

where the notation $\begin{pmatrix} j_1 & j_2 & j \\ m_1 & m_2 & m \end{pmatrix}$ represents the Wigner 3j-symbol. Using the Wigner-Eckart theorem, the matrix element $\langle F, m_F | \, e\hat{r} \, | F', m'_F\rangle$ can be rewritten as the product of the reduced matrix element $\langle F || e\, r || F'\rangle$ and the Clebsch-Gordan coefficient $\langle F', 1, m'_F, q | F, m_F\rangle$

$$\langle F, m_F | \, e\hat{r} \, | F', m'_F\rangle = \langle F || e\, r || F'\rangle (-1)^{F'-1+m_F} \sqrt{2F+1} \begin{pmatrix} F' & 1 & F \\ m'_F & q & -m_F \end{pmatrix}. \tag{6.6}$$

Here $q = -1, 0, 1$ represents the σ_-, π and σ_+ polarizations of the light field, respectively. The term vanishes when $m'_F \neq m_F + q$ (total m conservation). Using the Wigner 6j-symbol represented by $\left\{ \begin{smallmatrix} j_1 & j_2 & j_3 \\ j_4 & j_5 & j_6 \end{smallmatrix} \right\}$, the reduced matrix term is further factorized into

$$\langle F||er||F'\rangle = \langle J||er||J'\rangle (-1)^{F'+J+I+1}\sqrt{(2F'+1)(2J+1)} \begin{Bmatrix} F' & 1 & F \\ J & I & J' \end{Bmatrix}. \tag{6.7}$$

Finally, the reduced term $\langle J||er||J'\rangle$ is related to the transition probability by the formula:

$$|\langle J||er||J'\rangle|^2 = 2c\epsilon_0 \frac{\hbar^2\Gamma^2}{8I_s} \frac{2J'+1}{2J+1} \tag{6.8}$$

where Γ and I_{sat} is the linewidth and saturation intensity of the $^1P_1 \longleftrightarrow (6s7s)^1S_0$ transition, respectively. Figure 6.2 shows the relative transition probabilities between different hyperfine sublevels of the $^1P_1$ and $(6s7s)^1S_0$ states.

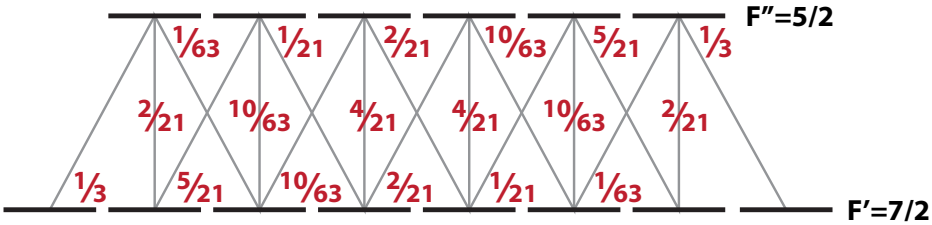

(a) Transition probabilities between $F' = 7/2$ and $F'' = 5/2$.

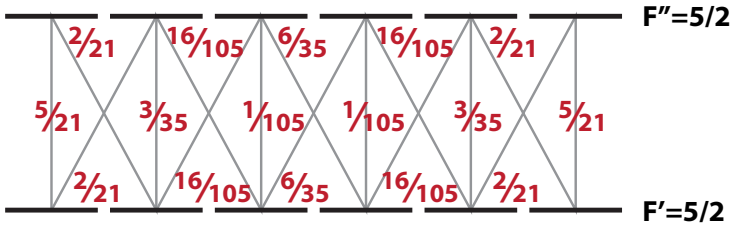

(b) Transition probabilities between $F' = 7/2$ and $F'' = 5/2$.

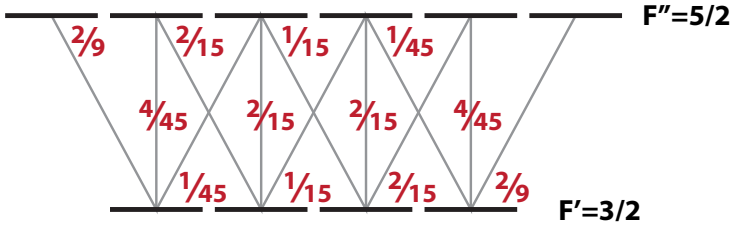

(c) Transition probabilities between $F' = 7/2$ and $F'' = 5/2$.

Figure 6.2: Transition probabilities between the different hyperfine sublevels of the $^1P_1$ states ($F' = 3/2, 5/2, 7/2$) and the $(6s7s)^1S_0$ state ($F'' = 5/2$).

6.1.2 Hyperfine splitting interaction

Here, the matrix elements $\langle m_J, m_I | H_{\text{hfs}} | m'_J, m'_I \rangle$ corresponding to the hyperfine splitting interaction are calculated. Equation 6.1 is rewritten as:

$$H_{\text{hfs}} = A_{173}\mathbf{I}\cdot\mathbf{J} + B'_{173}\left(\mathbf{I}\cdot\mathbf{J} + 2(\mathbf{I}\cdot\mathbf{J})^2 - \frac{2}{3}\mathbf{I}^2\mathbf{J}^2\right). \tag{6.9}$$

where $B'_{173} \equiv \frac{3B_{173}}{2I(2I-1)2J(2J-1)}$. To calculate the action of the operator $\mathbf{I}\cdot\mathbf{J}$ on the eigenstates, it is convenient to introduce the ladder operators $J_\pm, I_\pm$

$$J_\pm = J_x \pm i J_y \qquad , \qquad I_\pm = I_x \pm i I_y \tag{6.10}$$

which satisfy

$$\mathbf{I}\cdot\mathbf{J} = J_x I_x + J_y I_y + J_z I_z = J_z I_z + \frac{J_- I_+ + J_+ I_-}{2}. \tag{6.11}$$

In a similar way, $(\mathbf{I}\cdot\mathbf{J})^2$ results in:

$$\begin{aligned}
(\mathbf{I}\cdot\mathbf{J})^2 &= \left(J_z I_z + \frac{J_- I_+ + J_+ I_-}{2}\right)^2 \\
&= J_z^2 I_z^2 + \frac{1}{2} J_z I_z (J_- I_+ + J_+ I_-) + \frac{1}{2}(J_- I_+ + J_+ I_-) J_z I_z + \frac{1}{4}(J_- I_+ + J_+ I_-)^2 \\
&= J_z^2 I_z^2 + \frac{1}{2} J_z I_z (J_- I_+ + J_+ I_-) + \frac{1}{2}(J_- I_+ + J_+ I_-) J_z I_z \\
&+ \frac{1}{4}(J_-^2 I_+^2 + J_+^2 I_-^2 + J_- J_+ I_+ I_- + J_+ J_- I_- I_+).
\end{aligned} \tag{6.12}$$

The action of the different operators on the eigenstates $|m_J, m_I\rangle$ are:

$$\begin{aligned}
I_z |m_J, m_I\rangle &= m_I |m_J, m_I\rangle \\
J_z |m_J, m_I\rangle &= m_J |m_J, m_I\rangle \\
\mathbf{I}^2 |m_J, m_I\rangle &= \tilde{I} |m_J, m_I\rangle \\
\mathbf{J}^2 |m_J, m_I\rangle &= \tilde{J} |m_J, m_I\rangle \\
I_\pm |m_J, m_I\rangle &= \sqrt{\tilde{I} \pm m_I(m_I+1)} |m_J, m_I \pm 1\rangle \\
J_\pm |m_J, m_I\rangle &= \sqrt{\tilde{J} \pm m_J(m_J+1)} |m_J \pm 1, m_I\rangle
\end{aligned} \tag{6.13}$$

where $\tilde{I} = I(I+1)$ and $\tilde{J} = J(J+1)$. The diagonal matrix elements results in:

$$\langle m_J, m_I | H_{\text{hfs}} | m_J, m_I \rangle = A_{173} m_J m_I + B'_{173}\left([\tilde{J} - m_J^2][\tilde{I} - m_I^2] + 2m_J^2 m_I^2 - \frac{2}{3}\tilde{I}\tilde{J}\right) \tag{6.14}$$

The non-diagonal matrix elements are:

$$\langle m_J \pm 1, m_I \mp 1 | H_{\text{hfs}} | m_J, m_I \rangle = \left[\frac{A_{173}}{2} - B'_{173}(2 m_J m_I \pm m_J \mp m_I - 1/2) \right] \sqrt{(\tilde{J} - m_J^2 \pm m_J)(\tilde{I} - m_I^2 \mp m_I)} \tag{6.15}$$

$$\langle m_J \pm 2, m_I \mp 2 | H_{\text{hfs}} | m_J, m_I \rangle = \frac{B'_{173}}{2} \sqrt{\tilde{J} - m_J(m_J \mp 1)][\tilde{J} - (m_J \mp 1)(m_J \mp 2)][\tilde{I} - m_I(m_I \pm 1)][\tilde{I} - (m_I \pm 1)(m_I \pm 2)]} \tag{6.16}$$

6.1.3 Numerical results

Using the matrix elements obtained in Sec. 6.1.1 and Sec. 6.1.1 and applying the effective Hamiltonian procedure shown in Sec. 5.5 it is possible to calculate the eigenvalues numerically. The resultant eigenvalues for different light intensities are shown in Fig. 6.3 in the case of $\Delta_{\text{lat}}/2\pi = 1\,\text{THz}$.

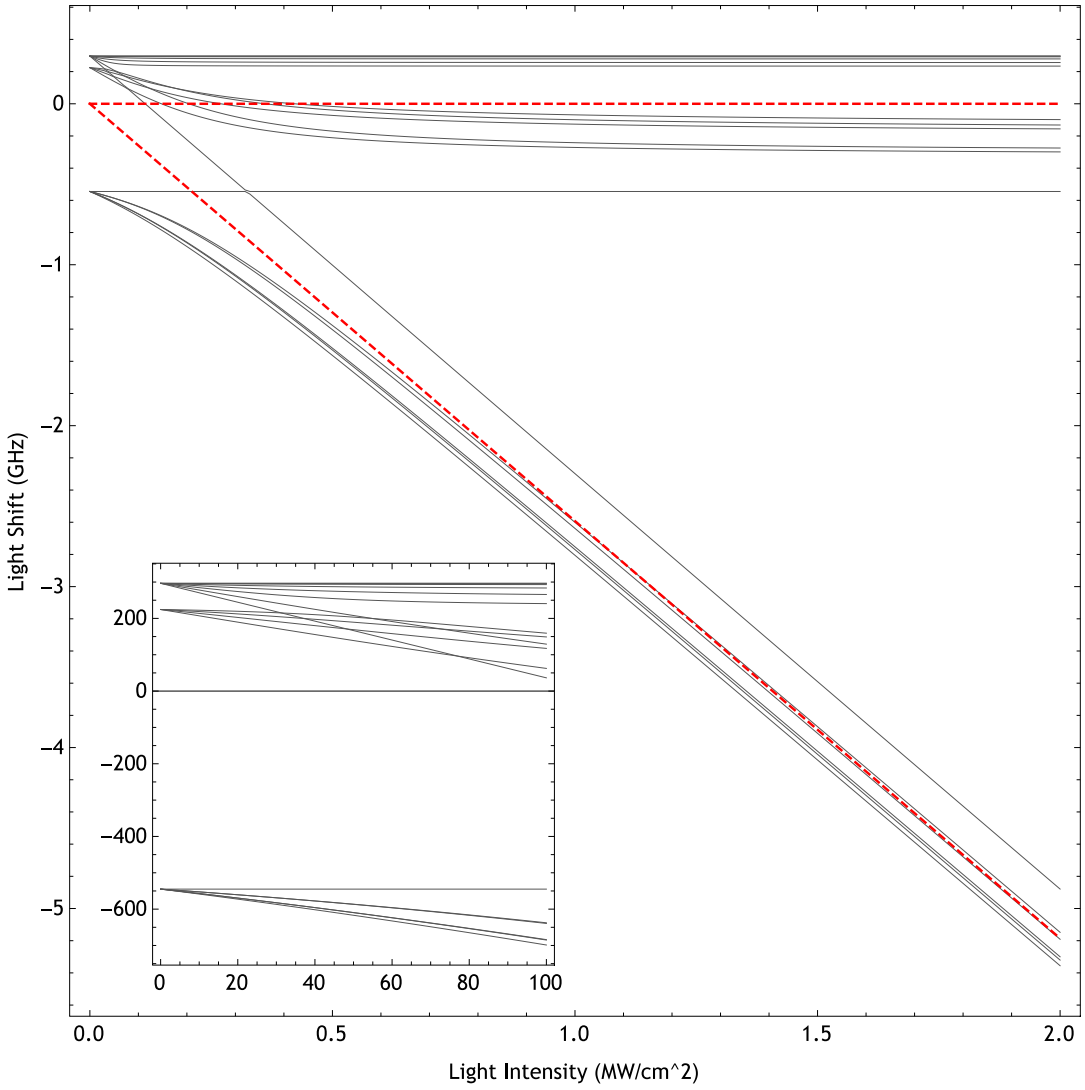

Figure 6.3: Eigenvalues of the total hamiltonian $H = H_{\text{hfs}} + H_{\text{stark}}$ as a function of the light intensity. The dotted lines in red are eigenvalues obtained for the bosonic ^{174}Yb.

For low light intensities ($I_{\text{lat}} < 100\,\text{kW/cm}^2$, $\Delta_{\text{stark}}/2\hbar < 200\,\text{MHz}$), F is a good quantum number and the resultant eigenvalues split in three groups corresponding to $F = 3/2, 5/2$ and $7/2$ (inset in Fig. 6.3). The AC stark effect can be treated as a second-order perturbation, resulting in light shifts that only depend on the m_F values and change linearly with the light intensity. For high intensities ($\Delta_{\text{stark}}/2\hbar = 1\,\text{GHz}$), the eigenvalues split according to m_J and results in a light shift similar to the bosonic case (red dotted lines in Fig. 6.3). Due to the hyperfine splitting interaction, each m_J group split in different sublevels which depends on m_F. This effect is analog to the Paschen-Back effect produced by strong magnetic fields. The results in this calculations are consistent with the results obtained with sodium, lithium and rubidium [103, 104, 105, 106].

Figure 6.4 shows the eigenvalues for two different lattice detuning $\Delta_{\text{lat}}/2\pi = 0.1, 10\,\text{THz}$. Note that the horizontal axis is scaled to the same ratio as $\Delta_{\text{lat}}/2\pi$ for the purpose of comparison. The resultant shapes are exactly the same as the obtained in Fig. 6.3. This means that the shape is only dependent on the interaction energies H_{hfs} and $H_{\text{stark}} \propto I_{\text{lat}}/\Delta_{\text{lat}}$.

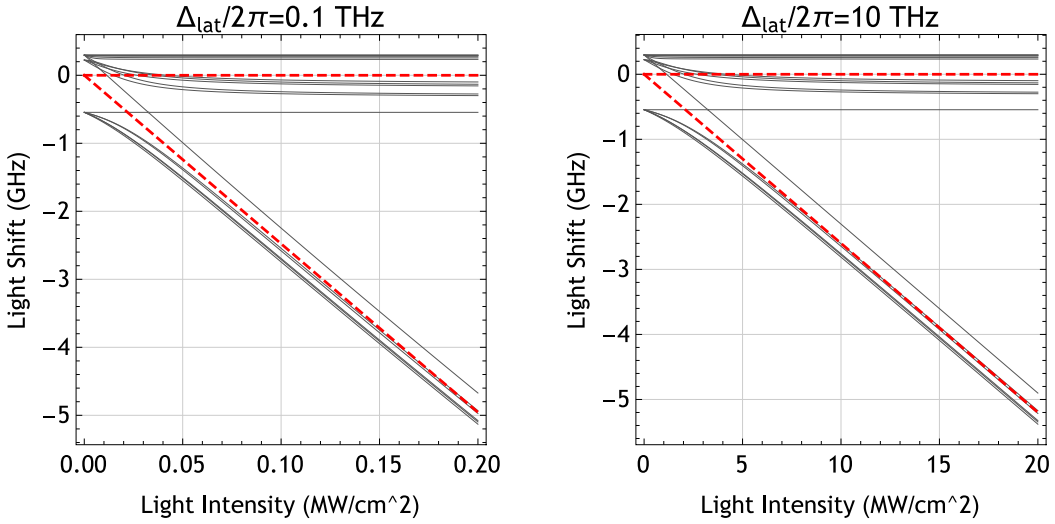

Figure 6.4: Eigenvalues of the total hamiltonian $H = H_{\text{hfs}} + H_{\text{stark}}$ as a function of the light intensity for $\Delta_{\text{lat}}/2\pi = 0.1$ and $10\,\text{THz}$.

6.2 Feasibility of the extension

The quantum gas microscope schema presented in this thesis can be easily extended to the ^{173}Yb fermionic isotope. The process to create a pancake-shaped condensate of atoms under the surface of the solid immersion lens requires only a few changes, which includes the modification of the cooling beams frequency and the insertion of an additional beam used to spin-polarize the atomic cloud before evaporative cooling. The deep potential method was analyzed in the influence of the hyperfine splitting interaction. For very large light shifts as

the used in the deep potential experiment ($\Delta_{\text{stark}}/2\pi \approx 3\,\text{GHz}$) the hyperfine splitting interaction ($\Delta_{\text{hfs}}/2\pi \approx 300\,\text{MHz}$) is one order of magnitude smaller, resulting in the breaking of hyperfine splitting analog to the Paschen-Back effect in strong magnetic fields. As the resultant light shift has the same gradient that in the case of the bosonic ^{174}Yb, which was tested experimentally in this work, it is possible to affirm that the procedure will also work for the ^{173}Yb fermionic isotope. Additionally, the hyperfine splitting interaction split each of the m_J eigenvalues into multiple m_F sublevels. This splitting might be beneficial to the deep potential method, as the resultant linewidth-broadening of the $^1\text{S}_0 \longleftrightarrow {}^1\text{P}_1$ transition would in theory reduce the effects of light shift inhomogeneities during fluorescence imaging.

Chapter 7

Conclusions

Quantum simulators using fermionic atoms are useful for studying the Fermi-Hubbard model, which is expected to be the key to elucidate the mechanism of high temperature superconductors. One of the biggest challenges to investigate the Fermi-Hubbard model is to reduce the temperature of the system, which is a requirement for the observation of anti-ferromagnetic order and d-wave super-fluidity.

The work presented in this thesis demonstrates the realization of a quantum gas microscope for ytterbium atoms, a tool capable of measuring and reducing the temperature of a Fermi-Hubbard system. Two big challenges were present in the development of a QGM: 1) How to prepare a thin sample of condensate atoms under the surface the solid immersion lens and 2) How to obtain a sufficient large number of atoms to realize high fidelity fluorescence imaging of atoms trapped in a two-dimensional optical lattice.

7.1 Experiment summary

In the first part of this thesis I presented a novel all-optical approach to load ultra-cold Yb atoms into a single layer of a standing wave directly below the surface of solid immersion lens (SIL). After loading the atoms into a magneto-optical-trap, two optical dipole trap beams were used to transport the atoms directly under the surface of the SIL. The new method realized here to create an "optical accordion" consists in reflecting a laser beam into the surface of the SIL. The resultant accordion potential was used to create a Bose-Einstein condensate and compress the atoms into a thin layer, positioned 2.6 μm below the surface of the lens. The all-optical scheme presented here can be applied to all atomic species regardless of the magnetic moment or energy structure. In fact, a similar schema was recently used to realize a quantum gas microscope of Lithium atoms [52].

The second part of this thesis focuses on how to load the disk-shaped condensate of atoms into a two-dimensional optical lattice and how to realize high fidelity fluorescence imag-

ing of the trapped atoms. To load the atoms into the optical lattice, the accordion system used to compress the atoms was transformed into a two-dimensional optical lattice by retro-reflecting each of the accordion beams. For single-site addressing of atoms in a two-dimensional optical lattice the conventional method until now was to laser cool the atoms while observing the resultant fluorescence. In contrast with this approach, the innovative idea presented here is to use a deep potential without cooling to contain the heated atoms during imaging. To create such a deep potential, the wavelength of the accordion beams the wavelength of the accordion beams was selected to be $\lambda = 1081\,\text{nm}$, which is detuned by only 4 nm to the $^1P_1 - ^1S_0$ transition (wavelength 1077 nm). The lifetime limitations of this system were studied in detail showing a good agreement with a simple model consisting in two losses. Finally, the performance of the quantum gas microscope was analyzed, resulting in a fidelity of 92% on the reconstruction algorithm mainly limited by atom losses due to the short lifetime. By using the ultraviolet strong transition combined with a solid immersion lens and high-resolution optics, the system presented here was able to resolve individual sites in an optical lattice with a 544-nm spacing, with a FHWM resolution of 318 nm.

7.2 Current quantum gas microscopes

Following the realization of two different quantum gas microscope for rubidium atoms in 2010 and 2011, the work presented here is the first realization of a quantum gas microscope for a species different than rubidium. At the time of this thesis and to the extent of my knowledge, a total of nine different quantum gas microscopes exist. The specifications for each of the quantum gas microscope including resolution, lattice spacing, exposure time, loss and hopping rates, and utilized method is summarized in Table. 7.1.

	Laboratory	Resol.	Spacing	Time	L	H	Method	Ref.
Rb	Harvard	700 nm	532 nm	∼1 s	2%	0%	PGC	[46]
Rb	MPQ	600 nm	640 nm	0.9 s	1%	0.5%	PGC	[47]
Yb	Titech	318 nm	544 nm	40 μs	8%	0%	Deep potential	
K	Strathclyde	630 nm	532 nm	1.5 s	9%	8%	EIT cooling	[56]
K	MIT	640 nm	532 nm	1 s	4.8%	1.2%	Raman cooling	[55]
K	Toronto	600 nm	527 nm	∼5 s	2%	5%	EIT cooling	[57]
Li	Harvard	520 nm	569 nm	1.9 s	2.6%	2.3%	Raman cooling	[52]
Li	MPQ	900 nm	1150 nm	1 s	2.5%	5%	Raman cooling	[53]
Yb	Kyoto	364 nm	266 nm	0.4 s	6.5%	6.7%	Sideband cooling	[58]

Table 7.1: Current quantum gas microscopes. The highlighted row corresponds to this work.

The quantum gas microscope presented in this work is characterized by:

High resolution The resolution of 318 nm obtained in this work is the highest resolution available for quantum gas microscopes up to the date. A high resolution is beneficial to reduce the number of required photons, as the fluorescence from each atom is distributed in less pixels.

Fast imaging time The fast imaging times $40\,\mu$s are five order of magnitude smaller compared with other experiments. The advantage of having such short imaging times is that the system is robust against mechanical instabilities in the optical system.

No hopping effects Due to the lack of a cooling method and the presence of a radiative force, atoms are unlikely to hop to a neighbor site and stay pinned. This is also an advantage as hopping effects are difficult to compensate. In contrast, loss effects can be compensated by data averaging.

The "deep potential" schema presented here does not depend on the energy level structure and is completely all optical, and thus, can be adapted in theory to any atomic species. In practice, however, this method is well suited for heavy species having small recoil energies $(\hbar k)^2/2m$, such as europium, erbium, dysprosium, holmium, ytterbium and mercury.

7.3 Possible improvements

The following technical modifications would improve the fidelity of the quantum gas microscope for ytterbium atoms:

Accordion power Increasing the power of the optical lattice lattice power from $P_{\text{lat}} = 2.1\,\text{W}$ to $P_{\text{lat}} = 10\,\text{W}$ would increase the lifetime to ∼3000 photons. The loss ratio in this case decreases from 8% to 5%.

Objective Lens and CCD camera The transmission of the objective lens can be improved from the actual 54% to ∼80% by using custom-made objective lenses specially designed for NUV. By using a different CCD camera, the quantum-efficiency can be increased from to $0.5e^-$/photon to $\sim 0.7e^-$/photon. Both of these upgrades would result in a total collection efficiency of 10%, which is two times larger than the current value. Doubling the collection efficiency allows one to half the exposure time to 20μs and threshold to 75 photons, further decreasing the loss ratio from 5% to ∼2.5%.

Retro-reflected excitation beam A retro-reflected excitation beam would in theory increase the lifetime by ∼10% in the current setup ($P_{\text{lat}} = 2.1\,\text{W}$). Note that if the lattice power is increased to $P_{\text{lat}} = 10\,\text{W}$, the effect of this modification becomes negligible.

7.4 Tasks

A remaining task is the evaluation of photo-association (PA) effects. The characteristic time for PA inelastic collisions resulting in the loss of a pair of atoms is in the order of a few to tens of microseconds [107, 108]. In quantum gas microscope experiments using cooling techniques such as PGC, Raman Cooling and EIT Cooling, the exposure time is in the order of seconds (cf. Table 7.1), which is five orders of magnitude larger than the PA characteristic time. Photo-association losses in those experiments can be considered instantaneous, and the measured fluorescence reflects the parity projection of the original atom-number distribution. For the quantum gas microscope presented in this work the exposure time is 40 μs, which is comparable to the characteristic PA time. The fluorescence is then expected to increase in case of multiple occupied sites, as pair of atoms emit a number of photons before being lost. In order to investigate the effects of PA it is necessary to study a system where the number of atoms is well determined, such as a Mott insulator. Current experiments focus in the observation of the Superfluid-to-Mott-insulator transition at single atom level, which would be useful to elucidate the effects of PA.

Note that PA effects will not affect the fluorescence in the case of the ^{173}Yb fermionic isotope. Multiple occupancy of fermions in a single-site is limited to atoms with different spin, as the occupation of atoms with the same spin is forbidden by the Pauli exclusion principle. Employing spin-selective excitations mediated by the $^1S_0 \longleftrightarrow {}^3P_2$ transition, it is possible to circumvent PA effects by measuring each spin separately.

7.5 Future experiments

Future experiments will focus on the study of the Fermi-Hubbard model using the ^{173}Yb fermionic isotope and the quantum gas microscope. The current quantum gas microscope schema can be applied to any ytterbium isotope without major changes in the system (cf. Section 6).

One of the biggest challenges to determine the phase diagram of the Fermi-Hubbard model will be the reduction of the temperature of the system, which is a requirement for the observation of the anti-ferromagnetic phase and the d-wave super-fluidity. The ultra-narrow transition in ytterbium combined with the high-resolution of the quantum gas microscope will be a key feature to reduce the temperature of the system using theoretically proposed “spatial filtering” techniques [59, 60].

Appendix A

Laser cooling and trapping

A.1 Optical dipole trap

When an electric field produced by a laser beam interacts with an atom, the energy levels of the atom shift. The interaction Hamiltonian H_{int} for the dipole interaction is defined by

$$H_{\text{int}} = -\mu \cdot \mathbf{E} \tag{A.1}$$

where μ and $\mathbf{E}$ represents the dipole momentum and electric field, respectively. Using the perturbation theory, the energy shift δE_i induced in the energy level E_i is given by:

$$\delta E_a = \sum_{a \neq b} \frac{|\langle a|H_{\text{int}}|b\rangle|^2}{E_a - E_b} \tag{A.2}$$

where $|i\rangle$ is the eigenstate of the unperturbed Hamiltonian. Using the second quantization representation, the electric field for a laser beam with frequency ω, can be written as

$$\mathbf{E}(\mathbf{r}) = \sqrt{\frac{\hbar\omega}{2V\epsilon_0}}\hat{\mathbf{e}}\left[\hat{a}e^{i\mathbf{k}\cdot\mathbf{r}} + \hat{a}^\dagger e^{-i\mathbf{k}\cdot\mathbf{r}}\right] \tag{A.3}$$

where V is the volume of the system, and **e** is the polarization of the light. Substituting this equation into Eq. A.1, the dipole interaction can be represented as

$$H_{\text{int}} = -\sqrt{\frac{\hbar\omega}{2V\epsilon_0}}\hat{\mathbf{e}}\cdot\mu\left[\hat{a}e^{i\mathbf{k}\cdot\mathbf{r}} + \hat{a}^\dagger e^{-i\mathbf{k}\cdot\mathbf{r}}\right]. \tag{A.4}$$

To solve $\langle a|H_{\text{int}}|b\rangle$, let's consider the dressed states $\langle a,n|$ and $\langle b,n'|$. Knowing that the annihilation and creation operator $\hat{a}$ satisfies $\hat{a}|n\rangle = \sqrt{n}|n-1\rangle$ and $\hat{a}^\dagger|n\rangle = \sqrt{n+1}|n+1\rangle$:

$$\left|\langle a,n|H_{\text{int}}|b,n'\rangle\right|^2 = \frac{\hbar\omega}{2V\epsilon_0}\hat{\mathbf{e}}\cdot\left|\langle a|\mu|b\rangle\right|^2\left[(n+1)\delta(n,n'-1) + n\delta(n,n'+1)\right] \tag{A.5}$$

furthermore, for a very large number of photons $n \approx n+1$ and thus,

$$\begin{aligned}\delta E_{a,n} &= \sum_{b\neq a,n'} \frac{n\hbar\omega}{2V\epsilon_0}\hat{\mathbf{e}}\cdot\left|\langle a|\mu|b\rangle\right|^2 \frac{\delta(n,n'-1)+\delta(n,n'+1)}{E_{a,n}-E_{b,n'}} \\ &= -\sum_{b\neq a} \frac{n\hbar\omega}{2V\epsilon_0}\hat{\mathbf{e}}\cdot\left|\langle a|\mu|b\rangle\right|^2 \left(\frac{1}{\hbar\omega_{ba}+\hbar\omega}+\frac{1}{\hbar\omega_{ba}-\hbar\omega}\right) \\ &= -\sum_{b\neq a} \frac{n\hbar\omega c}{V}\frac{1}{2\hbar\epsilon_0 c}\hat{\mathbf{e}}\cdot\left|\langle a|\mu|b\rangle\right|^2 \left(\frac{1}{\omega_{ba}+\omega}+\frac{1}{\omega_{ba}-\omega}\right)\end{aligned} \tag{A.6}$$

for $\omega_{ba} = \omega_b - \omega_a$. The spontaneous decay rate Γ_{ab}, the laser beam intensity $I(\mathbf{r})$, and the saturation intensity $I_{\text{sat}}$are defined by:

$$\Gamma_{ab} = \frac{\omega_{ba}^3}{3\pi\epsilon_0\hbar c^3}\left|\langle a|\mu|b\rangle\right|^2 \quad , \quad I(\mathbf{r}) = \frac{n\hbar\omega c}{V} \quad , \quad I_{\text{sat}} = \frac{\hbar\Gamma_{ab}\omega_{ba}^3}{12\pi c^2} \tag{A.7}$$

Finally, considering a linear polarization, Eq. A.6 can be rewritten as

$$\delta E_a(\mathbf{r}) = -\sum_{b\neq a} \frac{\hbar\Gamma_{ab}^2}{8}\frac{I(\mathbf{r})}{I_{\text{sat}}}\left(\frac{1}{\omega_{ba}+\omega}+\frac{1}{\omega_{ba}-\omega}\right) \tag{A.8}$$

and for near resonant frequencies $\omega \approx \omega_{ab}$ in a two-level atom, the expression can be approximated to:

$$\delta E(\mathbf{r}) = -\frac{\hbar\Gamma^2}{8}\frac{I(\mathbf{r})}{I_{\text{sat}}}\frac{1}{\Delta} \tag{A.9}$$

In the case of a far-detuned laser in a two-level system, the scattering rate is related to the light shift by the equation

$$\hbar\Gamma_{\text{sc}} = \frac{\Gamma}{\Delta}\delta E(\mathbf{r}). \tag{A.10}$$

Note that for a constant light shift δE, the scattering rate can be reduced by using large detunings Δ.

A.1.1 Optical dipole trap generated by a Gaussian beam

A red-tuned focused Gaussian laser beam is the simplest way to create a dipole trap providing three-dimensional confinement. This type of confinement is often referred as optical tweezers. The spatial intensity distribution of a focused Gaussian beam with power P propagating along the z axis is given by

$$I(\mathbf{r},z) = \frac{2P}{\pi w(z)^2}\exp\left(-2\frac{r^2}{w^2(z)}\right) \tag{A.11}$$

where r denotes the radial coordinate, and $w(z)$ depends on the axial coordinate z via

$$w(z) = w_0\sqrt{1+\left(\frac{z}{z_0}\right)^2} \tag{A.12}$$

where w_0 is the beam waist, and $z_0 = k\,w_0^2/2$ is the Rayleigh length. Substituting this equation in Eq. A.8, the dipole potential U_{dip} generated by a Gaussian beam results in:

$$U_{\text{dip}}(\mathbf{r}) = -\sum_{b\neq a}\frac{\hbar\Gamma_{ab}^2}{4I_{\text{sat}}}\frac{P}{\pi w(z)^2}\exp\left(-2\frac{r^2}{w^2(z)}\right)\frac{\omega_{ba}}{\omega_{ba}^2-\omega^2} \tag{A.13}$$

For two-energy level system a red-detuned laser beam ($\omega > \omega_0$) will produce a attractive potential in the ground state and a repulsive potential in the excited state, as shown in Fig. A.1.

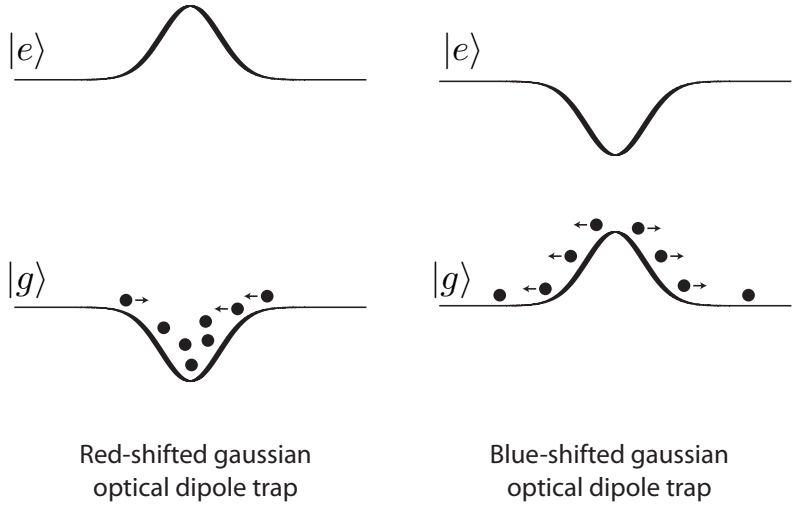

Figure A.1: Potential energy generated by a Gaussian beam in the case of a two-energy level system.

A.1.2 Standing Wave

When two counter-propagating with the same frequency interfere as in Fig. A.2, a standing wave with periodicity of half the wavelength is formed. By combining the standing wave generated by a red-detuned laser beam in one or more directions an optical lattice is created.

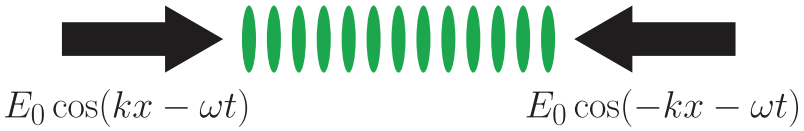

Figure A.2: Standing wave resulting from the interference of two counter-propagating waves

The total electric field generated by two counter-propagating beams is given by:

$$E = E_0 \cos(kx - \omega t) + E_0 \cos(-kx - \omega t) \tag{A.14}$$

in the case that the two beams have the same amplitude E_0. The light intensity is proportional to the square of the electric field

$$\begin{aligned} I \propto |E|^2 &= |E_0|^2 [\cos(kx - \omega t) + \cos(-kx - \omega t)]^2 \\ &= \frac{|E_0|^2}{4} \left[e^{i(kx-\omega t)} + e^{-i(kx-\omega t)} + e^{i(-kx-\omega t)} + e^{-i(-kx-\omega t)} \right]^2 \\ &= \frac{|E_0|^2}{4} \left[\left(e^{i\omega t} + e^{-i\omega t} \right) \left(e^{ikx} + e^{-ikx} \right) \right]^2 \\ &= 4|E_0|^2 \cos^2(\omega t) \cos^2(kx) \end{aligned} \tag{A.15}$$

resulting in a standing wave in the x direction, having a peak intensity four times bigger than the intensity of a single propagating-wave. In the case of two counter-propagating beams with two different amplitudes

$$E = E_0 \cos(kx - \omega t) + E_1 \cos(-kx - \omega t) \tag{A.16}$$

it is still possible to calculate the intensity with a more complicated calculation, resulting in:

$$|E|^2 = |E_1|^2 \left[(1 - \alpha + \alpha^2) + 4\alpha \cos^2(kx) \right] \cos^2(\omega t) \tag{A.17}$$

where $\alpha = E_2/E_1$ is the ratio between the two amplitudes. When $\alpha \neq 1$, the total intensity is formed by the sum of a standing wave and a propagating wave (constant intensity, also called offset intensity). Note that Eq. A.17 reverts to Eq. A.15 for $\alpha = 1$.

By combining a three different standing waves in the three directions, an optical lattice

$$U_{\text{lattice}} = V_0 \left[\cos^2(kx) + \cos^2(ky) + \cos^2(kz) \right] \tag{A.18}$$

is formed.

The periodicity of the standing wave can also be changed by crossing two different beams as shown in Fig. A.3. For two waves propagating in the directions $\hat{k_1} = (\cos\theta, \sin\theta)$ and $\hat{k_1} = (\cos\theta, -\sin\theta)$, the resultant standing wave intensity is given by:

$$\begin{aligned} I \propto |E|^2 &= |E_0|^2 \left[\cos(kx\cos\theta + ky\sin\theta - \omega t) + \cos(kx\cos\theta - ky\sin\theta - \omega t) \right]^2 \\ &= 4|E_0|^2 \cos^2(ky\sin\theta) \cos^2(kx\cos\theta - \omega t) \end{aligned} \tag{A.19}$$

which has a periodicity of $\lambda/2\sin\theta$.

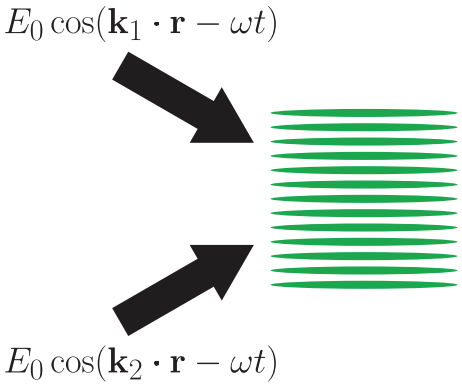

Figure A.3: Standing wave from the interference of two crossing propagating-waves.

A.2 Potential under the solid immersion lens

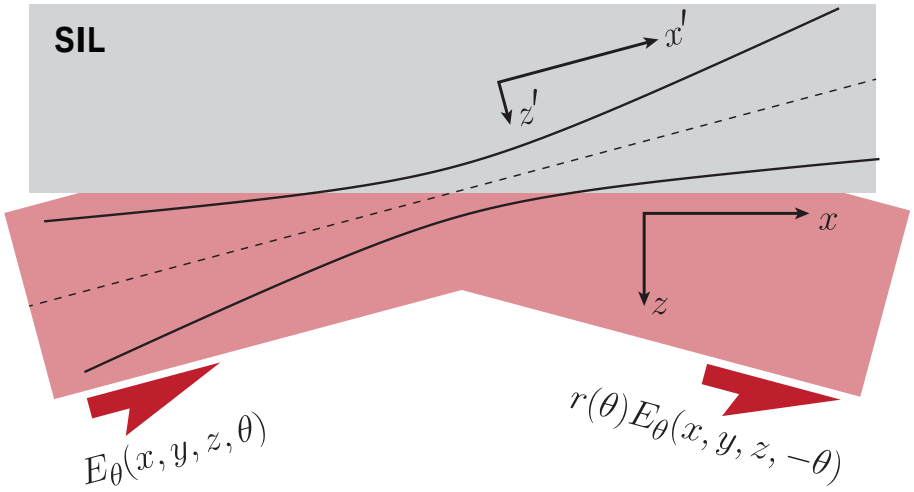

Figure A.4: Potential energy generated by a Gaussian beam in the case of a two-energy level system.

The electric field of a Gaussian propagating in the x' axis

$$E_{\text{gauss}}(x',y',z') = E_0\sqrt{\frac{w_{0z}}{w_z(x')}}\sqrt{\frac{w_{0y}}{w_y(x')}}\exp\left(\frac{z'^2}{w_z(x')^2}\right)\exp\left(\frac{y'^2}{w_y(x')^2}\right)\cos(kx'-\omega t) \quad \text{(A.20)}$$

where the complex term related to the radius of curvature and the Gouy phase was neglected. The Gaussian beam in terms of the coordinates (x,y,z) can be obtained by a rotation of coordinates given by

$$\begin{cases} x' = x\cos\theta + z\sin\theta \\ y' = y \\ z' = -x\sin\theta + z\cos\theta \end{cases} \quad \text{(A.21)}$$

resulting in

$$E_\theta(x,y,z,\theta) \equiv E_{\text{gauss}}(x\cos\theta + z\sin\theta, y, -x\sin\theta + z\cos\theta) \quad \text{(A.22)}$$

where θ is the angle of incidence. The sum of the incident beam and reflected beam can be written as:

$$E_{\text{acc}}(x,y,z,\theta) = E_{\theta}(x,y,z,\theta) + r(\theta)E_{\theta}(x,y,z,-\theta) \tag{A.23}$$

where $r(\theta)$ is the reflectivity (including phase) of the SIL surface for a s-polarized light

$$r(\theta) = \frac{\sin\theta - n\sqrt{1-\frac{\cos^2\theta}{n^2}}}{\sin\theta + n\sqrt{1-\frac{\cos^2\theta}{n^2}}} \tag{A.24}$$

according to the Fresnel equations. For two optical accordion orthogonal to each other, the total relative intensity is calculated by the sum of each accordion separately:

$$I_{\text{acc}}(x,y,z,\theta) = \frac{1}{{E_0}^2}\langle |E_{\text{acc}}(x,y,z,\theta)|^2 + |E_{\text{acc}}(y,x,z,\theta)|^2 \rangle \tag{A.25}$$

where $\langle \cdots \rangle$ denotes the time average.

Finally, the potential depth can be calculated multiplying the relative intensity by the Eq. A.8

$$U_{\text{acc}}(x,y,z) = -I_{\text{acc}}(x,y,z,\theta_{\text{acc}}) \sum_{b\neq a} \frac{\hbar\Gamma_{ab}^2}{2I_{\text{sat}}} \frac{P_{\text{lat}}}{\pi w_{0z} w_{0y}} \left(\frac{1}{\omega_{ba} + \omega_{\text{lat}}} + \frac{1}{\omega_{ba} - \omega_{\text{lat}}} \right) \tag{A.26}$$

Fig. A.5 shows the potential in the ground state for two different angles of incidence and input powers.

The trap parameters such as potential depth in the z direction and trap frequencies were summarized in Table A.1. For deep angles of incidences both trap frequencies are roughly proportional to $\sqrt{P_{\text{lat}}}$ and the vertical trap frequency ω_z is proportional to $\sin\theta_{\text{acc}}$.

P_{lat}(W)	θ_{acc}(°)	$z_0(\mu$m)	$U_z(\mu$K)	$\omega_z/2\pi$ (kHz)	$\omega_{\text{xy}}/2\pi$ (kHz)	$\omega_z/\omega_{\text{xy}}$
0.095	0.7	17.5	1.04	0.27	0.078	3.5
1.1	0.7	15.0	47.4	1.1	0.28	4.0
2.1	0.7	14.9	95.0	1.5	0.38	4.0
0.095	1	13.5	3.4	0.45	0.096	4.7
1.1	1	12.4	71	1.6	0.33	4.9
2.1	1	12.4	139	2.2	0.45	4.9
0.095	6	2.60	8.5	2.9	0.17	25
1.1	6	2.57	105	9.7	0.40	25
2.1	6	2.57	200	13	0.55	25

Table A.1: Optical accordion: Trap parameters for different angles of incidence and input powers.

The potential for a retro-reflected optical accordion that forms an optical lattice can be

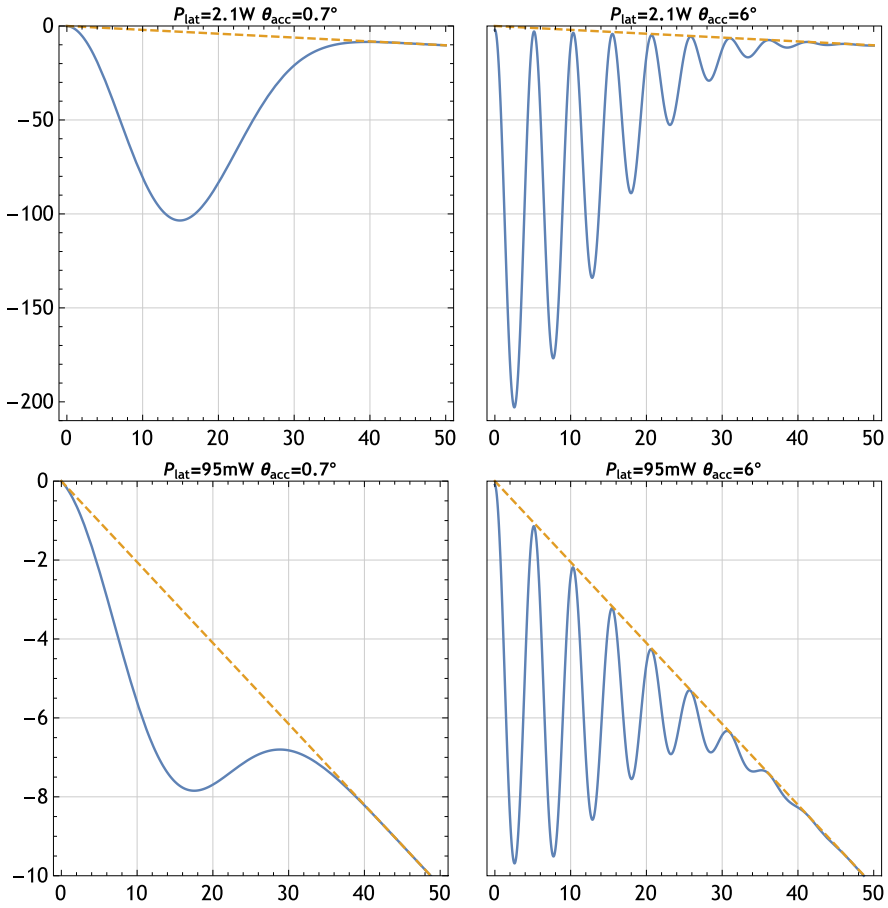

Figure A.5: Potential generated by an optical accordion for two different incident angles and input power.

calculated using Eq. A.23 by the formula

$$E_{\text{lat}}(x,y,z,\theta) = E_{\text{acc}}(x,y,z,\theta) + r(\theta)\sqrt{T}\,E_{\text{acc}}(x,y,z,\pi+\theta) \tag{A.27}$$

where T is the transmission of the optical elements used for retro-reflection (see Fig. 5.2). The relative intensity is defined in a similar way as in the accordion potential case:

$$I_{\text{lat}}(x,y,z,\theta) = \frac{1}{{E_0}^2}\langle |E_{\text{lat}}(x,y,z,\theta)|^2 + |E_{\text{lat}}(y,x,z,\theta)|^2\rangle. \tag{A.28}$$

The resultant potential profile in the z direction and x direction is shown in Fig. A.6 for an angle of incidence of $\theta_{\text{acc}} = 6°$. The potential depth is roughly $4\sqrt{0.5} = 2.8$ times bigger than the potential of the optical accordion as only 50% of the total power can be retro-reflected due to optical losses (see Fig. 5.2).

The potential depth in the z direction V_z is roughly two times bigger than the potential barrier in the xy direction (lattice depth). For simple calculations purposes and for the sim-

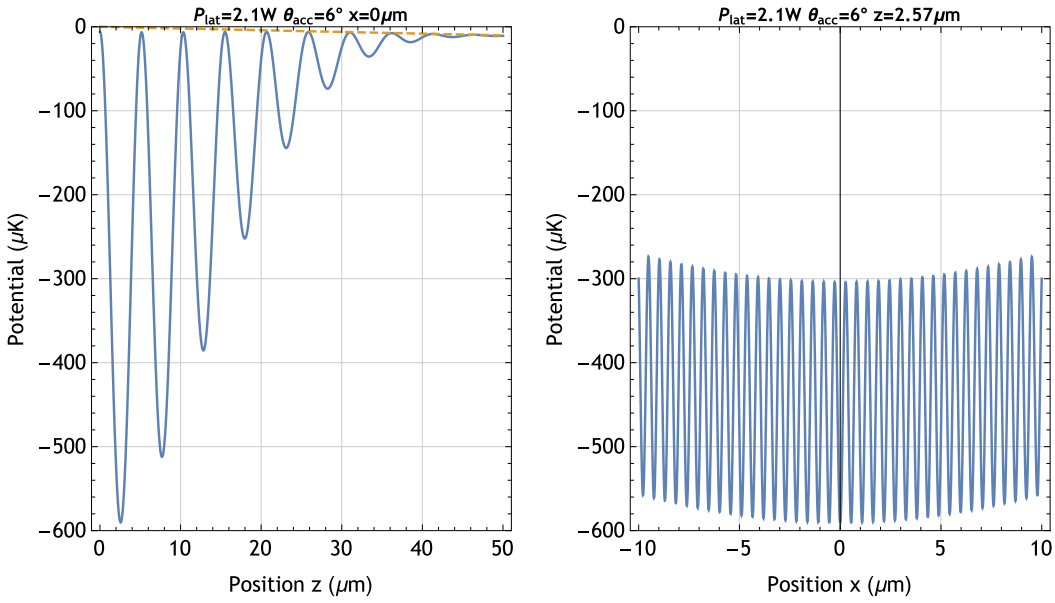

Figure A.6: Potential energy generated by a Gaussian beam in the case of a two-energy level system.

ulations in Chapter 3 the potential can be approximated to:

$$V(x,y,z) = -V_0 \sin^2(k_z z)\left(\cos^2(k_x x) + \cos^2(k_y y)\right) \tag{A.29}$$

by neglecting the effects of the harmonic envelope in the xy directions and the Gaussian profile in the z direction. The important parameters for the optical lattice trap were summarized in Table A.2. The trap frequency of the harmonic envelope in the x, y directions ω_{har} was included as it represents an important parameter to calculate the atomic distribution of a Mott-insulator.

P_{lat}(W)	$z_0(\mu\text{m})$	$V_z(\mu\text{K})$	$V_0(\mu\text{K})$	V_0/E_r	$\frac{\omega_z}{2\pi}$(kHz)	$\frac{\omega_{xy}}{2\pi}$(kHz)	$\frac{\omega_{har}}{2\pi}$(Hz)
0.007	2.71	1.4	0.95	20	1.3	8.6	52
1.1	2.57	305	150	3185	17	109	655
2.1	2.57	584	286	6080	23	150	905

Table A.2: Optical lattice: Potential and trap parameters for $\theta_{\text{acc}} = 6°$ and different input powers.

A.3 Evaporative Cooling

The local number density of atoms at the position $\mathbf{r}$ in a trap is $n(\mathbf{r})$. As long as trap volume and temperature do not change and no new atoms are loaded into the trap, this density evolves in time according to

$$\frac{dn(\mathbf{r},t)}{dt} = -\alpha n(\mathbf{r},t) - \beta n(\mathbf{r},t)^2 - \gamma n(\mathbf{r},t)^3 - O(n^4) \tag{A.30}$$

where α, β, γ are rate coefficients for different kinds of loss mechanism, e.g. background gas collisions (α), two-body inelastic collisions as radiative escape or photoassociation (β), or three-body collisions (γ). Integrating over all the volume gives an expression related to the total number of atoms N

$$\frac{dN(t)}{dt} = -\alpha N(t) - \beta \int_V n(\mathbf{r})^2 d\mathbf{r} - \gamma \int_V n(\mathbf{r},t)^3 d\mathbf{r} \tag{A.31}$$

The single-particle loss coefficient α takes into account collisions with the background gas in the vacuum apparatus. When the density is small enough that the two-body collisions and three-body collisions can be disregarded, eq. A.31 can be easily solved:

$$N(t) = N_0\, e^{-\alpha t} \tag{A.32}$$

where n_0 is the initial density of atoms. α is then equal to the inverse of the 1/e lifetime $\tau = 1/\alpha$.

The two-body loss coefficient β describes trap loss due to ultra-cold binary inelastic collisions. Inelastic collisions occurs when two atoms collide and the kinetic energy is not conserved. In general, such trap loss becomes important if the colliding atoms are not in their absolute ground state. Consequently, this type of loss can occur in a MOT due to light-assisted binary collisions involving atoms in the excited state, but it is negligibly small in an optical dipole trap.

Three-body losses, as described by the coefficient γ in Eq. A.31, become relevant only at extremely high densities, far exceeding the conditions of a MOT. In a collision of three atoms, a bound dimer can be formed and the third atom takes up the released energy, so that all three atoms are lost from the trap. As a far-detuned dipole trap allows one to completely suppress binary collision losses by putting the atoms into the absolute internal ground state, it represents an interesting tool for measurements on three-body collisions. The three-body collision rate for ^{174}Yb was experimentally calculated as $\gamma = (4.2 \pm 1.5) \times 10^{-29} \mathrm{cm}^6\mathrm{s}^{-1}$ [109].

Evaporative cooling in a optical dipole trap is directly related to two-body elastic collisions. When two atoms collide in an elastic way it results in two atoms having different kinetic energy. When the resultant high energy atom has enough energy to escape the trap, evaporation occurs and the overall temperature in the trap is decreased after thermalization.

Evaporation efficiency can be technically controlled by limiting the depth of the potential to $\eta k_B T$. In principle, there is no upper bound for the efficiency of evaporative cooling. This can be demonstrated by the following extreme example: With an extremely large η, one just

has to wait for the event that one particle has all the energy of the system. Evaporating a single particle then cools the whole system to zero temperature. Unfortunately, this cooling strategy would take an almost infinite amount of time. It is thus important to considerate both the efficiency and cooling speed of the cooling process.

A.3.1 Efficiency of evaporation

Evaporative cooling happens on a exponential scale, which means that the characteristic quantities for the evaporation process are therefore logarithmic derivatives. The efficiency of the evaporation process is defined as:

$$\zeta = \frac{d(\log T)}{d\log N)} = \frac{\dot{T}/T}{\dot{N}/N} \tag{A.33}$$

where T is the average temperature on the system, and N is the total number of atoms. This dimensionless quantity represents how much temperature the system decreases compared to the decrease in the number of trapped atoms.

A.3.2 Speed of evaporation

We consider particles at density n_0 in a box potential, and we assume that η is large enough. For an untruncated Maxwell-Boltzmann distribution, almost all the atoms with energy higher than $\eta k_B T$ that involve a collision will be removed from the trap. Thus, to calculate the rate it suffices to divide the number of atoms $N_{\mathrm{h}}$with energy larger than $\eta k_B T$ by the collision time τ_{el}.

$$\frac{dN}{dt} = -\frac{N_{\mathrm{h}}}{\tau_{\mathrm{el}}} \tag{A.34}$$

For η large enough, the number of atoms with energy larger than $\eta k_B T$ can be approximated as:

$$N_{\mathrm{h}} = 2N e^{-\eta}\sqrt{\frac{\eta}{\pi}} \tag{A.35}$$

The collision time can be expressed as

$$\frac{1}{\tau_{\mathrm{el}}} = n_0\,\sigma\,\upsilon_{\mathrm{h}} \tag{A.36}$$

where σ is the elastic collision cross section and υ is the velocity of the particles. On the other hand, the velocity of atoms with energy higher than $\eta k_B T$ is

$$\upsilon_{\mathrm{h}} = \sqrt{\frac{2\eta k_B T}{m}} = \frac{\sqrt{\pi\eta}\,\bar{\upsilon}}{2} \tag{A.37}$$

where $\bar{v}$ is the mean thermal velocity. Thus, replacing these equations the rate of evaporation results in:

$$\frac{dN}{dt} = -\frac{N_{\mathrm{h}}}{\tau_{\mathrm{el}}} = -2N e^{-\eta}\sqrt{\frac{\eta}{\pi}} n_0 \sigma \upsilon_{\mathrm{h}} = -2N n_0 \sigma \eta e^{-\eta}. \tag{A.38}$$

List of Figures

List of Tables

Bibliography

[1] Theodor W Hänsch and Arthur L Schawlow. Cooling of gases by laser radiation. *Optics Communications*, 13(1):68–69, 1975.

[2] D Wineland and H Dehmelt. Proposed: Laser fluorescence spectroscopy of tl+ mono-ion oscillator iii. *Bull. Am. Phys. Soc*, 637:168, 1975.

[3] D. J. Wineland, R. E. Drullinger, and F. L. Walls. Radiation-pressure cooling of bound resonant absorbers. *Phys. Rev. Lett.*, 40:1639–1642, Jun 1978.

[4] William D. Phillips and Harold Metcalf. Laser deceleration of an atomic beam. *Phys. Rev. Lett.*, 48:596–599, Mar 1982.

[5] John V. Prodan, William D. Phillips, and Harold Metcalf. Laser production of a very slow monoenergetic atomic beam. *Phys. Rev. Lett.*, 49:1149–1153, Oct 1982.

[6] C Audoin. Caesium beam frequency standards: Classical and optically pumped. *Metrologia*, 29(2):113, 1992.

[7] Masao Takamoto, Feng-Lei Hong, Ryoichi Higashi, and Hidetoshi Katori. An optical lattice clock. *Nature*, 435(7040):321–324, 2005.

[8] Hidetoshi Katori. Optical lattice clocks and quantum metrology. *Nature Photonics*, 5(4):203–210, 2011.

[9] Ichiro Ushijima, Masao Takamoto, Manoj Das, Takuya Ohkubo, and Hidetoshi Katori. Cryogenic optical lattice clocks. *Nature Photonics*, 9(3):185–189, 2015.

[10] TL Nicholson, SL Campbell, RB Hutson, GE Marti, BJ Bloom, RL McNally, W Zhang, MD Barrett, MS Safronova, GF Strouse, et al. Systematic evaluation of an atomic clock at 2 [times] 10-18 total uncertainty. *Nature communications*, 6, 2015.

[11] Satyendra Nath Bose. Plancks gesetz und lichtquantenhypothese. *Z. phys*, 26(3):178, 1924.

[12] Albert Einstein. *Quantentheorie des einatomigen idealen Gases*. Akademie der Wissenshaften, in Kommission bei W. de Gruyter, 1924.

[13] JF Allen and AD Misener. Flow of liquid helium ii. *Nature*, 141(3558):75, 1938.

[14] P Kapitza. Viscosity of liquid helium below the l-point. *Nature*, 141(3558):74, 1938.

[15] F. London. On the bose-einstein condensation. *Phys. Rev.*, 54:947–954, Dec 1938.

[16] Allen Miller, David Pines, and Philippe Nozières. Elementary excitations in liquid helium. *Phys. Rev.*, 127:1452–1464, Sep 1962.

[17] P. C. Hohenberg and P. C. Martin. Superfluid dynamics in the hydrodynamic ($\omega\tau \ll 1$) and collisionless ($\omega\tau \gg 1$) domains. *Phys. Rev. Lett.*, 12:69–71, Jan 1964.

[18] R. A. Cowley and A. D. B. Woods. Neutron scattering from liquid helium at high energies. *Phys. Rev. Lett.*, 21:787–789, Sep 1968.

[19] Naoto Masuhara, John M. Doyle, Jon C. Sandberg, Daniel Kleppner, Thomas J. Greytak, Harald F. Hess, and Greg P. Kochanski. Evaporative cooling of spin-polarized atomic hydrogen. *Phys. Rev. Lett.*, 61:935–938, Aug 1988.

[20] M. H. Anderson, J. R. Ensher, M. R. Matthews, C. E. Wieman, and E. A. Cornell. Observation of bose-einstein condensation in a dilute atomic vapor. *Science*, 269(5221):198–201, 1995.

[21] K. B. Davis, M. O. Mewes, M. R. Andrews, N. J. van Druten, D. S. Durfee, D. M. Kurn, and W. Ketterle. Bose-einstein condensation in a gas of sodium atoms. *Phys. Rev. Lett.*, 75:3969–3973, Nov 1995.

[22] M. R. Andrews, C. G. Townsend, H.-J. Miesner, D. S. Durfee, D. M. Kurn, and W. Ketterle. Observation of interference between two bose condensates. *Science*, 275(5300):637–641, 1997.

[23] Juliette Billy, Vincent Josse, Zhanchun Zuo, Alain Bernard, Ben Hambrecht, Pierre Lugan, David Clément, Laurent Sanchez-Palencia, Philippe Bouyer, and Alain Aspect. Direct observation of anderson localization of matter waves in a controlled disorder. *Nature*, 453(7197):891–894, 2008.

[24] Giacomo Roati, Chiara DâĂŹErrico, Leonardo Fallani, Marco Fattori, Chiara Fort, Matteo Zaccanti, Giovanni Modugno, Michele Modugno, and Massimo Inguscio. Anderson localization of a non-interacting bose–einstein condensate. *Nature*, 453(7197):895–898, 2008.

[25] J. R. Abo-Shaeer, C. Raman, J. M. Vogels, and W. Ketterle. Observation of vortex lattices in bose-einstein condensates. *Science*, 292(5516):476–479, 2001.

[26] KW Madison, F Chevy, W Wohlleben, and J Dalibard. Vortices in a stirred bose-einstein condensate. *Journal of modern optics*, 47(14-15):2715–2723, 2000.

[27] Zoran Hadzibabic, Peter Krüger, Marc Cheneau, Baptiste Battelier, and Jean Dalibard. Berezinskii–kosterlitz–thouless crossover in a trapped atomic gas. *Nature*, 441(7097):1118–1121, 2006.

[28] Ph. Courteille, R. S. Freeland, D. J. Heinzen, F. A. van Abeelen, and B. J. Verhaar. Observation of a feshbach resonance in cold atom scattering. *Phys. Rev. Lett.*, 81:69–72, Jul 1998.

[29] S Inouye, MR Andrews, J Stenger, H-J Miesner, DM Stamper-Kurn, and W Ketterle. Observation of feshbach resonances in a bose–einstein condensate. *Nature*, 392(6672):151–154, 1998.

[30] T Kraemer, M Mark, P Waldburger, JG Danzl, C Chin, B Engeser, AD Lange, K Pilch, A Jaakkola, H-C Nägerl, et al. Evidence for efimov quantum states in an ultracold gas of caesium atoms. *Nature*, 440(7082):315–318, 2006.

[31] C. A. Regal, M. Greiner, and D. S. Jin. Observation of resonance condensation of fermionic atom pairs. *Phys. Rev. Lett.*, 92:040403, Jan 2004.

[32] M. W. Zwierlein, C. A. Stan, C. H. Schunck, S. M. F. Raupach, A. J. Kerman, and W. Ketterle. Condensation of pairs of fermionic atoms near a feshbach resonance. *Phys. Rev. Lett.*, 92:120403, Mar 2004.

[33] J. Kinast, S. L. Hemmer, M. E. Gehm, A. Turlapov, and J. E. Thomas. Evidence for superfluidity in a resonantly interacting fermi gas. *Phys. Rev. Lett.*, 92:150402, Apr 2004.

[34] T. Bourdel, L. Khaykovich, J. Cubizolles, J. Zhang, F. Chevy, M. Teichmann, L. Tarruell, S. J. J. M. F. Kokkelmans, and C. Salomon. Experimental study of the bec-bcs crossover region in lithium 6. *Phys. Rev. Lett.*, 93:050401, Jul 2004.

[35] C. Chin, M. Bartenstein, A. Altmeyer, S. Riedl, S. Jochim, J. Hecker Denschlag, and R. Grimm. Observation of the pairing gap in a strongly interacting fermi gas. *Science*, 305(5687):1128–1130, 2004.

[36] G. B. Partridge, K. E. Strecker, R. I. Kamar, M. W. Jack, and R. G. Hulet. Molecular probe of pairing in the bec-bcs crossover. *Phys. Rev. Lett.*, 95:020404, Jul 2005.

[37] Martin W Zwierlein, Jamil R Abo-Shaeer, Andre Schirotzek, Christian H Schunck, and Wolfgang Ketterle. Vortices and superfluidity in a strongly interacting fermi gas. *Nature*, 435(7045):1047–1051, 2005.

[38] Richard Feynman. Simulating physics with computers. *International Journal of Theoretical Physics*, 21:467–488, 1982. 10.1007/BF02650179.

[39] Immanuel Bloch, Jean Dalibard, and Sylvain Nascimbène. Quantum simulations with ultracold quantum gases. *Nature Physics*, 8(4):267–276, 2012.

[40] J George Bednorz and K Alex Müller. Possible high tc superconductivity in the ba-la-cu-o system. *Zeitschrift für Physik B Condensed Matter*, 64(2):189–193, 1986.

[41] W. Hofstetter, J. I. Cirac, P. Zoller, E. Demler, and M. D. Lukin. High-temperature superfluidity of fermionic atoms in optical lattices. *Phys. Rev. Lett.*, 89:220407, Nov 2002.

[42] Robert Jördens, Niels Strohmaier, Kenneth Günter, Henning Moritz, and Tilman Esslinger. A mott insulator of fermionic atoms in an optical lattice. *Nature*, 455(7210):204–207, 2008.

[43] Patrick A. Lee, Naoto Nagaosa, and Xiao-Gang Wen. Doping a mott insulator: Physics of high-temperature superconductivity. *Rev. Mod. Phys.*, 78:17–85, Jan 2006.

[44] H. J. Schulz. Superconductivity and antiferromagnetism in the two-dimensional hubbard model: Scaling theory. *EPL (Europhysics Letters)*, 4(5):609, 1987.

[45] Matthias Troyer and Uwe-Jens Wiese. Computational complexity and fundamental limitations to fermionic quantum monte carlo simulations. *Phys. Rev. Lett.*, 94:170201, May 2005.

[46] Waseem S. Bakr, Jonathon I. Gillen, Amy Peng, Simon Folling, and Markus Greiner. A quantum gas microscope for detecting single atoms in a hubbard-regime optical lattice. *Nature (London)*, 462:74–77, Nov 2009.

[47] Jacob F. Sherson, Christof Weitenberg, Manuel Endres, Marc Cheneau, Immanuel Bloch, and Stefan Kuhr. Single-atom-resolved fluorescence imaging of an atomic mott insulator. *Nature (London)*, 467:68–72, Sep 2010.

[48] Jonathan Simon, Waseem S. Bakr, Ruichao Ma, M. Eric Tai, Philipp M. Preiss, and Markus Greiner. Quantum simulation of antiferromagnetic spin chains in an optical lattice. *Nature (London)*, 472:307–312, Apr 2011.

[49] Philipp M. Preiss, Ruichao Ma, M. Eric Tai, Alexander Lukin, Matthew Rispoli, Philip Zupancic, Yoav Lahini, Rajibul Islam, and Markus Greiner. Strongly correlated quantum walks in optical lattices. *Science*, 347(6227):1229–1233, 2015.

[50] Peter Schauß, Johannes Zeiher, Takeshi Fukuhara, S Hild, M Cheneau, T Macrì, T Pohl, Immanuel Bloch, and Christian Groß. Crystallization in ising quantum magnets. *Science*, 347(6229):1455–1458, 2015.

[51] Martin Miranda, Ryotaro Inoue, Yuki Okuyama, Akimasa Nakamoto, and Mikio Kozuma. Site-resolved imaging of ytterbium atoms in a two-dimensional optical lattice. *Phys. Rev. A*, 91:063414, Jun 2015.

[52] Maxwell F. Parsons, Florian Huber, Anton Mazurenko, Christie S. Chiu, Widagdo Setiawan, Katherine Wooley-Brown, Sebastian Blatt, and Markus Greiner. Site-resolved imaging of fermionic ^{6}Li in an optical lattice. *Phys. Rev. Lett.*, 114:213002, May 2015.

[53] Ahmed Omran, Martin Boll, Timon A. Hilker, Katharina Kleinlein, Guillaume Salomon, Immanuel Bloch, and Christian Gross. Microscopic observation of pauli blocking in degenerate fermionic lattice gases. *Phys. Rev. Lett.*, 115:263001, Dec 2015.

[54] Daniel Greif, Maxwell F Parsons, Anton Mazurenko, Christie S Chiu, Sebastian Blatt, Florian Huber, Geoffrey Ji, and Markus Greiner. Site-resolved imaging of a fermionic mott insulator. *arXiv preprint arXiv:1511.06366*, 2015.

[55] Lawrence W. Cheuk, Matthew A. Nichols, Melih Okan, Thomas Gersdorf, Vinay V. Ramasesh, Waseem S. Bakr, Thomas Lompe, and Martin W. Zwierlein. Quantum-gas microscope for fermionic atoms. *Phys. Rev. Lett.*, 114:193001, May 2015.

[56] Elmar Haller, James Hudson, Andrew Kelly, Dylan A. Cotta, Bruno Peaudecerf, Graham D. Bruce, and Stefan Kuhr. Single-atom imaging of fermions in a quantum-gas microscope. *Nat Phys*, 11(9):738–742, Sep 2015. Letter.

[57] G. J. A. Edge, R. Anderson, D. Jervis, D. C. McKay, R. Day, S. Trotzky, and J. H. Thywissen. Imaging and addressing of individual fermionic atoms in an optical lattice. *Phys. Rev. A*, 92:063406, Dec 2015.

[58] Ryuta Yamamoto, Jun Kobayashi, Takuma Kuno, Kohei Kato, and Yoshiro Takahashi. An ytterbium quantum gas microscope with narrow-line laser cooling. *New Journal of Physics*, 18(2):023016, 2016.

[59] D C McKay and B DeMarco. Cooling in strongly correlated optical lattices: prospects and challenges. *Reports on Progress in Physics*, 74(5):054401, 2011.

[60] Jean-Sébastien Bernier, Corinna Kollath, Antoine Georges, Lorenzo De Leo, Fabrice Gerbier, Christophe Salomon, and Michael Köhl. Cooling fermionic atoms in optical lattices by shaping the confinement. *Phys. Rev. A*, 79:061601, Jun 2009.

[61] Kosuke Shibata, Ryuta Yamamoto, Yu Seki, and Yoshiro Takahashi. Optical spectral imaging of a single layer of a quantum gas with an ultranarrow optical transition. *Phys. Rev. A*, 89:031601, Mar 2014.

[62] Shinya Kato, Seiji Sugawa, Kosuke Shibata, Ryuta Yamamoto, and Yoshiro Takahashi. Control of resonant interaction between electronic ground and excited states. *Phys. Rev. Lett.*, 110:173201, Apr 2013.

[63] Nist - basic atomic spectroscopic data, 2015. Accessed: 2015-12-01.

[64] K. Honda, Y. Takahashi, T. Kuwamoto, M. Fujimoto, K. Toyoda, K. Ishikawa, and T. Yabuzaki. Magneto-optical trapping of yb atoms and a limit on the branching ratio of the $^1P_1$ state. *Phys. Rev. A*, 59:R934–R937, Feb 1999.

[65] C. W. Hoyt, Z. W. Barber, C. W. Oates, T. M. Fortier, S. A. Diddams, and L. Hollberg. Observation and absolute frequency measurements of the $^1s_0$-$^3p_0$ optical clock transition in neutral ytterbium. *Phys. Rev. Lett.*, 95:083003, Aug 2005.

[66] Z. W. Barber, J. E. Stalnaker, N. D. Lemke, N. Poli, C. W. Oates, T. M. Fortier, S. A. Diddams, L. Hollberg, C. W. Hoyt, A. V. Taichenachev, and V. I. Yudin. Optical lattice induced light shifts in an yb atomic clock. *Phys. Rev. Lett.*, 100:103002, Mar 2008.

[67] AV Gorshkov, M Hermele, V Gurarie, C Xu, PS Julienne, J Ye, P Zoller, E Demler, MD Lukin, and AM Rey. Two-orbital su (n) magnetism with ultracold alkaline-earth atoms. *Nature Physics*, 6(4):289–295, 2010.

[68] Andrew J. Daley, Martin M. Boyd, Jun Ye, and Peter Zoller. Quantum computing with alkaline-earth-metal atoms. *Phys. Rev. Lett.*, 101:170504, Oct 2008.

[69] Iris Reichenbach and Ivan H. Deutsch. Sideband cooling while preserving coherences in the nuclear spin state in group-ii-like atoms. *Phys. Rev. Lett.*, 99:123001, Sep 2007.

[70] K Shibata, S Kato, A Yamaguchi, S Uetake, and Y Takahashi. A scalable quantum computer with ultranarrow optical transition of ultracold neutral atoms in an optical lattice. *Applied Physics B*, 97(4):753–758, 2009.

[71] S Kato, K Shibata, R Yamamoto, Y Yoshikawa, and Y Takahashi. Optical magnetic resonance imaging with an ultra-narrow optical transition. *Applied Physics B*, 108(1):31–38, 2012.

[72] S Uetake, A Yamaguchi, D Hashimoto, and Y Takahashi. High-resolution laser spectroscopy of ultracold ytterbium atoms using spin-forbidden electric quadrupole transition. *Applied Physics B*, 93(2-3):409–414, 2008.

[73] Y. S. Bai and T. W. Mossberg. Lifetime and oscillator-strength studies involving the $(6s6p)^3P_1$-$(6s7s)^1S_0$ transition of atomic yb. *Phys. Rev. A*, 35:619–621, Jan 1987.

[74] Masaaki Kitagawa, Katsunari Enomoto, Kentaro Kasa, Yoshiro Takahashi, Roman Ciuryło, Pascal Naidon, and Paul S. Julienne. Two-color photoassociation spectroscopy of ytterbium atoms and the precise determinations of s-wave scattering lengths. *Phys. Rev. A*, 77:012719, Jan 2008.

[75] Dipankar Das, Sachin Barthwal, Ayan Banerjee, and Vasant Natarajan. Absolute frequency measurements in yb with 0.08 ppb uncertainty: Isotope shifts and hyperfine structure in the 399-nm $^1s_0 \rightarrow ^1p_1$ line. *Phys. Rev. A*, 72:032506, Sep 2005.

[76] D. L. Clark, M. E. Cage, D. A. Lewis, and G. W. Greenlees. Optical isotopic shifts and hyperfine splittings for yb. *Phys. Rev. A*, 20:239–253, Jul 1979.

[77] Kanhaiya Pandey, Alok K. Singh, P. V. Kiran Kumar, M. V. Suryanarayana, and Vasant Natarajan. Isotope shifts and hyperfine structure in the 555.8-nm $^1S_0 \rightarrow ^3P_1$ line of yb. *Phys. Rev. A*, 80:022518, Aug 2009.

[78] S. Lukman Winoto, Marshall T. DePue, Nathan E. Bramall, and David S. Weiss. Laser cooling at high density in deep far-detuned optical lattices. *Phys. Rev. A*, 59:R19–R22, Jan 1999.

[79] S. E. Hamann, D. L. Haycock, G. Klose, P. H. Pax, I. H. Deutsch, and P. S. Jessen. Resolved-sideband raman cooling to the ground state of an optical lattice. *Phys. Rev. Lett.*, 80:4149–4152, May 1998.

[80] Vladan Vuletić, Cheng Chin, Andrew J. Kerman, and Steven Chu. Degenerate raman sideband cooling of trapped cesium atoms at very high atomic densities. *Phys. Rev. Lett.*, 81:5768–5771, Dec 1998.

[81] R. Zhang, N. V. Morrow, P. R. Berman, and G. Raithel. Laser cooling in an optical lattice that employs raman transitions. *Phys. Rev. A*, 72:043409, Oct 2005.

[82] Giovanna Morigi, Jürgen Eschner, and Christoph H Keitel. Ground state laser cooling using electromagnetically induced transparency. *Phys. Rev. Lett.*, 85(21):4458, 2000.

[83] Giovanna Morigi. Cooling atomic motion with quantum interference. *Phys. Rev. A*, 67(3):033402, 2003.

[84] Jun Woo Cho, Han-gyeol Lee, Sangkyung Lee, Jaewook Ahn, Won-Kyu Lee, Dai-Hyuk Yu, Sun Kyung Lee, and Chang Yong Park. Optical repumping of triplet-p states enhances magneto-optical trapping of ytterbium atoms. *Phys. Rev. A*, 85:035401, Mar 2012.

[85] Minsoo Song, Duseong Yoon, and Taihyun Yoon. Doppler-free two-photon spectroscopy of yb atoms and efficient generation of a cascade of two photons at 611.3 nm and 555.8 nm. *Journal of the Korean Physical Society*, 2011.

[86] M Baumann, M Braun, A Gaiser, and H Liening. Radiative lifetimes and g j factors of low-lying even-parity levels in the yb i spectrum. *Journal of Physics B: Atomic and Molecular Physics*, 18(17):L601, 1985.

[87] WF Meggers and JL Tech. 1st spectrum of ytterbium (yb i). *JOURNAL OF RESEARCH OF THE NATIONAL BUREAU OF STANDARDS*, 83(1):13–70, 1978.

[88] YS Bai and TW Mossberg. Lifetime and oscillator-strength studies involving the (6s6p) 3 p 1-(6s7s) 1 s 0 transition of atomic yb. *Physical Review A*, 35(2):619, 1987.

[89] T. Loftus, J. R. Bochinski, and T. W. Mossberg. Magnetic trapping of ytterbium and the alkaline-earth metals. *Phys. Rev. A*, 66:013411, Jul 2002.

[90] Tai Hyun Yoon, Chang Yong Park, and Sung Jong Park. Laser-induced birefringence in a wavelength-mismatched cascade system of inhomogeneously broadened yb atoms. *Phys. Rev. A*, 70:061803, Dec 2004.

[91] S. M. Mansfield and G. S. Kino. Solid immersion microscope. *Applied Physics Letters*, 57(24):2615–2616, 1990.

[92] Kazuhito Honda. PhD thesis.

[93] Vapor pressure data, 2015. Accessed: 2015-12-01.

[94] T. Kuwamoto, K. Honda, Y. Takahashi, and T. Yabuzaki. Magneto-optical trapping of yb atoms using an intercombination transition. *Phys. Rev. A*, 60:R745–R748, Aug 1999.

[95] J. I. Gillen, W. S. Bakr, A. Peng, P. Unterwaditzer, S. Fölling, and M. Greiner. Two-dimensional quantum gas in a hybrid surface trap. *Phys. Rev. A*, 80:021602, Aug 2009.

[96] T. C. Li, H. Kelkar, D. Medellin, and M. G. Raizen. Real-time control of the periodicity of a standing wave: an optical accordion. *Opt. Express*, 16(8):5465–5470, Apr 2008.

[97] Paul F. Goldsmith. *Quasioptical Systems: Gaussian Beam Quasioptical Propogation and Applications*. Wiley-IEEE Press, 1993.

[98] K Akiba, K Kashiwagi, M Arikawa, and M Kozuma. Storage and retrieval of nonclassical photon pairs and conditional single photons generated by the parametric down-conversion process. *New Journal of Physics*, 11(1):013049, 2009.

[99] J. Söding, D. Guéry-Odelin, P. Desbiolles, F. Chevy, H. Inamori, and J. Dalibard. Three-body decay of a rubidium bose–einstein condensate. *Applied Physics B*, 69(4):257–261, 2014.

[100] Takeshi Fukuhara, Yosuke Takasu, Mitsutaka Kumakura, and Yoshiro Takahashi. Degenerate fermi gases of ytterbium. *Phys. Rev. Lett.*, 98:030401, Jan 2007.

[101] Shintaro Taie, Rekishu Yamazaki, Seiji Sugawa, and Yoshiro Takahashi. An su (6) mott insulator of an atomic fermi gas realized by large-spin pomeranchuk cooling. *Nature Physics*, 8(11):825–830, 2012.

[102] Shintaro Taie, Yosuke Takasu, Seiji Sugawa, Rekishu Yamazaki, Takuya Tsujimoto, Ryo Murakami, and Yoshiro Takahashi. Realization of a SU(2) × SU(6) system of fermions in a cold atomic gas. *Phys. Rev. Lett.*, 105:190401, Nov 2010.

[103] L. Windholz and M. Musso. Stark-effect investigations of the sodium D_2 line. *Phys. Rev. A*, 39:2472–2480, Mar 1989.

[104] L. Windholz, M. Musso, G. Zerza, and H. Jäger. Precise stark-effect investigations of the lithium d_1 and d_2 lines. *Phys. Rev. A*, 46:5812–5818, Nov 1992.

[105] Andreas Neuzner, Matthias Körber, Stephan Dürr, Gerhard Rempe, and Stephan Ritter. Breakdown of atomic hyperfine coupling in a deep optical-dipole trap. *Phys. Rev. A*, 92:053842, Nov 2015.

[106] Yun-Jhih Chen, Luís Felipe Gonçalves, and Georg Raithel. Measurement of rb $5P_{3/2}$ scalar and tensor polarizabilities in a 1064-nm light field. *Phys. Rev. A*, 92:060501, Dec 2015.

[107] Ionut D. Prodan, Marin Pichler, Mark Junker, Randall G. Hulet, and John L. Bohn. Intensity dependence of photoassociation in a quantum degenerate atomic gas. *Phys. Rev. Lett.*, 91:080402, Aug 2003.

[108] C. McKenzie, J. Hecker Denschlag, H. Häffner, A. Browaeys, Luís E. E. de Araujo, F. K. Fatemi, K. M. Jones, J. E. Simsarian, D. Cho, A. Simoni, E. Tiesinga, P. S. Julienne, K. Helmerson, P. D. Lett, S. L. Rolston, and W. D. Phillips. Photoassociation of sodium in a bose-einstein condensate. *Phys. Rev. Lett.*, 88:120403, Mar 2002.

[109] Takeshi Fukuhara, Seiji Sugawa, Yosuke Takasu, and Yoshiro Takahashi. All-optical formation of quantum degenerate mixtures. *Phys. Rev. A*, 79:021601, Feb 2009.

Acknowledgements

First and foremost I would like to thank my advisor Prof. Mikio Kozuma. Since I started this research under his advice in my fourth year of undergraduate, he taught me all the theoretical and experimental aspects of ultracold atoms. During the six years of research in this laboratory, he encouraged my research and allowed me to grow as a research scientist.

I would also like to express my gratitude to the members of the examination committee, Kiyotaka Aikawa, Akihisa Koga, Hideto Kanamori, Mikio Kozuma and Yusuke Nishida, who dedicated their time and interest and provided helpful comments.

I acknowledge all the people who collaborated experimentally and theoretically in the realization of this project: Atsushi Noguchi, Yujiro Eto, Akimasa Nakamoto, Hitomi Ono, Yuki Okuyama, Ryusuke Hisatomi, Izumi Shomura, Naoki Tambo, Takahiro Ogino, Honda Kazuhito, Ryotaro Inoue and Mikio Kozuma. I would also like to thank to the former members of the ERATO Project: Shin Inouye, Tetsuo Kishimoto, Takashi Mukaiyama and Masahito Ueda who provided insightful ideas and helpful comments, specially during the first stages of this project.

Finally, this project would have not been possible without all the generous financial support. Everyday financial support for my Ph.D. course was provided by the Japan Society for the Promotion of Science.